Downloaded from orbit.dtu.dk on: May 05, 2023

DTU Library

Recycling CO2 into Sustainable Hydrocarbon Fuels: Electrolysis of CO2 and H2O

Graves, Christopher R.

Publication date:
2010

Document Version
Publisher's PDF, also known as Version of record

Link back to DTU Orbit

Citation (APA):
Graves, C. R. (2010). *Recycling CO2 into Sustainable Hydrocarbon Fuels: Electrolysis of CO2 and H2O*. Columbia University.

General rights
Copyright and moral rights for the publications made accessible in the public portal are retained by the authors and/or other copyright owners and it is a condition of accessing publications that users recognise and abide by the legal requirements associated with these rights.

- Users may download and print one copy of any publication from the public portal for the purpose of private study or research.
- You may not further distribute the material or use it for any profit-making activity or commercial gain
- You may freely distribute the URL identifying the publication in the public portal

If you believe that this document breaches copyright please contact us providing details, and we will remove access to the work immediately and investigate your claim.

Recycling CO_2 into Sustainable Hydrocarbon Fuels: Electrolysis of CO_2 and H_2O

Christopher Ronald Graves

Submitted in partial fulfillment of the
requirements for the degree
of Doctor of Philosophy
in the Graduate School of Arts and Sciences

COLUMBIA UNIVERSITY
2010

©2010

Christopher R Graves
All Rights Reserved

ABSTRACT

Recycling CO_2 into Sustainable Hydrocarbon Fuels: Electrolysis of CO_2 and H_2O

Christopher Ronald Graves

Great quantities of hydrocarbon fuels will be needed for the foreseeable future, even if electricity based energy carriers begin to partially replace liquid hydrocarbons in the transportation sector. Fossil fuels and biomass are the most common feedstocks for production of hydrocarbon fuels. However, using renewable or nuclear energy, carbon dioxide and water can be recycled into sustainable hydrocarbon fuels in non-biological processes which remove oxygen from CO_2 and H_2O (the reverse of fuel combustion). Capture of CO_2 from the atmosphere would enable a closed-loop carbon-neutral fuel cycle.

The purpose of this work was to develop critical components of a system that recycles CO_2 into liquid hydrocarbon fuels. The concept is examined at several scales, beginning with a broad scope analysis of large-scale sustainable energy systems and ultimately studying electrolysis of CO_2 and H_2O in high temperature solid oxide cells as the heart of the energy conversion, in the form of three experimental studies. The contributions of these studies include discoveries about electrochemistry and materials that could significantly improve the overall energy use and economics of the CO_2-to-fuels system.

The broad scale study begins by assessing the sustainability and practicality of the various energy carriers that could replace petroleum-derived hydrocarbon fuels, including other hydrocarbons, hydrogen, and storage of electricity on-board vehicles in batteries, ultracapacitors, and flywheels. Any energy carrier can store the energy of any energy source. This sets the context for CO_2 recycling – sustainable energy sources like solar and wind power can be used to provide the most energy-dense, convenient fuels which can be readily used in the existing infrastructure. The many ways to recycle CO_2 into hydrocarbons, based on thermolysis, thermochemical loops, electrolysis, and photoelectrolysis of CO_2 and/or H_2O, are critically reviewed. A process based on high temperature co-electrolysis of CO_2 and H_2O to produce syngas (CO/H_2 mixture) is identified as a promising method. High temperature electrolysis makes very efficient use of electricity and heat (near-100% electricity-to-syngas efficiency), provides high reaction rates, and the syngas produced can be catalytically converted to hydrocarbons in well-known fuel synthesis reactors (e.g. Fischer-Tropsch).

The experimental studies of high temperature electrolysis are made at different scales – at the cell level, electrode level, and in materials and microstructure development. The results include cell performance and durability, insight into electrode reaction mechanisms, and new

high-performance electrode materials. The experimental studies make extensive use of electrochemical impedance spectroscopy and systematic variation of test conditions to examine the electrochemical phenomena. Variation of the material composition itself within families of related materials was an additional parameter used in the electrode level and materials studies that revealed more information than studying a single material would have.

Using full cells, the performance and durability of a solid oxide cell applied for co-electrolysis of CO_2 and H_2O was investigated. High initial performance was observed but the long-term durability needs to be improved. Based on these results, an analysis of the energy balance and economics of an electrolysis-based synthetic fuel production process, including CO_2 air capture and Fischer-Tropsch fuel synthesis, determined that the system can feasibly operate at 70% electricity-to-liquid fuel efficiency (higher heating value basis) and that the price of electricity needed to produce competitive synthetic gasoline (at USD$2/gal, or $0.53/L, wholesale) is 2-3 U.S. cents per kWh. For $3/gal ($0.78/L) gasoline, 4-5 cents per kWh is needed. Fuel production may already be economical in some regions that have inexpensive renewable electricity, such as Iceland. The dominant costs of the process are the electricity cost and the capital cost of the electrolyzer, and this capital cost is significantly increased when operating intermittently (on renewable power sources such as solar and wind). Low cell internal resistance, low degradation, and low manufacturing cost each contribute to a low electrolyzer capital cost, and can be traded off. One straightforward path to affordability is by improving the durability of the high current density cell operation ($\geq$1 A/cm^2) that is already possible with these cells. The negative-electrode, a composite of nickel and yttria-stabilized zirconia (YSZ), is often the major site of cell degradation, including in the co-electrolysis results presented here.

To better understand the reaction mechanisms at the negative-electrode that limit performance and durability, different metal electrodes including nickel were studied using a simplified point-contact electrode geometry with a well-defined three-phase boundary (TPB; the electrode/electrolyte/gas interface where the electrochemical reactions take place). The simple geometry is useful for isolating the electrochemical properties without the effects of the complex microstructure of technological porous electrodes. Widely different impedance responses of the different metals to the same changes in test conditions (gas composition, temperature, and polarization) were observed, indicating that the same reaction mechanisms are not shared by the different metals, contrary to some recent studies. Evidence was also found that supports the explanation that impurities segregated to the TPB play a major role and are largely responsible for inconsistencies in the electrode kinetics literature. The significance of microstructure at the TPB was also revealed – the electrode polarization resistance was reduced by an order of magnitude when subjected to extreme conditions of oxidation-reduction and strong cathodic polarization, which induced the formation of a micro/nanostructured TPB. Possible reaction mechanisms for H_2O/CO_2 reduction and H_2/CO oxidation are discussed.

Novel ceramic materials based on molybdates with varying Mo valence were synthesized as possible alternative negative-electrode materials. The phase, stability, microstructure and electrical conductivity were characterized. The electrochemical activity for H_2O/CO_2 reduction and H_2/CO oxidation was studied using simplified geometry electrodes, similar to the metals study. Unique phenomena were observed for some of the molybdate materials – they decomposed into multiple phases and formed a nanostructured surface upon exposure to operating conditions (in certain reducing atmospheres). The new phases and surface features enhanced the electronic conductivity and electrocatalytic activity. Preparing an electrode by performing controlled decomposition to form multiple desirable phases and a desirable microstructure (which can take place *in situ*) using these materials is a novel way to produce potentially high-performance electrodes for solid oxide cells. By modifying the composition, it was possible to prevent decomposition. Other members of the molybdate family exhibited similarly high electronic conductivity and electrocatalytic activity but did not decompose. The high activity was the result of a different mechanism, probably related to the defect chemistry of the material. The polarization resistances of the best molybdate materials were two orders of magnitude lower than that of donor-doped strontium titanates. Many of the molybdate materials were significantly activated by cathodic polarization, and they exhibited higher performance for cathodic (electrolysis) polarization than anodic (fuel cell) polarization, which makes them especially interesting for use in electrolysis electrodes. Whereas nearly all of the molybdates showed higher performance for H_2O electrolysis than CO_2 electrolysis, one with vanadium showed nearly equal performance, and a non-molybdate which exhibits some complementary properties to the best molybdates, Gd-doped ceria in nanoparticle form, was found to be an excellent electrocatalyst for CO_2 electrolysis and CO oxidation (moreso than for H_2O/H_2 for which it is known to be good).

Recycling CO_2 into Sustainable Hydrocarbon Fuels: Electrolysis of CO_2 and H_2O

Copyright 2010 by

Christopher R Graves
crg2109@columbia.edu
christopher.r.graves@gmail.com

May, 2010

Dissertation Thesis for Doctor of Philosophy

Department of Earth & Environmental Engineering
Columbia University
http://www.eee.columbia.edu

&

Lenfest Center for Sustainable Energy
The Earth Instite at Columbia University
http://www.energy.columbia.edu

&

Fuel Cells and Solid State Chemistry Division
Risø National Laboratory for Sustainable Energy, DTU
http://www.risoe.dk

Table of Contents

List of Figures

List of Tables

List of Abbreviations

AC	Alternating current
ADIS	Analysis of differences in impedance spectra
AFM	Atomic force microscope
ASR	Area-specific resistance
ASR_P	Area-specific polarization resistance
CCS	Carbon capture and storage
CGO	Gd-doped ceria
CNLS	Complex nonlinear least-squares
DC	Direct current
DOD	Depth-of-discharge
DRT	Distribution of relaxation times
E_A	Activation energy
EDX	Energy-dispersive X-ray spectroscopy
EIS	Electrochemical impedance spectroscopy
GHG	Greenhouse gas
HEV	Hybrid electric vehicle
IS	Impedance spectra
i-V	Polarization curve
LDC	La-doped ceria
LM	Amorphous La-Mo-O
LSM	Lanthanum strontium manganite
LSR_P	Length-specific polarization resistance
MIEC	Mixed ionic electronic conductor
OCV	Open circuit voltage
PEM	Polymer electrolyte membrane
PHEV	Plug-in hybrid electric vehicle
pO_2	Partial pressure of oxygen
pX	Partial pressure of gas X (e.g. H_2)
PV	Photovoltaic
RMS	Root mean square
R_P	Polarization resistance
R_S	Serial resistance
RWGS	Reverse water-gas shift
SCM	Sr_2CoMoO_6
SCP	Strong cathodic polarization

SEM	Scanning electron microscope/microscopy
SFM	Sr_2FeMoO_6
SM	$SrMoO_3$
SMM	Sr_2MgMoO_6
SMW	Sr_2MgWO_6
SNM	Sr_2NiMoO_6
SNW	Sr_2NiWO_6
SOC	Solid oxide cell
SOEC	Solid oxide electrolysis cell
SOFC	Solid oxide fuel cell
STM	$SrTi_{0.5}Mo_{0.5}O_3$
STN	$Sr_{0.94}Ti_{0.9}Nb_{0.1}O_3$
STNM502525	$Sr_2Ti_{0.5}Ni_{0.25}Mo_{0.25}O_3$
SVM	$SrV_{0.5}Mo_{0.5}O_3$
TPB	Three-phase boundary
TPBL	Three-phase boundary length
USD	United States dollars
V2G	Vehicle-to-grid
WGS	Water-gas shift
WTT	Well-to-tank
WTW	Well-to-wheels
XRD	X-ray diffraction
YSZ	Yttria-stabilized zirconia
Z	Impedance
Z_{imag}	Imaginary part of the impedance
Z_{real}	Real part of the impedance

To Kalee

Acknowledgements

I would like to express my sincere gratitude to my advisors and colleagues who made this work possible. This research was conducted partly in New York at the Earth & Environmental Engineering Department and the Lenfest Center for Sustainable Energy at Columbia University and partly in Denmark at the Fuel Cells and Solid State Chemistry Division at Risø National Laboratory for Sustainable Energy. I was lucky to find two equally enjoyable research groups and learn from and contribute to both. The acknowledgements for the two sides of the collaboration are given in two columns. I thank the following people for giving me knowledge and insight, and lending their expertise and time, at various stages of the research:

At Columbia

Klaus Lackner — for making it all happen; for teaching me about all aspects of energy conversion and sustainability; for teaching me how to think, in your perhaps indescribable way of looking at complex things and honing in on unique important aspects, how to use basic physical principles, and the value of order-of-magnitude comparisons and logical arguments over precise accounting; for the many insightful discussions about carbon management and energy systems; and for giving me the opportunity and freedom to pursue this research path.

Alan West — for teaching me about electrochemistry and electrode kinetics modeling; for helping me to focus the experimental studies; and for generously giving me space in your lab to set up and conduct preliminary high temperature experiments.

Paul Duby — for introducing me to electrochemistry; for teaching me how to work in a lab and supporting my initial interest in aqueous CO_2 electrolysis experiments; for giving me a foundation in thermodynamics and chemistry; and for guidance and support throughout.

At Risø

Mogens Mogensen — for teaching me about high temperature electrochemistry; for inviting me to your excellent lab and research group to conduct my experimental work in the presence of some of the greatest expertise in the field; for the many valuable discussions lending me your deep understanding of electrochemistry and materials; for encouraging, supporting and guiding my experiments while also giving me plenty of room to explore.

Sune Ebbesen — for the initial daily help and teaching me electrochemical cell characterization techniques; for the many insightful discussions about experiments and electrochemistry; for being receptive to work with an unknown guest PhD student ☺ and having a productive time working together.

Bhaskar Reddy Sudireddy — for teaching me theory and lab procedures for preparing ceramic materials and characterization their properties, and for the nice cooperation in the materials study.

Konrad Tarka — for help with materials synthesis and a productive "Summer of Molybdates and Titanates." Best of luck on your master's project!

Jen Wade — for teaching me how to assemble high-temperature experimental set-ups and helping me begin experiments, and for the valuable discussions and productive times.

Tuncel Yegulalp — for introducing me to data analysis and modeling techniques.

The first/second generation Lackner group — for being such an enjoyable group full of ideas and enthusiasm to embark on the fascinating and wild ride of PhD studies under Klaus. I hope that we keep in touch throughout our new careers!

Søren Koch, *Jens Borchsenius*, and *Ebtisam Abdellahi* — for helping me set up and improve lab experiments. *Søren Koch* and *Karin Vels Hansen* — for having built an excellent automated control and data acquisition system the usefulness of which cannot be overstated.

Nikos Bonanos, Tânia Ramos, Kent Kammer Hansen, and *Karin Vels Hansen* — for many valuable discussions about impedance spectroscopy and materials.

Søren Højgaard Jensen, Anne Hauch, Peter Blennow, Jens Høgh, and *Karin Vels Hansen* for each writing excellent, well-documented and inspirational dissertations that gave me a basis for parts of my experimental work, and for discussing your work with me.

Jason Wang, a great office-mate and friend.

The rest of my fellow students and colleagues at Columbia and Risø. You are too many to mention but have all contributed. The enjoyable discussions and working environments were greatly appreciated.

Uncle Pat for being genuine and supportive, wish you were here to see the outcome.

Special thanks to my *friends* and *family* for support and understanding while I tended to almost completely disappear and become a hermit for well over a year.

Of course to my *Kalee* for love, patience, and support, and for taking a leap and joining the cross-Atlantic journey to Denmark. Without you this truly would not have been possible.

—

I would also like to thank the authors of the free and open-source Python libraries NumPy and Matplotlib, which made the data analysis and plotting enjoyable.

Financial support from the American Chemical Society Petroleum Research Fund, from the Lenfest Center for Sustainable Energy, and from the Programme Commission on Sustainable Energy and Environment, The Danish Council for Strategic Research, via the SERC project, is gratefully acknowledged.

Chapter 1

1. Introduction

Great quantities of hydrocarbon fuels will be needed for the foreseeable future, even if electricity based energy carriers begin to partially replace liquid hydrocarbons in the transportation sector. Fossil fuels and biomass are the most common feedstocks for production of hydrocarbon fuels. However, using renewable or nuclear energy, carbon dioxide and water can be recycled into sustainable hydrocarbon fuels in a non-biological process. Sustainable gasoline and diesels, or natural gas if desired, could substitute directly for their current fossil fuel-derived counterparts. Capture of CO_2 from the atmosphere would enable a closed-loop fuel cycle. These CO_2-recycled fuels would therefore be carbon-neutral. When produced using solar energy, the fuel cycle would be similar to that of biofuels. However, since the fuels are produced in a non-biological process, they would not share the disadvantages of biofuels in terms of land use, resource use, interference with food supplies, and other impacts to the environment and biosphere. Such fuels could also provide a more secure fuel supply than biofuels, their production being insensitive to natural phenomena such as droughts and diseases.

Renewable and nuclear energy sources, as heat, electricity, and light, can drive the splitting of CO_2 and H_2O to reverse the process of combustion and produce fuels. The purpose of this work was to develop critical components of a system that recycles CO_2 into sustainable hydrocarbon fuels. The concept is examined at several scales, beginning with a broad scope analysis of large-scale sustainable energy systems and ultimately studying electrolysis of CO_2 and H_2O in high temperature solid oxide cells as the heart of the energy conversion, in the form of three experimental studies of electrolysis of CO_2 and H_2O. The contributions of these studies include discoveries about electrochemistry and materials that could significantly improve the overall energy use and economics of the entire CO_2-to-fuels system.

The study begins by considering global-scale energy flows, which provide context for the motivation for recycling CO_2 into fuels. As it progresses it re-focuses on finer details of important parts of the CO_2 recycling process. At each stage potentially critical improvements to the system are identified and then pursued. As a result, in consecutive chapters, the scale of the system being studied tends to become smaller from global to macro to micro scale, eventually to experimental studies of the micro- and nano-scale phenomena of metal and ceramic electrodes of solid oxide electrolysis cells. These details – the materials, the electrochemical reaction rates, and the durability of the electrodes – are important; they largely define the energy

use and economics of the entire fuel production system. At the beginning of each small-scale study, the potential impact on the full system is described, tying each study to the big picture. The progressive re-focusing of scope and scale is illustrated in **Figure 1-1**.

Following is a brief overview of the chapters of this thesis. Then in the following sections, to provide background for electrolysis cell technology, an introduction to electrolysis and electrochemical energy conversion is given, followed by a brief overview of electrochemical impedance spectroscopy (EIS), one of the most-used analytical techniques in this thesis. Other experimental techniques that were used are also discussed.

Chapter 2 examines the many energy carriers that could replace petroleum-derived hydrocarbon fuels. These include other hydrocarbons like coal-to-liquids and biofuels, other chemical energy carriers like hydrogen and ammonia, and storage of electricity on-board vehicles in batteries, ultracapacitors, and flywheels. Any energy carrier can carry energy from any energy source (fossil carbon, nuclear, biomass, and solar, wind, and other renewable energy sources). The pathways from the various energy sources to energy carriers are examined in terms of their relative sustainability and practicality if implemented at a large scale. This study of global scale energy flows sets the context for hydrocarbons produced by recycling CO_2. CO_2 recycling yields an especially interesting energy carrier – sustainable energy sources like solar and wind power can be used to provide the most energy-dense, convenient fuels which can be readily used in the existing infrastructure.

Chapter 3 examines the various possible technological pathways that could be taken to recycle CO_2 into hydrocarbon fuels using renewable or nuclear energy. The state-of-the-art enabling technologies at each stage of the pathway (CO_2 capture, H_2O and CO_2 dissociation, and fuel synthesis) are critically reviewed. Methods of dissociation include heat, electricity, and sunlight driven methods – thermolysis, thermochemical loops, electrolysis, and photoelectrolysis. Capturing CO_2 from the atmosphere using a solid sorbent, electrolyzing H_2O and CO_2 in high temperature solid oxide cells to yield a mixture of H_2 and CO (syngas), and producing gasoline or diesel from the syngas in a catalytic reactor (e.g. Fischer-Tropsch) is identified as one of the most promising, feasible routes. High temperature electrolysis makes efficient use of electricity and heat and provides high reaction rates, and integrates well with fuel synthesis, enabling use of part of the waste heat and further improving the efficiency of the system. An analysis of the economics and energy balance for this process is presented, based on the experimental results of **Chapter 4**. The potential of the process is assessed, in terms of what technological progress is needed to achieve large-scale, economically competitive production of sustainable fuels by this method. Opportunities are discussed for fuel production using inexpensive, intermittent renewable energy (e.g. surplus wind power, or solar arrays built in remote, sunny locations such as deserts) and constant-supply power sources such as hydroelectric, geothermal, and nuclear.

Chapters 4, **5**, and **6** present three experimental studies of electrolysis of CO_2 and H_2O using solid oxide cells. The studies were made at different scales – at the cell level, electrode

level, and materials and microstructure development. The experimental studies make extensive use of electrochemical impedance spectroscopy in conjunction with systematic variation of test conditions to examine the electrochemical phenomena. Variation of the material composition itself within families of similar materials was an additional parameter which was used in the electrode level and materials studies, which aimed to gain better understanding of the materials and electrochemistry versus studying a single material alone.

Chapter 4 presents an experimental study of the performance and durability of co-electrolysis of CO_2 and H_2O using a solid oxide electrolysis cell. The cell resistance is broken down into contributions of several processes in the electrodes and electrolyte using an impedance analysis technique that enables clear visual identification of the processes. The technique is used to determine which processes degrade during long-term durability testing at three different current densities. High initial performance was observed for co-electrolysis, but the negative-electrode, a composite of nickel and yttria-stabilized zirconia (YSZ), is often the major site of cell degradation, including in the co-electrolysis results presented here.

Therefore, to try to better understand the reaction mechanisms at the negative-electrode that limit performance and durability, the experimental study presented in **Chapter 5** was carried out. The electrode kinetics of CO_2 and H_2O electrolysis and CO and H_2 oxidation at the metal-YSZ interface were studied using a simplified point-contact electrode geometry with a well-defined electrode-electrolyte (metal-YSZ) interface. The simple geometry is useful for isolating the electrochemical properties without the effects of the complex microstructure of technological porous electrodes. A parameter used, which is uncommon in most studies, was the variation of the metal material itself – by comparing the same reactions using different metals (Ag, Au, Cu, Ni, Pd, and Pt) under identical conditions, the similarities and differences of the electrochemical responses between the different metals revealed more information about the reactions than a single material would have. Possible reaction mechanisms, and a number of interesting phenomena that occur at the metal-YSZ interface, are discussed.

In **Chapter 6**, the metal based electrode is abandoned in favor of studying alternative electrode materials composed entirely of ceramic oxides. Ceramics can provide high electronic conductivity and electrocatalytic activity like nickel based electrodes, and additionally some ceramic materials have greater stability, can provide enhanced electrocatalytic activity via mixed ionic-electronic conductivity and/or nanostructured surfaces, and can be cheaper to produce since much of the material is made of oxygen. Fundamental properties (phase, microstructure, and electrical conductivity in the high-temperature reducing conditions relevant for solid oxide cell negative electrodes) of families of molybdate and titanate based ceramic materials were characterized. Certain material compositions exhibited very interesting properties, providing a nanostructured surface with high electronic conductivity upon exposure to operating conditions (high temperature reducing atmosphere). These materials were tested as electrodes to determine their electrocatalytic activity for H_2O/CO_2 reduction and H_2/CO oxidation. The decomposed materials, as well as other materials from related molybdate families, exhibited very high

electrocatalytic activity. Based on the results, new materials and methods are proposed for preparing high-performance electrode materials for solid oxide cells.

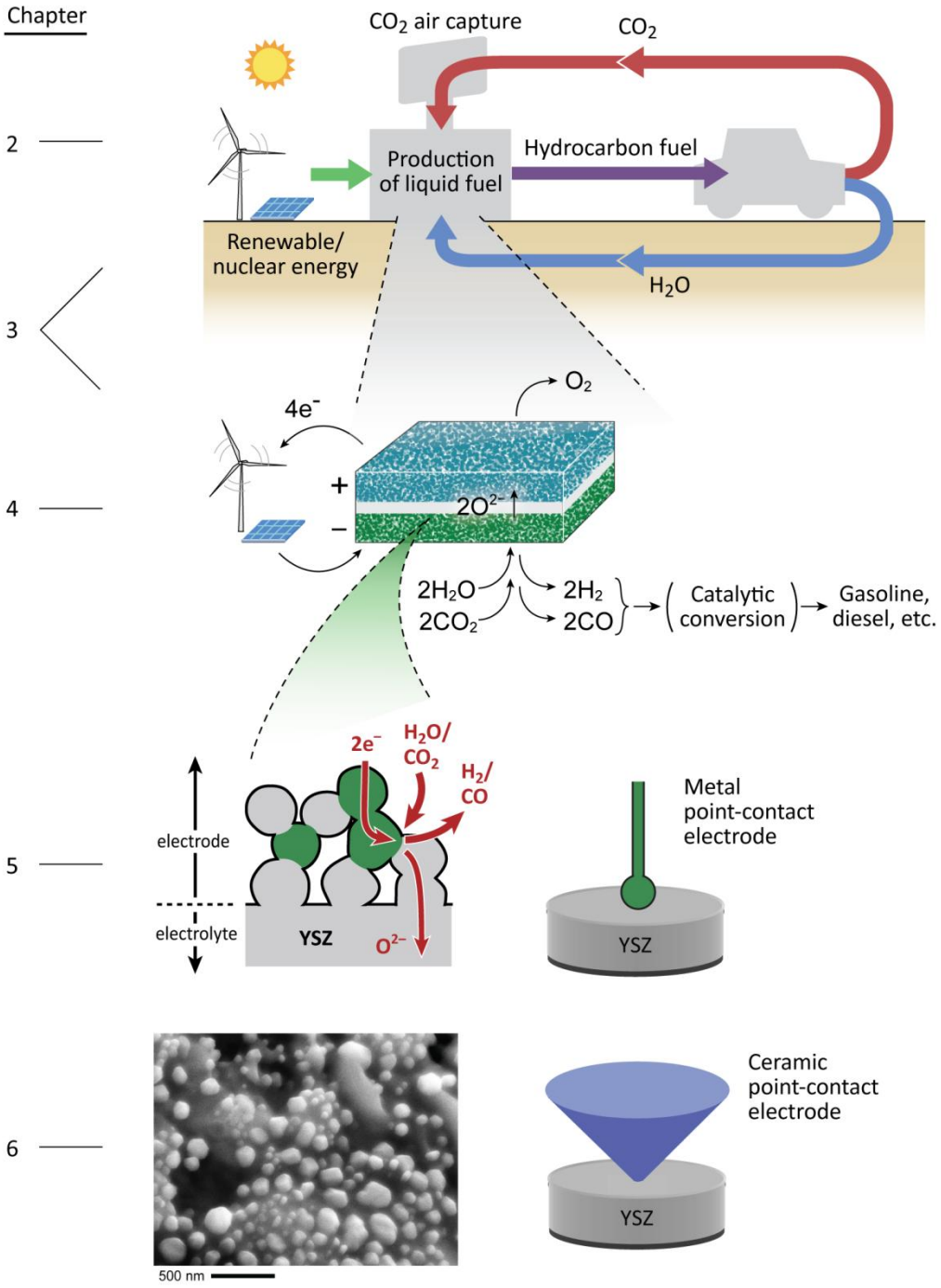

Figure 1-1. Illustration of the progression of the studies in this thesis from broad global-scale energy systems to a focus on electrochemical cells, electrodes and electrode materials.

1.1. Electrochemical Energy Conversion and Solid Oxide Cells

This section provides a brief introduction to high temperature electrolysis cells with solid oxide electrolytes. Solid oxide cells, as well as most low temperature cells[i], can be operated reversibly, as either a fuel cell or as an electrolyzer.

In fuel cell mode, fuel is supplied to one electrode and oxidant (such as air) is supplied to the other, creating a potential difference (voltage) across the cell which drives the electrode reactions and the transport of ions across the electrolyte to complete the electrical circuit, producing electricity and oxidizing the fuel to water and CO_2. A variety of fuels can be supplied, such as hydrogen, carbon monoxide, natural gas/methane, and even other hydrocarbons and carbon-rich fuels like coal although they typically need to be gasified first by reforming with steam or CO_2.

In electrolysis mode, gaseous oxides such as steam and carbon dioxide are supplied to one electrode (and at the other electrode, no reactants are needed but a sweep gas of air or oxygen is often supplied) and a voltage is applied across the cell. This drives the electrolysis of the H_2O and/or CO_2, splitting these oxides by removal of an oxygen atom, which is transported as an oxide ion across the electrolyte to the other electrode where the oxide ions recombine to produce gaseous oxygen. Fuels such as H_2 and CO are thus produced, which can be reformed into other fuels such as methane or liquid hydrocarbons. At the other electrode a valuable stream of pure O_2 can be easily obtained if a sweep gas of O_2 is used.

A diagram of a solid oxide cell in both modes of operation, along with the corresponding electrode reactions, is shown in **Figure 1-2**. Depicted is a planar-geometry solid oxide cell (as opposed to tubular geometry and other existing geometries). Planar cells are stacked with electrical interconnect plates between the electrodes of adjacent cells to form a cell stack. The electrolyte is a dense thin oxide ion conducting ceramic, usually yttria-stabilized zirconia. The electrolyte layer is sandwiched between the two porous electrodes, which are typically made of a composite of the electrolyte material and an electron conducting material (either a metal or an electronically conductive ceramic) that also provides electrocatalytic activity for the reactions (or sometimes other materials are added to enhance electrocatalytic activity). The typical materials

[i] The ability of an electrochemical cell to operate reversibly as either a fuel cell or an electrolysis cell depends only on the cell geometry, not on any limitation of the electrochemistry. That is, the cell must be constructed such that either type of reactant – the fuel molecules or oxidized molecules – can be supplied to the electrode reaction sites. An example of a cell that is not designed to operate reversibly is a simple aqueous electrolysis cell where the electrodes are immersed in the aqueous electrolyte. Water is split and H_2 gas is evolved. There is no easy way to supply H_2 to the electrodes and run this type of cell as a fuel cell.

that make up the electrodes are described in **Chapter 3**, **section 3.2.2.3.2**, and the chapters thereafter present studies of these and other electrode materials.

Because the solid oxide electrolyte conducts oxide ions, solid oxide cells can oxidize CO and reduce CO_2 in addition to H_2/H_2O, which cannot be done with proton exchange membrane (PEM) cells or alkaline cells because their electrolytes conduct protons (H^+) and hydroxide ions (OH^-) respectively. The high temperature operation is also advantageous for both thermodynamic and reaction kinetics reasons, increasing energy efficiency and lowering the cost, as discussed further in **sections 3.2.2.3** and **3.2.2.3.2**.

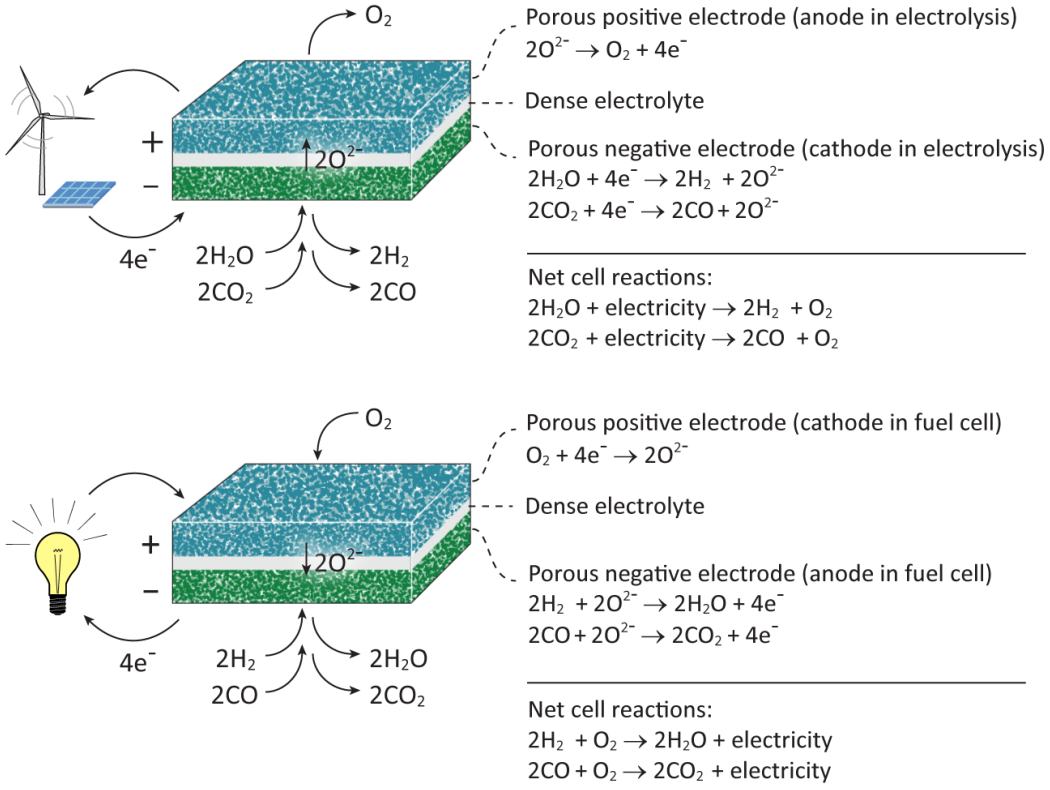

Figure 1-2. A solid oxide cell operated as an electrolysis cell and as a fuel cell.

1.1.1. Thermodynamics

The reversible potential of the cell, E_{rev}, which is typically the voltage measured at open circuit (OCV), is defined by the equilibrium gas composition and thermodynamics according to equations (**1.1**) (the Nernst equation) and (**1.2**). The Nernst equation is shown with H_2/H_2O gasses; for CO/CO_2 one simply substitutes pCO for pH_2 and pCO_2 for pH_2O. In the case that both types of gas atmospheres are supplied as a mixture ($H_2/H_2O/CO/CO_2$) then all of the gas

partial pressures could be included. It is important to note that the equilibrium composition becomes more complicated due to interactions between the gasses via the water-gas shift reaction ($CO + H_2O \leftrightarrow CO_2 + H_2$).

$$E_{rev} = E^0 - \frac{R \cdot T}{n \cdot F} \cdot \ln\left(\frac{P_{H_2} \cdot P_{O_2}{}^{½}}{P_{H_2O}}\right) \tag{1.1}$$

$$E^0 = \frac{-\Delta G_{rxn}}{n \cdot F} \tag{1.2}$$

E^0 is the reversible potential at the operating temperature, which is defined by the Gibbs free energy of the reaction ΔG_{rxn} (in this case the net cell reaction $H_2O \leftrightarrow H_2 + ½\,O_2$). ΔG_{rxn} is a function of temperature as shown in **Figure 3-4**; E^0 =1.23 V at 25 °C and E^0 =0.96 V at 850 °C. R is the ideal gas constant, T is the operating temperature, n is the number of electrons transferred per mole product H_2 or CO (n = 2 for these reactions, see **Figure 1-2** where 2 moles of product are produced per 4 electrons), F is Faraday's number, and pH_2 and pH_2O are the equilibrium gas partial pressures at the negative electrode and pO_2 is the oxygen partial pressure at the positive electrode. The electrodes are referred to as "negative" and "positive" electrodes[ii] because it has not yet been defined which mode the cell will be operated in, fuel cell or electrolysis. In electrolysis, the negative electrode is the cathode because it is where electrochemical reduction is occurring and the positive electrode is the anode where oxidation is occurring. In fuel cell mode, the negative and positive electrodes are named oppositely, as the "anode" and "cathode" respectively.

Another useful thermodynamic property of electrolysis cells is the thermoneutral voltage, E_{th} as defined in equation (1.3).

$$E_{th} = \frac{\Delta H_{rxn}}{n \cdot F} \tag{1.3}$$

For the cell reactions shown in **Figure 1-2** ($H_2O \rightarrow H_2 + ½\,O_2$ and $CO_2 \rightarrow CO + ½\,O_2$) which are the main focus of this thesis, $E_{th} > E_{rev}$. To operate below E_{th}, heat must be supplied to the cell from an external source because the cell is self-cooling. Operating above E_{th} results in heat production from the cell, which arises from the ohmic "Joule" heating in the cell, and the cell must be cooled. Note, however, that there are some possible reactions, such as $CO_2 \rightarrow C + O_2$, for which ΔS_{rxn} has an opposite sign, and so $E_{th} < E_{rev}$. In that case, any applied electrolysis potential would produce heat.

[ii] based on their electrical terminal connections to either the power supply or electrical load; see **Figure 1-2**.

For CO_2 electrolysis E_{th} is about 1.47 V. For H_2O electrolysis, the H_2O must be supplied to the cell electrode as steam. This lowers the E_{th} from about 1.48 V (water electrolysis) to 1.3 V (steam electrolysis) since part of the energy has already been supplied in the phase transition $H_2O(l) \rightarrow H_2O(g)$. However, unless steam is already available, the water must be vaporized to steam by the system upstream of the cell, and if this is to be done by electrical heating then the cell–vaporizer system can isothermally be operated at the 1.48 V with a heat exchanger included to transfer the heat being produced by the cell (the cell at 1.48 V produces heat because it is operated about 0.18 V above the "true" E_{th}) to the vaporizer. A heat exchanger is needed anyway to transfer heat from the outlet gasses of the cell to the inlet gasses in order to conserve heat. Because heat exchangers are not 100% efficient and the insulation around the cell stack is also imperfect, isothermal operation of the system requires operating somewhat above E_{th} to accommodate heat losses. If 10% of the heat produced is lost to the surroundings, the cell must be operated at 10% higher voltage. See also **section 3.2.2** with **Figure 3-4** for more information about the thermodynamics including the enthalpy and Gibbs free energy values, and **section 3.3** for more discussion about cell operation.

1.1.2. Kinetics

A typical current density versus voltage (i-V) polarization curve of a solid oxide cell at 850 °C, with 50% H_2 + 50% H_2O[iii] supplied to the negative-electrode and oxygen or air supplied to the positive-electrode, is depicted in **Figure 1-3** with the above described thermodynamic potentials labeled. The cell voltage is scanned downwards (resulting in fuel cell operation, producing current) and upwards (resulting in electrolysis operation, drawing current) from the OCV. The voltage difference between the applied potential and OCV is referred to by various terms – applying polarization, bias, or overpotential. These three terms are generally used interchangeably in this thesis. One can see in this hypothetical cell that for a given change in voltage, slightly more current is produced by fuel cell operation than is consumed in electrolysis. This means that, because the current density is directly proportional to the electrochemical reaction rates[iv] , the reaction rate is faster for fuel cell operation (in this case H_2 oxidation) than electrolysis operation (in this case H_2O reduction). This is observed in real cells as well, as will be seen for the cell studied in **Chapter 4**. The net reaction rates can be described by the area-specific resistance (ASR) which is the change in cell voltage divided by the change in

[iii] 50% H_2 + 50% H_2O is one useful gas composition for characterizing the cells operated reversibly in fuel cell and electrolysis mode. In real cell operation, the gasses supplied would be closer to 100% H_2 for fuel cell operation and 100% H_2O for electrolysis operation (although some electrode materials, including the traditional negative electrode material, are unstable in 100% H_2O so some H_2 is also supplied, which can be recirculated H_2 that was produced by the electrolysis reaction).

[iv] As defined by Faraday's law, assuming that a negligible amount of current is due to parasitic reactions, which is known to be true for the majority of fuel cells/electrolyzers including solid oxide cells

current density (the slope of the i-V curve). Because the i-V curve has curvature, one must define common points – the arrows mark ±0.75 A/cm^2 in the figure – and calculate the ASR based on a chord from OCV to those points. In this example, OCV is at 0.90 V, the potential at +0.75 A/cm^2 is 0.74 V and the potential at –0.75 A/cm^2 is 1.12 V. Therefore the fuel cell ASR is 0.21 Ω cm^2 (= (0.90 – 0.74) / 0.75) and the electrolysis ASR is 0.29 Ω cm^2 (= (0.90 – 1.12) / –0.75). These are not far from real values measured at these conditions. In comparison with low-temperature PEM and alkaline cells, solid oxide cells have much lower ASR.

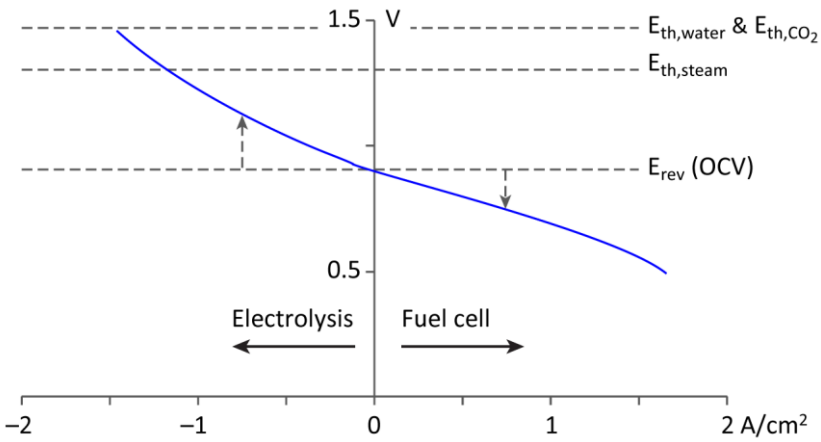

Figure 1-3. Illustration of a typical polarization curve for a solid oxide cell at 850 °C in 50% H_2 + 50% H_2O with important thermodynamic potentials labeled.

The relative lack of curvature of the i-V curve in comparison with low-temperature cells, especially near OCV, indicates very fast electrode reaction kinetics with high exchange current densities for both electrodes. The traditional fundamental relationships used to describe electrode kinetics, the Butler-Volmer equation and its derivatives, cannot be used in their basic forms to describe the i-V curves of these high temperature cells because these equations are based on electrochemical charge-transfer as the rate-limiting step. The electrode reactions still contribute to the cell resistance but reaction processes such as adsorption/desorption and diffusion may be slower than the actual electrochemical reactions in these electrodes. Other contributions to the cell resistance are gas concentration based effects (based on gas diffusion and non-equilibrium gas conversion) in the electrodes and in the gas flow channels, and finally the ohmic resistance of the ion-conducting electrolyte (as well as the ohmic resistance of the electron-conducting materials in the electrode, the interconnect plates, the wiring, etc, however this is all typically negligible). These complex processes are studied throughout this thesis, in **Chapters 4**, **5**, and **6**. The resistance of a single electrode can be isolated and studied individually, which is employed in **Chapters 5** and **6**.

Increasing the temperature even higher can further reduce the ASR, however higher temperature can also cause the performance to degrade more quickly as the materials and

microstructures are more unstable. The performance and durability of a solid oxide electrolysis cell is examined in **Chapter 4**. The performance and durability of electrode materials are studied in **Chapters 5** and **6**.

1.2. Experimental Techniques

A number of experimental and analytical techniques are employed throughout this thesis. **Chapters 4, 5**, and **6** include electrochemistry studies, and **Chapter 6** also includes a study of other fundamental properties of materials – phase, microstructure, and electrical conductivity.

The electrochemistry studies include performing polarization curves like the one described in the prior section. When testing single electrodes instead of full cells, the OCV is expressed as zero and then the voltage axis corresponds to overpotential. The electrochemistry studies also make heavy use of electrochemical impedance spectroscopy (EIS), a powerful experimental technique. The use of EIS to study electrochemical cells, for detailed mechanistic studies and as a diagnostic tool, has grown considerably during the last three decades [1]. In addition to applying direct current electricity, which is how cells are actually operated, alternating currents can be applied. In EIS a small amplitude periodic alternating-current is used. Applied to an electrochemical system at equilibrium or at a non-equilibrium steady-state, the small amplitude perturbs the system without disturbing the equilibrium or steady-state. Sinusoidal AC signals with amplitudes of a few mV or mA (depending on if the measurement is voltage-controlled or current-controlled) and frequency range of around 1 MHz to 1 mHz are typically used for studying solid oxide cells and their electrodes. The measured frequency-dependent response of the electrochemical system provides information about the reactions that take place at different rates, as well as other non-reaction processes that have different relaxation times, and about the capacitance of the processes. EIS is useful to study complex systems and to aid in identifying their mechanisms. Impedance measurements can take a long time when including the low-frequency data points (a single data point at 10 mHz takes at least 1.67 minutes and each data point is measured more than once to ensure noise-free data, and several data points per frequency decade are typically measured), so it is important that the system is nearly at steady-state during measurement or else the measurement will include drift and make data interpretation difficult or impossible.

There are a number of ways to present impedance data. The most typical for the systems studied here are Nyquist and Bode plots. An ideal simulated impedance spectrum is shown in these types of plots in **Figure 1-4**. The measured impedance magnitude (the ratio of the measured voltage and current) and phase angle (the phase shift between the measured voltage and current sine waves) are converted into complex Cartesian coordinates using Euler's formula and displayed as the real part of the complex impedance, Z_{real}, and the imaginary part of the complex impedance, Z_{imag}, as a function of the perturbation frequency f. In the Nyquist plot, a

perfect semicircle is seen. From Z_{imag} in the Bode plot, one can identify the summit frequency of this impedance process at 9 kHz. The Nyquist and Bode plots provide complementary views of the impedance spectrum. Note that Z_{imag} is often shown as $-Z_{imag}$ in impedance plots for visual convenience – most impedance data are in the negative Z_{imag} regime, which corresponds to capacitive impedance. Positive Z_{imag} corresponds to inductive impedance and is usually only present in impedance measurements made on this type of electrochemical cells due to stray inductance from the test set-up.

Electrical circuits can sometimes produce the same impedance data and one can derive such equivalent circuits from an electrochemical model of a system. Such circuits are useful for understanding impedance spectra. For this ideal case, an electrical circuit perfectly describes the data, and it can be derived from fundamental electrochemical principles via the Butler-Volmer equation. This is illustrated in **Figure 1-5a**. The corresponding circuit is a resistor R_S in series with a parallel R-C subcircuit. R_S is ohmic resistance in the cell, for example the distance of electrolyte material between the working electrode and the reference electrode[v] (and ohmic resistance in the measurement setup, e.g. wiring, however this is usually negligible compared with electrolyte resistance). The R-C subcircuit corresponds to the charge transfer resistance of the electrochemical reaction, R_{ct}, and the capacitance of the double-layer of charged species at the electrode-electrolyte interface. Note that the values of the elements are not fixed as the equivalent circuit diagram might imply – the charge transfer resistance R_{ct}, for example, varies with temperature and DC bias, and other parameters often depend on these and other experimental conditions such as the composition of the supplied gasses or liquids.

In the Nyquist plot both R_S and R_{ct} are easily identified on the Z_{real} axis. Separating the ohmic resistance and electrode processes is the first simple use for impedance measurements. From the summit frequency f_s (the frequency at which the imaginary component reaches a maximum) and R_{ct} one can calculate the double layer capacitance C_{dl} according to equation (1.4). C_{dl} is usually normalized to the interfacial area, e.g. units of $\mu F/cm^2$.

$$C_{dl} = \frac{1}{2 \cdot \pi \cdot f_s \cdot R_{ct}} \tag{1.4}$$

One can imagine that there is another R-C type process in series, with a different characteristic

[v] For single-electrode measurements, a reference electrode is typically used and positioned at some distance from the working electrode. It has extremely high impedance and a negligible amount of current flows. The voltage difference between working and reference electrodes is measured, and the current flows between the working electrode and a counter electrode is measured.

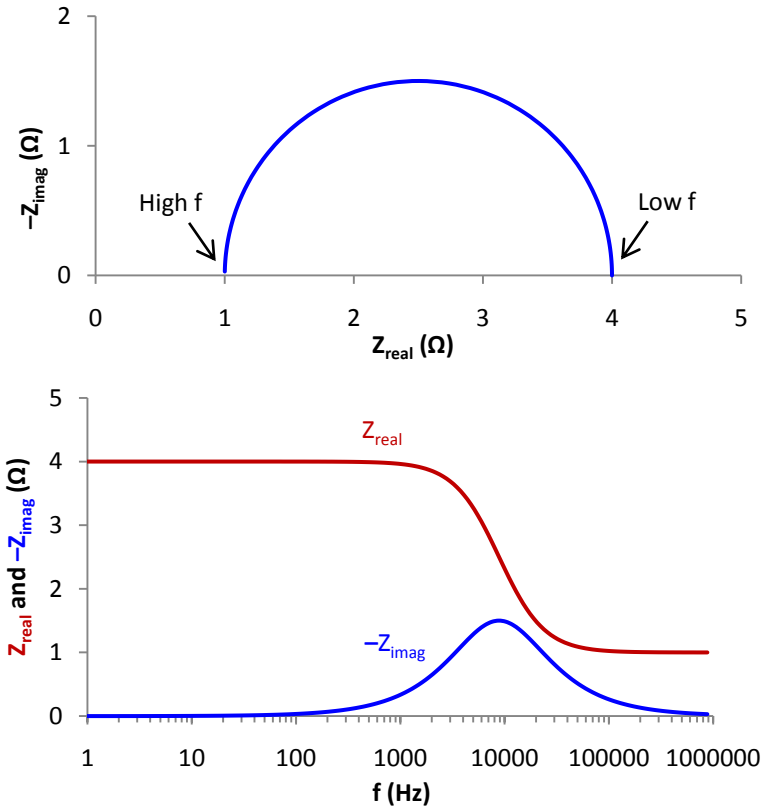

Figure 1-4. Simulated impedance spectrum for charge transfer at an ideal electrode.

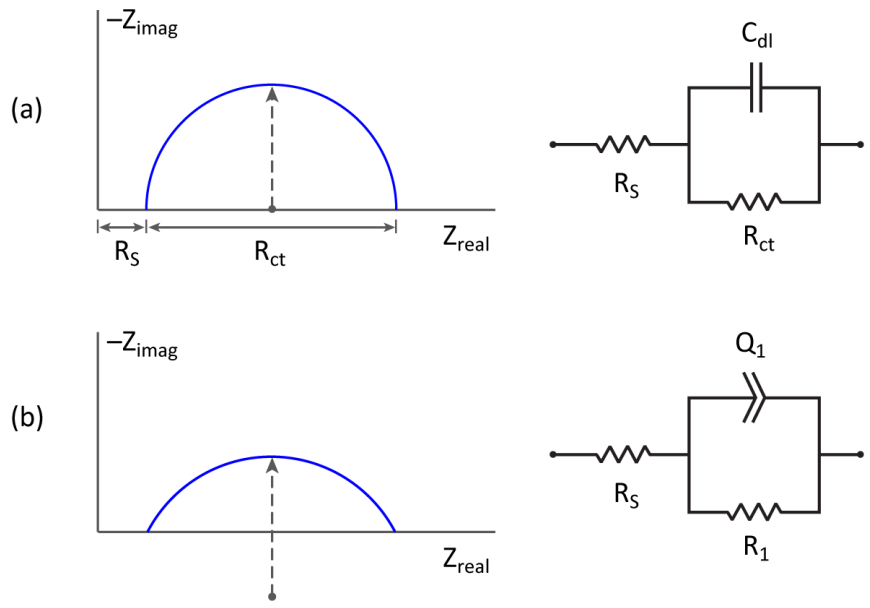

Figure 1-5. Examples of impedance spectra and corresponding equivalent circuits. (a) Charge transfer reaction at an ideal electrode with perfect capacitance, and (b) charge transfer with imperfect capacitance.

frequency, for example when measuring across two different electrodes with different reaction rates as in the case of a full cell. Other phenomena and rate-limiting mechanisms besides charge-transfer, such as adsorption/desorption and diffusion of species, can also appear as semicircles or resemble semicircles. Gas concentration effects (not related to the electrochemical reactions) can also shown up as a R-C type process [2] [3] [4]. Another serial process would result in another semicircle adjacent to – or overlapping if the frequencies are close enough – the first semicircle. In this way multiple semicircles can be present, and it is useful to define the total resistance (at the low-frequency intercept with the Z_{real} axis) minus R_S as the total polarization resistance, R_P.

In actual measurements, such a perfect semicircle is seldom encountered. Often the semicircle is depressed (**Figure 1-5b**). The reasons for this are dependent on the system and are a matter of debate, but most likely are related to a non-homogeneous electrode surface and/or interface in which reactions rates and capacitances have a wider distribution, with slightly different magnitudes and relaxation times. The impedance Z of a depressed semicircle has been modeled directly as a system with a distribution of time constants [5]. An equivalent circuit element called the constant phase element, Q, was introduced to describe such depressed arcs. Whereas the time constant τ of an R-C circuit is $\mathrm{R} \cdot \mathrm{C} = \tau$, for an R-Q circuit it is defined as $\mathrm{R} \cdot \mathrm{Q} = \tau^n$. The impedance Z of an R-Q circuit is therefore

$$\mathrm{Z} = \frac{\mathrm{R}}{1 + \mathrm{R} \cdot \mathrm{Q} \cdot (\mathrm{j} \cdot \omega)^{\mathrm{n}}} \tag{1.5}$$

where R is the resistance of the parallel resistor (R_1 in **Figure 1-5b**), Q is the constant phase element parameter, j is the imaginary unit, and ω is the angular frequency ($\omega = 1/\tau$). Note that for $n = 1$, the equation corresponds to that of a capacitor. To calculate the full impedance of the R(RQ) circuit shown in **Figure 1-5b**, the serial resistor R_S is simply added to equation (1.5). The "true" or quasi-equivalent capacitance of a constant phase element in an R-Q circuit can be derived simply from the definitions of the time constants for the R-C and R-Q given above: $\mathrm{C_{eq}} = (\mathrm{R} \cdot \mathrm{Q})^{1/\mathrm{n}}/\mathrm{R}$. Since $\omega = 1/\tau$ and $\tau = \mathrm{R} \cdot \mathrm{C}$, this can also be expressed as $\mathrm{C_{eq}} = \mathrm{Q} \cdot {\omega_S}^{\mathrm{n}-1}$ where ω_S is the summit frequency of the depressed arc. $\omega_S = 2 \cdot \pi \cdot f_s$ in reference to the f_s in equation (1.4).

A number of other equivalent circuit elements that do not exist in electrical circuits have also been introduced to describe various phenomena observed in electrochemical impedance data, such as diffusion limitations. For more information, the textbooks listed below are referred to.

Equivalent circuits are also sometimes used as a "measurement model" [6] before knowing enough to try to model the system, as a means to condense the impedance data and try to identify some characteristics such as the number of processes. The data can be fit to an

equivalent circuit using complex nonlinear least-squares (CNLS) regression. Other transformations of impedance data are also useful to try to more clearly understand the data [1]. Techniques such as analysis of differences in impedance spectra (ADIS) [7] and transformation to the distribution function of relaxation times (DRT) [8-10] increase the frequency domain resolution, enabling clearer visual identification of peaks of specific processes at their characteristics frequencies. The DRT method is used in **Chapter 4**. Ideally, the distribution function of relaxation times $\gamma(\tau)$ could be obtained directly from an impedance spectrum using the convolution equation (1.6) [1, 8-10].

$$Z(\omega) = R_S + Z_{pol}(\omega) = R_S + R_{pol}\int_0^\infty \frac{\gamma(\tau)}{1 + j\cdot\omega\cdot\tau}d\tau \quad \text{with} \int_0^\infty \gamma(\tau)\,d\tau = 1 \tag{1.6}$$

where $Z(\omega)$ is the impedance data, R_S is the ohmic part of the impedance, $Z_{pol}(\omega)$ is the polarization part of the impedance, and R_{pol} is the polarization resistance of the impedance. However, in practical measurements, only part of the entire impedance spectrum $Z(\omega)$ is sampled at a limited number of discrete points over a finite frequency range. The deconvolution must therefore be solved numerically, however erroneous results are obtained due to large amplification of experimental error. Algorithms have been developed to minimize these errors, by extrapolating the data at high and low frequency to artificially enlarge the frequency range of the data and by filtering data in Fourier space (performing a Fourier transform on the data, applying a filter, and then performing the inverse Fourier transform) to reduce noise [1, 8-10].

In all cases it is useful to compare measurements taken with small changes in experimental conditions and keeping as many of the other parameters fixed as possible. Parameter changes can then be correlated with changes in the impedance response, which can help to reveal the number of and nature of the impedance processes and possible reaction mechanisms. With modern automated control and data acquisition systems, variation of test conditions can be performed in a systematic and thorough manner over the course of hours to months without the experimenter sitting at the test set-up. This is used extensively in **Chapters 4** and **5**. For further information about impedance spectroscopy, good textbooks have been recently published [5, 11].

Besides electrochemical properties, other properties of the electrode materials are studied in **Chapters 4**, **5**, and **6**. The techniques used are generally more straightforward and well-known than impedance spectroscopy. Before and/or after the electrochemistry tests, surfaces and interfaces were most often examined with a scanning electron microscope (SEM) (and occasionally an atomic force microscope, AFM) to characterize the microstructure, and sometimes the energy-dispersive X-ray spectrometer (EDX) equipped in the SEM was used to

identify material phases. X-ray diffraction (XRD) and 4-point DC conductivity tests were additionally employed to characterize phase and conductivity, respectively, in **Chapter 6**. The conductivity tests were also used to indirectly study phase stability.

1.3. References

1. Jensen SH, Hjelm J, Hagen A, and Mogensen M, *Electrochemical impedance spectroscopy as diagnostic tool*, in *Handbook of Fuel Cells – Fundamentals, Technology and Applications*, W. Vielstich, H. Yokokawa, and H.A. Gasteiger, Editors. (2009), John Wiley & Sons, Ltd.
2. Primdahl S and Mogensen M, *Gas conversion impedance: A test geometry effect in characterization of solid oxide fuel cell anodes.* Journal of the Electrochemical Society, (1998). **145**(7): p. 2431-2438.
3. Primdahl S and Mogensen M, *Gas diffusion impedance in characterization of solid oxide fuel cell anodes.* Journal of the Electrochemical Society, (1999). **146**(8): p. 2827-2833.
4. Jacobsen T, Hendriksen PV, and Koch S, *Diffusion and conversion impedance in solid oxide fuel cells.* Electrochimica Acta, (2008). **53**(25): p. 7500-7508.
5. Barsoukov E and Macdonald JR, *Impedance Spectroscopy: Theory, Experiment, and Applications*. 2 ed. (2005): Wiley-Interscience. 616.
6. Agarwal P, Orazem ME, and Garcia-Rubio LH, *Measurement Models for Electrochemical Impedance Spectroscopy.* Journal of the Electrochemical Society, (1992). **139**(7): p. 1917-1927.
7. Jensen SH, Hauch A, Hendriksen PV, Mogensen M, Bonanos N, and Jacobsen T, *A method to separate process contributions in impedance spectra by variation of test conditions.* Journal of the Electrochemical Society, (2007). **154**(12): p. B1325-B1330-B1325-B1330.
8. Smirnova AL, Ellwood KR, and Crosbie GM, *Application of Fourier-Based Transforms to Impedance Spectra of Small-Diameter Tubular Solid Oxide Fuel Cells.* Journal of the Electrochemical Society, (2001). **148**(6): p. A610-A615.
9. Schichlein H, Müller AC, Voigts M, Krügel A, and Ivers-Tiffée E, *Deconvolution of electrochemical impedance spectra for the identification of electrode reaction mechanisms in solid oxide fuel cells.* Journal of Applied Electrochemistry, (2002). **32**(8): p. 875-882.
10. Leonide A, Sonn V, Weber A, and Ivers-Tiffee E, *Evaluation and modeling of the cell resistance in anode-supported solid oxide fuel cells.* Journal of the Electrochemical Society, (2008). **155**(1): p. B36-B41-B36-B41.
11. Orazem ME and Tribollet B, *Electrochemical Impedance Spectroscopy*. (2008): Wiley-Interscience. 560.

Chapter 2

2. Replacing Petroleum with Sustainable Energy Carriers

This chapter gives an overview of the many energy carriers that could be used in the transportation sector as an alternative to gasoline, diesel and other petroleum-derived hydrocarbon fuels. These include other hydrocarbons like coal-to-liquids and biofuels, other chemical energy carriers like hydrogen and ammonia, and storage of electricity on-board vehicles in batteries, ultracapacitors, and flywheels. Any energy carrier can carry energy from any energy source. The sustainability and practicality of the many possible energy-source-to-carrier pathways are examined, emphasizing looking at many aspects of the energy systems to assess sustainability and practicality. Such thorough examination using a multitude of metrics seems to be necessary and should lead to more useful assessments than studies that focus on providing a single value "score" for a given energy technology or conversion pathway.

Liquid hydrocarbons are the most practical transportation fuels, due to their high energy density, ease of handling and compatibility with existing infrastructure. Electric propulsion is the most sustainable, because it has the highest life-cycle energy efficiency and eliminates emissions from the vehicle. In the near term, plug-in hybrid electric vehicles may be able to inherit the best qualities of each, significantly reducing liquid fuel demand with minimal battery size and enabling a gradual transition to a transportation infrastructure largely powered by electricity. As electricity production becomes cleaner this can have a significant impact on greenhouse gas emissions. Renewable resources may be ideally suited for providing transportation energy, where their intermittency does not cause added expenses as it does in the electric grid.

The continued need for hydrocarbons calls for developing means to produce them sustainably. Biomass is not likely a sustainable energy source at the scale needed, with the possible exception of algae. Sustainable use of hydrocarbons on board of a vehicle depends on technologies that capture carbon dioxide from the atmosphere and either sequester it, or recycle it into a fuel using renewable or nuclear energy. Recycling CO_2 into hydrocarbons using renewable or nuclear energy, in a non-biological process, appears to be the long term sustainable solution. This method of producing hydrocarbon fuels is further examined in **Chapter 3**.

2.1. Introduction

Transportation fuels are energy carriers that can be stored on board vehicles for propulsion and other energy needs. Liquid hydrocarbons stand out because of their high energy density and ease of handling. As a result much of the transportation sector operates on gasoline, diesel or kerosene. The specific choice of fuels has in part been determined by the chemical composition of natural petroleum, from which these fuels are derived through a simple distillation process.

A transition from petroleum-derived fuels to other energy carriers is desirable and may prove necessary for a number of reasons: petroleum resources may prove too limited to sustain a growing world economy; the uneven geographic distribution of petroleum reserves already leads to economic and political tensions; and the greenhouse gas (GHG) emissions from petroleum consumption must be eliminated.

Even though the distillation of petroleum may provide the most direct route to liquid hydrocarbon fuels, there are many other ways of producing them. Technologies exist to convert coal, natural gas or biomass into liquid hydrocarbon fuels. It is also possible to use non-fossil energy to dissociate carbon dioxide and water, and then use the resulting energy-rich gas mixtures as the starting point for fuel synthesis.

Hydrocarbon liquids are not the only means of carrying energy on board a vehicle. Other options include gaseous hydrocarbons, hydrogen, chemical hydrides, and electricity based storage systems (batteries, ultracapacitors, flywheels, and compressed air). Some of these energy carriers or the means by which they store energy may also be of interest for non-portable energy storage applications like large-scale storage of solar electricity to even out the intermittent supply.

Any energy carrier can carry energy from any energy source. Energy sources include fossil carbon, renewable energy sources including biomass, and nuclear energy. The current dependence on fossil carbon cannot last indefinitely as the supply is clearly finite. However, vast coal resources could last for hundreds of years. Combined with carbon dioxide capture and storage (CCS), fossil fuels could satisfy the world's energy demand for centuries without contributing to the greenhouse effect [1]. Similarly, the resource base for nuclear energy could last for many centuries. Solar energy, among the renewable forms of energy, is virtually inexhaustible.

An overview of the major energy carriers and the major energy resources is presented here with analysis and discussion about their relative sustainability and practicality for large scale use. The scale is set by world demand. The world consumes around 85 million barrels of oil per day, of which roughly two-thirds are used in the transportation sector [2, 3].

2.2. Sustainability and Practicality

Relevant metrics of sustainability and practicality are listed in **Table 2-1**. High sustainability calls for efficient use of land and resources, low impacts on the environment (the climate, the air, water and human health), and planning ahead for future energy resources so as to avoid lock-in into an unsustainable system. High practicality calls for affordable vehicles that do not make consumers sacrifice convenience and performance relative to today's vehicles, while also considering the inertia that is inherent in creating new large infrastructures.

Table 2-1. Metrics used to analyze the energy carriers

Sustainability	Practicality
• Energy yield per land area • Environmental and human health impacts • Net energy balance • Life cycle CO_2 emissions • Water consumption	• Energy density • Infrastructure change • Vehicle change • Economics

Several stages in the life cycle of an energy carrier must be considered. First there is the conversion of an energy resource into the carrier, then there is the transport and distribution of the energy carrier, followed by the storage of the energy carrier on board of the vehicle, and finally the stored energy is used for vehicle propulsion. It is usually possible to apply the metrics of sustainability and practicality listed in **Table 2-1** separately to each stage in the life cycle. Since these stages are well defined it is possible to analyze them separately. A complete well-to-wheel (WTW) analysis, or a well-to-tank (WTT) analyis can be performed by combining the appropriate stages. One can simplify the analysis, because different energy sources can be used to create the same energy carrier; different energy carriers can result in very similar energy utilization. Some measures are only associated with certain stages, or at least dominated by certain stages. For example, the energy yield per land area is associated with the energy sources, while the energy density of the energy carrier is most relevant for the on-board storage stage of the life cycle.

Environmental and human health impacts are a qualitative parameter. The net energy balance ratio, R_{NEB}, is the ratio of the useful energy obtained versus the energy expended to collect and utilize that energy. R_{NEB} has often been used in life-cycle analyses [4-6]. The emissions of CO_2 and other greenhouse gases are accounted for as CO_2-equivalent (CO_2e) emissions [7]. Life-cycle estimates inevitably have large variability, depending on the boundary conditions of the analysis, the sources of the data, and other factors. In this study we attempt to determine reasonable estimates by drawing from life cycle analysis literature, and discuss the

uncertainties. While some parts of the analysis are based on United States data, the arguments presented apply to energy carriers in the global context.

In defining sustainability it must be acknowledged that no technology or process can be sustained indefinitely; sustainability is linked to a specific scale of operation and a specific time frame [8, 9]. Wind energy at very large scales is not sustainable [10], nor are fossil fuels at very long time scales. As a result, "sustainable" and "renewable" are not synonymous, and technologies that cleanly harness the vast resources of fossil fuels to satisfy a very large demand can be considered sustainable during a useful time frame of a century or more, even though they cannot satisfy such a demand indefinitely.

Energy present in the energy source is converted into other forms, possibly multiple times before it is eventually applied to its final goal. The systems, chemicals and electromagnetic states that carry the energy after it has been extracted from the resource and before it has been used up in the final application we loosely refer to as energy carriers. Electricity can carry energy from one location to another, and thus it (or the electric grid) can be considered an energy carrier. However, in the context of transportation there is not only a spatial transfer but also a temporal transfer. Energy will have to be put on board a vehicle long before it is applied to locomotion or other needs within a vehicle. As a result, energy in the transportation sector is rarely carried as electricity, but it will take the form of electrochemical energy in batteries, electrostatic energy in ultracapacitors, kinetic energy in flywheels, or compression energy in compressed air tanks. Alternatively the energy could be stored in chemical form as in liquid hydrocarbon fuels, hydrogen, ammonia or other forms.

The main focus of this study is on various energy carriers for private automobiles. Busses, ships and airplanes have unique criteria for suitable energy carriers and propulsion systems, which we also briefly consider. Different energy systems will lead to different optimizations in the design of a vehicle. For example the high power density available in flywheels makes saving weight on the car far less important than it is for a heavy battery, which is ultimately limited in the rate it can deliver power to the drive train. On the other hand, it is difficult to make a comparison between different technologies, if all else has to be optimized to fit to the particular options. This study therefore assumes that all components outside of the drive train are similar to each other and comparable to today's average vehicles. Specifically, it is assumed that all cars use similar structural materials and do not take advantage of special lightweight materials to improve overall efficiency. Of course, all technologies are likely to take advantage of such advances as they become affordable.

The pathways from energy source to carrier and its use in vehicle propulsion are shown in **Figure 2-1** along with the constraints that may impede the sustainability or practicality of a pathway. In the following sections each energy source and energy carrier is discussed in terms of these constraints.

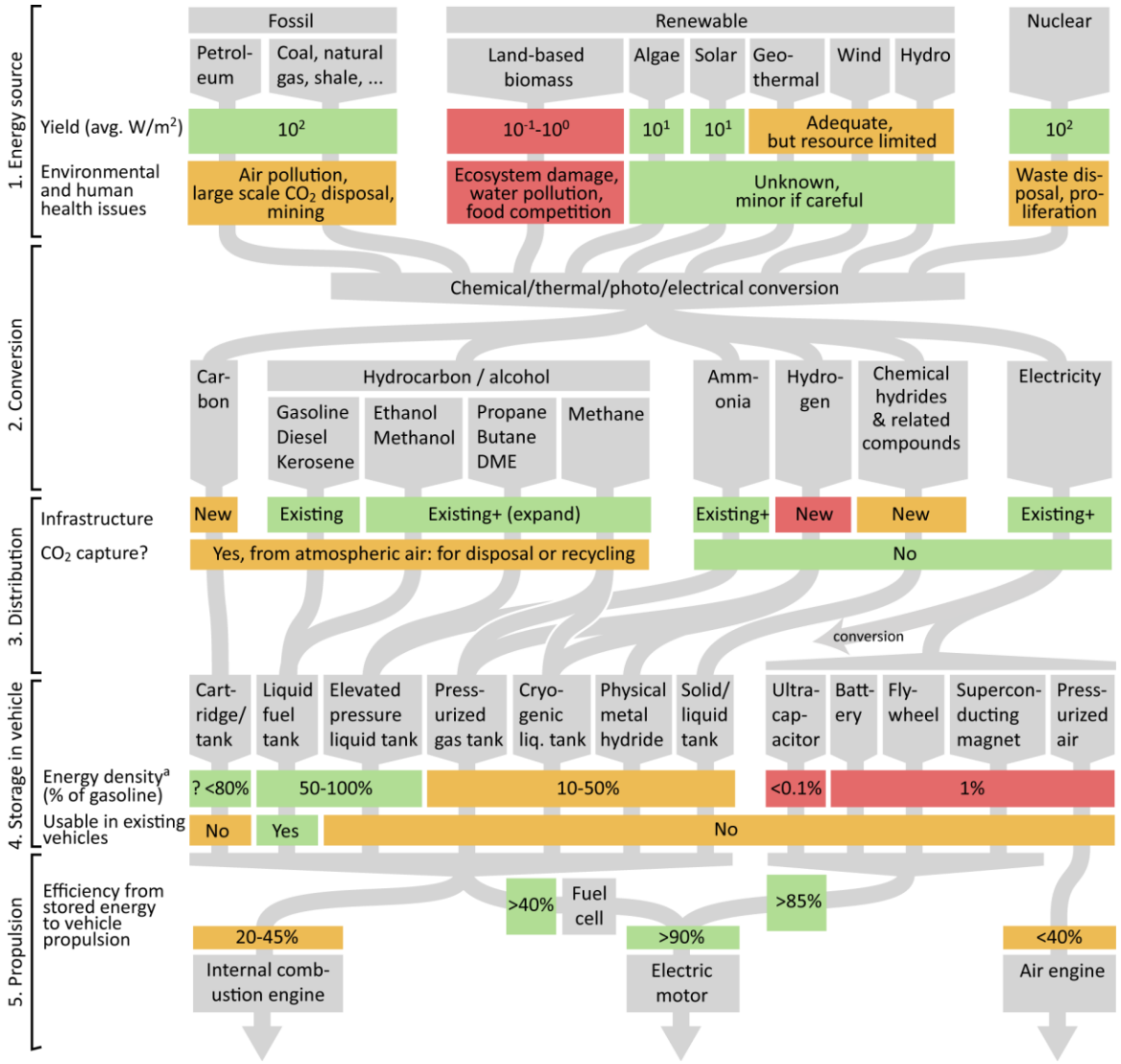

Figure 2-1. Diagram of energy flows for each energy carrier, starting from energy sources, with metrics of sustainability and practicality at each stage. Pathways with high sustainability and practicality can be traversed by following metrics colored green and avoiding those colored red. Yellow boxes indicate metrics with a potentially significant—but not insurmountable—impediment to large-scale sustainability or practicality. "Solar" refers to both photovoltaic and concentrated solar thermal sources. [a]Gravimetric energy density, or specific energy (e.g. J/kg). Volumetric energy density is typically in a similar range.

2.3. Energy Sources

2.3.1. Fossil

Fossil energy sources can provide electricity or they can be used as the chemical energy feedstock to produce hydrocarbons or hydrogen. Fossil fuels are certainly practical, evidenced by their domination of the primary energy supply.

In terms of sustainability, the low land area requirements of fossil resources are rivaled only by nuclear energy. However, how that land is used is a concern. A large scale switch to coal-derived transportation fuels, for example, would accelerate the depletion of coal resources and increase coal mining. Air pollution is another environmental concern, and whether coal is used for electricity generation or in chemical conversions to produce liquid hydrocarbon or hydrogen fuels, it will most likely increase water use, and significantly [11]. In general, large scale implementation of fossil-derived alternatives to oil may exacerbate land, air, and water pollution. These issues are not roadblocks to sustainability but do need to be carefully managed.

Ultimately, sustainable use of fossil resources depends on CCS technologies. Electricity and hydrogen produced from fossil resources can be rendered carbon neutral by capturing CO_2 emissions at the production plant and storing it safely and permanently. In this case, the energy carriers contain no carbon. If hydrocarbon fuels are desired, however, producing them from coal or natural gas would increase the total CO_2 emissions associated with each mile travelled relative to the carbon-free energy carriers and relative to today's petroleum emissions, by emitting GHGs both at the production plant and at the vehicle [12]. Then, CO_2 must be captured from the atmosphere as well in order to handle the vehicle emissions. Capture could be accomplished by growing biomass [13] or with an industrial air capture process [1, 13-17]. However, as we discuss in the next section, large-scale use of biomass in the energy sector may not be sustainable.

Depending on how it is implemented, CCS may have significant environmental impacts [18]. For example, sites for geologic injection of CO_2 need be carefully selected and monitored, and large-scale mineral carbonation would involve large mining operations. The fossil fuel land footprint, of which mining already makes up the majority, would increase with CCS—though not likely to a constraining level. New fossil energy power plants and synthetic fuel plants can supply the needed scale for transportation energy, but to be sustainable an enormous effort must be undertaken to develop these CCS technologies and to carefully sequester carbon emissions.

2.3.2. Biomass

Biomass is a well-known energy source that sustains human and animal life. Therefore it is clearly sustainable at a reasonable scale. With rising oil prices, its use as a feedstock to produce biofuels is growing rapidly and many of these fuels are heavily subsidized [19-21]. Today's biofuels market is dominated by bioethanol, produced from corn and sugarcane feedstocks, and biodiesel, produced from rapeseed and other oils. In development are so-called advanced biofuels, including cellulosic ethanol and thermochemical conversion of biomass to liquids via gasification and pyrolysis. Advanced biofuels aim to utilize more parts of the plant as well as a wide range of herbaceous, woody, and waste feedstocks. Biomass can be treated

similarly to fossil fuels using thermochemical processes, similarly yielding hydrocarbons, hydrogen, and electricity. With CCS, biohydrogen and electricity could even be carbon negative.

However, biomass may be less sustainable than fossil fuels at the necessary scale. First, biomass needs one to two orders of magnitude more land than other energy sources to provide a given amount of energy. Even with fertilizer-intensive agriculture, the yield of biomass per land area is very low, capturing less than 1% of incident solar energy [22]. The maximum observed efficiency for non-agricultural grasses, near the theoretical limit of photosynthetic biomass, is around 4% [23]. Then, only the above-ground part of the biomass is harvested, part of that is utilized in a conversion process, and the conversion process consumes energy as well. This results in an actual fuel ethanol efficiency from solar energy, using corn and sugarcane feedstocks, of around 0.16-0.24% [22]. Today's biodiesel has even lower yields. Solar electric and solar thermal devices are two orders of magnitude more efficient at converting sunlight into usable energy. Diverting the entire current corn harvest to ethanol would supply about 12% of current U.S. gasoline consumption [4]. Already, 33% of the US corn crop was used to produce fuel ethanol in 2009, up from 23% in 2007 – the fraction has been steadily increasing for the last decade [24]. The Energy Policy Act 2005 called for a further doubling of ethanol production by 2012, which would then supply around 2% of petroleum-based transportation energy [2, 25]. To fully replace U.S. gasoline today with corn ethanol would require at least 700 million hectares, roughly 90% of the total contiguous U.S. land area and four times the current agricultural land [26]. Sugarcane needs about half the amount of fertile land, when grown in Brazil. Land area would still be a constraint even if similar yields were possible in the U.S. Switchgrass and other bioenergy crops used in advanced biofuels processes, which utilize a greater fraction of the above ground plant matter, still would not improve yields [27]. On the other hand, the use of bio-wastes and residues do not use additional land—but they can meet only a small fraction of fuel demand. Unless advances are made in developing algae—which needs far less land and does not need fertile land for its aquatic cultivation [28]—as an affordable fuel feedstock, biomass cannot scale up to meet demand and replace petroleum. Although most of the above numbers pertain to liquid biofuels, the arguments hold for the other bioenergy products.

Then, there are significant environmental and societal impacts resulting from how that land is used. To maximize yields, crop farmers use the kind of intensive agriculture practices that have enhanced sugarcane yields in Brazil more than 2.5 times what they were in 1979 [22]. Yields are maximized via usage of fertilizers, pesticides, and insecticides, which take energy to produce and are detrimental to the environment and human health if used at large scales [29]. Corn ethanol in particular is fertilizer and pesticide intensive [4, 30]. Apart from water pollution by runoff of these chemicals, water resources are also affected by using water for irrigation and for refinery operation [31, 32], and many times more water may end up being consumed than in current gasoline production ([11, 33]). Monoculturing from widespread use of an individual

crop and soil erosion can damage ecosystems [27]. These effects can be minimized by using diverse biomass feedstocks in advanced conversion processes [34, 35]. Careless use of biomass for energy will therefore shift pollution from the atmosphere (in the case of fossil fuels) to the hydrosphere and the biosphere. The vertical axis in **Figure 2-2** illustrates this tradeoff between yield and environmental impact. The midpoint would correspond to low-yield, low-impact biomass, such as switchgrass and high-diversity grassland that can be grown on less fertile soil and using less fertilizer [27, 34]. Economics, however, would likely drive farmers toward higher yields at the expense of increased environmental impact.

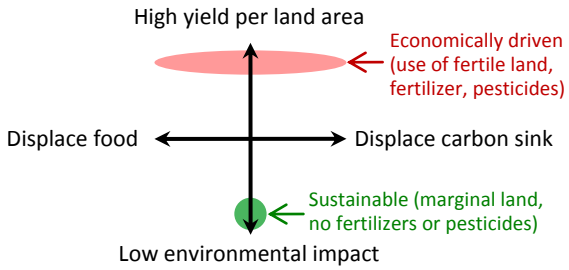

Figure 2-2. Tradeoffs that impede the sustainability of the large-scale use of land-based biomass as an energy source.

Today, crops grown for fuel compete with food crops for land or even directly displace food, thereby affecting the availability and price of food [29, 36-38]. Instead, it would be desirable to grow biomass on land not currently being used for crops. However, roughly two-thirds of earth's total land area is already covered by biomass and the rest is classified as urban and wasteland (marginal land) [39]. Recklessly displacing carbon sinks such as forests with energy crops can cause a large increase in GHG emissions [38, 40-43] in addition to potential adverse effects on biodiversity. In such a case, even fossil fuels without CCS may be preferred from a climate change perspective. For example, displacing carbon-rich dense tropical forest with relatively sparse grassland for bioenergy should be avoided since it reduces the carbon stock of the area, creating a carbon debt. Therefore, the most fertile high-yielding lands should be avoided. Instead, grassland for bioenergy could displace existing grassland. In this case, the carbon stock in the above-ground part of the plant will still be less than it was, on average, since the crop will be on an agricultural growth-harvest cycle and not continually present on the land. Then, the only way energy crops can be made carbon-neutral is by first sequestering, rather than releasing, much or all of the above-ground carbon in the biomass that is about to be displaced, followed by practicing sustainable agriculture that does not deplete soil organic carbon. The agricultural method (and resulting soil carbon balance) is an important variable in determining the carbon debt resulting from land use change [44]. If advanced biomass energy tends towards converting the entire above-ground part of the plant to fuel to improve yields, this part of the plant will not contribute to soil carbon as it does in sustainable agriculture. Finally, planting on

marginal lands instead would not displace a carbon sink, and it could be possible to enrich soil carbon, resulting in a net sequestration of carbon [34]. The horizontal axis in **Figure 2-2** illustrates the tradeoff between displacing food and displacing carbon sinks. Marginal lands are the environmentally sustainable midpoint. Economics will favor planting energy crops on land where biomass already thrives, displacing either a carbon sink or displacing agriculture.

These tradeoffs suggest that large-scale, land-based production of biomass for energy is a no-win situation because economics and sustainability are at odds. The sustainable way to grow biomass for energy is on low-yielding, marginal land and to avoid improving yields with fertilizers and other traditional agricultural methods, which can only be achieved with strict policies. Following this path would result in cultivation of low-yielding biomass on only a small fraction of the earth's land area, exacerbating the land area constraint and therefore further limiting the scale of biomass as an energy source. Furthermore, there is a reason biomass is not already thriving on the land. Yields will necessarily be low, and the energy inputs and corresponding costs needed to achieve practical yields on such infertile land may be prohibitively high. New advanced technologies do not overcome these drawbacks that are associated with constrained biomass availability [45]. Even if hybrid electric propulsion in vehicles reduces overall liquid fuel demand by a factor of two, the large-scale sustainability issues do not go away. It is important to carefully study the consequences and limit the growth of land-based bioenergy. Aquatic biomass (e.g. algae), which does not share all of the drawbacks of land-based biomass, should be further studied as an energy source. However, algae might not resolve the sustainability issues, and may in fact have higher environmental impacts in terms of energy use, GHG emissions, and water use [46]. Also, whereas the cost of biodiesel from palm oil is roughly competitive with recent petrodiesel prices, the cost of biodiesel from algae needs to come down by an order of magnitude [28].

2.3.3. Renewable and Nuclear

Renewable energy sources include solar (photovoltaic and concentrating thermal), wind, geothermal, and hydroelectric systems. These sources are typically associated with sustainability, though no energy conversion system comes without environmental impacts. Energy yield per land area is typically lower than fossil and nuclear energy, but high enough that land area is not a constraint to scaling up as it is with land-based biomass. However, geothermal and hydroelectric resources have a resource availability limitation. This does not mean that they should not be developed—only that they are unable to provide a large fraction of energy, transportation or otherwise. The sources that can sufficiently scale up need to be studied to understand potential full-scale impacts. A recent analysis has concluded that solar and wind power use the least amount of water for electricity generation, in comparison with fossil and nuclear power [47]. Wind turbines, for example, begin to have local and global climate effects upon approaching a certain scale [10]. Solar energy appears to be able to meet the full scale—a

typical example is that the incident solar energy reaching the earth's surface is equivalent to 9000 times the energy demand [48]. At present, however, aside from solar heat, solar energy is too expensive to be competitive with fossil, nuclear, and wind. Assuming the cost of solar power decreases as expected [49], solar will most likely make a significant contribution to the mix of energy sources that will make up the long-term future energy portfolio.

Nuclear provides more concentrated energy in terms of land area, including the power plant and other industrial plants. However, for nuclear fission to sustainably provide electrical or thermal energy to store as an energy carrier, solutions to the disposal of radioactive waste and the control of proliferation of bomb-suitable material must be found. In addition, the great amount of safety measures taken to avoid reactor accidents have significantly increased the cost of nuclear energy. These barriers to sustainability require significant policy efforts and research and development, but they are not insurmountable [50].

Renewable and nuclear sources harness thermal energy, kinetic energy and solar irradiation and are used today to deliver these types of energy directly or to generate electricity. The best and most efficient use of this energy is to directly deliver and use it as much as possible without conversions. However, chemical energy carriers, with their high energy density, are well suited for portable applications such as transportation, as will be discussed further below. Whereas fossil and biomass resources are best used in chemical-to-chemical conversions, renewable and nuclear sources close the door on such processes while opening the door to produce chemical energy carriers by thermolytic, thermochemical looping, electrochemical, photoelectrochemical and photochemical conversions. Most of these processes are in fundamental stages of research that aim to demonstrate viability [51].

Electrochemical energy systems are farther along—today, a small fraction of hydrogen is produced by water electrolysis using inexpensive hydroelectricity, and fuel cells, which have long held interest for their potential to generate electric power from fossil fuels more efficiently than conventional combustion-driven power plants, are heavily researched. High temperature solid oxide cells in particular are making significant progress and approaching economic viability. Recently, various large businesses in California have installed solid oxide fuel cells – by taking advantage of the large self-generation incentives in that state, producing power on-site from natural gas using these cells is economical. Solid oxide cells are also beginning to appear very attractive for efficient conversion of renewable or nuclear electricity to chemical energy by electrolysis, [52] and **Chapter 3**.

Intermittent resources like solar and wind are well suited to supply transportation energy: whereas their intermittency requires additional storage expenses in the power sector which requires energy on demand, vehicles store the energy on-board as an energy carrier, and with the right infrastructure the energy could be stored at any time of day, when it is available.

2.4. Energy Carriers

There is a broad distinction between chemical storage systems and electricity-based energy storage systems. Electricity-based energy carriers are charged by electrical energy and discharge electrical energy, with both energy storage and retrieval taking place on board the vehicle, whereas chemical energy carriers store energy upstream and only release this energy within the vehicle. This difference gives the two types of energy carriers very different properties. For example, chemical energy carriers typically use the air as a reactant and release the oxidized product chemicals back into the environment. The electricity-based energy carriers inherently have a lower energy density because they contain the energy storage mechanism and all of the stored energy on-board the vehicle.

2.4.1. Electricity-based energy carriers

Electricity based storage systems include batteries, ultracapacitors, and flywheels, which store electricity as electrochemical, electrostatic, and kinetic energy respectively. All have in common that they can use electric currents driven by an external voltage to increase their energy content, and later deliver the same energy as a current driven by an internal voltage, which drives an electric motor. Quite often these forms of energy storage can use the same interface for loading and unloading energy. These systems are well suited to recover kinetic energy during braking, and they could under certain circumstances even be used to return power back to the electric grid. Compressed air is also a possible transportation energy carrier which is based on storing electricity, however the electrical energy is converted to compression energy outside of the vehicle and a compressed air engine is used instead of an electric motor. It is also be possible to transmit electric power wirelessly to a vehicle while it is in transit [53]. This would reduce the required size of an electricity based storage system on-board the vehicle, or even eliminate it if an infrastructure was set up to transmit power to vehicles continuously or near-continuously. This is a relatively unexplored method.

Battery electric vehicles were introduced at the turn of the 20th century. Lithium ion (Li-ion) is becoming the dominant battery technology due to to its high energy and power density, charge-discharge efficiency and cycle life [54]. Li-ion batteries with a variety of electrode and electrolyte compositions are available [55], and research and development aims to maximize energy density while also ensuring safety. It also has a lower environmental impact and toxicity than other chemistries [56, 57], which is further improved by effective recycling programs [58, 59]. The theoretical maximum energy density of today's Li-ion cells is roughly 400 to 600 Wh/kg [60, 61], 3-5% the energy density of gasoline. The best actual energy densities of Li-ion batteries on the market are ~1% that of gasoline. Whereas a typical internal combustion engine (ICE) converts less than 20% of the fuel energy content [62, 63], Li-ion batteries powering electric motors convert around 80% of energy content [56, 59, 64].

Accounting for this factor-of-4 higher propulsion efficiency, available batteries are still 5 to 8 times the weight or volume of gasoline in terms of energy useable for propulsion. Liquid hydrocarbons are clearly extremely compact, convenient fuels. This partly stems from the fact that their combustion gets nearly 80% by weight of the reactants from air (as O_2). Future battery chemistries may offer higher energy densities; the theoretical energy density of the Li/O_2 electrochemical couple approaches that of liquid hydrocarbons.

Ultracapacitors are either electrochemical double layer capacitors that have extremely high capacitance or conventional capacitors with enhanced dielectrics [65]. The energy density of available ultracapacitors is up to 5 Wh/kg—an order of magnitude less than batteries [54]. Much higher energy densities have been claimed [65] but not demonstrated. At present, ultracapacitors are not suitable to solely power a vehicle. However, they offer some advantages over batteries: they can provide higher power output, higher efficiency and longer lifetimes. Therefore, ultracapacitors may complement batteries in electric vehicles, potentially extending the lifetime of batteries by handling damaging power bursts [66, 67].

Flywheel vehicles are at younger stages of development. Flywheels seem to have lower energy densities than batteries, and must ensure safety and deal with gyroscopic effects during vehicle manuevers.

The electricity-based energy carriers have several unique advantages over the others. They typically have a higher efficiency in using the stored energy for vehicle propulsion than hydrogen and hydrocarbons; whereas 15-20% of the energy in gasoline is typically converted to motion, and around 50% for a hydrogen fuel cell powering a 90%-efficient electric motor, a battery and ultracapacitor can have as high as 90 to 95% charge-discharge efficiency, respectively, powering a 90%-efficient electric motor. This high efficiency gives these energy carriers a higher net energy balance and lower life-cycle GHG emissions than the other energy carriers. They can also store regenerative energy, e.g. from the electric motor decelerating while braking the vehicle. As the vehicle gets older, its sustainability would improve as the sustainability of the electricity grid improves. Unlike hydrogen, distributing electricity to a vehicle does not need a complete infrastructure overhaul. To fully replace the approximately 14 million barrels per day (~0.85 TW) of petroleum fuel used in the transportation sector with electric vehicles would require expanding the present electricity generation capacity by about 20-25% [26]. The current electric grid would be expanded as electric vehicles are adopted, and the current idle night-time capacity can handle a significant amount of demand [68, 69], as we discuss further in **section 2.5** below. Long-range driving would need roadside recharging. Concerns that high-voltage charging stations are much slower than refilling a gasoline tank may not be so important because vehicles do not need to be fully refueled at a charging station. Cheaper refueling at home during off-peak hours will always be available—they only need to be refueled enough to get home. Charging also replenishes battery capacity nonlinearly, with a

faster rate initially; a 50% recharge takes much less than half the time of a full charge [70], further reducing charging time at a station.

Electricity based energy carriers also create an opportunity for cooperation between the transportation and electricity sectors. The energy carriers could double as power storage and return electricity to the grid[i]. Vehicles could be integrated into the electricity grid and provide load balancing by taking advantage of "vehicle-to-grid" (V2G) transmission, wherein power is pulled from the batteries of vehicles attached to the infrastructure to assist in meeting peak loads and given back to the batteries during the off-peak periods [71]. Similarly, V2G could also improve stability and reliability with intermittent sources like wind power, and provide uninterruptible emergency power to the home during grid outages [71]. Although implementation of V2G depends on a widespread electric vehicle charging/discharging infrastructure and a broad roll out of advanced "smart" grid technologies, it has been estimated to provide more value for the electric utility than the cost of implementation [72].

Used vehicle batteries can also be integrated into the grid as inexpensive power storage for intermittent sources. The end of life of a vehicle battery is usually defined as when 80% of its capacity remains. However, the battery still has useful life remaining, which can be used in stationary storage where the reduced energy density is not as important. There appear to be no overwhelming problems in implementation [73, 74], and utility companies have expressed interest in buying used vehicle batteries [75]. Arrangements in which the vehicle owner leases the batteries could also reduce the consumer's upfront costs, which would work with both the V2G and spent batteries scenarios. Altogether, there appears to be opportunity for economic cooperation between the cost of the vehicle and the cost of electricity grid management.

The major obstacles to the practicality of these energy carriers are their low energy densities and high costs. Low energy density limits the range the vehicle can be driven between recharges. Because of the low energy density, heavy trucks and aircraft are unlikely to be powered by batteries alone [76] and many electric vehicles are constructed of ultra-lightweight materials to reduce the needed battery size [64, 77]. Batteries powering a standard-weight compact sedan with a full 200 to 300 mile electric range can make up more than half the total vehicle weight. Even in ultra-light vehicles with that sort of range, the batteries account for one-third of the total weight [64]. Additionally, batteries and lightweight materials are themselves costly leading to vehicles that are several times more expensive than a conventional vehicle for the consumer. The battery pack itself in the Tesla Roadster costs as much as an entire new conventional car.

[i] Note that this would only be applicable for road transport, not airplanes and ships. However, airplanes and ships require a higher energy density energy carrier than the electricity based carriers, anyway.

The cost of replacing batteries during the vehicle lifetime is another key concern—but one that can be addressed through appropriate sizing. Battery cycle life is the number of charge-discharge cycles that could be withstood before capacity was lower than 80% of the initial capacity. For all batteries, the cycle life is enhanced in a nonlinear manner when the battery is charged after being only partially discharged. For instance, at only 50% depth-of-discharge (DOD), the cycle life may be about 3 times that of 100% DOD [59, 78]. Hybrid electric vehicle NiMH batteries rely on small DOD to achieve long lifetimes. An all-electric vehicle battery could therefore have a long life if it is generally oversized for day-to-day driving ranges.

Developments in batteries and economies of scale in manufacturing will of course bring the price down. Today's NiMH and Li-ion traction batteries cost more than $500-700/kWh [79, 80], whereas smaller Li-ion batteries for laptops and consumer electronics sell for far less. From 1994 to 2003, production cost for Li-ion batteries fell 86% as manufacturers increased production volume by a factor of 20 [81]. High capital price is partially offset by savings in fuel during vehicle operation. If electricity is available to the consumer at $0.10/kWh and gasoline at $3/gal, and the electricity is stored and used for propulsion with about 4 times the efficiency, the "fuel" cost of an electric vehicle is about one-third that of the gasoline engine vehicle [26].

2.4.2. Hydrogen

Today, hydrogen is primarily produced using fossil fuels. Steam-methane reforming is the dominant form of production, followed by gasification (of oil, refinery gas and coal). Water electrolysis accounts for the remaining 4% [51]. Coal-derived hydrogen can scale up to meet demand. Like fossil-derived hydrocarbons, the CO_2 emissions during fuel production would need to be captured and sequestered. However, hydrogen appears more attractive from a GHG management point of view because air-capture of CO_2 after fuel combustion would not be needed. It does not have this advantage over the electricity-based energy carriers.

Because hydrogen is gaseous at ambient conditions, it takes up several times the amount of storage space and weighs several times more than gasoline (accounting for the container), which is still much more compact than the electricity-based energy carriers. Its energy density on board the vehicle is not impractical. However, the energy density while distributing it to the vehicle is much lower than electricity. Consequently, distribution and storage systems suffer significant energy losses during transport of the fuel [82].

The requirements of a new distribution infrastructure and new vehicles put hydrogen at a significant disadvantage in terms of practicality. First, there is the need to duplicate or replace existing fuel distribution and storage systems. Whether tanker trucks or large-scale pipelines are used, the energy that must be spent to transport the hydrogen can be equivalent to a large fraction of the fuel's energy content. Storage on-board the vehicle, either as a pressurized gas, cryogenic liquid, or bound hydride, is difficult to do compactly and cost effectively.

The need for new vehicles with new propulsion systems is by itself only a potential constraint because the turnover rate of the vehicle fleet is fast enough that consumers will adopt new vehicles if they are convenient and affordable. Although the new system will be more efficient than current hydrocarbon drive-trains, it will be less efficient than electric drive trains. It is primarily due to the expenses and inefficiencies at each fuel cycle stage that the hydrogen economy has collected its share of critics [82-86]. Bossel illustrates the losses by comparing an electrolytic hydrogen economy with an electric vehicle economy, showing that the electric vehicle propulsion receives about 3 times more of the energy in the original electricity source than the propulsion of the fuel cell vehicle [82]. The increased fuel efficiency of fuel cells or new hydrogen-burning ICEs over hydrocarbon-burning engines is likely outweighed by their additional cost and the upstream energy expenditures. Fuel cells, though promising technologies, need to come down in cost by 1-2 orders of magnitude [87]. At present, the cost of all stages has been estimated as prohibitively high [51, 88, 89].

The energy penalties and cost of moving to a hydrogen system would only be worthwhile if it offers significant advantages over the other fuel cycles. This does not appear to be the case: of all the sustainability and practicality metrics, hydrogen only has the advantages of potentially reduced GHG management versus hydrocarbons and of greater energy density versus the electricity-based energy carriers. In addition, transitioning would have more technological lock-in than the other options [90].

Hydrocarbons can be seen as a means of hydrogen storage alongside carbon which are easier to handle, have higher energy density than hydrogen storage mechanisms and most importantly they can be used in the existing hydrocarbon fuel based infrastructure.

A kind of intermediate energy carrier with properties between those of hydrogen and hydrocarbons is ammonia [91], which is storage of hydrogen alongside nitrogen (NH_3). Ammonia is gaseous at ambient conditions but liquid under mild pressure. It is easier to store and has higher energy density than hydrogen. Ammonia is produced in greater quantities today, most of which is used as fertilizers. However, like hydrogen, ammonia would require a new infrastructure (although ammonia is already widely distributed, just not on the scale of fuels). It is more difficult to handle and more toxic than hydrocarbon fuels. Also, combustion of ammonia produces NO_X pollution, which would need to be resolved. A fuel cell could instead be used, powered either by hydrogen released from the ammonia by reforming the ammonia upstream or possibly directly by ammonia [92-94].

2.4.3. Hydrocarbons

Liquid hydrocarbons are produced today via chemical conversions of fossil and biomass resources. Coal and natural gas are converted via the Fischer-Tropsch process to yield liquids that closely resemble petroleum diesel and gasoline [95]. Today's biofuels (typically alcohols and

biodiesel) may have lower energy density and be unable to substitute directly, but biomass can be converted using reactors similar to those that perform fossil-to-liquids conversions—or fed together with fossil resources [96]—to yield fuels that can directly substitute for petroleum-derived fuels. In general, liquid hydrocarbons are the most practical energy carriers due to their high energy density and ability to readily substitute into the current transportation infrastructure and vehicles.

Use of fossil-derived synthetic hydrocarbons can result in lower tailpipe emissions of non-GHG pollutants than their petroleum counterparts [97] while typically having higher life-cycle GHG emissions, especially when the feedstock is coal [12]. As discussed in the fossil energy sources section above, management of these GHG emissions requires capturing CO_2 from the atmosphere and storing it in addition to CCS at the fuel production plant. Fossil-derived hydrocarbons have a WTW R_{NEB} of roughly 0.2. This is significantly less than the electricity-based energy carriers, mainly because of the lower efficiency of internal combustion engines than the electric drive trains.

Combustion of biofuels is generally cleaner than petroleum fuels because tailpipe emissions contain little sulfur. CO, particulates and unburnt hydrocarbons may also be moderately reduced, while in the case of biodesel, nitrogen oxides may be increased [27, 98]. As discussed in the biomass **section 2.3.2** above, the life-cycle GHG emissions associated with biofuels depend greatly on land use. When not displacing other carbon sinks, biofuels can significantly reduce GHGs. In terms of the energy balance, there have been many recent studies about current biofuels, with widely varying estimates. Variability derives from differing system boundaries, different data for a given process or stage, and whether a study assigns energy equivalent values to co-products. Corn ethanol was recently estimated, by two separate studies, to possess slightly more energy (WTT R_{NEB} = 1.19 to 1.25) than the energy expended to collect the biomass and produce the fuel [4, 6]. A WTT R_{NEB} of 1 implies that there is no reduction in total fossil fuel used. However, there is still a significant reduction in petroleum use—up to 94% [6, 99, 100]. Sugarcane has a much higher energy return [101], and advanced biofuels are expected to as well [6, 34, 102]. Even corn ethanol is seeing improvements in energy efficiency during production [103]. Therefore, although the WTT R_{NEB} for today's biofuels is low [4, 6, 102], we do not expect it to be a long-term constraint. The constraints associated with the biomass energy source appear to be much more severe.

Hydrocarbons can also be produced without the use of fossil or biomass resources. Processes that store the energy of the potentially most sustainable long-term sources (renewable and nuclear) as the most practical carrier (hydrocarbon) are under development. Such carbon-neutral, synthetic hydrocarbon fuels are based on the industrial capture of CO_2 from the air and the splitting of H_2O and/or CO_2 driven by affordable renewable or nuclear energy. This interesting means of producing hydrocarbons is the topic of **Chapter 3**.

2.5. Hybrids, Electricity and Hydrocarbons

In hybrid configurations, energy carriers might be combined in a fuel cycle that has the strengths of each, offering greater sustainability and practicality. Electricity-based energy carriers can co-power a vehicle along with hydrocarbons or hydrogen. Such hybrid electric vehicles (HEVs) have recently entered and gained popularity in the market. The small battery in today's standard HEV, which is charged by the engine and by regenerative braking, drives an electric motor during low power demand. Above a certain power demand threshold, the diesel or gasoline engine takes over. This also allows for a smaller, reduced power engine which operates more often in its range of highest efficiency while the electric motor handles the variable speeds during starting, stopping and idling. HEVs consume about 30% less fuel on average, with the bulk of those savings during low-power city driving [104]. More than one drive-train can be present in a vehicle, in a parallel or series configuration. The HEV described above uses a dual parallel drive-train. A vehicle that features a larger battery pack which drives the electric motor for longer distances and allows the consumer to charge the batteries by plugging into an electric outlet is known as a plug-in hybrid electric vehicle (PHEV). In the series configuration in new demonstration models for PHEVs, an engine serves to only charge the batteries which drive an electric motor [80]. Acting as an electric generator and without needing to handle power transients, the engine can run at near constant load near its peak efficiency.

PHEVs seem to work well with the driving habits of U.S. drivers. The average daily driving distance in the U.S. is about 33 miles [69]. The battery capacity can be designed to minimize size and weight while also maximizing the portion of vehicle propulsion provided electrically. On average, 31-39% of annual miles are the first 20 miles of daily driving and 63-74% are the first 60 miles [105]. In other words, the batteries in a PHEV-20 (20-mile electric-only range) and PHEV-60 can supply about one-third and two-thirds of the propulsion energy, respectively [106], or potentially more [54, 107]. The batteries in a PHEV-20 and -60 would account for about 4% and 11% respectively of the total vehicle weight [26]. This is much more feasible than powering a vehicle with a full 200-300 mile electric range, in which the batteries make up a large fraction of the total vehicle weight (discussed earlier). However, PHEV batteries are likely to be cycled more fully than batteries in HEVs and all-electrics. To ensure a sufficient cycle life at this high DOD, the battery must be carefully sized and have a good controls system.

PHEVs reduce hydrocarbon fuel demand, thereby reducing the amount of CO_2 that must be captured from the air and sequestered (in the case of fossil fuels) or recycled via biomass (in the case of biofuels). They enable a gradual transition to more sustainable fuel cycles. In the near term, petroleum fuel consumption is reduced by the one-third to two-thirds. Even when powered by today's coal or natural gas and accounting for electricity grid losses, the efficiency of generating the electricity, storing it in a battery and then providing vehicle propulsion is much higher than the gasoline ICE, reducing net GHG emissions significantly

[68, 104, 105]. At an aggressive but reasonable rate of vehicle adoption and a moderate rate of emissions reduction in the electricity sector, PHEVs could reduce U.S. GHG emissions by more than one Pacala-Socolow "stabilization wedge" [26, 108]. Together with the moderate grid decarbonization, nearly 4 wedges may be accounted for by 2050, or more than half of the total emissions reductions needed for stabilization at 2010 levels. In the long term, as electricity sources transition to a de-carbonized portfolio and liquid hydrocarbons are made carbon-neutral, emissions are further reduced. PHEVs also inherit the benefits of full electric vehicles, as discussed earlier: they can also cooperate with the electric grid, and as time goes by, the vehicle becomes greener as the grid that feeds it becomes greener.

The benefits of reducing liquid fuel demand with minimal battery size in PHEVs might extend to the economics of the vehicle. The capital cost of the battery and electric motor is many times higher than that of the IC engine. Liquid fuel consumption, which costs more than electricity, is simultaneously minimized. For a PHEV-20, the battery capital cost is about 5% of the full-range electric vehicle battery described above, and the operating cost is about 75% of a conventional fully gasoline-powered vehicle [26]. As batteries improve and become cheaper, they can gradually replace more of the propulsion energy, enabling affordable longer-range PHEVs that approach fully all-electric vehicles. If the liquid fuel need is low enough, even biomass may be able to supply it sustainably. PHEVs should be competitive if battery costs come down by a factor of 2 or if gasoline costs double [109]. This appears to be within reach based on the cost reductions that came with mass production of consumer batteries, as discussed earlier.

The fraction of vehicle propulsion supplied by electricity will most likely grow in the future as either electric vehicles or PHEVs are adopted. The remaining transportation energy will likely still be supplied by hydrocarbons, which calls for means to produce them sustainably. At present, biomass-based fuels do not seem to be an option that can scale up sustainably. Both fossil derived hydrocarbons and hydrocarbons produced from renewable or nuclear energy by recycling CO_2 could be CO_2-neutral and meet the large-scale demand. The CO_2-recycled hydrocarbons would be the long term sustainable solution since fossil fuel supplies are limited, CO_2 sequestration sites may be limited before fossil fuel supplies run out, and due to other environmental concerns besides CO_2. The two energy carrier scenarios in which both sustainable hydrocarbons and electricity power PHEVs are depicted in **Figure 2-3**. A long-term sustainable energy timeline for transportation in which electric propulsion and sustainable hydrocarbons scale up to meet total transportation energy by 2050 is illustrated in **Figure 2-4**.

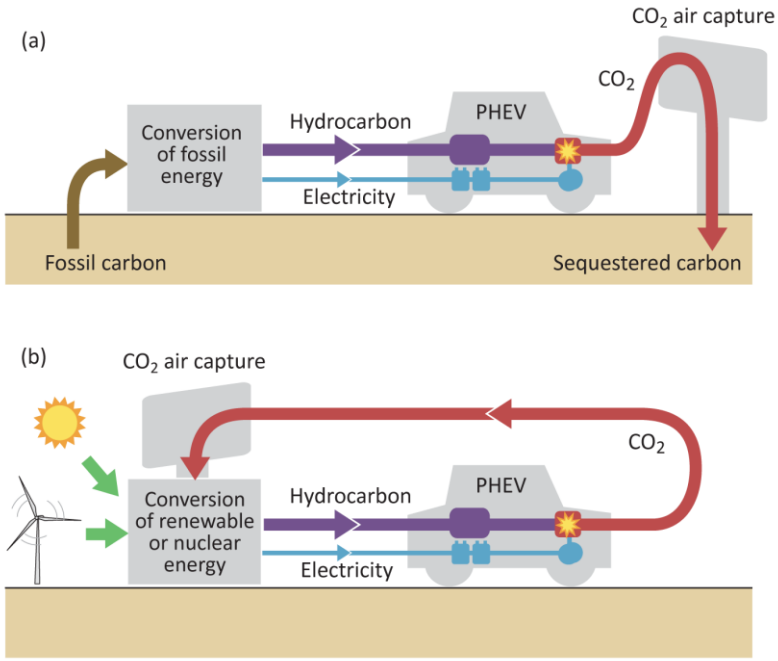

Figure 2-3. Diagrams of sustainable energy carrier scenarios in which both liquid hydrocarbon fuels and electricity are used to power PHEVs, based on (a) fossil energy sources, (b) renewable or nuclear resources (without biomass).

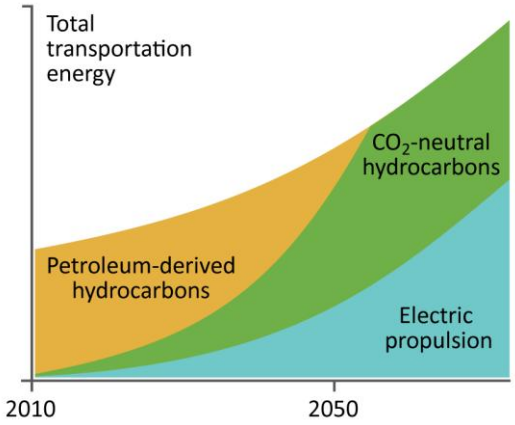

Figure 2-4. Proposed long-term sustainable energy timeline for transportation in which electric propulsion and sustainable hydrocarbons scale up to meet total transportation energy by 2050

2.6. Conclusions and Outlook

This study has reviewed the major energy sources and energy carriers and examined the sustainability and practicality of each. The many pathways that can connect nearly any energy source to any energy carrier were considered.

Liquid hydrocarbons are the most practical transportation fuels, due to their high energy density, ease of handling and compatibility with existing infrastructure. Electric propulsion is the most sustainable, because it has the highest life-cycle energy efficiency and eliminates emissions from the vehicle. In the near term, plug-in hybrid electric vehicles may be able to inherit the best qualities of each, significantly reducing liquid fuel demand with minimal battery size and enabling a gradual transition to a transportation infrastructure largely powered by electricity. As electricity production becomes cleaner this can have a significant impact on GHG emissions. Renewable resources may be ideally suited for providing transportation energy, where their intermittency does not cause added expenses as it does in the electric grid. With electricity powering transportation, there are opportunities for the two sectors to cooperate: e.g. storage and retrieval of electricity in vehicle batteries, which can assist matching grid supply and demand especially with intermittent electricity sources.

The continued need for hydrocarbons calls for developing means to produce them sustainably. Biomass is not likely a sustainable energy source at the scale needed, with the possible exception of algae. Sustainable use of hydrocarbons on board of a vehicle depends on technologies that capture carbon dioxide from the atmosphere and either sequester it, or recycle it into a fuel using renewable or nuclear energy. Recycling CO_2 into hydrocarbons using renewable or nuclear energy, in a non-biological process, appears to be the long term sustainable solution. This method of producing fuels is further examined in **Chapter 3**.

Most of the analysis presented here focused on individual stages in the life-cycle of energy carriers. Some important metrics that limit sustainability or practicality are associated with a particular stage and from these, calculations and logical arguments could be drawn about the sustainability and practicality for large-scale use of the energy carrier. Other metrics that are important encompass the entire life-cycle, such as environmental and human health impacts, net energy balance, life cycle CO_2 emissions, water consumption, and possible material supply limitations that arise in producing technologies at a large scale (for example, the metals and other materials used in photovoltaic cells, batteries, fuel cells and electrolysis cells). Further research that considers the entire life-cycles of the energy carriers would be useful. However, such life-cycle estimates must be done carefully as the outcome is very sensitive to the assumptions and defined boundaries of the system. Furthermore, efficiency and energy balance are not always all-important as many life-cycle analyses seem to assume. For example, when considering the same energy carrier (say, hydrocarbons) and either sunlight or coal as the energy sources, comparing the efficiencies of converting solar energy to that carrier and coal to that

carrier are meaningless. That a solar-to-hydrocarbon conversion may be only 10% efficient and a coal-to-hydrocarbon conversion may be 60% efficient does not mean that the latter is a six times better use of energy – it is a different type of energy with different supply. Another common metric used in life cycle analyses is the net greenhouse gas emissions that arise from all stages of the life-cycle of a product or energy conversion system – e.g. the construction, operation and maintenance. Such estimates are of course tied to a specific region and time. Taking photovoltaics (PV) as an example, every time a PV power plant is installed, the analysis becomes outdated – if PV were to scale up and comprise a significant fraction of electricity generation, the life-cycle greenhouse gas emissions of producing new PV panels would be much lower because more of the electricity used for producing the PV would come from PV itself.

The methods used here emphasize looking at many aspects of the energy systems to assess sustainability and practicality. Such thorough examination using a multitude of metrics seems to be necessary and should lead to more useful assessments than studies that focus on providing a single value "score" for a given energy technology or conversion pathway.

2.7. References

1. Lackner KS, *A Guide to CO_2 Sequestration.* Science, (2003). **300**(5626): p. 1677-1678.
2. EIA. *Basic petroleum Statistics* October 25, 2007]; Available from: http://www.eia.doe.gov/neic/quickfacts/quickoil.html.
3. IEA. *World Oil Statistics for 2006*. March 1, 2009]; Available from: http://www.iea.org/Textbase/stats/oildata.asp?COUNTRY_CODE=29.
4. Hill J, Nelson E, Tilman D, Polasky S, and Tiffany D, *Environmental, economic, and energetic costs and benefits of biodiesel and ethanol biofuels.* Proceedings of the National Academy of Sciences of the United States of America, (2006). **103**(30): p. 11206-11210.
5. Rydh CJ and Sanden BA, *Energy analysis of batteries in photovoltaic systems. part II: Energy return factors and overall battery efficiencies.* Energy Conversion and Management, (2005). **46**(11-12): p. 1980-2000.
6. Farrell AE, Plevin RJ, Turner BT, Jones AD, O'Hare M, and Kammen DM, *Ethanol can contribute to energy and environmental goals.* Science, (2006). **311**(5760): p. 506-508.
7. *Climate Change 2001: IPCC Third Assessment Report.* (2001), Intergovernmental Panel on Climate Change.
8. Yegulalp TM, Lackner KS, and Ziock H-J, *A review of emerging technologies for sustainable use of coal for power generation.* The International Journal of Surface Mining, Reclamation, and Environment, (2001). **15**: p. 52-68.
9. Lackner KS, *Can fossil carbon fuel the 21st century?* International Geology Review, (2002). **44**(12): p. 1122-1133.
10. Keith DW, DeCarolis JF, Denkenberger DC, Lenschow DH, Malyshev SL, Pacala S, et al., *The influence of large-scale wind-power on global climate.* Proceedings of the National Academy of Sciences, (2004). **101**: p. 16115-16120.
11. King CW and Webber ME, *Water Intensity of Transportation.* Environmental Science & Technology, (2008). **42**(21): p. 7866-7872.

12. Brandt A and Farrell A, *Scraping the bottom of the barrel: greenhouse gas emission consequences of a transition to low-quality and synthetic petroleum resources.* Climatic Change, (2007). **84**: p. 241-263.
13. Keith DW, Ha-Duong M, and Stolaroff J, *Climate Strategy with CO_2 Capture from the Air.* Climatic Change, (2005). **74**: p. 17-45.
14. Lackner KS, Ziock H-J, and Grimes P, *Carbon Dioxide Extraction from Air: Is it an Option?*, in *Proceedings of the 24th International Technical Conference on Coal Utilization & Fuel Systems*, B. Sakkestad, Editor. (1999): Clearwater, Florida. p. 885-896.
15. Zeman F, *Energy and Material Balance of CO_2 Capture from Ambient Air.* Environmental Science and Technology, (2007). **41**(21): p. 7558-7563.
16. Zeman F, *Experimental results for capturing CO_2 from the atmosphere.* Aiche Journal, (2008). **54**(5): p. 1396-1399.
17. Lackner KS, *Capture of carbon dioxide from ambient air.* The European Physical Journal - Special Topics, (2009). **176**(1): p. 93-106.
18. IPCC, *IPCC Special Report on Carbon Dioxide Capture and Storage*, B. Metz, et al., Editors. (2005), Intergovernmental Panel on Climate Change: Geneva, Switzerland.
19. *Biofuels - At What Cost? Government support for ethanol and biodiesel in OECD countries.* (2007), Global Subsidies Initiative, of the International Institute for Sustainable Development: Geneva, Switzerland.
20. Hamelinck CN and Faaij APC, *Outlook for advanced biofuels.* Energy Policy, (2006). **34**(17): p. 3268-3283.
21. *Biofuels in the U.S. Transportation Sector*, in *Annual Energy Outlook 2007.* (2007), U.S. Energy Information Administration: Washington, DC.
22. Kheshgi HS, Prince RC, and Marland G, *The potential of biomass fuels in the context of global climate change: Focus on transportation fuels.* Annual Review of Energy and the Environment, (2000). **25**: p. 199-244.
23. Zhu XG, Long SP, and Ort DR, *What is the maximum efficiency with which photosynthesis can convert solar energy into biomass?* Current Opinion in Biotechnology, (2008). **19**(2): p. 153-159.
24. USDA. *Feed Grains Database.* 5/1/2008]; Available from: http://www.ers.usda.gov/Data/feedgrains/.
25. *Energy policy Act of 2005* (Aug. 8, 2005), U.S. Senate and U.S. House of Representatives.
26. *See supporting information online.*
27. Greene N, *Growing Energy: How Biofuels Can Help End America's Oil Dependence.* (2004), National Resources Defense Council.
28. Chisti Y, *Biodiesel from microalgae.* Biotechnology Advances, (2007). **25**(3): p. 294-306.
29. Scharlemann JPW and Laurance WF, *Environmental science - How green are biofuels?* Science, (2008). **319**(5859): p. 43-44.
30. Donner SD and Kucharik CJ, *Corn-based ethanol production compromises goal of reducing nitrogen export by the Mississippi River.* Proceedings of the National Academy of Sciences, (2008). **105**(11): p. 4513-4518.
31. Schnoor JL, III OCD, Entekhabi D, Hiler EA, Hullar TL, and Tilman GD, *Water Implications of Biofuels production in the United States*, Washington, D.C.: The National Academies Press. 86.
32. Pimentel D, *Ethanol Fuels: Energy Balance, Economics, and Environmental Impacts are Negative.* Natural Resources Research, (2003). **12**(2): p. 127-134.
33. Chiu Y-W, Walseth B, and Suh S, *Water Embodied in Bioethanol in the United States.* Environmental Science & Technology. **0**(0).
34. Tilman D, Hill J, and Lehman C, *Carbon-Negative Biofuels from Low Input High Diversity Grassland Biomass.* Science, (2006). **314**: p. 1598-1600.

35. Landis DA, Gardiner MM, van der Werf W, and Swinton SM, *Increasing corn for biofuel production reduces biocontrol services in agricultural landscapes.* Proceedings of the National Academy of Sciences of the United States of America, (2008). **105**(51): p. 20552-20557.
36. Sagar AD and Kartha S, *Bioenergy and sustainable development?* Annual Review of Environment and Resources, (2007). **32**: p. 131-167.
37. Laurance WF, *Switch to corn promotes Amazon deforestation.* Science, (2007). **318**(5857): p. 1721-1721.
38. Searchinger T, Heimlich R, Houghton RA, Dong FX, Elobeid A, Fabiosa J, et al., *Use of US croplands for biofuels increases greenhouse gases through emissions from land-use change.* Science, (2008). **319**(5867): p. 1238-1240.
39. *World Development Indicators 2008*. (2008), (Data from the Food and Agriculture Organization of the United Nations): World Bank Publications. 418.
40. Fargione J, Hill J, Tilman D, Polasky S, and Hawthorne P, *Land clearing and the biofuel carbon debt.* Science, (2008). **319**(5867): p. 1235-1238.
41. Delucchi MA, *Conceptual and methodological issues in lifecycle analyses of transportation fuels*. (2004), University of California, Davis. Technical Report UCD-ITS-RR-04-45.
42. Kim S and Dale BE, *Life cycle assessment of various cropping systems utilized for producing biofuels: Bioethanol and biodiesel.* Biomass & Bioenergy, (2005). **29**(6): p. 426-439.
43. Righelato R and Spracklen DV, *Environment - Carbon mitigation by biofuels or by saving and restoring forests?* Science, (2007). **317**(5840): p. 902-902.
44. Kim H, Kim S, and Dale BE, *Biofuels, Land Use Change, and Greenhouse Gas Emissions: Some Unexplored Variables.* Environmental Science & Technology, (2009). **43**(3): p. 961-967.
45. Hedegaard K, ThyÃ¸ KA, and Wenzel H, *Life Cycle Assessment of an Advanced Bioethanol Technology in the perspective of Constrained Biomass Availability.* Environmental Science & Technology, (2008). **42**(21): p. 7992-7999.
46. Clarens AF, Resurreccion EP, White MA, and Colosi LM, *Environmental Life Cycle Comparison of Algae to Other Bioenergy Feedstocks.* Environmental Science & Technology. **44**(5): p. 1813-1819.
47. Fthenakis V and Kim HC, *Life-cycle uses of water in U.S. electricity generation.* Renewable and Sustainable Energy Reviews. In Press**.**
48. *Basic Research Needs for Solar Energy Utilization*. (2005), U.S. Department of Energy, Basic Energy Sciences: Washington, D.C.
49. Curtright AE, Morgan MG, and Keith DW, *Expert Assessments of Future photovoltaic Technologies.* Environmental Science & Technology, (2008). **42**(24): p. 9031-9038.
50. Sailor WC, Bodansky D, Braun C, Fetter S, and van der Zwaan B, *Nuclear power - A nuclear solution to climate change?* Science, (2000). **288**(5469): p. 1177-1178.
51. *IEA Energy Technology Essentials: Hydrogen production & Distribution*. (April 2007). ETE 05.
52. Hauch A, Ebbesen SD, Jensen SH, and Mogensen M, *Highly efficient high temperature electrolysis.* Journal of Materials Chemistry, (2008).
53. Covic GA, Boys JT, Kissin MLG, and Lu HG, *A Three-Phase Inductive power Transfer System for Roadway-Powered Vehicles.* Industrial Electronics, IEEE Transactions on, (2007). **54**(6): p. 3370-3378, and references therein.
54. Burke AF, *Batteries and ultracapacitors for electric, hybrid, and fuel cell vehicles.* Proceedings of the Ieee, (2007). **95**(4): p. 806-820.
55. Tarascon JM and Armand M, *Issues and challenges facing rechargeable lithium batteries.* Nature, (2001). **414**(6861): p. 359-67.
56. Van den Bossche P, Vergels F, Van Mierlo J, Matheys J, and Autenboer W, *SUBAT: An assessment of sustainable battery technology.* Journal of Power Sources, (2006). **162**(2): p. 913-919.

57. Matheys J, Autoenboer WV, Timmermans J-M, Mierlo JV, Bossche PVd, and Maggetto G, *Influence of Functional Unit on the Life Cycle Assessment of Traction Batteries.* Int J LCA, (2007). **12**(3): p. 191-196.
58. Matheys J, Timmermans J-M, Autenboer WV, Mierlo JV, Maggetto G, Meyer S, et al. *Comparison of the Environmental impact of 5 Electric Vehicle Battery technologies using LCA.* in *13th CIRP International Conference on Life Cycle Engineering.* (2006). Leuven.
59. Rydh CJ and Sanden BA, *Energy analysis of batteries in photovoltaic systems. part I: performance and energy requirements.* Energy Conversion and Management, (2005). **46**(11-12): p. 1957-1979.
60. Dhameja S, *Electric vehicle battery systems.* (2001): Newnes Press.
61. Crompton TR, *Battery Reference Book.* Third ed. (2000): Newnes Press.
62. Shi YX, Cai NS, Li C, Bao C, Croiset E, Qian JQ, et al., *Simulation of electrochemical impedance spectra of solid oxide fuel cells using transient physical models.* Journal of the Electrochemical Society, (2008). **155**(3): p. B270-B280-B270-B280.
63. Colella WG, Jacobson MZ, and Golden DM, *Switching to a US hydrogen fuel cell vehicle fleet: The resultant change in emissions, energy use, and greenhouse gases.* Journal of Power Sources, (2005). **150**: p. 150-181.
64. Eberhard M and Tarpenning M. *The 21st Century Electric Car (white paper).* September 24, 2007 Jan 1, 2008]; Available from: http://www.teslamotors.com/learn_more/white_papers.php.
65. Weir RD and Nelson CW, *Electrical-energy-storage-unit (EESU) Utilizing Ceramic and Integrated-Circuit Technologies for Replacement of Electrochemical Batteries.* (2001). USPTO
66. Lam LT and Louey R, *Development of ultra-battery for hybrid-electric vehicle applications.* Journal of Power Sources, (2006). **158**(2): p. 1140-1148.
67. Faggioli E, Rena P, Danel V, Andrieu X, Mallant R, and Kahlen H, *Supercapacitors for the energy management of electric vehicles.* Journal of Power Sources, (1999). **84**(2): p. 261-269.
68. Stephan CH and Sullivan J, *Environmental and energy implications of plug-in hybrid-electric vehicles.* Environmental Science & Technology, (2008). **42**(4): p. 1185-1190.
69. Kintner-Meyer M, Schneider KP, and Pratt RG, *Impacts Assessment of plug-In Hybrid Vehicles on Electric Utilities and Regional U.S. power Grids. part 1: Technical Analysis.* (2006), Pacific Northwest National Laboratory: Richland, WA. PNNL-SA-53700.
70. Rantik M, *Life Cycle Assessment of Five Batteries for Electric Vehicles under Different Charging Regimes.* (1999), Chalmers University of Technology. KFB-Meddelande 1999:28.
71. Kempton W and Tomic J, *Vehicle-to-grid power implementation: From stabilizing the grid to supporting large-scale renewable energy.* Journal of Power Sources, (2005). **144**(1): p. 280-294.
72. Tomic J and Kempton W, *Using fleets of electric-drive vehicles for grid support.* Journal of Power Sources, (2007). **168**(2): p. 459-468.
73. Gifford P. *Used NiMH Batteries for Rural Electrication in Mexico* in *Advanced Battery Readiness Ad Hoc Working Group Meeting.* (2000). Washington, DC: Sandia National Laboratories.
74. Cready E, Lippert J, Pihl J, Weinstock I, Symons P, and Jungst RG, *Technical and Economic Feasibility of Applying Used EV Batteries in Stationary Applications.* (2003), Sandia National Laboratories: Albuquerque, NM and Livermore, CA. SAND2002-4084.
75. *PG&E's Battery power plans Could Jump Start Electric Car Market.* (June 12, 2007) Jan 1, 2008]; Available from: http://blogs.business2.com/greenwombat/2007/06/photo_green_wom.html.
76. Eberhardt JJ. *Fuels of the Future for Cars and Trucks.* in *2002 Diesel Engine Emissions Reduction (DEER) Workshop.* (2002). San Diego, California.
77. *1999 General Motors EV1 w/NiMH* (1999).
78. Rosenkranz C. *Deep Cycle Batteries for plug-in Hybrid Application.* in *EVS-20 plug-in Hybrid Workshop.* (2003). Monaco.

79. Gaines L and Cuenca R, *Costs of Li-ion Batteries for Vehicles*. (2000), Argonne National Laboratory, Center for Transportation Research: Argonne, IL. ANL/ESD-42.
80. Voelcker J, *Lithium Batteries for Hybrid Cars*, in *IEEE Spectrum Online*. (2007).
81. *The Emergence of Hybrid Vehicles*. (2006), AllianceBernstein Research on Strategic Change. INS–0955–0606.
82. Bossel U, *Does a hydrogen economy make sense?* Proceedings of the IEEE, (2006). **94**(10): p. 1826-37.
83. Hammerschlag R and Mazza P, *Questioning hydrogen*. Energy Policy, (2005). **33**(16): p. 2039-2043.
84. Kreith F and West R, *Fallacies of a hydrogen economy: A critical analysis of hydrogen production and utilization*. Journal of Energy Resources Technology-Transactions of the Asme, (2004). **126**(4): p. 249-257.
85. Demirdoven N and Deutch J, *Hybrid cars now, fuel cell cars later*. Science, (2004). **305**(5686): p. 974-976.
86. Olah GA, *After oil and gas: methanol economy*. Catalysis Letters, (2004). **93**(1-2): p. 1-2.
87. Åhman M, Modig G, and Nilsson LJ. *Transport fuels for the future - the long-term options and a possible development path*. in *Risø International Energy Conference, 23 - 25 May 2005*. (2005). Roskilde, Denmark: Risoe National Laboratory.
88. Ogden J, *Prospects for Building a Hydrogen Energy Infrastructure*. Annu. Rev. Energy Environ., (1999). **24**: p. 227-79.
89. Weiss MA, Heywood JB, Drake EM, Schafer A, and AuYeung FF, *On the Road in 2020: A life-cycle analysis of new automobile technologies*. (2000), Massachusetts Institute of Technology, Energy Laboratory. MIT EL 00-003.
90. Keith D and Farrell A, *Rethinking hydrogen cars*. Science, (2003). **301**(5631): p. 315-316.
91. Zamfirescu C and Dincer I, *Using ammonia as a sustainable fuel*. Journal of Power Sources, (2008). **185**(1): p. 459-465.
92. McKee DW, Scarpellino JAJ, Danzig IF, and Pak MS, *Improved Electrocatalysts for Ammonia Fuel Cell Anodes*. Journal of The Electrochemical Society, (1969). **116**(5): p. 562-568.
93. Pelletier L, McFarlan A, and Maffei N, *Ammonia fuel cell using doped barium cerate proton conducting solid electrolytes*. Journal of Power Sources, (2005). **145**(2): p. 262-265.
94. Ganley JC, *An intermediate-temperature direct ammonia fuel cell with a molten alkaline hydroxide electrolyte*. Journal of Power Sources, (2008). **178**(1): p. 44-47.
95. Dry ME, *The Fischer-Tropsch process: 1950-2000*. Catalysis Today, (2002). **71**(3-4): p. 227-241.
96. Kintisch E, *The greening of Synfuels*. Science, (2008). **320**(5874): p. 306-308.
97. Rehnlund B, Blinge M, Larsen U, and Schramm J, *Synthetic gasoline and diesel oil produced by Fischer-Tropsch Technology - A possibility for the future?*, in *IEA Advanced Motor Fuels Agreement, Annex XXXI Report*. (2006).
98. *A Comprehensive Analysis of Biodiesel Impacts on Exhaust Emissions*. (2002), U.S. Environmental Protection Agency. EPA420-P-02-001.
99. Brinkman N, Wang M, Weber T, and Darlington T, *Well-to-Wheels Analysis of Advanced Fuel/Vehicle Systems — A North American Study of Energy Use, Greenhouse Gas Emissions, and Criteria pollutant Emissions* (2005), General Motors Corporation and Argonne National Laboratory.
100. Groode TA, *Review of Corn Based Ethanol Energy Use and Greenhouse Gas Emissions*. (2006), Massachusetts Institute for Technology, Laboratory for Energy and the Environment. LFEE 2007-01 RP.

101. de Oliveira MED, Vaughan BE, and Rykiel Jr. EJ, *Ethanol as Fuel: Energy, Carbon Dioxide Balances, and Ecological Footprint.* BioScience, (2005). **55**(7): p. 593-602.
102. Schmer MR, Vogel KP, Mitchell RB, and Perrin RK, *Net energy of cellulosic ethanol from switchgrass.* Proceedings of the National Academy of Sciences of the United States of America, (2008). **105**(2): p. 464-469.
103. Wu M, *Analysis of the Efficiency of the U.S. Ethanol Industry 2007.* (2008), Center for Transportation Research, Argonne National Laboratory.
104. *Environmental Assessment of plug-In Hybrid Electric Vehicles, Volume 1: Nationwide Greenhouse Gas Emissions.* (2007), Electric Power Research Institute and Natural Resources Defense Council: Palo Alto, California. 1015325.
105. Parks K, Denholm P, and Markel T, *Costs and Emissions Associated with plug-In Hybrid Electric Vehicle Charging in the Xcel Energy Colorado Service Territory* (2007), National Renewable Energy Laboratory: Golden, Colorado. Technical Report NREL/TP-640-41410.
106. Vyas A, Santini D, Duoba M, and Alexander M, *Plug-in Hybrid Electric Vehicles: How Does One Determine Their potential for Reducing U.S. Oil Dependence.* (2007), Argonna National Laboratory.
107. Markel T and Simpson A, *Plug-in Hybrid Electric Vehicle Energy Storage System Design*, in *Advanced Automotive Battery Conference.* (2006), National Renewable Energy Laboratory: Baltimore, Maryland.
108. Pacala S and Socolow R, *Stabilization wedges: Solving the climate problem for the next 50 years with current technologies.* Science, (2004). **305**(5686): p. 968-972.
109. Lemoine DM, Kammen DM, and Farrell AE, *An innovation and policy agenda for commercially competitive plug-in hybrid electric vehicles.* Environmental Research Letters, (2008). **3**(1).

Chapter 3

3. Sustainable Hydrocarbon Fuels by Recycling CO_2 with Renewable/Nuclear Energy

Chapter 2 identified hydrocarbon fuels produced by CO_2 recycling as a promising sustainable and practical energy carrier – sustainable energy sources like solar and wind power can be used to provide the most energy-dense, convenient fuels which can be readily used in the existing infrastructure. This chapter[i] examines the fuel cycle for recycling CO_2 into hydrocarbon fuels. Production of such fuels would be similar to hydrogen production while distribution and consumption would be similar to that of other hydrocarbons. Initially, CO_2 captured from large industrial sources could be utilized. In the long term, the capture of CO_2 from the atmosphere would enable a closed-loop hydrocarbon fuel cycle.

First, a critical review of the many possible technological pathways that can be taken to recycle CO_2 into hydrocarbon fuels using renewable or nuclear energy (as heat, electricity, and/or sunlight) is presented. The state-of-the-art enabling technologies at each stage of the pathway (CO_2 capture, H_2O and CO_2 dissociation, and fuel synthesis) are examined. A pathway based on electrolyzing H_2O and CO_2 in high temperature solid oxide cells to yield a mixture of H_2 and CO (syngas) is identified as one of the most promising, feasible routes due to its efficient use of electricity and heat.

An analysis of the economics and energy balance for this process is presented. The potential of the process is assessed, in terms of what technological progress is needed to achieve large-scale, economically competitive production of sustainable fuels by this method. Opportunities are discussed for fuel production using inexpensive, intermittent renewable energy (e.g. surplus wind power, or solar arrays built in remote, sunny locations such as deserts) and constant-supply power sources such as hydroelectric, geothermal, and nuclear.

---

[i] This chapter has been published in modified form as: Graves C, Ebbesen S D, Mogensen M, and Lackner K S, *Sustainable Hydrocarbon Fuels by Recycling CO_2 and H_2O with Renewable or Nuclear Energy*. Renewable & Sustainable Energy Reviews, 2010. doi:10.1016/j.rser.2010.07.014.

3.1. Introduction

Hydrocarbon fuels provide the majority of all transportation energy, and petroleum is the dominant feedstock from which transportation fuels are produced. Hydrocarbons [ii] produced from other feedstocks (fossil and biomass), as well as carbon-free energy carriers (such as hydrogen, batteries and ultracapacitors), are potentially more sustainable alternatives. The benefits of hydrocarbons over carbon-free energy carriers include higher energy density and use of existing infrastructure (fuel distribution and vehicles). While increased use of electric propulsion will likely reduce liquid fuel demand, hydrocarbons will continue to be needed—especially as fuels in aircraft, sea vessels, and haulage vehicles, and they also provide the chemical building blocks for much of the chemical industry. Their widespread use calls for means to produce them sustainably.

As a direct replacement for petroleum-based hydrocarbons, biofuels and fossil carbon derived synthetic fuels (e.g. coal derived liquid fuels) are receiving the most attention. Their sustainability depends largely on the source of the feedstock and, in the case of fossil carbon based fuels, on the availability of carbon capture and storage technologies and sites. Similar hydrocarbons can also be produced without using fossil fuels or biomass. Using renewable and/or nuclear energy (as heat, electricity, and/or light), carbon dioxide and water can be recycled into hydrocarbon fuels (**Figure 3-1**) in a non-biological process. Initially, CO_2 captured from large industrial sources (e.g. aluminum plants) could be utilized. In the long term, the capture of CO_2 from the atmosphere [2] would enable a closed-loop hydrocarbon fuel cycle (**Figure 3-1**).

When solar energy drives the dissociation of CO_2 and H_2O, the fuel cycle is comparable to that of biofuels: synthetic "trees" collect CO_2 from the air and use solar energy to fix it as carbon (**Figure 3-2**). However, this fuel cycle avoids the biomass intermediate product, which consumes a lot of resources to cultivate (water, fertilizer, etc) and needs to be processed further to produce a fuel. Far less land would be needed for photovoltaic or solar thermally driven fuel production than for land-based biofuel production; even with low-efficiency solar panels driving the process, the components would cover less than a tenth of the land area that is needed to grow typical biomass used for energy[iii]. The land also need not be fertile nor artificially fertilized, avoiding competition with food agriculture and other important

[ii] "Hydrocarbons" will be used throughout this article to refer to a range of carbonaceous fuels, including gasoline, diesel, alcohols, dimethyl ether, etc.

[iii] Typical biomass captures less than 1% of solar energy, and further energy losses in conversion of biomass to fuel result in a fuel ethanol efficiency from solar energy, using corn and sugarcane feedstocks, of around 0.16-0.24% [3]. Commercial solar panels convert around 10-30% of sunlight to electricity, and fuel production from electricity can be accomplished with around 70% efficiency, as will be seen later in this article.

land uses. In fact, as will be discussed later, one potentially optimal location for this process is the desert. A remote, sunny desert site could provide the inexpensive solar electricity and/or heat to run the process, and the system could be built right at that site. Algae-based biofuels share some of these same advantages over land-based biofuels. Still, like all biomass, aquatic biomass is optimized to support the life processes of the living organism, not to produce fuel. Further, living organisms are vulnerable to performance loss due to changes in environmental conditions or interaction with other living organisms. Even with genetic engineering it seems unlikely that an organism can be created that matches the efficiency, robustness, and economy that can be achieved by a more direct energy conversion.

In comparison with hydrogen as a fuel, CO_2-recycled fuels are a form of chemical storage of hydrogen alongside carbon. Production of such fuels would be similar to hydrogen production (and likely even involve the production of H_2 by H_2O dissociation) while distribution and consumption would be similar to that of other hydrocarbons (**Figure 3-2**). Fuel production can use a variety of sustainable resources, and the fuel is distributed and consumed using the existing hydrocarbon fuel based infrastructure and vehicles. The difficulties of a large-scale hydrogen-only fuel cycle—the significant efforts needed to store and distribute the highly volatile gas and to build an entirely new infrastructure—are avoided.

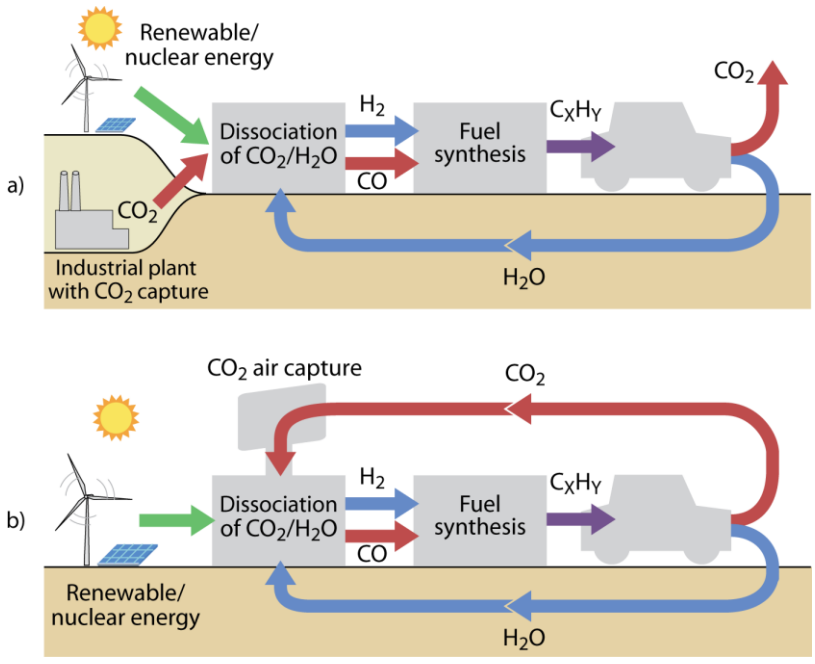

Figure 3-1. CO_2-recycled synthetic fuel cycles. a) once-through re-use of CO_2, resulting in net CO_2 emissions of approximately ½ versus the emissions that would occur without any re-use (both from the industrial plant and from transportation), b) continuous closed-loop carbon recycling via air capture of CO_2, resulting in near zero net emissions. These approximations neglect life-cycle emissions of energy generation, CO_2 capture, materials, construction, etc. C_XH_Y represents hydrocarbon fuel.

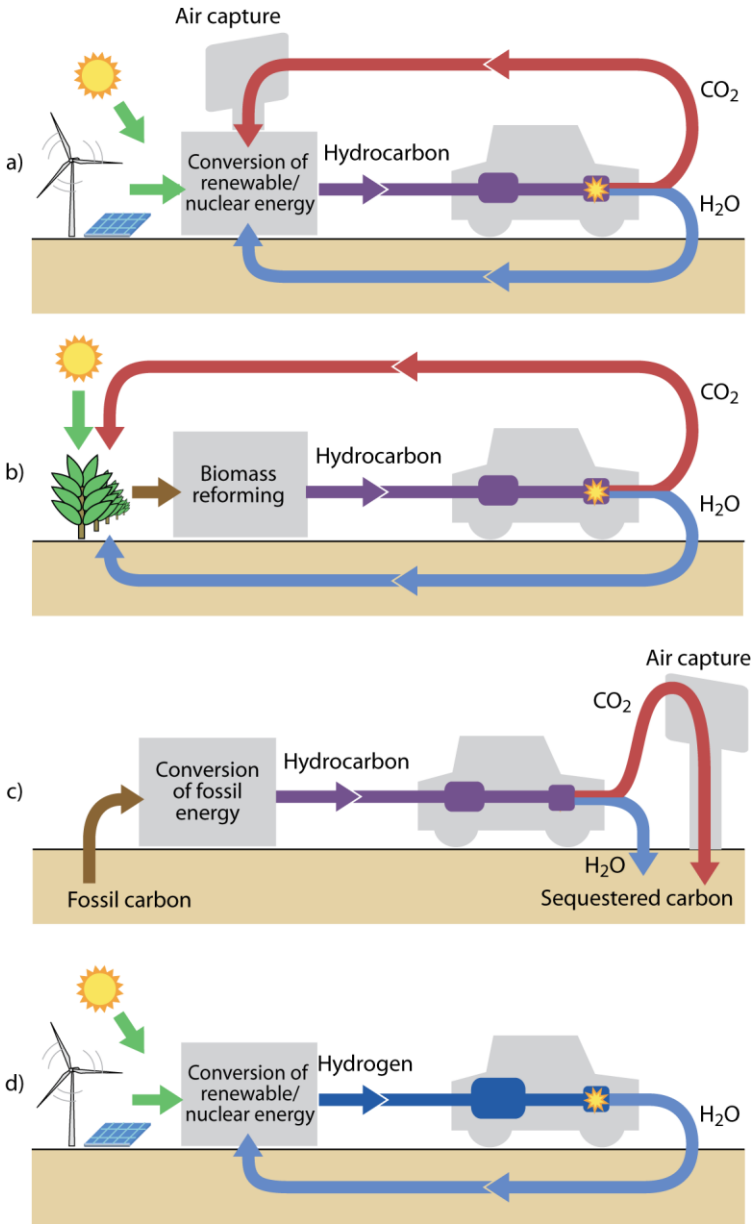

Figure 3-2. Comparison of carbon-neutral fuel cycles for hydrocarbons produced using (a) renewable/ nuclear energy (shown as solar and wind energy), (b) biomass, (c) fossil fuel. (d) Hydrogen produced by solar/wind energy is also shown for comparison with (a). Whereas the renewable energy based cycles (a, b, and d) are considered materially closed, the fossil fuel based cycle (b) is carbon-neutral but the carbon is stored in an oxidized form.

Recycling CO_2 into a hydrocarbon fuel would open a new sector, the transportation fuel sector, to renewable energy, which was previously not accessible to renewable energy sources apart from biomass. Because liquid transportation fuels are a high value form of energy, CO_2 recycling using renewable energy could facilitate growth of renewable energy sources by

providing a potentially economical way of delivering renewable energy to the consumer. Synthetic fuel production using intermittent renewable electricity advantageously provides a large time-flexible demand for renewable electricity; synthetic fuels can be made preferentially when excess electricity supply is available, reducing the demand for energy storage systems that are designed to accept and return electric power (e.g. pumped hydro storage, compressed air storage, batteries, etc.).

The fuel cycles of carbon-neutral hydrocarbons from various sources, alongside a hydrogen fuel cycle, are illustrated in **Figure 3-2**. A more thorough analysis of the sustainability of various energy carriers, including CO_2-recycled synthetic fuels, is a topic of future work.

This article examines the possible electrochemical, thermochemical, and photochemical pathways to produce CO_2-recycled synthetic fuels, and it reviews the current status of the enabling technologies at each stage of the pathway (CO_2 capture, H_2O/CO_2 dissociation, and fuel synthesis). This review mainly focuses on the dissociation stage, where the major energy conversion takes place. High temperature electrolysis of H_2O and/or CO_2 in a solid oxide cell to yield CO and H_2 (syngas) followed by catalytic fuel synthesis is identified as one of the most promising routes. The technical and economic details of this particular process are then examined and the potential of the process is assessed, in terms of what technological progress is needed to make implementation feasible and the circumstances (physical location of deployment and energy market conditions) that would enable affordable implementation.

3.2. CO_2-recycled Synthetic Fuel Pathways

The synthetic fuel production process has several stages: (1) collection of energy, (2) collection of the oxides, H_2O and CO_2, (3) dissociation of the oxides, and (4) fuel synthesis from the products of stage 3. Within each stage, there are a number of technology options. **Figure 3-3** presents a map of the possible pathways from the feedstocks to hydrocarbon fuels. Except for direct sunlight-driven processes, the energy collection stage can be considered external to the process; other pathways are not tied to a specific energy source but rather to intermediate heat or electricity. The energy can drive the dissociation of either CO_2 or H_2O, or both, resulting in energy-rich gas mixtures which are readily converted to convenient fuels. Shown in Figure 3-1 is the production of syngas (a mixture of H_2 and CO) for fuel synthesis. Syngas is typically produced from coal and natural gas and used as a building block in well-known hydrocarbon fuel synthesis processes (e.g. Fischer-Tropsch synthesis). Alternatively CO_2 and H_2O dissociation and fuel synthesis, and even CO_2 capture, might be combined into a single step. Integration of multiple stages can be beneficial e.g. in terms of improved process simplicity and heat management. Some processes aim to combine all of the pieces into a single step (e.g. photochemical or photoelectrochemical dissociation of CO_2 and H_2O that yields hydrocarbons directly from a single unit). However, integration can also result in much more

difficult materials requirements, overly tight design constraints, and lower flexibility in operation than using a larger number of steps with each step optimized for its particular function. This will be further discussed in section 3.2.2.

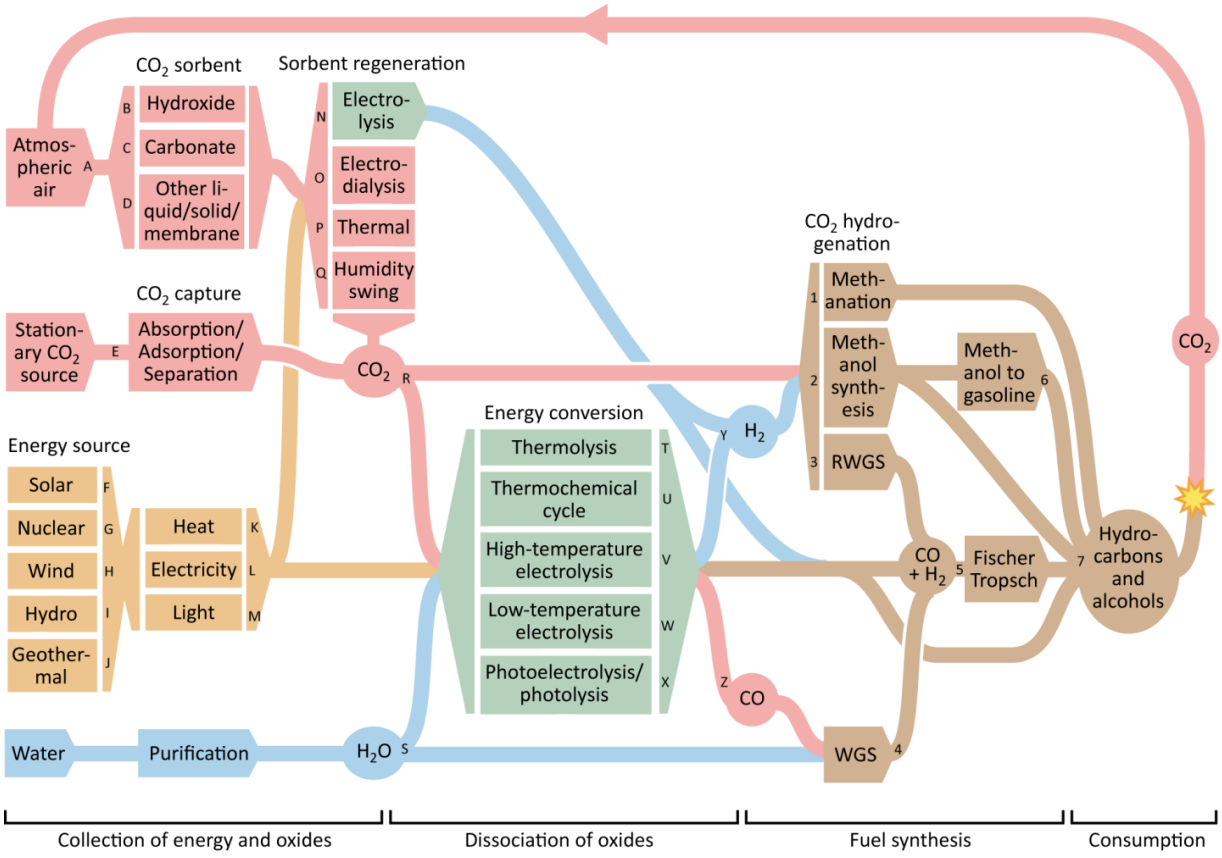

Figure 3-3. Map of the possible pathways from H_2O and CO_2 to hydrocarbon fuels. "Fischer Tropsch" represents any of a variety of catalytic fuel synthesis processes similar to the original Fischer-Tropsch processes.

Following is a review of work that considers the entire cycle.

The concept of CO_2-recycled synthetic hydrocarbon fuels is not new. Likely spurred by the oil crisis of the 1970s, Steinberg and Dang [4-8] first envisioned the closed-loop version of CO_2-recycled synthetic fuels with CO_2 captured from ambient air. In a series of journal articles and patents, they explored various options to capture CO_2 from the atmosphere using hydroxide or carbonate absorbents, produce H_2 by water electrolysis, and synthesize methanol by reaction of the CO_2 with H_2, with nuclear fission or fusion supplying the electricity and heat. They proposed using the nuclear power plant cooling tower as part of the air capture absorption system. They also considered stripping CO_2 from sea water, and using exhaust CO_2 from industrial plants. Lewis and Martin [9] patented a similar process but with a thermally driven rather than electrically driven CO_2 air capture absorbent regeneration cycle. A similar nuclear powered synthetic fuel process was outlined by Corbett and Salinas [10] followed by its

extension to a naval sea vessel with on-board nuclear generator [11]. All of the above processes were based on a low temperature electrolysis dissociation step. Recently, Martin and Kubic [12, 13] proposed a slight variation on these processes.

Phillips and Isenberg [14] proposed a different (but also nuclear-driven) process beginning with mineral carbonates (therefore an indirect air capture of CO_2), decomposing them to release CO_2, electrolyzing the CO_2 at high temperature in a solid oxide cell to yield CO, and reacting the CO with steam via a multi-step process to synthesize hydrocarbon fuels. Yamauchi et al [15] proposed a CO_2-based methanol synthesis process using H_2 from high temperature electrolysis of H_2O, without much consideration as to how the CO_2 would be obtained.

Research on the hydroxide-based air capture processes continued through the 1990s by Bandi et al [16] and Stucki et al [17], without the direct tie to nuclear energy or any specific energy source. Weimer et al (also with Bandi) introduced a solar electricity and heat based process with thermally driven air capture absorbent regeneration and high temperature electrolysis of H_2O [18] or co-electrolysis of H_2O and CO_2 [19] providing the dissociation step.

Hashimoto et al [20] described a process to produce H_2 by seawater electrolysis powered by solar panels installed in the desert and to synthesize CH_4 by combining the H_2 with exhaust CO_2 collected from industrial plants. Jensen et al [21-23] have demonstrated a direct solar-driven process that, via combined high-temperature thermolysis and photolysis of CO_2, yields CO for synthetic fuel production. Miller and co-workers [24] are developing a solar-driven process based on H_2O and/or CO_2 dissociation using ferrites in a thermochemical cycle. They propose to use the resulting H_2 and/or CO for methanol synthesis.

Mignard et al [25, 26] worked out energy balances and cost estimates of several processes for synthesis of methanol and gasoline from industrial waste CO_2 and marine (wind and wave) energy driving the low temperature H_2O electrolysis and fuel synthesis. Olah et al [27-29] have advocated a "methanol economy" and proposed methanol synthesis by reacting H_2 with air-captured CO_2 or by low-temperature electrolysis of air-captured CO_2 in water to yield syngas followed by methanol synthesis.

Recently there has been a surge of renewed interest in synthetic fuel cycles based on high temperature electrolysis of H_2O, CO_2, or both [30-38] (and see **Chapter 4**). All of this work has focused on the performance and durability of the electrolysis cells in the dissociation stage of the process. **Table 3-1** summarizes the above review with each full cycle concept mapped to the pathways of **Figure 3-3**, using the letter codes that label each step in **Figure 3-3**. It is evident that the majority of the early work was based on a nuclear energy source ("G"), low temperature electrolysis ("W"), and methanol synthesis ("2"). More recently the concept has been often based on solar ("F") and wind ("H") energy and high temperature electrolysis ("V").

Table 3-1. History of work done on the full synthetic fuel cycle concept, using the codes of **Figure 3-3** to map the pathways. Arrows indicate that the process was integrated into the prior stage. *Italics* indicate that a process was only briefly mentioned.

Years	Reference(s)	Energy collection	CO_2 collection	Dissociation	Fuel synthesis
1970s	[4]	GL	DN	N7	←
	[5]	G(K+L)	(C/D)(N/P)(R+Y)	SWY	27
	[7]	G(K+L)	ER	SWY	267
	[7]	GL	DN(R+Y)	←	267
	[9]	G…	DPR	…Y	(1/2)7
1980s	[10, 11]	G(K+L)	DOR	SWY	267
	[14]	G(K+L)	minerals-PR	RVZ	(Z+S)…7
1990s	[16]	…L	DOR	(R+S)W(Y+Z+1)	27
	[17]	…L	DN(R+Y)	SWY	27
	[15]	G(K+L)	*ER*	SVY	27
	[18, 19]	F(K+L)	D(O/P)R	SWY	27
	[19]	F(K+L)	DPR	(R+S)V5	57
	[20]	FL	*ER*	SWY	17
2000s	[22, 23]	F(K+L)	*ER*	RTZ	457
to	[27-29]	…L	DPR	(R+S)W5 / SWY	27 / 57
today	[25, 26]	(H+I)L	*ER*	SWY	(2/3)(5/6)7
	[34]	…L	BN(R+Y)	(R+S)V5	57
	[12]	G(K+L)	CN(R+Y)	S(W/V)Y	267
	[24]	FK		(R/S)U(Y/Z/5)	57[a]
	[35]	G(K+L)	*biomass*	(R+S)V5	57
	[36]	(F/H)L	*ER*	(R+S)V5	57
	[30-33, 37-39]	(F/H/I/J)L	BPR / A…R	(R+S)V5	57

[a]The cited reference does not include fuel synthesis but based on the name of their research program and interviews, the authors have the intention to produce liquid hydrocarbon fuels.

Zeman and Keith [40] recently reviewed various means of attaining carbon-neutral hydrocarbons, including producing hydrocarbons from a CO_2 feedstock. To produce fuels from CO_2, they advocate using fossil resources. In their proposed CO_2 recycling process, hydrogen is produced from fossil resources in a carbon-neutral manner by capturing and sequestering the CO_2 emissions during the conversion, CO_2 is captured from the atmosphere, and hydrocarbons are synthesized from the H_2 and air-captured CO_2. Although such a process is feasible, it usually does not make sense to use fossil energy in a CO_2 recycling process. The fossil resource already contains carbon in an energetic state. Using this fossil carbon to drive a CO_2 recycling scheme results in generation of more CO_2 which must then be sequestered. The same end result could be achieved by sequestering the captured CO_2 in the first place rather than recycling it. Indeed, their proposed CO_2 recycling pathway is actually an alternate version of the pathway shown in **Figure 3-2c**—producing a fossil-based hydrocarbon and then using off-site air-capture of CO_2 with sequestration to offset emissions from consumption of the fuel—which they also consider. It is more limited and most likely more expensive than the **Figure 3-2c** pathway in that the air

capture site, the fossil resource, and the CO_2 storage site must all be located at the same site or materials must be transported between sites, whereas the **Figure 3-2c** pathway enables independent placement of the air-capture device at any appropriate CO_2 storage site. Since the pathway does not actually need CO_2 as a feedstock, it does not fall under the "fuels produced by recycling CO_2" scope. Neither of these carbon-neutral fossil fuel based pathways are materially closed cycles, but they are useful to consider in defining the scope of CO_2-recycled fuels.

In the following sections the work on individual stages of the cycle is reviewed, including greater detail about the individual stages of the full cycle work reviewed above.

3.2.1. Collection of H_2O and CO_2

Large-scale implementation of any pathway will use large quantities of water. The only sustainable source will be non-potable water such as sea water. To supply the quantity of water needed for dissociation (to provide the hydrogen atoms that get incorporated into the fuel), the cost of desalination will add very little to the synthetic gasoline end product cost – desalinated water is typically produced for less than USD\$1/m^3 [41] which corresponds to only a small fraction of 1 U.S. cent per gal or L of synthetic gasoline. However, water consumption generally can far exceed the water amounts that are needed to provide the hydrogen atoms that get incorporated into the fuel. The required quality of this additional water will depend on the specific processes used. In any case, even if significant quantities of fresh water are needed, it is unlikely that the cost of desalination will make up a significant fraction of the total cost of fuel production. Another proposed source of H_2O is the atmosphere [28]. While perhaps an unnecessary and expensive effort, combined with air-capture of CO_2, both feedstocks would then be extracted from the air, enabling a highly location-independent process.

CO_2 is routinely captured from large industrial plants. The various methods have been reviewed elsewhere [42]. Apart from industrial plants, another non-atmospheric CO_2 source is geothermal vents. Geothermal power plants therefore release this stored CO_2. In Iceland there is interest in managing these CO_2 emissions— including interest in recycling them into fuel [43].

Removing CO_2 from air was first studied in the 1940s by Spector and Dodge using an alkaline absorbent as a means to obtain CO_2-free air [44]. The use of alkaline chemical absorbents has dominated the work done in scrubbing the air to obtain concentrated CO_2. Metal hydroxides such as KOH, $Ca(OH)_2$, and NaOH readily react with CO_2 to form carbonates. Typically hydroxide solutions have been used or proposed [4, 7, 9-11, 16, 18, 19, 33, 45-55], and the reaction proceeds as follows:

$$CO_2 + 2OH^- \rightarrow CO_3^{2-} + H_2O$$

To release the bound CO_2, the absorbent must then be regenerated with electrical or thermal energy. Alternatively, a carbonate solution has been used to absorb CO_2 [5, 6, 12, 14, 56], forming bicarbonate:

$$CO_2 + CO_3^{2-} + H_2O \rightarrow 2HCO_3^-$$

The CO_2 binds more weakly to a carbonate than to a hydroxide. While absorption into a carbonate requires a longer contact time between the air and the absorbent and/or more of the absorbent, it has the advantage that less energy is needed to release the CO_2 and regenerate the absorbent. In a study comparing the energy demand of several means of air capture, dilute carbonate solution as absorbent was found to require the least amount of energy [5]. However, the absorption rates may be too slow for an economical process.

Other CO_2 absorption media have been examined as well as materials that CO_2 adsorbs onto [5, 57]. A variety of geometries for the air contactor have been tested, including packed beds [52] and spray towers [53]. Any process that consumes natural mineral carbonates and leaves behind the oxide or hydroxide form of the mineral could also be considered a method of capturing carbon dioxide from the air, as the waste product is likely to recarbonate with CO_2 extracted from the air. A process starting from natural mineral carbonates e.g. calcite ($CaCO_3$) to make synthetic fuels with nuclear energy has been proposed [14]. However, the authors did not consider the possibility of closing the carbon cycle by letting the resulting CaO absorb CO_2 from the air.

Once CO_2 has been captured, the absorption or adsorption medium must be regenerated to release the CO_2 and prepare it for capture again. The regeneration of alkaline solutions can be electrically driven via electrodialysis [16, 18, 45, 46] or thermally driven by cycles involving calcination of $CaCO_3$ or other carbonates [9, 18, 19, 47, 49, 51, 52]. Another alternative, electrolysis of the spent absorbent, is an integration of absorbent regeneration and dissociation stages, from which H_2 and O_2 production accompanies release of CO_2 [4, 13, 17, 34]. Since most CO_2-recycled fuel production processes include H_2 production anyway, electrolytic regeneration offers a potentially low energy demand if efficient electrolytic cells are developed. However, the CO_2 and O_2 are disadvantageously released together from the anode compartment of the electrolysis cell, requiring subsequent gas-phase separation. Alternatively a three-compartment cell could facilitate separate release of the CO_2 and O_2 [7, 8, 34]. An integration of absorbent regeneration and fuel synthesis, by reacting H_2 directly with $CaCO_3$ to yield hydrocarbons, has also been proposed [9].

Recently, a new process involving using a solid adsorbent which is regenerated by a humidity swing has been developed and significantly reduces the energy demands and cost of the process [2]. Whereas thermal air capture cycles have been estimated to need 400-700 kJ heat per mol CO_2 and electrodialysis cycles around 400 kJ electricity per mol CO_2 [52], this process has been estimated to need only 50 kJ electricity per mol CO_2. The cost of air capture has been

estimated from as high as $100-200 per tonne of CO_2 (tCO_2) [40, 51] to a long term cost as low as $30/$tCO_2$ [2] for this new method.

3.2.2. Dissociation of H_2O and CO_2

Dissociation of H_2O, CO_2, or mixtures of both is the stage with the largest energy conversion, because this is where the energy is stored as fuel or fuel precursors. The minimum required energy is the enthalpy of the reactions:

$$H_2O \rightarrow H_2 + \tfrac{1}{2}\, O_2 \quad \Delta H_r^\theta = 286 \text{ kJ/mol}$$

$$CO_2 \rightarrow CO + \tfrac{1}{2}\, O_2 \quad \Delta H_r^\theta = 283 \text{ kJ/mol}$$

Electrical energy can be used to drive the dissociations via electrolysis. However, heat can generally be obtained at a lower cost than electricity. For example, converting solar energy to heat can theoretically be carried out more efficiently and more inexpensively than photovoltaic (PV) conversion to electricity, which suggests that splitting water in solar furnaces should be preferred over the electrolytic splitting of water. However, using heat for dissociation is a more difficult process, requiring expensive materials that are stable at very high temperature (for thermolysis) or requiring a complicated multiple-step process that needs careful materials handling and heat management at each step (for thermochemical cycles), as will be discussed further in the following sections.

H_2O dissociation for H_2 production has been much more widely researched than CO_2 dissociation. Rather than disassociating the CO_2 directly, hydrogen may be used to reduce CO_2 to CO via the reverse water-gas shift (RWGS) reaction,

$$H_2 + CO_2 \underset{\text{WGS}}{\overset{\text{RWGS}}{\rightleftarrows}} H_2O + CO$$

The same reactants may be used with different conditions and catalysts in hydrogenation reactions to directly produce fuels such as methanol – these have been the most studied reactions in CO_2-recycled synthetic fuel research and will be discussed further in section 3.2.3. Alternatively, CO_2 can be dissociated instead, and the resulting CO used to reduce H_2O to H_2 in the water-gas shift (WGS) reaction. **Figure 3-4** shows the thermodynamics of the dissociation and WGS reactions.

In some cases, splitting CO_2 may have advantages. For example, when the reactant (H_2O or CO_2) should be gaseous, water requires vaporization to steam whereas room temperature CO_2 is already a gas and can be used directly. On the other hand, if low temperature heat (>100 °C) is available to produce steam, the energy consumption of the actual dissociation can be reduced to 249 kJ/mol. Finally, separating the products from unconverted reactants may be easier with H_2/H_2O because the H_2O can simply be condensed to liquid, whereas CO/CO_2 would require gas phase separation.

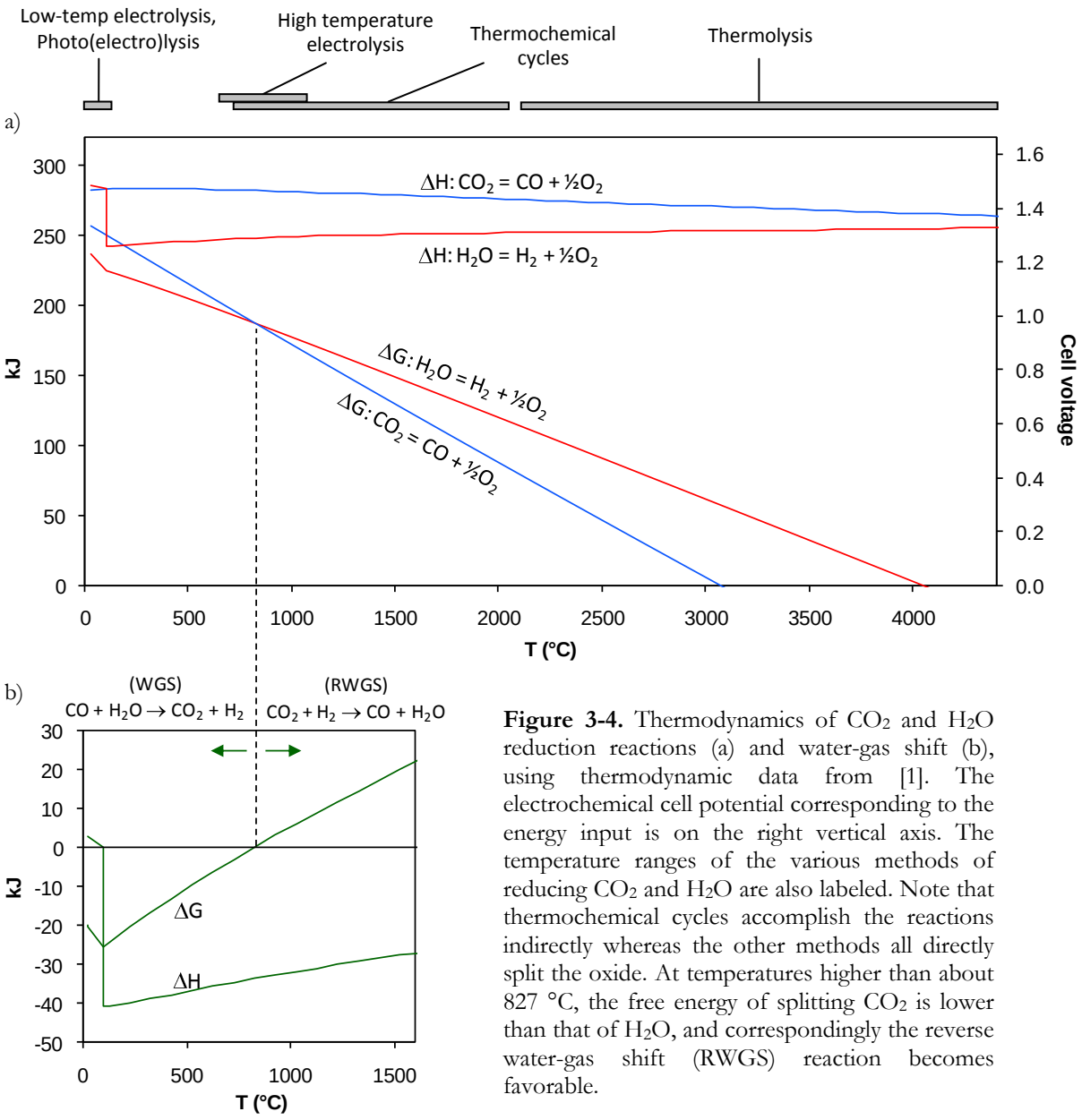

Figure 3-4. Thermodynamics of CO_2 and H_2O reduction reactions (a) and water-gas shift (b), using thermodynamic data from [1]. The electrochemical cell potential corresponding to the energy input is on the right vertical axis. The temperature ranges of the various methods of reducing CO_2 and H_2O are also labeled. Note that thermochemical cycles accomplish the reactions indirectly whereas the other methods all directly split the oxide. At temperatures higher than about 827 °C, the free energy of splitting CO_2 is lower than that of H_2O, and correspondingly the reverse water-gas shift (RWGS) reaction becomes favorable.

3.2.2.1. Thermolysis

It is possible to split H_2O and CO_2 by thermolysis (by the direct use of heat) at extremely high temperatures. The thermodynamics of CO_2 and H_2O dissociation shows that thermolysis occurs fully only at temperatures exceeding 3000 and 4000 °C respectively (**Figure 3-4**). Literature mentions a temperature range of 2000-2500 °C for H_2O thermolysis [58-60], although the equilibrium constant is only around 0.02 [1] and the product gases, H_2 and O_2, must be separated effectively at high temperature, or rapidly quenched to avoid recombination and then separated at lower temperature. Recombination reduces both the efficiency and

fraction of H_2O or CO_2 converted. 2500 °C is a reasonable upper limit because high-temperature ceramics such as zirconia begin to decompose at higher temperatures. Such high temperature heat could be supplied by combustion of fuels in an oxygen or chlorine atmosphere, but for thermolytic fuel production this would be self-defeating since more fuel would be consumed for heat generation than could be produced by thermolysis using the generated heat. Concentrated solar furnaces and a variety of electric furnaces are the two other methods that can provide high temperature heat for CO_2/H_2O thermolysis.

Jensen et al have developed a CO_2 thermolysis chamber driven by concentrated sunlight. CO_2 thermolysis could be carried out at lower temperature than H_2O thermolysis according to the thermodynamics (**Figure 3-4**). In addition, the absorption spectrum of CO_2 is shifted at higher temperatures such that in their chamber the CO_2 is in part photolyzed by the solar irradiation [22]. The observed peak conversion of solar energy to chemical energy was 5%, with expectation of 20% for a mature system [23]. While the demonstrated yield is low, the system also produced unutilized high temperature heat which could be used to drive a steam turbine, giving an additional 25% efficiency for electrical energy [23] (which could be used to produce more CO or H_2 via electrolysis[iv], see section 3.2.2.3). If these goals could be met, the total conversion efficiency would be nearly 50%, suggesting a very promising process. However, the majority of energy output from the system is not in the form of thermolysis products but rather electricity, which could have been produced more cheaply. The expensive materials required and complicated gas handling and separations, and heat management, may outweigh the savings from high efficiency. The concentrated sunlight reached ca. 2400 °C in the chamber, indicated by the partially melted zirconia rod at the focal point [23]. The stability of materials can also be strained by thermal shocks due to intermittency of the solar heat source (e.g. rapid transients in sunlight due to clouds). Despite some promising results, because the temperature, materials, and separation requirements for direct solar thermolysis are so severe, development of an economically viable process is unlikely in the near future [59].

An electromagnetic field can be used to excite gaseous H_2O or CO_2 (or at least the electrons in gaseous H_2O or CO_2) to extremely high temperatures (thousands to tens of thousands degrees), which results in plasma based decomposition. In so-called thermal plasmas, the electron temperatures are close to that of the discharge gas, whereas in non-thermal plasmas (also called non-equilibrium or cold plasmas), the electron temperature is far above that of the discharge gas [62]. An advantage of plasma based dissociation over direct solar thermolysis is that the high temperature zone is not in contact with any surfaces, so less expensive materials are needed. However, since plasma based dissociation is driven by electricity, it competes with

[iv] Indeed, a study by Baykara et al [61] concluded that H_2 production by solar H_2O thermolysis is less economical and less efficient than H_2 production by processes in which solar H_2O thermolysis is combined with H_2O electrolysis.

the other method of electrically-driven dissociation, electrolysis. Givotov et al [63] reported an electricity-to-fuel energy efficiency of 80% for non-thermal plasma decomposition of CO_2, however CO_2 conversion was only 20%, which would require more energy to be spent on subsequent gas phase separation of CO, O_2 and CO_2. Much higher (>90%) CO_2 conversion has been demonstrated using plasma micro-reactors, at the expense of reduced efficiency [64, 65]. For plasma decomposition of H_2O, Givotov et al [63] reported a lower efficiency (<40%) than for CO_2 plasmolysis, with lower conversion as well (<6%). At present, electrolysis is superior to plasma based dissociation because it provides a higher efficiency conversion with the products automatically separated (see section 3.2.2.3). However, it is not impossible that plasma based dissociation could become feasible if the efficiency and rates can be improved and if the cost of the reactors is relatively lower than that of electrolyzers.

3.2.2.2. Thermochemical cycles

Thermochemical cycles split H_2O or CO_2 through a series of thermally driven chemical reactions at lower temperatures than thermolysis. Product separation is simpler and often inherent in the cycle's reaction steps; one step will yield the H_2 (or CO) and a separate one will yield the O_2. Such cycles can be driven by nuclear reactor heat [66, 67] or concentrated sunlight [59, 60, 68]. Two-step cycles are most often based on reducing a metal oxide while evolving the O_2 in the first step and in the second step oxidizing the metal or lower-valence metal oxide by reaction with H_2O (or CO_2) thereby producing H_2 (or CO):

$$M_xO_y \rightarrow M_xO_{y-1} + \tfrac{1}{2}\,O_2\,(g)$$

$$M_xO_{y-1} + H_2O(g) \rightarrow M_xO_y + H_2\,(g)$$

The first step requires temperatures up to 2000 °C depending on the cycle. Fewer steps results in lower losses associated with products separation, heat transfer, and transfer of materials between each step. However, there are cycles with 3 or more steps with a maximum temperature below 1000 °C.

The high temperature (usually 2-step) cycles are considered with concentrated solar heat because concentrated sunlight can provide high temperature heat. The high temperature step places thermal demands on materials, and may require difficult product separation. Both of these disadvantages are shared with direct thermolysis, because both processes operate at extreme temperatures. The most well known of this type of cycle is the ZnO/Zn cycle:

$$ZnO(s) \rightarrow Zn(g) + \tfrac{1}{2}O_2(g) \qquad 1600\text{-}2000\ ^\circ C$$

$$Zn(s) + H_2O(l) \rightarrow ZnO(s) + H_2(g) \qquad 300\text{-}400\ ^\circ C$$

The ΔG_r of the first step is zero at 1982 °C [59]. In the high temperature step, a gaseous phase of the reduced Zn metal is produced. The gaseous Zn and O_2 require quenching to avoid

recombination just as in direct water thermolysis. The hydrolysis step also has difficulties, including the formation of a passivating layer, which reduces the reaction rate [69].

Similar two-step cycles aim to overcome these issues, favoring gas-solid separations and/or lower temperatures. The basic ferrite cycle (FeO/Fe_3O_4) enables gas-solid separations, but has proven to be impractical [24, 69, 70]. Recent investigations have focused on cycles using modified ferrites (substituted with Co, Ni, or Mn) or ceria based materials as the oxidation-reduction media for dissociation of H_2O to yield H_2 [24, 69, 71-76], CO_2 to yield CO [24, 75, 77], or both to yield syngas [75, 78-81]. These materials can be reduced at a lower temperature (<1500 °C) and both the oxidized and the reduced phases remain solid, as with the basic ferrite cycle. Ceria and doped ceria are especially interesting materials in that they can release oxygen without a change in crystal structure, cycling between the oxidized oxygen-stoichiometric phase and the reduced oxygen-deficient phase [79]. Ceria-based materials might therefore be expected to retain their microstructure through the redox cycles. Although the microstructure may be redox-stable, the high temperature of the reduction step can lead to coarsening of the microstructure. Grain growth (and a corresponding loss of activity) was observed in porous ceria reduced at 1500 oC - but only during the first 100 cycles, whereafter the performance was stable for hundreds of cycles [79]. Despite the initial performance loss, the high long-term durability suggests that ceria-based materials are a promising thermochemical cycle redox medium. For ferrites and modified ferrites, which are more prone to sintering than ceria-based materials, supporting the material on or combining the material with zirconia or yttria-stabilized zirconia inhibits sintering and improves durability [23,71,74]. Sintering also might not be an issue for some materials. It appears that other ceria-based materials enable a much lower temperature cycle; Cr-doped ceria was recently reported to be significantly reduced at only 465 °C and re-oxidized at 65 °C [82]. Ceria is also a known catalyst for many reactions involving gasses containing carbon and hydrogen [75, 82]. Addition of Ni to Sm-doped ceria was found to catalyze direct formation of CH_4 with high selectivity when using a low temperature oxidation step (400 °C) [79]. At other conditions, Ni was found to catalyze the deposition of carbon [79], which might be a desirable product in some cases. Ferrite cycles have also been studied for reduction of CO_2 to carbon [78, 83-85]. Finally, it is worth noting that while ceria based materials offer a number of potential advantages, cerium oxides have high molecular weights, which can be a disadvantage since flows of heavy solids should be minimized.

Similar materials have been tested in 3-step cycles with the involvement of hydroxide,

$$M_xO_y \rightarrow M_xO_{y-1} + \tfrac{1}{2}\,O_2\ (g)$$

$$M_xO_{y-1} + 2\,NaOH \rightarrow Na_2O{\cdot}M_xO_y + H_2\ (g)$$

$$Na_2O{\cdot}M_xO_y + H_2O \rightarrow M_xO_y + 2\,NaOH\ (g)$$

e.g. Fe_3O_4/Fe_2O_3 as the reduced and oxidized metal oxides respectively [86]. The introduction of hydroxides is motivated by their higher reactivity compared to that of water which should result in faster reaction rates. The corrosive nature of NaOH, the need to separate liquid $NaOH/Mn_2O_3$ mixtures and the reduced efficiency due to having three steps can each present difficulties.

In all of these high-temperature cycles, thermal management is extremely important to attain an efficient and economical process. With this in mind, research in solar thermochemical cycles also includes the design and development of efficient heat recuperating solar collectors. Diver et al [24, 73] have developed a counter-rotating ring system to optimize heat exchange between the oxidation and reduction steps, and have demonstrated its use for H_2O and CO_2 dissociation cycles using modified ferrites supported on YSZ or ceria-doped zirconia with a reduction temperature of 1400 °C.

Lower temperature cycles can be suitable for use with heat from nuclear reactors. The 3-step sulfur-iodine (SI) cycle, invented by General Atomics in the 1970s, operates below 1000 °C and has received much attention for integration with heat from high-temperature nuclear reactors [67]. The 4-step calcium–bromine–iron (UT-3) cycle has similarly low operating temperature. The corrosive nature of the chemicals presents material problems. Copper-chloride and magnesium-chloride cycles aim to lessen the corrosion problems of the higher temperature cycles by operating at around 500 °C [66, 67]. These cycles have also been proposed as hybrid electrochemical-thermochemical cycles with electrolysis driving one of the reactions in the cycle in order to lower the maximum cycle temperature by enabling a non-spontaneous step [66, 67]. While a greater number of steps lowers the maximum temperature needed, each additional step lowers the efficiency as more materials must be handled and more heat must be managed, and multi-step cycles often involve corrosive chemicals.

The above mentioned cycles are just a few possibilities. Hundreds of possible cycles have been identified for hydrogen production with a variety of maximum operating temperatures [87]. Despite detailed studies of a number of these cycles, they face a number of obstacles: (1) expensive materials (or equivalently, short material lifetimes) associated with high temperatures, rapid temperature transients and/or corrosive chemical intermediates, (2) difficult separations of the chemical intermediates, (3) energy losses across multiple steps from heat exchange, and (4) undesired side reactions. The solar-to-heat conversion efficiency is limited by re-radiation losses and the heat-to-chemicals conversion efficiency is limited by thermodynamics [87, 88], with further energy losses from heat recuperation and from separation and quench steps. Practical efficiencies for the net solar-to-chemicals conversion have been estimated in the range of 16-25%, depending on the process [59]. This is in the same range as what can be attained using solar thermal electric or photovoltaic devices coupled to electrolyzers. The economic benefits from the slightly higher efficiency of a thermochemical process may easily be outweighed by the economic cost of exotic materials. An economic

estimate based on hydrogen production using the latest promising thermochemical cycles versus using commercial alkaline electrolysis cells concluded that, when driven by the same concentrated solar thermal power source, the technologies have comparable costs [89]. The achievable electrolysis cost for a given electricity cost may be lower than estimated in that study because high temperature electrolysis has the potential to be significantly cheaper than today's commercial alkaline electrolysis [32].

3.2.2.3. Electrolysis

An electrolysis cell dissociates H_2O or CO_2 using electricity. Attractive in its simplicity, electrolysis performs the dissociation in a single step without any need for moving parts, and the products are released separately in the anode and cathode compartments of the cell. For solar conversion, a PV cell could be coupled to an electrolysis cell, which would comprise a full system without moving parts. Thermolytic and thermochemical reactors, on the other hand, need a mechanical sun-tracking system to concentrate the direct incident sunlight to collect high temperature heat. Electrolysis cells, like photovoltaic cells, are ideal for mass production and automated maintenance.

An especially interesting property of an electrolysis cell is the ability to choose the efficiency at which it operates. For example, the enthalpy of H_2O dissociation corresponds to a cell voltage of 1.48 V whereas the free energy corresponds to a H_2O electrolysis reversible potential of 1.23 V at 25 °C and 0.96 V at 850 °C (**Figure 3-4**). Assume for a moment that the internal resistance is a constant 1 Ω at any applied voltage for both a low-temperature cell (25 °C) and a high-temperature (850 °C) cell, and that the open-circuit voltages (OCV) are at the reversible potentials[v]. Then, isothermal operation of the cells, by applying the thermoneutral voltage of 1.48 V[vi], yields currents of 0.25 A [= (1.48 V – 1.23 V) / 1 Ω] and 0.52 A [= (1.48 V – 0.96 V) / 1 Ω] respectively. Both cells are being run at 100% efficiency in electricity-to-chemical energy conversion. From the higher rate of hydrogen production it is clear the high temperature cell has an advantage – even for the same internal resistance, more hydrogen is being produced because part of the dissociation energy is supplied as heat (the difference in ΔH and ΔG shown in **Figure 3-4**), which is being supplied as the inevitable Joule heat produced by the internal electrical resistance of the cell (alternatively, high- temperature heat from an

[v] This assumes that the activities or partial pressures of the reactants and products (H_2, O_2, and H_2O) are such that the Nernst potential is the same as the reversible potential—that the equilibrium constant in the Nernst equation is 1, e.g. for a high temperature cell, $pH_2/pH_2O = 1$ and $pO_2 = 1$ are assumed. In reality, for practical implementation it would be desirable to supply a much higher H_2O content, e.g. pH_2/pH_2O should approach zero, resulting in an OCV lower than 0.96 V, which would increase the current to greater than 0.52 A in the calculation that follows.

[vi] Note that the high temperature cell is electrolyzing steam. The thermoneutral voltage for the steam electrolysis reaction at 850 °C is 1.29 V, but the thermoneutral voltage for the cell is still 1.48 V if one includes the heat exchanger that is needed to generate steam for the cell if liquid water is the input.

external source could be used to supply part of the heat demand). The advantage is further boosted because in reality high-temperature cells nearly always have lower internal resistance than low-temperature cells—even with equivalent catalytic activity, higher reaction rates are achieved because the reactions are thermally activated to a greater degree. These differences between low and high temperature electrolysis cells can be seen in the polarization curves illustrated in Figure 3-5.

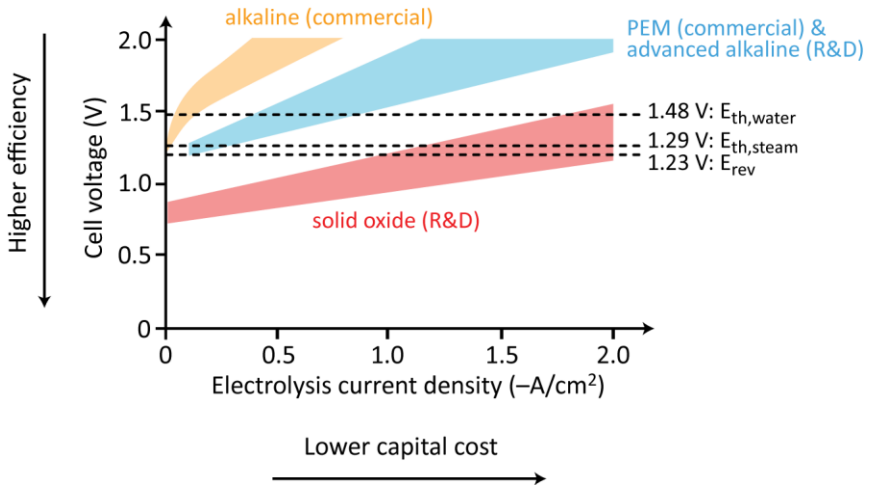

Figure 3-5. Typical ranges of polarization curves for different types of state-of-the-art water electrolysis cells. $E_{th,water}$ and $E_{th,steam}$ are the thermoneutral voltages for water and steam electrolysis respectively. E_{rev} is the reversible potential for water electrolysis at standard state. These curves are representative based on [32, 36-39, 90-102]

The cost of hydrogen produced by H_2O electrolysis, C_{H_2} (in \$/GJ), can be estimated as follows:

$$C_{H_2} = C_{op} + C_{cap}$$

$$C_{op} = \frac{C_{electricity}}{\eta_{electrolysis}} + C_{O\&M} \qquad C_{cap} = \frac{C_{investment}}{Q_{H_2\,prod}}$$

$$\eta_{electrolysis} = \frac{E_{th}}{E_{op}} \cdot \eta_{current} \qquad C_{investment} = \frac{C_{stack}}{t_{stack\,life}} + \frac{C_{bal\,of\,sys}}{t_{sys\,life}}$$

$$E_{th} = \frac{\Delta H_{f,H_2O(l)}}{n \cdot F} \qquad Q_{H_2\,prod} = I \cdot f_{util} \cdot \frac{\Delta H_{f,H_2O(l)}}{n \cdot F}$$

$$I = i \cdot A_{cell} = \frac{E_{op} - E_{Nernst}}{ASR} \cdot A_{cell}$$

where C_{op} is the operating cost and C_{cap} is the capital cost of the entire electrolysis system. These costs are in turn given by the above expressions in which $C_{electricity}$ is the cost of electricity, $\eta_{electrolysis}$ is the electricity-to-chemical energy conversion efficiency at which the electrolyzer is operating[vii], $C_{O\&M}$ is the operating and maintenance cost per unit of output, E_{th} is the thermoneutral voltage of water electrolysis, E_{op} is the cell operating voltage, $\eta_{current}$ is the current efficiency (the fraction of the current that drives the desired reactions) which is very close to 100% for all types of state-of-the-art electrolysis cells, $\Delta H_{f,H_2O(l)}$ is the enthalpy of formation of water (or equivalently, the enthalpy of the water electrolysis reaction, or equivalently the higher heating value (HHV) of hydrogen), n is 2 (mol of electrons per mol product H_2 in the electrochemical reaction), F is Faraday's number (96485 C/mol), $C_{investment}$ is the investment cost of the system including financing, $Q_{H_2\ prod}$ is the average rate at which H_2 is produced in kW, C_{stack} and $t_{stack\ life}$ are the investment cost and lifetime of a cell stack respectively, $C_{bal\ of\ sys}$ and $t_{sys\ life}$ are the investment cost and lifetime of the balance of system respectively, I is the cell operating current averaged across the cell's operating life, f_{util} is the fraction of time the cell is utilized over its life (sometimes called the capacity factor), i is the current density (e.g. A/cm^2), A_{cell} is the active area of the cell, E_{Nernst} is the equilibrium Nernst potential at the given conditions, and ASR is the internal area-specific resistance of the cell averaged across the operating life.

This is a simplified method which assumes time-averaged parameters; in reality, many of the parameters vary with time. Clearly, $C_{electricity}$ varies with time regardless of the source. $\eta_{electrolysis}$ might vary with time depending on how the electrolyzer is being operated; if potentiostatic operation (constant E_{op}) is used throughout the operating life then the efficiency will not vary with time. $C_{O\&M}$ varies with time e.g. as unexpected events occur such as equipment failures. $C_{investment}$ may vary with time as the interest rate may vary during amortization. The time variability of the cell operating current I may be one of the most important parameters in terms of its potential impact on the capital cost. In reality I, t_{life} and f_{util} are encompassed together in the equation $\int_0^{t_{life}} I(t)\,dt$. $I(t)$ accounts for the intermittency $(1 - f_{util})$, which includes start-stop operation and/or smoother time-varying current operation, as well as cell degradation since $I(t)$ is also a function of the time-varying internal resistance. t_{life} may also depend on the functional form of $I(t)$. For example, the end of life may be declared when the operating current drops below half of the initial operating current due to

[vii] Since the electrolysis efficiency is defined as the thermoneutral voltage over the operating voltage and the cell can be operated at a lower voltage than the thermoneutral voltage (where the cell internal resistance does not supply enough heat), theoretically efficiencies greater than 100% are possible if external heat is available to supply the remaining energy required. However, such an external heat supply must be accounted for in the system energy balance, therefore the system will have an upper limit of 100% efficiency. The heat could be supplied by external electrical heating, giving 100% as the upper limit for the net efficiency of electricity to chemicals for the system.

degradation. Degradation may also be compensated for to maintain current density, e.g. by increasing the cell voltage (slightly lowering the efficiency) or the operating temperature.

The operating current I or $I(t)$ must be included in any economics estimation that involves variability with time, e.g. intermittency of a renewable or surplus power supply or a time-varying electricity price. Estimates in the literature that present the capital cost in terms of per watt of hydrogen produced are already optimized for a certain type of operation – usually near-constant operation (at near-100% capacity factor), e.g. including cell degradation but insignificant intermittency.

The cost is optimized between the capital cost and the operating cost. Although it is possible to operate any electrolyzer at near-100% electricity-to-chemical energy efficiency, it is not always economically optimal to do so; some cells cannot attain a sufficiently high current density at the thermoneutral voltage. In that case, it would be desirable to operate a cell at lower than 100% efficiency ($E_{op} > E_{th}$, resulting in excess heat being generated in the cell) if the larger operating voltage (E_{op}) is needed in order to achieve a higher hydrogen production rate (higher current density). For example, commercial alkaline electrolyzers are typically operated at 1.8-2 V (around 70-80% efficiency based on the higher heating value of H_2) at 0.2-0.5 A/cm^2 [90-92, 95, 98, 102]; they are run at non-optimal efficiency. This operating point is chosen due to the low current density attained at lower operating voltages, evident in the polarization curve (Figure 3-5). Some efficiency is sacrificed to lower the capital cost. This can explain why it is often cited that electrolysis can be performed with "up to 73% efficiency" [95] – based on the materials and system cost, lifetime, capacity factor, and internal resistance of the alkaline cells being referred to, the lowest cost operation is at an operating voltage of about 2 V (= 1.48 V / 73%). This current-voltage (i-V) operating point is optimal for the manufacturing cost of the cells, a near-100% capacity factor and a specific electricity price. Intermittent operation (e.g. running on intermittent solar or wind power) increases the capital cost of the electrolyzer and therefore results in a lower efficiency optimum i-V operating point.

In the design, manufacture and operation of an electrolysis system, 4 parameters can be controlled:

Affecting the operating cost, C_{op}:

1. the energy efficiency (via the operating voltage, E_{op})

Affecting the capital cost, C_{cap}:

2. the cost of producing the cell stack and balance of system, $C_{investment}$
3. the operating current density, i)
4. the operating lifetimes $t_{stack\ life}$ and $t_{sys\ life}$

For the most economical hydrogen production, E_{op} and $C_{investment}$ should be as low as possible and i and t_{life} should all be as high as possible (and since E_{op} and i are proportional and inversely proportional to the ASR respectively, the ASR should be as low as possible). In

other words, the cells should be cheap to produce and run efficiently at high throughputs for a long time.

3.2.2.3.1. Low-temperature electrolysis

Alkaline water electrolysis cells are the dominant type of cells in commercial operation today [95, 103, 104]. The electrode reactions are:

$$\text{Cathode: } 2\,H_2O(l) + 2e^- \rightarrow H_2(g) + 2OH^-(aq)$$
$$\text{Anode: } 2\,OH^-(aq) \rightarrow 2e^- + \tfrac{1}{2}\,O_2(g) + H_2O(l)$$

The electrolyte is typically a 30 wt% KOH solution and the operating temperature is 70-100 °C. The electrodes are typically porous Raney nickel electrodes which are formed by electrodeposition of a Ni-Al or Ni-Zn alloy onto a metallic (often mesh) substrate followed by leaching of the Al or Zn by a strong hydroxide solution, leaving behind a porous Ni structure. Alkaline electrolysis cells are operated with an efficiency and current density as described just above. Alkaline cells, operated in the reverse direction as fuel cells, were developed and used for space exploration since the 1960s [105]. Alkaline cells have a potential economic advantage in the ability to easily replace each cell rather than the entire stack as in other cell types. The durability of alkaline electrolyzers is sufficiently high, giving a typical operating life of 10-20 years [95, 103, 104]. For the latest commercial cells, durability was not found to suffer greatly when operating on intermittent renewable electricity (older technology suffered degradation while resting at open circuit conditions for extended periods of time). However, the capital cost for an alkaline electrolyzer stack and system has been estimated at \$7.5 to \$9 per GJ of H_2 produced, assuming near-100% capacity factor operation [95, 103, 106]. Intermittent operation increases the capital cost significantly even with optimization of operation (sacrificing efficiency to increase the current density). Alkaline electrolyzers may become viable if the manufacturing cost can be reduced to a small fraction of what it is now.

Advanced alkaline electrolysis cells are at a pre-commercial stage. Such cells are typically operated at higher temperature and/or higher pressure [90, 91, 93, 94, 100, 103, 107-110] which both enhances the current density at a given cell voltage and yields high pressure hydrogen, which is needed in any case for the subsequent fuel synthesis reactors. Advanced cells also often have micro- or nano-structured electrodes made up of higher surface area nickel, alloys or composites containing nickel, or ceramic materials to improve current density [20, 94, 111-113]. Long-term durability of advanced alkaline electrolysis has been demonstrated [94, 114].

Since seawater is naturally alkaline, seawater electrolysis can use modified alkaline electrolysis cells [20]. The cells must be modified to avoid evolution of chlorine gas. Although seawater electrolysis is in fact conventionally used to produce chlorine, the scale of electrolysis operation needed to produce the fuels needed to satisfy the world's demand for transportation

fuels would exceed world demand for chlorine by many orders of magnitude. Therefore, due to the toxicity of chlorine, oxygen would be the preferred anode product from a seawater electrolysis cell. Since the anode potential for oxygen evolution is lower than that of chlorine evolution, the cell must be operated with an anode potential within a range above the oxygen evolution potential and below the chlorine potential. Therefore, new anode materials such as Mo- and W-doped MnO_2 are being developed to achieve high anodic efficiency [111]. However, it may be unnecessary to deal with seawater in an electrolysis cell since obtaining pure water by desalination adds only a negligible cost to the fuel production process, as discussed in section 3.2.1.

Related to alkaline electrolysis is the co-electrolysis of H_2O and CO_2 using aqueous carbonate or bicarbonate electrolyte [16, 115-123]. The CO_2 can be supplied by being bubbled in or dissolved in the aqueous media, or supplied from the gas phase to a gas diffusion electrode. The majority of research in aqueous co-electrolysis of CO_2 and H_2O has focused on improving current efficiency (product selectivity) at a given potential rather than maximizing energy efficiency (for lower operating cost) or current density (for lower capital cost). The CO_2 and H_2O are electrocatalytically reduced to products such as HCOOH, CO, CH_4, C_2H_4, and higher hydrocarbons and alcohols, depending on the cathode composition and cell parameters. For example, copper electrodes were found to selectively produce methane, methanol and other hydrocarbons over just H_2 and CO, whereas Au and Ag selectively produce CO [115, 116, 119]. The cathode reaction for methanol is as follows:

$$CO_2(aq) + 6\,H^+ + 6\,e^- \rightarrow CH_3OH(l) + H_2O(l)$$

Cu and Ag metal electrodes have shown low durability due to accumulation of carbon particles during CO_2 reduction [124-126]. Metal alloy cathodes were shown to have increased durability and inhibit poisoning over pure metals [127, 128]. Reactivation of the electrodes by briefly pulsing an anodic current has also been explored [128-131]. Electrodes made of transition metal complexes [120, 132], e.g. phthalocyanine–Co/Ni, are able to coordinate the CO_2 molecule and electrocatalytically reduce it with high selectivity (but not high efficiency). Though they have lower durability, their promise lies in being less expensive than pure metals. Because the solubility of carbon dioxide in water (~0.036 M at STP) is low, rate limitation from mass transport of CO_2 to the surface results in limiting current densities of –10 to –20 mA/cm^2 under 1 atm CO_2 [133, 134]. Electrolyzing bicarbonate, which has a higher solubility (~1 M) than CO_2, has not been found to enhance the reaction rate. Gas diffusion electrodes enable higher current densities. Centi et al [122, 123] reported the production of CO and small fractions of various long-chain C_{5+} hydrocarbons at a gas diffusion electrode. However, they used an electrode with expensive Pt and Pd nanoclusters, and found the maximum product selectivity was at the low current density of –20 mA/cm^2.

Overall, the overpotentials needed (to either selectively produce such hydrocarbon products or to produce H_2/CO) are at present too high for a viable electrolyzer. With these types of cells, reasonable current densities have only been achieved at a very low efficiency – a current density of –100 mA/cm^2 requires application of about 3 V to produce a mixture of methane and hydrogen with small amounts of ethylene and carbon monoxide [121] or a mixture of potassium formate and hydrogen [135]. This results in an impractically high operating cost in comparison with other types of cells (**Figure 3-5**). Therefore, a cell with such a high internal resistance would need to be run at higher efficiency (lower current density). The current density at a given efficiency is a factor of 100 lower than higher performance cells, so the capital cost must be a factor of 100 lower to be competitive. As such an extremely low capital cost (via very cheap materials and/or very long lifetime) seems unlikely, this technology needs a significant breakthrough in reaction rates to be feasible. Perhaps state-of-the-art alkaline water electrolysis cells (or advanced alkaline cells operating at elevated temperature and pressure) could be modified to work more effectively for aqueous co-electrolysis (or H_2O electrolysis combined with catalytic CO_2 hydrogenation to hydrocarbons at a gas diffusion cathode).

Proton exchange membrane (PEM) cells operate at a similar temperature range and are also commercially available. In PEM cells, protons are selectively conducted across a polymer membrane and the following electrode reactions take place:

$$\text{Cathode: } 2\,H^+(aq) + 2e^- \rightarrow H_2(g)$$

$$\text{Anode: } H_2O(l) \rightarrow 2\,H^+(aq) + 2e^- + \tfrac{1}{2}\,O_2(g)$$

Because PEM cell electrodes contain expensive noble metal electrocatalysts (typically Pt particles) and expensive membranes their capital cost is higher than that of alkaline cells. To compensate for this higher cost, they are operated at higher current density (**Figure 3-5**). With IrO_2 and Pt electrodes, Yamaguchi et al demonstrated –1 A/cm^2 current density at 1.54 V at 80 °C under atmospheric pressure [136]. Such high current densities do not seem to be high enough to offset the cost of the expensive materials; at present, high capital cost appears to be an obstacle to affordable PEM-based electrolysis. Less expensive materials are needed.

Recently an interesting method of preparing an inexpensive water electrolysis oxygen-evolving anode was reported by Nocera and co-workers [137, 138] wherein a catalyst layer bearing Co or Ni is formed in-situ on an inert surface from a near-neutral pH aqueous solution. A very thin layer—perhaps even a monolayer—of the catalyst might suffice and the benign electrolyte does not demand expensive materials for the cell components and housing. Therefore, if a similar hydrogen-evolving cathode can be developed, this type of cell might be cheap to produce. However, these electrodes produce H_2 at only 1 mA/cm^2 at an overpotential of >400 mV. As this current density is more than 100 and 1000 times lower than that of alkaline electrolysis cells and high temperature electrolysis cells respectively, the cost per unit of electrode area of this type of electrolysis system would have to be more than 100-1000 times

lower than the other electrolysis systems to be competitive in terms of H_2 production price, assuming they have a similar operating life. However, the operating life of this type of cell might be significantly longer due to the possibly self-healing nature of the catalyst layer which is constantly re-forming on the surface. Furthermore, due to the potentially simple construction and materials requirements of the cell, the cell production cost could indeed be orders of magnitude lower than the other cell types, and future electrode designs might yield improved current density. This electrode technology and cell type is at a very early stage of research. Further study and development of this type of cell is necessary to assess economic viability.

Electrolyzing CO_2 in non-aqueous organic solvents such as methanol or acetonitrile can yield CO [117, 132] via the cathode reaction

$$2\,CO_2 + 2\,e^- \rightarrow CO + CO_3^{2-}.$$

Similarly, electrolysis of supercritical CO_2 has also been examined. Pure supercritical CO_2 exhibits zero or negligible conductivity, so electrolytes composed of additives dissolved in supercritical CO_2 [16] or ionic liquids (as solvent and electrolyte into which supercritical CO_2 is dissolved) [139] have been studied. Co-production of CO and H_2 via electrolysis of supercritical CO_2 and water dissolved in an ionic liquid electrolyte has been initially demonstrated [139]. The large overpotentials observed in that study may be the result of the use of a basic unoptimized cell, so at present it is difficult to assess the potential of this method.

3.2.2.3.2. High-temperature electrolysis

As mentioned earlier, performing electrolysis at high temperature has both a thermodynamic advantage and an advantage in reaction rates. With increasing temperature, a larger portion of heat and corresponding smaller portion of electricity is needed for the dissociation. This can be seen in the lower open-circuit voltage for the high temperature cells in **Figure 3-5**. This heat can be supplied from external sources, or it can be the Joule heat that is inevitably produced, due to the internal electric resistance of the cell, when applying the overvoltage necessary to achieve sufficient production rates. Rather than losing this ohmic heat, it is used in the disassociation of steam and/or CO_2. High temperature electrolysis therefore relies in part on thermolysis pushing the equilibrium toward dissociation. The high temperature also results in faster reaction kinetics which reduces the need for expensive catalyst materials. These differences between low and high temperature electrolysis cells can be seen in the polarization curves illustrated in **Figure 3-5**. These advantages enable very efficient operation (at near the thermoneutral voltage) at very high current densities (potentially leading to low capital cost).

There are two types of high temperature electrolyzers (typically >600 °C operation), those with molten carbonate electrolytes and those with solid oxide electrolytes. Since the electrolytes of solid oxide electrolysis cells (SOECs) and molten carbonate cells conduct O^{2-} and

CO_3^{2-} ions respectively, they can electrolyze CO_2 to CO in addition to H_2O to H_2. However, electrolysis using molten carbonate cells to produce H_2 or CO carries a disadvantage, in that a mol of CO_2 is effectively transported across the cell for every mol of fuel produced:

$$\text{Cathode: } H_2O(g) + CO_2(g) + 2e^- \rightarrow H_2(g) + CO_3^{2-}$$
$$\text{or } \quad 2\,CO_2(g) + 2e^- \rightarrow CO(g) + CO_3^{2-}$$
$$\text{Anode: } \quad CO_3^{2-} \rightarrow 2e^- + \tfrac{1}{2}\,O_2(g) + CO_2(g)$$

This CO_2 is released at the anode along with O_2, resulting in a mixed product stream there. Additional energy must then be spent to separate the CO_2 and O_2, as the CO_2 can of course not be released to the atmosphere, and the CO_2 will be needed again for the cathode reaction. The only report of such molten carbonate based electrolysis was a preliminary report made by a NASA research group with the intention to electrolyze CO_2 from the CO_2-rich atmosphere of Mars to produce breathable oxygen [140].

Recently, direct electrolysis of molten carbonate to produce CO and O_2 was reported [141]. The cell used differs from that of the above-mentioned molten carbonate cells in that molten carbonate is not only the electrolyte but the reactant as well:

$$\text{Cathode: } \quad CO_3^{2-} + 2e^- \rightarrow CO(g) + 2\,O^{2-}$$
$$\text{Anode: } \quad CO_3^{2-} \rightarrow 2e^- + \tfrac{1}{2}\,O_2(g) + CO_2(g)$$

The oxide ions that are produced at the cathode facilitate re-absorption of the CO_2 produced at the anode as well as additional CO_2:

$$2\,CO_2(g) + 2\,O^{2-} \rightarrow 2\,CO_3^{2-}$$

Indeed, the amount of CO_2 measured at the anode outlet gas stream was less than 0.005 atm. This cell type therefore does not have the problem of separating CO_2 from the output oxygen stream. The authors state that CO_2 at a partial pressure of just a few percent can be absorbed from the feed gas stream by the carbonate melt. The current densities attained are low (<100 mA/cm^2) and the long-term durability is unknown, but the electrode and container materials are inexpensive (only titanium and graphite) and the performance of the cell has not been optimized. Both types of molten carbonate cell technology share the disadvantage that the molten carbonate is corrosive which limits the choice of stable materials for the electrodes and other components.

Solid oxide electrolysis cells (SOECs) do not suffer from the above problem. Their electrode reactions are (depending on whether they are operating on steam or CO_2 input feed streams):

$$\text{Cathode: } H_2O(g) + 2e^- \rightarrow H_2(g) + O^{2-} \text{ or}$$
$$CO_2(g) + 2e^- \rightarrow CO(g) + O^{2-}$$
$$\text{Anode: } O^{2-} \rightarrow 2e^- + \tfrac{1}{2} O_2(g)$$

As with low-temperature electrolysis, cells designed as solid oxide fuel cells (SOFCs) can be used reversibly for electrolysis. However, due to differing conditions (the gas compositions at the electrodes and the direction of polarization across cell components and across interfaces between materials) between fuel cell and electrolysis operation, it may be desirable to make specialized cells for optimal electrolysis performance.

Electrolysis of CO_2, H_2O, and co-electrolysis of CO_2/H_2O mixtures using solid oxide cells was first demonstrated in the 1960s under NASA contracts, for the purpose of O_2 production for life support and propulsion in submarines and spacecraft [142-147] and research on using the cells for this purpose continues to this day [148-153]. The first solid oxide electrolysis research project unrelated to space exploration appears to be the HOT ELLY project in Germany started in 1975 [154], which focused on H_2 production. The most common material composition of typical state-of-the-art SOECs today were already being used – a porous metal-ceramic Ni-YSZ composite cathode and a porous ceramic composite anode composed of lanthanum strontium manganite and YSZ, sandwiching a dense ceramic YSZ electrolyte (YSZ = yttria-stabilized zirconia, a material that conducts O^{2-} ions at high temperatures). The performance, durability and materials used in high temperature electrolysis cells have been recently reviewed [100, 155]. A variety of alternative materials with improved properties for SOFCs are under development [156-159], many of which might be appropriate for use in SOECs. Much work has been done in testing cells and optimizing electrode and electrolyte materials for steam electrolysis [32, 99, 160-180], CO_2 electrolysis [14, 32, 33, 39, 99, 148, 174, 181-183], and co-electrolysis of both H_2O and CO_2 simultaneously to produce syngas [19, 30, 34-38, 174, 184-186] (and see **Chapter 4**). In co-electrolysis, CO_2 may be either electrolyzed or indirectly split via reverse-WGS. One can see in **Figure 3-4** that the WGS equilibrium can go either way at the operating temperatures of an SOEC. Since CO_2 electrolysis has a slightly higher resistance than H_2O electrolysis [32, 35-39, 99, 174], it is expected that part of the CO produced results from RWGS. Whether part of the syngas is produced by the WGS equilibrium has little effect on the energy demand of syngas production in the cell, because the cell's internal resistance can supply the heat needed for either the electrochemical or catalytic reactions. Systems integrating steam SOECs with solar [18, 19, 187-189] and nuclear energy [67, 190] have been examined and SOECs have been proposed for use in CO_2-recycled synthetic fuel cycles [15, 18, 19, 34, 37, 38] (and see **Chapter 4**).

A high current density of -3.6 A/cm^2 was reported when operating an SOEC for steam electrolysis at 950 °C at 1.48 V [32]. At 850 °C a similar cell showed area specific resistances (ASRs) of 0.19 and 0.24 Ω cm^2 for H_2O electrolysis and CO_2 electrolysis respectively, measured

from open circuit to –0.16 A/cm^2 (**Chapter 4** and [37]). In recent studies of co-electrolysis of H_2O and CO_2 including the one presented in **Chapter 4**, the ASR was in between that of H_2O and CO_2 electrolysis [35-38].

The long-term durability of SOECs has been a topic of recent studies [37-39, 168, 174-179]. At least at lower current densities, the cells were found to have sufficient durability for co-electrolysis of H_2O and CO_2 (see **Chapter 4** and [37, 38]). However, at higher current densities, the cells degrade significantly faster (see **Chapter 4**). Durable high current density operation will be desirable and perhaps necessary for an economical process, based on the economics discussion above (see also **section 3.3.2**). Therefore, further work in improving the durability may be necessary. The instability of the Ni-based electrode when exposed to an oxidizing atmosphere is also an issue that may need resolution before large-scale commercial use of these cells. With current cells, it would be necessary to ensure that the Ni-based electrode of each cell is always kept in a reducing atmosphere through all gas supply interruptions and unexpected incidents during operation, e.g., the cell would require a fail-safe gas recirculation system. However, depending on the cell construction [191-193] and the temperature at which an oxidation event occurs [194, 195], the performance of cells with Ni-based negative electrodes may be largely unaffected through tens of such events. Alternatively, electrodes based on ceramic materials that exhibit higher stability through reduction-oxidation (redox) cycles and similarly high electrocatalytic activity as Ni-based electrodes have been developed and demonstrated in small-scale cells [159, 196-198]. If this type of redox-stable electrode can be integrated into a full-scale commercial cell, replacement of the Ni-YSZ electrode with this type of alternative electrode would likely be the preferred solution to this issue.

While higher temperature operation enables greater fuel production rates, it can result in performance degradation by damaging the electrode structures via sintering and agglomeration as well as putting strain on the cell interconnect, housing and other materials that make up the balance of system components. Lower temperature operation disadvantageously increases the thermodynamic electrical energy demand and requires more electrical energy per unit fuel produced (slower kinetics), but also enables the survival of optimized microstructures and nanoparticles (which promote faster kinetics) against sintering and agglomeration, thereby potentially evening out the cell performance. Lower temperature also retards Ni oxidation, potentially improving the stability of the Ni electrode, as mentioned above. Therefore, there is likely an optimal operating temperature for a given cell based on its materials, construction and performance.

The estimated investment cost of a solid oxide cell stack per unit of electrode area is about the same as that estimated for low-temperature alkaline and advanced alkaline electrolyzer stacks at large-scale mass production [90, 103, 199-201], and the H_2/CO production rate is much higher, leading to a lower capital cost. Solid oxide cells clearly offer both the lowest capital cost and the lowest operating cost. Furthermore, since solid oxide electrolysis cells can

produce syngas directly via co-electrolysis of H_2O and CO_2, they reduce the system cost by eliminating the need for a RWGS reactor in the CO_2-recycled fuel production process. They also enable an improvement in the net system efficiency via utilization of the waste heat of exothermic Fischer-Tropsch type reactors that would be used for fuel synthesis (this is further examined in section 3.3.1). However, heat management is more complicated for these high temperature cells and can more easily lead to energy losses, as well as higher capital costs due to materials and equipment failures or simply additional system costs that have been underestimated. Finally, durable performance at the high current densities that may be necessary remains yet to be proven.

3.2.2.4. Photoelectrolysis

While an electrolysis cell could be powered by a PV source, an interesting combination of the two is a photoelectrochemical (PEC) cell for hydrogen production [98, 202]. Such a cell has as either its anode or cathode a semiconductor photoelectrode immersed in an aqueous solution. The photoelectrode collects photons creating excited electrons which electrolyze water molecules at the interface with the aqueous electrolyte. At the interface, the electrode can be coated with an electrocatalyst that enhances the electrolysis reaction.

In principle, such integration reduces the system capital cost and enables higher efficiency by reducing the losses in transporting electricity from the PV cell to the electrolysis cell, eliminating current collectors and interconnections between devices. In practice, several characteristics of the photoelectrode must be satisfied simultaneously: the electronic band gap of the photoelectrode must be low enough for efficient photon collecting from the solar spectrum (<2.2 eV) and high enough such that the excited electrons have enough energy to split water (>1.23 eV or typically at least 1.6-1.7 eV for sufficient rates), the band edges must straddle the water electrolysis redox potentials, and the photoelectrode must be stable and resistant to corrosion in the aqueous electrolyte [202]. These constraints rule out most inexpensive, conventional PV, yet the photoelectrode should also have a similar photoconversion efficiency as conventional PV to give this option an advantage over a PV-electrolysis system made up of separate units. Research focuses on a multitude of electrodes, including semiconductor oxides such as TiO_2, $CaTiO_3$, $SrTiO_3$ and composite oxides tailored to yield appropriate band gaps, and multijunction cells with two or more semiconductor layers, e.g. Si as one layer with the other layer (GaInPN, $CuGaSe_2$, etc) protecting it from corrosion.

Sunlight-driven dissociation of H_2O directly on TiO_2 is an active field of research. However, the broad band gap of TiO_2 limits the efficiency of absorbing sunlight [203]. Several approaches to widen the wavelength sensitivity range of TiO_2 have been studied, including doping with transition metals or nitrogen, and dye photosensitization [203]. While research in dye-sensitized solar electric cells have made progress towards practical implementation, dye-sensitized water photolysis cells have not produced significant yields and the materials have

been unstable [98]. Such chemistries begin to resemble photosynthesis, and have been called "artificial photosynthesis" [204].

With a tandem electrode configuration of two semiconductor layers, *p*-$GaInP_2$ and GaAs, 15% solar-to-chemical (higher heating value of H_2) efficiency has been reported [205], around half the reported photovoltaic efficiency for this combination (without water splitting). A similar cell with Si and $Al_{0.15}Ga_{0.85}As$ semiconductor layers gave higher efficiency (22%, close to the reported photovoltaic efficiency) when RuO_2/Pt electrocatalysts were added [206]. An alternative PEC cell may be formed by suspending the semiconductor as tiny particles in solution and optionally loading the particles with catalysts [203, 207]. However, in such a powder suspension, the produced H_2 and O_2 gasses more easily recombine than in the electrode based system, because the H_2 and O_2 production sites are located so close to each other [203].

Photoelectrochemical processes that form organic compounds from aqueous CO_2 have also been studied [208, 209]. As with their hydrogen-only analogues, much work needs to be done in developing stable materials that match solar collection band gaps to electrochemical reduction energies. TiO_2 has also been examined for photolysis of CO_2 [210, 211]. TiO_2 nanotubes with Pt and Cu catalysts were reported to have a factor of 20 rate increase for CH_4 production than without the Pt and Cu catalysts [212]. However, in that study the CH_4 yield was only 32 nmol/cm^2/hr, equivalent to ~0.01% solar-to-chemical conversion efficiency, and the CH_4 was only present as a trace gas constituent at the ppm level. CO_2 may also be supplied to non-aqueous electrolytes, which offer higher CO_2 solubility as well as an environment for potentially improved semiconductor material stability compared with water-containing systems [213].

For photoelectrolysis cells, no single material has been found that satisfies the stringent constraints [202]. The tandem semiconductor configurations are too expensive for commercial PV and may be too expensive for photoelectrochemical water splitting cells as well. The catalysts are expensive, just as they are for fuel cells and electrolysis cells. Also, long-term stability in aqueous electrolyte is uncertain. Even if a material that fulfills all of the requirements is found, it is unclear whether integrating devices into a single photoelectrochemical cell simplifies the process. With a single device, the H_2O and CO_2 must be brought to the sunlight, whereas with two devices the electrons from the PV must be transported to the electrolyzer. As mentioned above, the efficiencies that have been obtained with expensive materials are not better than what can be obtained using a PV cell powering an electrolysis cell. Photoelectrolysis of H_2O and/or CO_2 needs significant breakthroughs to become a feasible method of dissociation. At present, PV coupled to electrolysis is a more appropriate technology for solar hydrogen production than photoelectrolysis [214].

3.2.3. Catalytic Fuel Synthesis

Some of the dissociation processes produce hydrocarbons directly, but in most cases it is simpler and often beneficial to produce one or both components (CO/H_2) of syngas and catalyze fuel synthesis from these energy-rich precursors. Fischer-Tropsch synthesis (FTS) was developed in the 1920s and has been used economically as part of coal-to-liquids (CTL) and natural gas-to-liquids (GTL) projects [215]. The reaction can be represented by:

$$2\,H_2(g) + CO(g) \rightarrow -CH_2-(l) + H_2O(g) + 165\ kJ_{\ (at\ 400K)}\ [216]$$

where $-CH_2-$ is part of a hydrocarbon chain. A variety of hydrocarbons can be produced; chain growth depends on the catalyst, syngas composition, and reactor temperature and pressure. High-temperature (300-350°C) yields gasoline and low molecular mass olefins over Fe-based catalysts while low-temperature reactors (200-240°C) yield diesel and high molecular mass linear waxes over Fe or Co-based catalysts. The water-gas shift reaction competes under certain conditions. Synthesis typically yields hydrocarbon chains with a distribution of chain lengths, up to gasoline- or diesel-like fuel distributions.

Methanol can be produced in a Fischer-Tropsch-like reaction. Traditional methanol synthesis is carried out by reforming fossil-derived syngas over a $Cu\text{-}ZnO/Al_2O_3$ catalyst [26] according to

$$CO(g) + 2\,H_2(g) \rightarrow CH_3OH(l) + 128\ kJ_{\ (at\ 298K)}$$

with up to 18% CO_2 in the syngas. High methanol selectivity requires high pressures and low temperatures. The same catalyst can be used for methanol synthesis from CO_2 and H_2, according to

$$CO_2(g) + 3\,H_2(g) \rightarrow CH_3OH(l) + H_2O(g) + 87\ kJ_{\ (at\ 298K)}\ [26].$$

It has been stated that this type of methanol synthesis reactor (not necessarily with this particular catalyst) is commercially available with operating parameters of 50-100 bar and 200-300 °C [18]. Modified catalysts, such as those with ZrO_2-modified Al_2O_3 supports, show improvements by enhancing the dispersion of the copper particles [208, 217]. Zeolite membrane reactors also show promising results [218]. It has been shown that the carbon source in such methanol synthesis is exclusively CO_2 and therefore the reaction mechanism involves hydrogenation of the adsorbed CO_2, which proceed through an intermediate species of formate ($HCOO^-$) [219]. Methanol synthesis by CO_2 hydrogenation was demonstrated as early as 1927 [220]. Many proposed CO_2-derived fuel cycles include methanol synthesis by CO_2 hydrogenation (**Table 3-1**).

Methanol-to-gasoline reactors that reform the methanol product to higher hydrocarbons have been investigated. They exhibit varying selectivity, over zeolite catalysts [26]

or H-Fe silicate catalysts [208]. Methanol synthesis and reformation to gasoline have been combined in single-step CO_2 hydrogenation reactors with varying selectivities using similar Fe-based catalysts [208]. The operating conditions for these various reactors range from around 220-300 °C and 10 to 100 atm.

Alternative catalysts, such as Al_2O_3-supported Ni or TiO_2-supported Ru [208], instead favor the methanation of CO_2. CO_2 methanation, also known as the Sabatier process, is an exothermic reaction usually performed at temperatures of 300-400 °C:

$$CO_2(g) + 4\,H_2(g) \rightarrow CH_4(g) + 2\,H_2O(g) + 165\ kJ_{\ (at\ 298K)}.$$

A variety of other catalysts [208, 221, 222] selectively promote CO production via the reverse water-gas shift reaction (RWGS),

$$CO_2(g) + H_2(g) + 41\ kJ_{\ (at\ 298K)} \rightarrow CO(g) + H_2O(g).$$

However, unlike the other CO_2 hydrogenation reactions, this reaction is endothermic and spontaneously yields essentially full conversion at high temperatures exceeding approximately 830 °C (see **Figure 3-4**), at atmospheric pressure. A methanol synthesis process has been developed in which a RWGS reactor is paired with a conventional methanol synthesis reactor [223]. Similarly, producing hydrocarbons by a single-step direct hydrogenation is an active field of research [224-228]:

$$CO_2(g) + 3\,H_2(g) \rightarrow -CH_2-(l) + 2\,H_2O(g) + 125\ kJ_{\ (at\ 400K)}$$ [216].

This reaction would be advantageous since it is less exothermic than the Fischer-Tropsch reaction (this is further discussed in section 3.3.1).

Finally, processes that perform fuel synthesis involving reactants other than just $CO_2/CO/H_2O/H_2$ have been proposed. One is the hydrogenation of $CaCO_3$ to yield hydrocarbons while regenerating $Ca(OH)_2$ as an air capture absorbent [9]. Another is a hydrothermal process that uses Fe as a reducing agent with CO_2 in an elevated-temperature aqueous system (e.g. near hydrothermal vents in the ocean) to directly yield CH_4 [229]. This is similar to a thermochemical cycle in that the oxidized Fe must be regenerated.

3.3. A Promising Pathway Based on Electrolysis in Solid Oxide Cells

3.3.1. Process and Energy Balance

Of the CO_2 air capture technologies reviewed, the solid adsorbent and humidity swing method appears to have the lowest energy demand (section 3.2.1). Thermal regeneration methods could also be feasible if heat management is carefully integrated with the rest of the

fuel production process, but at present the energy demand and need for moving a lot of materials render these methods less economical. Electrolytic regeneration with byproduct H_2 production may become feasible with further developments of the electrolytic cell. We choose the humidity swing method for this study.

Of the dissociation technologies reviewed, high temperature electrolysis using solid oxide cells appears to be one of the most promising (section 3.2.2.3.2). Recent developments and performance improvements have brought solid oxide electrolysis cells close to practical implementation. Efficient co-electrolysis of H_2O and CO_2 has been demonstrated with low cell degradation rates [37, 38] (and see **Chapter 4**). By supplying the proper ratio of H_2O and CO_2, syngas can be produced with a composition tailored for catalytic fuel synthesis. Despite the potential heat management complexity and the as yet unproven durability at very high current densities discussed at the end of section 3.2.2.3.2, we choose the solid oxide electrolyzer over other means of dissociation. This is not to say that other means of dissociation are not worthwhile. However, critical aspects of the feasibility of heat and light driven processes have not been sufficiently demonstrated (sections 3.2.2.1, 3.2.2.2, and 3.2.2.4), and because of the inherently more limited current densities of alkaline electrolyzers their capital cost is at present too expensive for intermittent operation (section 3.2.2.3.1). A pathway based on capture of CO_2 from the atmosphere, high-temperature co-electrolysis of H_2O and CO_2, and Fischer-Tropsch synthesis is therefore chosen for the following analysis.

Weimer et al first proposed the use of solid oxide cells for a CO_2-recycled synthetic fuel cycle [18, 19]. The proposed process used a KOH absorbent to capture CO_2 from the air, regenerated the resulting K_2CO_3 to KOH (releasing CO_2) by reacting with CaO and H_2O, and calcining the resulting $CaCO_3$ in a thermal absorbent regeneration process. Steam and the captured CO_2 are supplied together to a solid oxide cell stack for co-electrolysis, yielding syngas. The syngas is sent to a catalytic methanol synthesis reactor for methanol production. The fuel synthesis is exothermic and the authors note that the waste heat can be used to heat water to produce steam.

Here is proposed a similar process along with the energy balance, economic estimate, and discussion about implementing the process, using published experimental data when possible. The differences are the use of a new type of CO_2 air capture process which uses far less energy and costs less [2], the use of today's state-of-the-art solid oxide cells for co-electrolysis, and the use of conventional Fischer-Tropsch synthesis. Isothermal operation of the cells can be attained just above the thermoneutral voltage, taking into account small heat exchange losses as the hot outlet gasses are used to preheat the inlet gasses. Therefore the cells would operate at slightly lower than the 100% operating efficiency of an electrolysis cell that was mentioned in section 3.2.2.3.

The initial internal resistance of the cell stack is assumed to be 0.3 Ω cm^2 at 850 °C based on single-cell results [37, 38] and assuming some additional ohmic losses from the stack

interconnects. Although the cells can be run at more than –1.5 A/cm^2 at the thermoneutral voltage based on this area-specific resistance[viii], an initial current density of –0.5 A/cm^2 is assumed to minimize cell degradation, which can occur at high current densities [37, 38] (and see **Chapter 4**). Therefore the remaining heat needed is supplied by electrical heating very close to the cells; summing the internal Joule heating and this additional electrical heating, a voltage corresponding to the thermoneutral voltage plus 8% (to accommodate heat exchange losses) is supplied in total. Cell performance has been observed to degrade at a low rate of 0.003 mV/h for co-electrolysis operated at a fixed –0.25 A/cm^2 [37, 38] (and see **Chapter 4**) – we assume this same degradation rate can be achieved when operated at the higher current density of –0.5 A/cm^2 assumed above. The cell stack is assumed to operate with a high $CO_2 + H_2O$ conversion (reactant utilization), which should give a composition sufficiently rich in $CO + H_2$ for Fischer Tropsch synthesis. The ability to operate efficiently at >90% conversion has been demonstrated [101], but no long-term durability tests have been reported. Overall, the assumptions are closely based on today's reported solid oxide cell technology with reasonable minor improvements.

Figure 3-6 shows a simplified process diagram and **Table 3-2** presents an energy balance estimate based on the assumptions. From the energy balance, electrolysis is clearly the major energy-consuming step and therefore electricity is expected to dominate the operating cost. Fischer-Tropsch synthesis (FTS) is exothermic, putting out waste heat and steam, both of which are not well utilized in existing fossil-to-liquids synthetic fuel processes [230]. However, in this process, the low-grade heat is enough to preheat the CO_2 and H_2O (to make steam) to 250 °C for the electrolyzer. This lowers the thermoneutral voltage to 1.35 V and increases the net system efficiency. The voltage applied to the cell and resistive heater is slightly higher to compensate for the assumed heat exchanger efficiency of 93%: 1.35 V / 93% = 1.45 V. The higher heating value of $–CH_2–$ is 647 kJ/mol. Assuming the process is entirely driven by electricity and the waste heat is utilized as described, the total electrical energy input would be 928 kJ/mol (**Table 3-2**) and the net electricity-to-fuel efficiency would be about 70%. This is approximately double the efficiency estimated for a low temperature electrochemical process which does not include CO_2 capture nor liquid hydrocarbon fuel synthesis (it yields a gaseous mixture of CH_4, H_2, C_2H_4 and CO) [121].

Heat losses are almost entirely due to the excess heat resulting from Fischer-Tropsch synthesis. Less exothermic fuel synthesis would improve the net efficiency. As described in section 3.2.3, hydrocarbon or methanol synthesis from CO_2 and H_2, instead of CO and H_2, is less exothermic. If this type of synthesis matures and proves to be efficient, it may therefore be

[viii] Assuming a reactant stream composed of >90% reactants with $H_2O/CO_2 = 2$ to yield the proper syngas ratio for Fischer-Tropsch and the remaining 1-10% as recycled syngas, the OCV is 0.7-0.8 V. Since the reactants are preheated by the exothermic Fischer-Tropsch reaction, the thermoneutral voltage in this case is between the steam electrolysis thermoneutral voltage (1.29 V) and that of CO_2 electrolysis (1.47 V). See references [37] and [38] for a polarization curve that illustrates this.

preferable, which would make steam electrolysis preferable over co-electrolysis for this process. Another option to possibly improve the net efficiency is integrating fuel synthesis with the cell or into the outlet of the cell [31, 231]. While this may simplify heat management, to fully realize the benefits of this would also require the development of cells that run in the same temperature range as fuel synthesis – then the heat generated in fuel synthesis reactions would contribute to heating the cell, resulting in minimal heat loss, in theory. The typical materials used for solid oxide electrolysis cells would not be adequate for such low temperature operation, in terms of the electrolyte conductivity and the catalytic activity of the electrodes; new materials would be needed. Alternatively, advanced alkaline water electrolysis cells could be operated at an elevated temperature that provides conditions for catalytic fuel synthesis by CO_2 hydrogenation, and CO_2 could be injected into the cathode compartment where H_2 is being produced (as mentioned near the end of **section 3.2.2.3.1**).

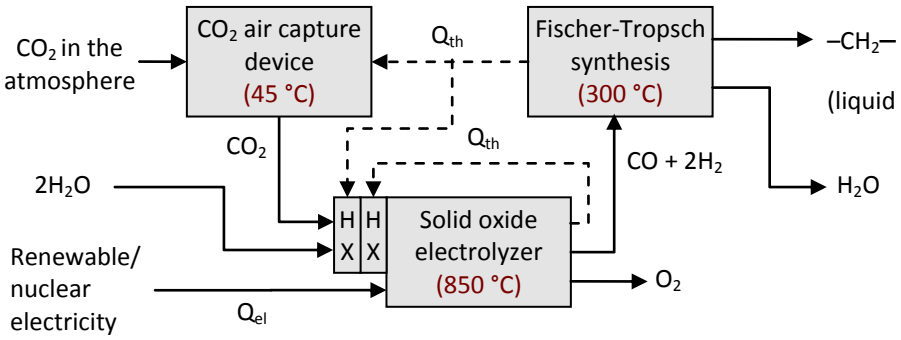

Figure 3-6. Schematic of the proposed CO_2-recycled synthetic fuel production process. $–CH_2–$ represents a hydrocarbon, which could also be represented as a longer-chain molecule such as C_8H_{18}. HX: heat exchanger.

Table 3-2. Energy balance for the process shown in **Figure 3-6**. Units of the Q terms are kJ electricity per mol $–CH_2–$ and kJ heat per mol $–CH_2–$ for Q_{el} and Q_{th} respectively. η_{HX} is the heat exchange efficiency.

		input				output		
Stage	Reaction	η_{HX}	Q_{el}	Q_{th}	T (°C)	Q_{th}	T (°C)	Fuel
CO_2 air capture	CO_2 *(atmosphere)* → CO_2 *(concentrated)*		50		45		45	
H_2O desalination	2 H_2O *(l, seawater)* → 2 H_2O *(l, pure)*		0.1		20		20	
CO_2 + H_2O pre-heating	CO_2 *(g)* + 2 H_2O *(l)* → CO_2 *(g)* + 2 H_2O *(g)*	93%		121	20		250	
Electrolysis system[a]	2 H_2O *(g)* + CO_2 *(g)* → 2 H_2 *(g)* + CO *(g)* + 1.5 O_2 *(g)*	93%	838		250		50	
Syngas compression	(2 H_2 + CO) *(g, 1 bar)* → (2 H_2 + CO) *(g, 20 bar)*		30		50		300	
Fischer-Tropsch	2 H_2 *(g)* + CO *(g)* → $–CH_2–$ *(l)* + H_2O *(l)*				300	209	20	647
Auxiliary components			10					
Total			928					647

[a] The electrolysis system includes the cell stack which operates at 850 °C, an ohmic heater for operating the cell below the thermoneutral voltage, a heat exchanger which heats the inlet gasses to 850 °C and cools the outlet gasses to just above the temperature of the inlet gasses, and a condenser which cools the product gasses to 50 °C and collects unconverted water.

If the process is driven by an intermittent power source, the efficiency will likely be somewhat lower. For example, if the electrolyzer is driven by solar power, the cells must either be heated up and cooled down each day (thermal cycling) or kept hot throughout the night, and they should be kept hot during power supply interruptions (e.g. due to clouds). This extra heating uses energy, lowering net efficiency. However, preliminary analysis of the heat management energy consumption for a well-insulated cell stack indicates that the impact on the net efficiency may be minor. In this analysis, these additional energy expenditures are encompassed in the "auxiliary components" in the energy balance (**Table 3-2**).

The degradation rate we assumed may in fact be lower because there may be fewer impurities in the gas stream, which likely contribute to the degradation [39], because the gases will be supplied from clean air-captured CO_2 and vaporized H_2O in the renewable fuel cycle rather than the way they are supplied in the lab tests – CO_2 which originates from fossil resources and therefore contains trace sulfur and other contaminants, and H_2 (also fossil-originated) and O_2 which are combusted to make steam for the lab tests [37, 39]. CO_2-recycled fuels will also have higher purity (e.g. without sulfur contaminants) than fossil- or biomass-derived fuels.

On the other hand, cell performance may degrade more quickly, if driven by an intermittent power source – the long-term durability of cells has not yet been extensively tested with such a degree of start-stop operation of applied voltage. If thermal cycling is necessary, degradation may be faster [232]. However, this depends on the cell; some studies have observed only minor degradation through tens of thermal cycles [99, 193, 232].

If a high pressure electrolysis cell is developed, the syngas compression step can be replaced with an electrolysis-stage H_2O + CO_2 compression step (in addition to potential improvements in the cell current density, as has been demonstrated for low temperature electrolyzers – see section 3.2.2.3.1).

No energy credit (and in the next section, no economic credit) is given for the high-purity byproduct O_2 generated at the anode during electrolysis.

Overall, the analysis presented here is simplified and requires more investigation into operation parameters and heat management strategies before implementation. However, it is useful to estimate the energy balance and economics.

3.3.2. Economics and Implementation

Based on the above energy balance and the assumptions of **Table 3-3**, the cost of the process is estimated in **Figure 3-7a**. The cost estimate assumes mass production of the components. It shows that synthetic gasoline could be produced by this process at USD $2/gal ($0.53/L or $15/GJ), a price competitive with the current wholesale price of conventional

gasoline, if electricity costs \$0.02/kWh. The cost of producing synthetic diesel would be similar. It is clear that electricity makes up the majority of the total cost. This supports running the electrolysis cells as near 100% efficiency as possible, as we have assumed. However, the electrolysis capital cost depends on the current, the degradation rate, the cell lifetime, and the intermittency with which the cell is used (see section 3.2.2.3), all of which are uncertainties since the technology is not fully mature and operation has not been fully optimized. If the cell stack is driven solely by a solar electricity source it will only be used about 20% of the time, which will increase the capital cost by a factor of five[ix] assuming that the lifetime of the cell stack is not extended by only operating it part of the time.

Table 3-3. Assumptions for cost estimate (also see **Table 3-2** for assumed electricity consumption).

Cost of CO_2 capture	\$30	per tCO_2 [2] and [see section 3.2.1], broken down into 0.32 kWh/$kgCO_2$ electricity and \$15/tCO_2 capital cost based on [2]
Cost of H_2O	\$1	per m^3 [see section 3.2.1]
Cost of fuel synthesis	\$1.50	per GJ Fischer-Tropsch gasoline or diesel from syngas[a] [215, 230]
Cost of dissociation		
Operating temperature	850	°C
Electrolysis cell stack	\$2000	per m^2 investment including financing[b]
Stack life	5	Years
Balance of system	\$5000	per m^2 investment including financing[b]
Balance of system life	20	years
Initial current density	–0.50	A cm^{-2}
Initial stack ASR	0.30	Ω cm^2
Average degradation rate	0.006	mΩ cm^2 h^{-1} (based on galvanostatic degradation rates [37, 38])
Capacity factor	100%	= 1 – intermittency
Operating and maintenance	\$0.5	per GJ fuel[c]

[a] Fischer-Tropsch diesel has been estimated as economically competitive when crude oil is at around \$20/barrel [230]. The cost of synthetic gasoline production by FT is similar, although the process is more complex [215]. This includes the cost of natural gas and reforming it to syngas, which typically accounts for 60-70% of the capital and running costs of the total plant [215]. With 6.1 GJ per barrel oil equivalent, this gives somewhat less than \$1.50/GJ for producing fuel from syngas; therefore \$1.50/GJ is a conservative estimate. Similar estimates have been made for methanol synthesis [233, 234].

[b] This falls within the range of estimates for the cost of manufacturing in large-scale mass production and installing the stack and system [32, 200, 201, 235]. Note that the stack life is shorter than the system life, so stacks will be replaced several times during the operating life of the system.

[c] This operating and maintenance cost corresponds to around 10% of the installed capital cost, which is in a similar range as or larger than O&M cost estimates for relevant industrial plants such as coal and natural gas based liquid fuel production [236, 237], but lower than estimates for large alkaline electrolysis plants [95, 238]. The level of automation of the facility will likely have a large impact on the O&M cost.

[ix] The CO_2 capture and fuel synthesis costs may not be affected much because they could still be operated continually by using buffers for the electricity and gasses. Since these stages consume relatively little energy the total cost should not be significantly affected by including a small electricity storage system (which could even be some of the produced syngas or synthetic fuel, e.g. using some of the solid oxide cells reversibly as fuel cells to produce electricity) and gas storage reservoirs for the CO_2 and if needed, syngas

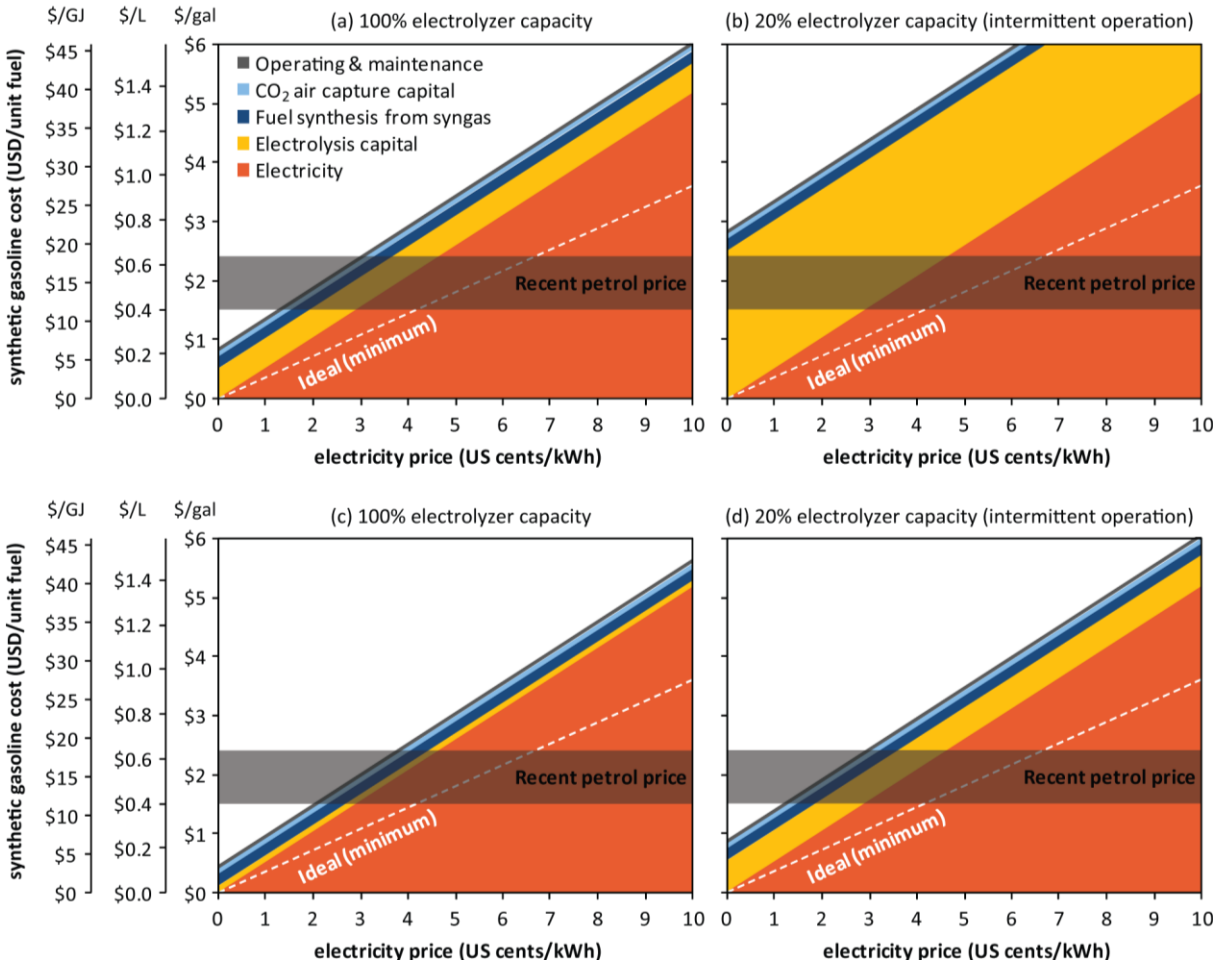

Figure 3-7. Estimate of synthetic fuel cost vs electricity price using (a) the assumptions of **Table 3-3** including constant operation, (b) the same assumptions but with highly intermittent operation (a 20% capacity factor), and operating the electrolyzer at a higher current density with (c) constant operation and (d) highly intermittent operation. See discussion in the text about the higher current density scenario.

The sensitivity of the fuel production cost to intermittent operation of the electrolyzer is examined in **Figure 3-7b**, which uses the same assumptions as before but with a capacity factor of 20%. The capital cost has increased so much that even if the electricity was free, economically competitive fuels cannot be produced. In fact, commercial alkaline electrolyzers could be used at nearly the same cost in this case. However, as discussed earlier, solid oxide electrolysis cells can easily run at a higher current density without impacting the efficiency; we limited the current density to prevent degradation. If we instead assume that the cell stack could be run at –2 A/cm^2, the approximate full current density attainable at 1.45 V, with a degradation rate only three times higher than was assumed at –0.5 A/cm^2, then fuel production at USD $2/gal becomes feasible with highly intermittent operation, with an electricity price of 2 U.S. cents per kWh (**Figure 3-7d**). At constant operation the electrolyzer capital cost becomes almost negligible, enabling competitive fuel production using electricity priced at 3 U.S. cents

per kWh (**Figure 3-7c**). Alternatively, the same fuel production costs can be attained by operating at a more modest –1 A/cm^2 with the same 5 year stack lifetime and driving the investment cost down to half.

Another uncertainty which must be considered is the cost of capturing CO_2 from the atmosphere. For every \$10/tCO_2 increase in the cost of CO_2 capture, the cost of the fuel produced will increase by 6 U.S. cents per gal (2 cents/L or \$0.45/GJ). While the fuel production price is less sensitive to the cost of air capture than to the electricity cost, it is not insignificant.

From this simple analysis several conclusions can be made about the process:

- With a constant power supply, synthetic gasoline can be produced at around \$2/gal (\$0.53/L) only if the electricity price is less than 3 U.S. cents/kWh. This is true for the base case of the electrolyzer technology and in case of significant technology improvements (even if the electrolyzer had zero capital cost). If a higher gasoline price of \$3/gal (\$0.78/L) is competitive, the price of electricity driving the synthetic fuel process must be 4-5 U.S. cents/kWh, which is a similar range to recent average wholesale electricity prices in the U.S.

- Regarding the capital cost, intermittency is a very important factor which deserves a more detailed economic analysis. Without intermittency, electricity—not the electrolyzer capital cost—dominates the cost of fuel production. However, with intermittent power, economical fuel production using 2 U.S. cents/kWh electricity will depend on some improvements in electrolyzer technology – greater durability in high current density operation and/or lower investment cost. Optimizing cells to maintain durable performance while operating at the high current density attainable at the thermoneutral voltage is a straightforward way to reduce the capital cost. Reducing the investment cost may require focus on the balance of system components since these components may dominate the investment cost [200, 201].

- Fuel synthesis and CO_2 air capture are stages that would not be present for a hydrogen fuel cycle. The hydrogen fuel cycle would instead have a high cost of distribution since a new infrastructure would need to be built. In the CO_2-recycled fuel production process, the net cost of fuel synthesis and CO_2 air capture together is at most \$6/GJ fuel (based on an capture cost of \$100/tCO_2, which is on the high end of estimates for air capture [51]). A hydrogen distribution infrastructure including filling stations has been estimated to cost at least this much if not several times more [239, 240] depending on the level of market penetration. These costs would come in the form of massive capital investments which would demand immediate widespread adoption of hydrogen fueled vehicles in order to be economical. CO_2-recycled hydrocarbon fuels, on the other hand, can

smoothly substitute into the existing hydrocarbon fuel infrastructure and scale up naturally as the market demands.

From an economic standpoint, the process should always be run with a constant-supply power source because constant operation lowers the capital cost. Therefore, hydroelectric, geothermal, or nuclear power would be preferable. Iceland appears to be in a unique position, as mentioned in Sec 2.1. Iceland has an abundance of inexpensive geothermal and hydroelectric energy. Due to Iceland's isolated location the country cannot export this energy directly as electricity. The country exports this energy embedded in products like aluminum. Producing synthetic hydrocarbon fuels by this method would be another, potentially extremely valuable, avenue to exporting this low cost renewable energy.

In most cases, though, excess constant-supply power is not available. Synthetic fuel production will compete with other electricity consumers for a time-varying supply of electricity. Since synthetic fuel production does not *need* electricity on demand, it could take advantage of intermittent electricity sources which do not work well on the power grid. Storage of intermittent renewable energy as synthetic fuels could be an advantageous way to get that renewable energy to the consumer, as mentioned in the introduction (section 3.1).

The most advantageous intermittent electricity sources would be those that are situated in ideal locations for energy collection, which can include remote locations far from existing electricity grid infrastructure. Solar power in a sunny desert is one such scenario that can provide cheap intermittent electricity. Solar insolation can be several times higher in the desert than in regions that need fuel. Therefore, a renewable electricity source that is currently too expensive to situate near the electric grid to provide grid electricity might be used in a remote location to economically produce high value fuels. Furthermore, PV deployment in non-grid applications can benefit the cost learning-curve for PV cells [241], accelerating the cost reductions necessary for PV to become competitive in the grid. If the synthetic fuel technology were to be implemented in the dry desert, water supply might be a concern. However, the water needed for electrolysis and other components of the process could simply be transported to the site by the same means that the fuel product would be transported away from the site. The volume of water required for producing the hydrogen embedded in fuel only slightly exceeds the amount of fuel produced.

Solid oxide electrolysis cells are also being considered for integration with wind power. Excess bursts of wind power could be very cheap, but such a power source would be highly intermittent, requiring a very inexpensive electrolysis capital cost to produce gasoline for less than USD $2-3 per gallon.

On the other hand, grid-connectivity could be advantageous. Operating the solid oxide cells reversibly, as electrolysis cells when the renewable electricity is supplied and as fuel cells when consumers demand electricity, may be an advantageous method of large-scale electricity

storage for managing intermittent electricity sources like solar and wind, as an alternative to (or in cooperation with) other means of storage such as in batteries or compressed air energy storage. Excess supply could be used for transportation fuel production by CO_2 recycling. In such a scenario, since the cells would be operated in fuel cell mode in addition to electrolysis mode, the capacity factor of the cells would be higher than for cells dedicated to electrolysis only, which could improve the economics.

In discussing the economics of synthetic hydrocarbons, one study concluded that "only under exceptional circumstances would one form of secondary energy (electricity) be converted to another (hydrogen)" [40]. However, one should make a clear distinction between primary electric energy and secondary electric energy. The latter is produced (e.g. from fossil fuel) in order to satisfy customer demand. The former is the result of physical constraints and it is delivered whenever the system (e.g. the photovoltaic panel or wind turbine) is ready to produce electricity. Clearly, secondary electricity is far more valuable than primary electricity. Primary electricity can be converted to whatever form of energy is more valuable than itself. So the circumstances under which electricity would be converted to fuel need not be exceptional: the value of chemical fuels need only be greater than the value of carbon-neutral electricity. Today, this is already the case in some locations. Iceland is one example, as mentioned above. In Norway, another country with an abundance of renewable energy sources, the pre-tax price of diesel fuel is about twice the pre-tax price of electricity on an energy equivalent basis[x] [242]. These are circumstances in which the CO_2-recycled fuel process might be first implemented – where economic viability is closest to being within reach. In the long term, as renewable and nuclear energy sources scale up and other countries become renewably powered like Iceland and Norway, as gas prices rise, and as the technologies involved in the CO_2 recycling process are improved, the circumstances will become more and more common and the economics of the synthetic fuel process will become more favorable.

Since CO_2-recycled synthetic fuels are environmentally friendly (potentially moreso than biofuels), they might go to market without the same level of taxation as gasoline in some countries. This would give these clean fuels an advantage as they would be competing against the post-tax price of gasoline rather than the wholesale price. A price on CO_2 emissions would likely further improve the economic competitiveness of CO_2-based synthetic fuels. Finally, the potentially greater sustainability of CO_2-recycled fuels over fossil or biomass derived fuels, as

[x] Regarding the use of pre-tax prices: Although the end-user post-taxation price of liquid fuels is higher than that of electricity in most parts of the world, liquid fuels are more heavily taxed than electricity, so one must compare the pre-tax prices [242]. Regarding energy equivalence: \$0.03/kWh is equivalent to \$1.10/gal or \$0.29/L gasoline based on an energy density of 34.5 MJ per L gasoline. Energy-equivalent prices are based on an ideal energy conversion – if one could simply turn electrical energy into hydrocarbon fuel without paying anything (energy, equipment, etc) for the conversion. Based on the cost estimates shown in **Figure 3-7**, one can see that the conversion might add from \$0.45/gal to \$2.85/gal (\$0.12 to \$0.75/L) depending on the technologies.

well as independence from the geographic and supply related issues of conventional fuels, could also give CO_2-recycled fuels a market advantage.

3.4. Conclusion

This article has reviewed and analyzed numerous ways sustainable hydrocarbon fuels could be produced from CO_2, H_2O, and renewable and/or nuclear energy. A process to produce such fuels has three stages: (1) CO_2 capture, (2) storage of the renewable or nuclear energy as chemical energy by dissociation of CO_2 and/or H_2O, and (3) fuel synthesis using the dissociation products. Combining more than one stage into a single unit is possible, but there may be benefits to optimizing each stage separately. The status of the enabling technologies for each stage was examined, with special focus on the various thermochemical, electrochemical and photochemical energy conversion technologies that could be used for dissociation of H_2O and CO_2, the stage with the highest energy consumption. Capturing CO_2 from the atmosphere using a solid sorbent, electrolyzing H_2O and CO_2 in high temperature solid oxide cells to yield a mixture of H_2 and CO (syngas), and producing gasoline or diesel from the syngas in a catalytic reactor (e.g. Fischer-Tropsch) was identified as one of the most promising, feasible routes and analyzed further in terms of energy balance and economics.

Based on the energy balance and economics estimates presented for this particular co-electrolysis based cycle, the state-of-the-art technologies at each stage of the cycle can be combined to work together efficiently today with an electricity-to-liquid fuel conversion efficiency of about 70%, and with mass production of the components, economic viability is feasible. With an electricity price of less than 3 U.S. cents per kWh from a constant power supply (e.g. geothermal, hydroelectric, or nuclear), the synthetic fuel price could be competitive with gasoline at around USD $2 per gallon ($0.53/L). If a higher gasoline price of $3/gal ($0.78/L) is competitive, the price of electricity driving the synthetic fuel process must be 4-5 U.S. cents/kWh, which is a similar range to recent average wholesale electricity prices in the U.S. Intermittent power sources would significantly increase the the capital cost of the electrolyzer. With intermittent operation, economical fuel production most likely requires additional technology development on the electrolysis system to reduce the capital cost (via achieving durable high current density operation and/or lower manufacturing cost). Several developments could enable competitive fuel production using any inexpensive sustainable power sources:

- Further development of the CO_2 air capture process and full-scale demonstration, followed by cost reductions from mass production. In the near term, however, CO_2 collected from industrial sources rather than the atmosphere could be used in the non-closed-loop version of the synthetic fuel process.

- Demonstration of durable operation of solid oxide electrolysis cell stacks at high current densities (≥1 A/cm^2). Since the existing cells can be efficiently operated at such high current densities at the thermoneutral voltage, operating at this point would be a straightforward way to improve the economics, if performance at this operating point can be maintained over long-term operation.

- Demonstration of intermittent cell operation, which may require development of specialized power management and heat management schemes.

Circumstances for initial implementation were discussed. Sites with excess inexpensive constant-supply renewable power, such as those available in Iceland, are ideal. However, since these circumstances are rare, large-scale implementation depends on using inexpensive, intermittent renewable energy (e.g. solar arrays built in remote, sunny locations such as the desert, or excess wind power supply) and/or constant-supply nuclear power for synthetic fuel production.

With feasible technology development and mass production of the process components, CO_2-recycled hydrocarbon fuels can be produced at the scale needed to replace transportation fuels at a price competitive with more conventional fossil-derived hydrocarbons, especially if oil and CO_2 sequestration costs are high. The potentially greater sustainability of CO_2-recycled fuels over fossil or biomass derived fuels, as well as independence from the geographic and supply related issues of conventional fuels, could also give CO_2-recycled fuels a market advantage.

3.5. References

1. *FactSage 5.5 software*.
2. Lackner KS, *Capture of carbon dioxide from ambient air*. The European Physical Journal - Special Topics, (2009). **176**(1): p. 93-106.
3. Kheshgi HS, Prince RC, and Marland G, *The potential of biomass fuels in the context of global climate change: Focus on transportation fuels*. Annual Review of Energy and the Environment, (2000). **25**: p. 199-244.
4. Steinberg M, *Electrolytic synthesis of methanol from CO_2*. (1976). USPTO 3,959,094.
5. Steinberg M, *Production of Synthetic Methanol Fom Air and Water Using Controlled Thermonuclear Reactor Power—I. Technology and Energy Requirement*. Energy Conversion, (1977). **17**: p. 97-112.
6. Dang VD and Steinberg M, *Production of synthetic methanol from air and water using controlled thermonuclear reactor power--II. Capital investment and production costs*. Energy Conversion, (1977). **17**(4): p. 133-140.
7. Steinberg M, *Synthetic Carbonaceous Fuels and Feedstocks from Oxides of Carbon and Nuclear-Power*. Fuel, (1978). **57**(8): p. 460-468.
8. Steinberg M, *Synthetic carbonaceous fuels and feedstocks*. (1980). USPTO 4,197,421.
9. Lewis JG and Martin AJ, *Method for obtaining carbon dioxide from the atmosphere and for production of fuels*. (1979). USPTO 4,140,642.
10. Corbett MJ and Salina SC, *Production of synthetic hydrocarbons from air, water and low cost electrical power*. (1981). USPTO 4,282,187.
11. Corbett MJ, *Synfuel production ship*. (1986). USPTO 4,568,522.
12. Martin FJ and Kubic WL, *Green Freedom^{TM}: A Concept for Producing Carbon-Neutral Synthetic Fuels and Chemicals*. (2007), Los Alamos National Laboratory. LA-UR-07-7897.

13. Kubic WL and Martin FJ, *Method of producing synthetic fuels and organic chemicals from atmospheric carbon dioxide*. (2009). WIPO WO/2009/048685.
14. Phillips and Isenberg AO, *Hydrocarbon prodn. from inorganic carbonate minerals - and water, with process heat supplied by nuclear reactor*. (1984). USPTO 4428-905-A.
15. Yamauchi Y, Tokita Y, Murakami N, Takita K, Mori Y, Muraishi K, et al., *Method for producing methanol by use of nuclear heat and power generating plant*. (1994). USPTO 5,479,462.
16. Bandi A, Specht M, Weimer T, and Schaber K, *CO_2 Recycling for Hydrogen Storage and Transportation—Electrochemical CO_2 Removal and Fixation*. Energy Conversion and Management, (1995). **36**(6-9): p. 899-902.
17. Stucki S, Schuler A, and Constantinescu M, *Coupled CO_2 recovery from the atmosphere and water electrolysis: feasibility of a new process for hydrogen storage*. Int. J. Hydrogen Energy, (1995). **20**(8): p. 653-663.
18. Weimer T, Schaber K, Specht M, and Bandi A, *Methanol from atmospheric carbon dioxide: A liquid zero emission fuel for the future*. Energy Conversion and Management, (1996). **37**(6-8): p. 1351-1356.
19. Weimer T, Specht M, Bandi A, Schaber K, and Maier CU, *CO_2 removal and fixation solar high temperature syngas generation for fuel synthesis*. Energy Conversion and Management, (1997). **38**(Supplement 1): p. S379-S384.
20. Hashimoto K, Yamasaki M, Fujimura K, Matsui T, Izumiya K, Komori M, et al., *Global CO_2 recycling - novel materials and prospect for prevention of global warming and abundant energy supply*. Materials Science and Engineering a-Structural Materials Properties Microstructure and Processing, (1999). **267**(2): p. 200-206.
21. Jensen R and Lyman J. *Solar Conversion of CO_2 to Fuel*. in *Proceedings of the 4th International Conference on Greenhouse Gas Control Technology*. (1998). Interlaken, Switzerland.
22. Jensen RJ, Lyman JL, King JD, and Guettler RD, *Solar reduction of CO_2*. (2000). USPTO 6,066,187.
23. Traynor AJ and Jensen RJ, *Direct solar reduction of CO_2 to fuel: First prototype results*. Industrial & Engineering Chemistry Research, (2002). **41**(8): p. 1935-1939.
24. Miller J, Allendorf M, Diver R, Evans L, Siegel N, and Stuecker J, *Metal oxide composites and structures for ultra-high temperature solar thermochemical cycles*. Journal of Materials Science, (2008). **43**: p. 4714-4728.
25. Mignard D, Sahibzada M, Duthie JM, and Whittington HW, *Methanol synthesis from flue-gas CO_2 and renewable electricity: a feasibility study*. International Journal of Hydrogen Energy, (2003). **28**(4): p. 455-464.
26. Mignard D and Pritchard C, *Processes for the synthesis of liquid fuels from CO_2 and marine energy*. Chemical Engineering Research and Design, (2006). **84**(9 A): p. 828-836.
27. Olah GA, *Beyond Oil and Gas: The Methanol Economy*. Angewandte Chemie International Edition, (2005). **44**(18): p. 2636-2639.
28. Olah GA and Aniszfeld R, *Method for producing methanol, dimethyl ether, derived synthetic hydrocarbons and their products from carbon dioxide and water (moisture) of the air as sole source material*. (2008). USPTO 7,459,590.
29. Olah GA, Goeppert A, and Prakash GKS, *Chemical Recycling of Carbon Dioxide to Methanol and Dimethyl Ether: From Greenhouse Gas to Renewable, Environmentally Carbon Neutral Fuels and Synthetic Hydrocarbons*. Journal of Organic Chemistry, (2009). **74**(2): p. 478-498.
30. Jensen SH, Høgh JVT, Barfod R, and Mogensen M. *High Temperature Electrolysis of Steam and Carbon Dioxide*. in *Risø International Energy Conference*. (2003). Risø National Laboratory, Roskilde, Denmark.
31. Jensen SH and Mogensen M. *Perspectives of High Temperature Electrolysis Using SOEC*. in *19th World Energy Congress 2004*. (2004). Sydney, Australia.
32. Jensen SH, Larsen PH, and Mogensen M, *Hydrogen and synthetic fuel production from renewable energy sources*. International Journal of Hydrogen Energy, (2007). **32**(15): p. 3253-3257.
33. Ebbesen SD. *Carbon Dioxide Electrolysis for Production of Synthesis Gas in Solid Oxide Electrolysis Cells*. in *32nd International Conference & Exposition on Advanced Ceramics & Composites*. (2008). Daytona, FL, USA.
34. Hartvigsen J, Joshi AV, Elangovan S, Balagopal S, Gordon JH, and Hollist M, *Electrochemical Cell for the Production of Synthesis Gas Using Atmospheric Air and Water*. (2007). WIPO WO/2007/025280.
35. Stoots CM, O'Brien JE, Herring JS, and Hartvigsen JJ, *Syngas Production via High-Temperature Coelectrolysis of Steam and Carbon Dioxide*. Journal of Fuel Cell Science and Technology, (2009). **6**(1): p. 011014-12.
36. Zhan Z, Kobsiriphat W, Wilson JR, Pillai M, Kim I, and Barnett SA, *Syngas Production By Coelectrolysis of CO_2/H_2O: The Basis for a Renewable Energy Cycle*. Energy & Fuels, (2009). **23**(6): p. 3089-3096.
37. Ebbesen SD, Graves C, and Mogensen M, *Production of Synthetic Fuels by Co-Electrolysis of Steam and Carbon Dioxide*. International Journal of Green Energy, (2009). **6**(6): p. 646 – 660.

38. Graves C, Ebbesen SD, and Mogensen M, *Co-electrolysis of CO_2 and H_2O in solid oxide cells: Performance and durability*. Solid State Ionics. In Press, Corrected Proof, doi:10.1016/j.ssi.2010.06.014.
39. Ebbesen SD and Mogensen M, *Electrolysis of carbon dioxide in Solid Oxide Electrolysis Cells*. Journal of Power Sources, (2009). **193**(1): p. 349-358.
40. Zeman FS and Keith DW, *Carbon neutral hydrocarbons*. Philosophical Transactions of the Royal Society a-Mathematical Physical and Engineering Sciences, (2008). **366**(1882): p. 3901-3918.
41. Fritzmann C, Löwenberg J, Wintgens T, and Melin T, *State-of-the-art of reverse osmosis desalination*. Desalination, (2007). **216**(1-3): p. 1-76.
42. Thambimuthu KK, Soltanieh M, Abanades JC, Allam R, Bolland O, Davison J, et al., *Capture of CO_2*, in *IPCC Special Report on Carbon dioxide Capture and Storage*, Z. Abu-Ghararah and T. Yashima, Editors. (2005), Intergovernmental Panel on Climate Change. Working Group III. p. 105-178.
43. Shulenberger AM, Jonsson FR, Ingolfsson O, and Tran K-C, *Process for producing liquid fuel from carbon dioxide and water*. (2007). USPTO Application US 2007/0244208 A1.
44. Spector NA and Dodge BF, *Removal of Carbon Dioxide from Atmospheric Air*. Transactions of the American Institute of Chemical Engineers, (1946). **42**(5-6): p. 827-848.
45. Giner J, *Carbon Dioxide Absorber Means and Fuel Cell to Regenerate Absorbent*. (1970). USPTO 3,519,488.
46. Prigent M and Dezael C, *Process for Removing Carbon Dioxide from Gases*. (1972). USPTO 3,692,649.
47. Lackner KS, Ziock H-J, and Grimes P, *Carbon Dioxide Extraction from Air: Is it an Option?*, in *Proceedings of the 24th International Technical Conference on Coal Utilization & Fuel Systems*, B. Sakkestad, Editor. (1999): Clearwater, Florida. p. 885-896.
48. Elliott S, Lackner KS, Ziock HJ, Dubey MK, Hanson HP, Barr S, et al., *Compensation of Atmospheric CO_2 Buildup through Engineered Chemical Sinkage*. Geophys. Res. Lett., (2001). **28**(7): p. 1235-1238.
49. Zeman FS and Lackner KS, *Capturing carbon dioxide directly from the atmosphere*. World Resource Review, (2004). **16**(2): p. 157-172.
50. Baciocchi R, Storti G, and Mazzotti M, *Process design and energy requirements for the capture of carbon dioxide from air*. Chemical Engineering and Processing, (2006). **45**(12): p. 1047-1058.
51. Keith DW, Ha-Duong M, and Stolaroff J, *Climate Strategy with CO_2 Capture from the Air*. Climatic Change, (2005). **74**: p. 17-45.
52. Zeman F, *Energy and Material Balance of CO_2 Capture from Ambient Air*. Environmental Science and Technology, (2007). **41**(21): p. 7558-7563.
53. Stolaroff JK, Keith DW, and Lowry GV, *Carbon dioxide capture from atmospheric air using sodium hydroxide spray*. Environmental Science & Technology, (2008). **42**(8): p. 2728-2735.
54. Zeman F, *Experimental results for capturing CO_2 from the atmosphere*. Aiche Journal, (2008). **54**(5): p. 1396-1399.
55. Dubey MK, Ziock H, Rueff G, Elliott S, Smith WS, Lackner KS, et al., *Extraction of carbon dioxide from the atmosphere through engineered chemical sinkage*. ACS – Division of Fuel Chemistry Reprints, (2002). **47**(1): p. 81-84.
56. Georgievskii SS, Koval AI, Tumanovskii AA, and Ulybin VB, *Mathematical model of carbon dioxide synthesis by electrothermal decomposition of sodium bicarbonate*. Chemical Physics Reports, (1998). **17**(9): p. 1733-1738.
57. Olah GA, Goepert A, Meth S, and Prakash GKS, *Nano-Structure Supported Solid Regenerative Polyamine and Polyamine Polyol Absorbents for the Separation of Carbon Dioxide from Gas Mixtures Including the Air*. (2008). WIPO WO/2008/021700.
58. Kogan A, Spiegler E, and Wolfshtein M, *Direct solar thermal splitting of water and on-site separation of the products. III. Improvement of reactor efficiency by steam entrainment*. International Journal of Hydrogen Energy, (2000). **25**(8): p. 739-745.
59. Perkins C and Weimer AW, *Likely near-term solar-thermal water splitting technologies*. International Journal of Hydrogen Energy, (2004). **29**(15): p. 1587-1599.
60. Steinfeld A, *Solar thermochemical production of hydrogen - a review*. Solar Energy, (2005). **78**(5): p. 603-615.
61. Baykara SZ, *Hydrogen production by direct solar thermal decomposition of water, possibilities for improvement of process efficiency*. International Journal of Hydrogen Energy, (2004). **29**(14): p. 1451-1458.
62. Bockris JOM, Dandapani B, Cocke D, and Ghoroghchian J, *On the splitting of water*. International Journal of Hydrogen Energy, (1985). **10**(3): p. 179-201.

63. Givotov VK, Fridman AA, Krotov MF, Krasheninnikov EG, Patrushev BI, Rusanov VD, et al., *Plasmochemical methods of hydrogen production.* International Journal of Hydrogen Energy, (1981). **6**(5): p. 441-449.
64. Mori S, Yamamoto A, and Suzuki M, *Characterization of a capillary plasma reactor for carbon dioxide decomposition.* Plasma Sources Science & Technology, (2006). **15**(4): p. 609-613.
65. Yamamoto A, Mori S, and Suzuki M, *Scale-up or numbering-up of a micro plasma reactor for the carbon dioxide decomposition.* Thin Solid Films, (2007). **515**(9): p. 4296-4300.
66. Petri MC, Yıldız B, and Klickman AE, *US work on technical and economic aspects of electrolytic, thermochemical, and hybrid processes for hydrogen production at temperatures below 550°C.* Int. J. Nuclear Hydrogen Production and Application, (2006). **1**(1): p. 79-91.
67. Yildiz B and Kazimi MS, *Efficiency of hydrogen production systems using alternative nuclear energy technologies.* International Journal of Hydrogen Energy, (2006). **31**(1): p. 77-92.
68. Kodama T and Gokon N, *Thermochemical Cycles for High-Temperature Solar Hydrogen Production.* Chemical Reviews, (2007). **107**(10): p. 4048-4077.
69. Abanades S and Flamant G, *Thermochemical hydrogen production from a two-step solar-driven water-splitting cycle based on cerium oxides.* Solar Energy, (2006). **80**(12): p. 1611-1623.
70. Kodama T, Kondoh Y, Yamamoto R, Andou H, and Satou N, *Thermochemical hydrogen production by a redox system of ZrO_2-supported Co(II)-ferrite.* Solar Energy, (2005). **78**(5): p. 623-631.
71. Kaneko H, Miura T, Fuse A, Ishihara H, Taku S, Fukuzumi H, et al., *Rotary-Type Solar Reactor for Solar Hydrogen Production with Two-step Water Splitting Process.* Energy & Fuels, (2007). **21**(4): p. 2287-2293.
72. Kaneko H, Ishihara H, Taku S, Naganuma Y, Hasegawa N, and Tamaura Y, *Cerium ion redox system in CeO2– x Fe2O3 solid solution at high temperatures (1,273–1,673 K) in the two-step water-splitting reaction for solar H2 generation.* Journal of Materials Science, (2008). **43**(9): p. 3153-3161.
73. Diver RB, Miller JE, Allendorf MD, Siegel NP, and Hogan RE, *Solar Thermochemical Water-Splitting Ferrite-Cycle Heat Engines.* Journal of Solar Energy Engineering, (2008). **130**(4): p. 041001-8.
74. Abanades S, Legal A, Cordier A, Peraudeau G, Flamant G, and Julbe A, *Investigation of reactive cerium-based oxides for H2 production by thermochemical two-step water-splitting.* Journal of Materials Science, (2010). **45**(15): p. 4163-4173.
75. Chueh WC and Haile SM, *A thermochemical study of ceria: exploiting an old material for new modes of energy conversion and CO2 mitigation.* Philosophical Transactions of the Royal Society A: Mathematical, Physical and Engineering Sciences, (2010). **368**(1923): p. 3269-3294.
76. Kaneko H, Taku S, Naganuma Y, Ishihara T, Hasegawa N, and Tamaura Y, *Development of Reactive Ceramics for Conversion of Concentrated Solar Heat Into Solar Hydrogen With Two-Step Water-Splitting Reaction.* Journal of Solar Energy Engineering, (2010). **132**(2): p. 021202-4.
77. Loutzenhiser PG, Galvez ME, Hischier I, Stamatiou A, Frei A, and Steinfeld A, *CO2 Splitting via Two-Step Solar Thermochemical Cycles with Zn/ZnO and FeO/Fe3O4 Redox Reactions II: Kinetic Analysis.* Energy & Fuels, (2009). **23**: p. 2832-2839.
78. Shin HC, Oh JH, Choi BC, and Choi SC, *Design of an energy conversion system with decomposition of H_2O and CO_2 using ferrites.* physica status solidi (c), (2004). **1**(12): p. 3748-3753.
79. Chueh WC and Haile SM, *Ceria as a Thermochemical Reaction Medium for Selectively Generating Syngas or Methane from H_2O and CO_2.* ChemSusChem, (2009). **2**(8): p. 735-739.
80. Stamatiou A, Loutzenhiser PG, and Steinfeld A, *Solar Syngas Production via H2O/CO2-Splitting Thermochemical Cycles with Zn/ZnO and FeO/Fe3O4 Redox Reactions.* Chemistry of Materials, (2010). **22**(3): p. 851-859.
81. Stamatiou A, Loutzenhiser PG, and Steinfeld A, *Solar Syngas Production from H2O and CO2 via Two-Step Thermochemical Cycles Based on Zn/ZnO and FeO/Fe3O4 Redox Reactions: Kinetic Analysis.* Energy & Fuels, (2010).
82. Singh P and Hegde MS, *Ce0.67Cr0.33O2.11: A New Low-Temperature O2 Evolution Material and H2 Generation Catalyst by Thermochemical Splitting of Water.* Chemistry of Materials, (2009). **22**(3): p. 762-768.
83. Ehrensberger K, Palumbo R, Larson C, and Steinfeld A, *Production of carbon from carbon dioxide with iron oxides and high-temperature solar energy.* Industrial & Engineering Chemistry Research, (1997). **36**(3): p. 645-648.

84. Zhang CL, Li S, Wang LJ, Wu TH, and Peng SY, *Studies on the decomposition of carbon dioxide into carbon with oxygen-deficient magnetite I. Preparation, characterization of magnetite, and its activity of decomposing carbon dioxide.* Materials Chemistry and Physics, (2000). **62**(1): p. 44-51.
85. Zhang CL, Li S, Wang LJ, Wu TH, and Peng SY, *Studies on the decomposing carbon dioxide into carbon with oxygen-deficient magnetite II. The effects of properties of magnetite on activity of decomposition CO_2 and mechanism of the reaction.* Materials Chemistry and Physics, (2000). **62**(1): p. 52-61.
86. Charvin P, Abanades S, Lemort F, and Flamant G, *Hydrogen Production by Three-Step Solar Thermochemical Cycles Using Hydroxides and Metal Oxide Systems.* Energy & Fuels, (2007). **21**(5): p. 2919-2928.
87. Abanades S, Charvin P, Flamant G, and Neveu P, *Screening of water-splitting thermochemical cycles potentially attractive for hydrogen production by concentrated solar energy.* Energy, (2006). **31**(14): p. 2805-2822.
88. Fletcher EA and Moen RL, *Hydrogen and Oxygen from Water.* Science, (1977). **197**(4308): p. 1050-1056.
89. Graf D, Monnerie N, Roeb M, Schmitz M, and Sattler C, *Economic comparison of solar hydrogen generation by means of thermochemical cycles and electrolysis.* International Journal of Hydrogen Energy, (2008). **33**(17): p. 4511-4519.
90. Bailleux C, Damien A, and Montet A, *Alkaline electrolysis of water-EGF activity in electrochemical engineering from 1975 to 1982.* International Journal of Hydrogen Energy, (1983). **8**(7): p. 529-538.
91. Abe I, Fujimaki T, and Matsubara M, *Hydrogen production by high temperature, high pressure water electrolysis, results of test plant operation.* International Journal of Hydrogen Energy, (1984). **9**(9): p. 753-758.
92. Janjua MBI and Leroy RL, *Electrocatalyst performance in industrial water electrolysers.* International Journal of Hydrogen Energy, (1985). **10**(1): p. 11-19.
93. Divisek J, Malinowski P, Mergel J, and Schmitz H, *Improved construction of an electrolytic cell for advanced alkaline water electrolysis.* International Journal of Hydrogen Energy, (1985). **10**(6): p. 383-388.
94. Divisek J, Malinowski P, Mergel J, and Schmitz H, *Improved components for advanced alkaline water electrolysis.* International Journal of Hydrogen Energy, (1988). **13**(3): p. 141-150.
95. Ivy J, *Summary of Electrolytic Hydrogen Production: Milestone Completion Report.* (2004), National Renewable Energy Laboratory: Golden, Colorado. MP-560-35948. 28.
96. Oi T and Wada K, *Feasibility study on hydrogen refueling infrastructure for fuel cell vehicles using the off-peak power in Japan.* International Journal of Hydrogen Energy, (2004). **29**(4): p. 347-354.
97. Gutiérrez-Martín F, García-De María JM, Baïri A, and Laraqi N, *Management strategies for surplus electricity loads using electrolytic hydrogen.* International Journal of Hydrogen Energy, (2009). **34**(20): p. 8468-8475.
98. Holladay JD, Hu J, King DL, and Wang Y, *An overview of hydrogen production technologies.* Catalysis Today, (2009). **139**(4): p. 244-260.
99. Isenberg AO, *Energy-Conversion Via Solid Oxide Electrolyte Electrochemical-Cells at High-Temperatures.* Solid State Ionics, (1981). **3-4**(AUG): p. 431-437.
100. Hauch A, Ebbesen SD, Jensen SH, and Mogensen M, *Highly efficient high temperature electrolysis.* Journal of Materials Chemistry, (2008). **18**(20): p. 2331-2340.
101. Cable TL, Setlock JA, Farmer SC, and Eckel AJ, *Regenerative Performance of the NASA Symmetrical Solid Oxide Fuel Cell Design.* International Journal of Applied Ceramic Technology, In Press.
102. Gandía LM, Oroz R, Ursúa A, Sanchis P, and Diéguez PM, *Renewable Hydrogen Production: Performance of an Alkaline Water Electrolyzer Working under Emulated Wind Conditions.* Energy & Fuels, (2007). **21**(3): p. 1699-1706.
103. Swalla DR, *Feasibility Study of Hydrogen Production from Existing Nuclear Power Plants Using Alkaline Electrolysis - Final Technical Report October 1, 2006 – October 30, 2008*. (2008). DOE/ID/14789.
104. Jensen JO, Bandur V, Bjerrum NJ, Højgaard Jensen S, Ebbesen SD, Mogensen M, et al., *Pre-investigation of water electrolysis.* (2008), available at http://130.226.56.153/rispubl/NEI/NEI-DK-5057.pdf. 195.
105. Bacon FT, *Fuel cells, past, present and future.* Electrochimica Acta, (1969). **14**(7): p. 569-585.
106. Levene JI, Mann MK, Margolis RM, and Milbrandt A, *An analysis of hydrogen production from renewable electricity sources.* Solar Energy, (2007). **81**(6): p. 773-780.
107. Divisek J, Mergel J, and Niessen HF, *Production of hydrogen by the electrolytic decomposition of water in fused sodium hydroxide.* International Journal of Hydrogen Energy, (1980). **5**(2): p. 151-164.
108. Bailleux C, *Advanced water alkaline electrolysis: a two-year running of a test plant.* International Journal of Hydrogen Energy, (1981). **6**(5): p. 461-471.
109. Divisek J, Mergel J, and Schmitz H, *Improvements of water electrolysis in alkaline media at intermediate temperatures.* International Journal of Hydrogen Energy, (1982). **7**(9): p. 695-701.

110. Ganley JC, *High temperature and pressure alkaline electrolysis.* International Journal of Hydrogen Energy, (2009). **34**(9): p. 3604-3611.
111. Hashimoto K, Yamasaki M, Meguro S, Sasaki T, Katagiri H, Izumiya K, et al., *Materials for global carbon dioxide recycling.* Corrosion Science, (2002). **44**(2): p. 371-386.
112. Balej J, *Electrocatalysts for oxygen evolution in advanced water electrolysis.* International Journal of Hydrogen Energy, (1985). **10**(2): p. 89-99.
113. Shervedani RK and Madram AR, *Electrocatalytic activities of nanocomposite Ni81P16C3 electrode for hydrogen evolution reaction in alkaline solution by electrochemical impedance spectroscopy.* International Journal of Hydrogen Energy, (2008). **33**(10): p. 2468-2476.
114. Schiller G, Henne R, Mohr P, and Peinecke V, *High performance electrodes for an advanced intermittently operated 10-kW alkaline water electrolyzer.* International Journal of Hydrogen Energy, (1998). **23**(9): p. 761-765.
115. Hori Y, Kikuchi K, and Suzuki S, *Production of carbon monoxide and methane in electrochemical reduction of carbon dioxide at metal electrodes in aqueous hydrogen carbonate solution.* Chemistry Letters, (1985)(11): p. 1695-8.
116. Noda H, Ikeda S, Oda Y, and Imai K, *Electrochemical Reduction of Carbon Dioxide at Various Metal Electrodes in Aqueous Potassium Hydrogen Carbonate Solution.* Bulletin of the Chemical Society of Japan, (1990)(63): p. 2459-2462.
117. Halmann MM and Steinberg M, *Chapter 12: Electrochemical Reduction of CO_2*, in *Greenhouse Gas Carbon Dioxide Mitigation Science and Technology*. (1999), Lewis Publishers: Boca Raton, Florida. p. 411-488.
118. Olah GA and Prakash GKS, *Recycling of carbon dioxide into methyl alcohol and related oxygenates for hydrocarbons*. (1999). USPTO 5,928,806.
119. Chaplin RPS and Wragg AA, *Effects of process conditions and electrode material on reaction pathways for carbon dioxide electroreduction with particular reference to formate formation.* Journal of Applied Electrochemistry, (2003). **33**(12): p. 1107-1123.
120. Aulice Scibioh M and Viswanathan B, *Electrochemical reduction of carbon dioxide: a status report.* PINSA-A (Proceedings of the Indian National Science Academy) Part A (Physical Sciences), (2004). **70**(3): p. 407-62.
121. Gattrell M, Gupta N, and Co A, *Electrochemical reduction of CO_2 to hydrocarbons to store renewable electrical energy and upgrade biogas.* Energy Conversion and Management, (2007). **48**(4): p. 1255-1265.
122. Centi G, Perathoner S, Wine G, and Gangeri M, *Electrocatalytic conversion of CO_2 to long carbon-chain hydrocarbons.* Green Chemistry, (2007). **9**(6): p. 671-678.
123. Perathoner S, Gangeri M, Lanzafame P, and Centi G, *Nanostructured electrocatalytic Pt-carbon materials for fuel cells and CO_2 conversion.* Kinetics and Catalysis, (2007). **48**(6): p. 877-883.
124. Hori Y, Konishi H, Futamura T, Murata A, Koga O, Sakurai H, et al., *"Deactivation of copper electrode" in electrochemical reduction of CO_2.* Electrochimica Acta, (2005). **50**(27): p. 5354-5369.
125. Lee J and Tak Y, *Electrocatalytic activity of Cu electrode in electroreduction of CO_2.* Electrochimica Acta, (2001). **46**(19): p. 3015-3022.
126. Yano H, Shirai F, Nakayama M, and Ogura K, *Electrochemical reduction of CO_2 at three-phase (gas | liquid | solid) and two-phase (liquid | solid) interfaces on Ag electrodes.* Journal of Electroanalytical Chemistry, (2002). **533**(1-2): p. 113-118.
127. Kyriacou G and Anagnostopoulos A, *Electrochemical reduction of carbon dioxide at copper + gold electrodes.* Journal of Electroanalytical Chemistry, (1992). **328**(1-2): p. 233-43.
128. Ishimaru S, Shiratsuchi R, and Nogami G, *Pulsed electroreduction of CO_2 on Cu-Ag alloy electrodes.* Journal of the Electrochemical Society, (2000). **147**(5): p. 1864-1867.
129. Shiratsuchi R, Aikoh Y, and Nogami G, *Pulsed electroreduction of CO_2 on copper electrodes.* Journal of the Electrochemical Society, (1993). **140**(12): p. 3479-3482.
130. Shiratsuchi R and Nogami G, *Pulsed electroreduction of CO_2 on silver electrodes.* Journal of the Electrochemical Society, (1996). **143**(2): p. 582-586.
131. Jermann B and Augustynski J, *Long-term activation of the copper cathode in the course of CO_2 reduction.* Electrochimica Acta, (1994). **39**(11-12): p. 1891-1896.
132. Benson EE, Kubiak CP, Sathrum AJ, and Smieja JM, *Electrocatalytic and homogeneous approaches to conversion of CO_2 to liquid fuels.* Chemical Society Reviews, (2009). **38**(1): p. 89-99.
133. Hori Y, Ito H, Okano K, Nagasu K, and Sato S, *Silver-coated ion exchange membrane electrode applied to electrochemical reduction of carbon dioxide.* Electrochimica Acta, (2003). **48**(18): p. 2651-2657.

134. Hori Y and Suzuki S, *Electrolytic reduction of bicarbonate ion at a mercury electrode*. Journal of the Electrochemical Society, (1983). **130**(12): p. 2387-90.
135. Li H and Oloman C, *Development of a continuous reactor for the electro-reduction of carbon dioxide to formate – Part 2: Scale-up*. Journal of Applied Electrochemistry, (2007). **37**(10): p. 1107-1117.
136. Yamaguchi M, Shinohara T, Taniguchi H, Nakanori T, and Okisawa K. *Development of 2500 cm2 solid polymer electrolyte water electrolyzer in We-Net*. in *Proceedings of the 12th World Hydrogen Energy Conference*. (1998). Buenos Aires, Argentina: International Association for Hydrogen Energy.
137. Kanan MW and Nocera DG, *In Situ Formation of an Oxygen-Evolving Catalyst in Neutral Water Containing Phosphate and Co2+*. Science, (2008). **321**(5892): p. 1072-1075.
138. Dinca M, Surendranath Y, and Nocera DG, *Nickel-borate oxygen-evolving catalyst that functions under benign conditions*. Proceedings of the National Academy of Sciences of the United States of America, (2010). **107**(23): p. 10337-10341.
139. Zhao G, Jiang T, Han B, Li Z, Zhang J, Liu Z, et al., *Electrochemical reduction of supercritical carbon dioxide in ionic liquid 1-n-butyl-3-methylimidazolium hexafluorophosphate*. The Journal of Supercritical Fluids, (2004). **32**(1-3): p. 287-291.
140. Lueck DE. *Space Habitat Carbon Dioxide Electrolysis to Oxygen*. NASA Kennedy Space Center Research and Technology 2002 Report, Fluid System Technologies (2002); Available from: http://rtreport.ksc.nasa.gov/techreports/2002report/600%20Fluid%20Systems/609.html.
141. Kaplan V, Wachtel E, Gartsman K, Feldman Y, and Lubomirsky I, *Conversion of CO_2 to CO by Electrolysis of Molten Lithium Carbonate*. Journal of the Electrochemical Society, (2010). **157**(4): p. B552-B556.
142. Weissbart J and Smart WH, *Study of Electrolytic Dissociation of CO_2-H_2O Using a Solid Oxide Electrolyte*. (1967), National Aeronautics and Space Administration: United States. 97.
143. Oser W, *Electrochemical method for conversion of carbon dioxide*. (1967). USPTO 3,316,163.
144. Spacil HS and Tedmon JCS, *Electrochemical Dissociation of Water Vapor in Solid Oxide Electrolyte Cells*. Journal of the Electrochemical Society, (1969). **116**(12): p. 1618-1626.
145. Elikan L and Morris JP, *Solid Electrolyte System for Oxygen Regeneration*. (1969), Westinghouse Electric Corp., for National Aeronautics and Space Administration, Langley Research Center: Washington, D.C. CR-1359. 181.
146. Weissbart J, Smart WH, Inami SH, McCullough CM, and Ring SA, *Development of a CO_2-H_2O Solid Oxide Electrolysis System: First Annual Report, 29 Mar. 1968 - 29 May 1969*. (1969), National Aeronautics and Space Administration, Ames Research Center: Moffett Field, California. CR 73358. 65.
147. Elikan L, Morris JP, and Wu CK, *Development of a solid electrolyte carbon dioxide and water reduction system for oxygen recovery*. (1972), Westinghouse Electric Corp., for National Aeronautics and Space Administration, Langley Research Center: Washington, D.C. CR-2014. 181.
148. Isenberg AO and Verostko CE, *Carbon Dioxide Electrolysis With Solid Oxide Electrolyte Cells for Oxygen Recovery in Life Support Systems*. (1988), NASA Research Center SAE Technical Paper 881040.
149. Sridhar KR and Vaniman BT, *Oxygen production on Mars using solid oxide electrolysis*. Solid State Ionics, (1997). **93**(3-4): p. 321-8.
150. Sridhar KR and Iacomini CS, *Combined H_2O/CO_2 Solid Oxide Electrolysis for Mars In Situ Resource Utilization*. Journal of Propulsion and Power, (2004). **20**(5): p. 892-901.
151. Guan J, Doshi R, Lear G, Montgomery K, Ong E, and Minh N, *Ceramic oxygen generators with thin-film zirconia electrolytes*. Journal of the American Ceramic Society, (2002). **85**(11): p. 2651-2654.
152. Tao G, Sridhar KR, and Chan CL, *Study of carbon dioxide electrolysis at electrode/electrolyte interface: Part II. Pt-YSZ cermet/YSZ interface*. Solid State Ionics, (2004). **175**: p. 621-624.
153. Park JY and Wachsman ED, *Lower temperature electrolytic reduction of CO_2 to O_2 and CO with high-conductivity solid oxide bilayer electrolytes*. Journal of the Electrochemical Society, (2005). **152**(8): p. A1654-A1659.
154. Dönitz W, Schmidberger R, Steinheil E, and Streicher R, *Hydrogen production by high temperature electrolysis of water vapour*. International Journal of Hydrogen Energy, (1980). **5**(1): p. 55-63.
155. Ni M, Leung MKH, and Leung DYC, *Technological development of hydrogen production by solid oxide electrolyzer cell (SOEC)*. International Journal of Hydrogen Energy, (2008). **33**(9): p. 2337-2354.
156. Fergus JW, *Electrolytes for solid oxide fuel cells*. Journal of Power Sources, (2006). **162**(1): p. 30-40.
157. Goodenough JB and Huang YH, *Alternative anode materials for solid oxide fuel cells*. Journal of Power Sources, (2007). **173**(1): p. 1-10.

158. Tsipis E and Kharton V, *Electrode materials and reaction mechanisms in solid oxide fuel cells: a brief review, II. Electrochemical behavior vs. materials science aspects.* Journal of Solid State Electrochemistry, (2008). **12**(11): p. 1367-1391.
159. Irvine JTS, *Perovskite Oxide Anodes for SOFCs*, in *Perovskite Oxide for Solid Oxide Fuel Cells*, T. Ishihara, Editor. (2009). p. 167-182.
160. Olmer LJ, Viguie JC, and Schouler EJL, *An increase in the water vapor reduction rate by using an yttria-stabilized zirconia electrolyte with ceria-doped surface.* Solid State Ionics, (1982). **7**(1): p. 23-35.
161. Dönitz W and Erdle E, *High-temperature electrolysis of water vapor--status of development and perspectives for application.* International Journal of Hydrogen Energy, (1985). **10**(5): p. 291-295.
162. Maskalick NJ, *High temperature electrolysis cell performance characterization.* International Journal of Hydrogen Energy, (1986). **11**(9): p. 563-570.
163. Dönitz W, *High Temperature Electrolysis of Water Vapour*, in *Electrochemical Hydrogen Technologies: Electrochemical Production and Combustion of Hydrogen*, H. Wendt, Editor. (1990), Elsevier.
164. Perfiliev MV, *Problems of high-temperature electrolysis of water vapour.* International Journal of Hydrogen Energy, (1994). **19**(3): p. 227-230.
165. Eguchi K, Hatagishi T, and Arai H, *Power generation and steam electrolysis characteristics of an electrochemical cell with a zirconia- or ceria-based electrolyte.* Solid State Ionics, (1996). **86-8**: p. 1245-1249.
166. Hino R, Haga K, Aita H, and Sekita K, *R & D on hydrogen production by high-temperature electrolysis of steam.* Nuclear Engineering and Design, (2004). **233**(1-3): p. 363-375.
167. Uchida H, Osada N, and Watanabe M, *High-performance electrode for steam electrolysis: Mixed conducting ceria-based cathode with highly-dispersed Ni electrocatalysts.* Electrochemical and Solid State Letters, (2004). **7**(12): p. A500-A502.
168. Hauch A, Jensen SH, Ramousse S, and Mogensen M, *Performance and durability of solid oxide electrolysis cells.* Journal of the Electrochemical Society, (2006). **153**(9): p. 1741-1747.
169. O'Brien JE, Stoots CM, Herring JS, and Hartvigsen J, *Hydrogen production performance of a 10-cell planar solid-oxide electrolysis stack.* Journal of Fuel Cell Science and Technology, (2006). **3**(2): p. 213-219.
170. Elangovan S, Hartvigsen JJ, and Frost LJ, *Intermediate temperature reversible fuel cells.* International Journal of Applied Ceramic Technology, (2007). **4**(2): p. 109-118.
171. Herring JS, O'Brien JE, Stoots CM, Hawkes GL, Hartvigsen JJ, and Shahnam M, *Progress in high-temperature electrolysis for hydrogen production using planar SOFC technology.* International Journal of Hydrogen Energy, (2007). **32**(4): p. 440-450.
172. Marina OA, Pederson LR, Williams MC, Coffey GW, Meinhardt KD, Nguyen CD, et al., *Electrode performance in reversible solid oxide fuel cells.* Journal of the Electrochemical Society, (2007). **154**(5): p. B452-B459.
173. Yang X and Irvine JTS, *$(La_{0.75}Sr_{0.25})_{0.95}Mn_{0.5}Cr_{0.5}O_3$ as the cathode of solid oxide electrolysis cells for high temperature hydrogen production from steam.* Journal of Materials Chemistry, (2008). **18**(20): p. 2349-2354.
174. Elangovan S and Hartvigsen J, *Efficient Reversible Electrodes for Solid Oxide Electrolyzer Cells*. (2008). WIPO WO/2008/013783.
175. Hauch A, Ebbesen SD, Jensen SH, and Mogensen M, *Solid Oxide Electrolysis Cells: Microstructure and Degradation of the Ni/YSZ Electrode.* Journal of the Electrochemical Society, (2008). **11**(155): p. B1184-B1193.
176. Hartvigsen J, Elangovan S, O'Brien JE, Stoots CM, Herring JS, and Lessing P. in *6th European Solid Oxide Fuel Cell Forum*. (2004). Lucerne: European Fuel Cell Forum.
177. O'Brien JE, Stoots CM, Herring JS, and Hartvigsen JJ. *Performance of planar high-temperature electrolysis stacks for hydrogen production from nuclear energy*. (2007).
178. Stoots CM, O'Brien JE, Condie K, Moore-Mcateer L, Housley G, Hartvigsen JJ, et al., *The High-temperature Electrolysis Integrated Laboratory-scale Experiment.* Nuclear Technology, (2009). **166**(1): p. 32-42.
179. Jensen SH, Hauch A, Hendriksen PV, and Mogensen M, *Advanced Test Method of Solid Oxide Cells in a Plug-Flow Setup.* Journal of the Electrochemical Society, (2009). **156**(6): p. B757-B764.
180. Schiller G, Ansar A, Lang M, and Patz O, *High temperature water electrolysis using metal supported solid oxide electrolyser cells (SOEC).* Journal of Applied Electrochemistry, (2009). **39**(2): p. 293-301.
181. Isenberg AO and Verostko CE, *Carbon Dioxide and Water Vapor High Temperature Electrolysis*. (1989), NASA Research Center. SAE Technical Paper 891506.

182. Bidrawn F, Kim G, Corre G, Irvine JTS, Vohs JM, and Gorte RJ, *Efficient reduction of CO_2 in a solid oxide electrolyzer*. Electrochemical and Solid State Letters, (2008). **11**(9): p. B167-B170.
183. Green RD, Liu CC, and Adler SB, *Carbon dioxide reduction on gadolinia-doped ceria cathodes*. Solid State Ionics, (2008). **179**(17-18): p. 647-660.
184. Gottmann M, McElroy JF, Mitlitsky F, and Sridhar KR, *SORFC power and oxygen generation method and system*. (2006). USPTO 7,045,238 B2.
185. O'Brien JE, Stoots CM, Herring JS, and Hartvigsen JJ, *High-Temperature Co-electrolysis of Carbon Dioxide and Steam for the Production of Syngas; Equilibrium Model and Single-Cell Tests*, in *International Topical Meeting on the Safety and Technology of Nuclear Hydrogen*. (2007).
186. Stoots CM, O'Brien JE, and Hartvigsen JJ. *Syngas Production Via High-Temperature Co-electrolysis of Steam and Carbon Dioxide in a Solid-Oxide Stack*. in *Fuel Cell Science, Engineering & Technology Conference*. (2007).
187. Arashi H, Naito H, and Miura H, *Hydrogen-Production from High-Temperature Steam Electrolysis Using Solar-Energy*. International Journal of Hydrogen Energy, (1991). **16**(9): p. 603-608.
188. Licht S, *Efficient solar generation of hydrogen fuel - a fundamental analysis*. Electrochemistry Communications, (2002). **4**(10): p. 790-795.
189. Licht S, *STEP (Solar Thermal Electrochemical Photo) Generation of Energetic Molecules: A Solar Chemical Process to End Anthropogenic Global Warming*. The Journal of Physical Chemistry C, (2009).
190. Shin Y, Park W, Chang J, and Park J, *Evaluation of the high temperature electrolysis of steam to produce hydrogen*. International Journal of Hydrogen Energy, (2007). **32**(10-11): p. 1486-1491.
191. Laurencin J, Delette G, Sicardy O, Rosini S, and Lefebvre-Joud F, *Impact of 'redox' cycles on performances of solid oxide fuel cells: Case of the electrolyte supported cells*. Journal of Power Sources, (2010). **195**(9): p. 2747-2753.
192. Iwanschitz B, Sfeir J, Mai A, and Schutze M, *Degradation of SOFC Anodes upon Redox Cycling: A Comparison Between Ni/YSZ and Ni/CGO*. Journal of the Electrochemical Society. **157**(2): p. B269-B278.
193. Ihringer R, *2R-Cell™: Reliability of Anode Supported Thin Electrolyte Upon Multi Thermo and Redox Cycles*. ECS Transactions, (2009). **25**(2): p. 473-483.
194. Pihlatie M, Ramos T, and Kaiser A, *Testing and improving the redox stability of Ni-based solid oxide fuel cells*. Journal of Power Sources, (2009). **193**(1): p. 322-330.
195. Pihlatie M, Kaiser A, Larsen PH, and Mogensen M, *Dimensional Behavior of Ni--YSZ Composites during Redox Cycling*. Journal of the Electrochemical Society, (2009). **156**(3): p. B322-B329.
196. Blennow P, *Strontium Titanate-based Anodes for Solid Oxide Fuel Cells*, Ph.D. thesis. (2007), Lund University. p. 209.
197. Blennow P, Hansen KK, Wallenberg LR, and Mogensen M, *Strontium Titanate-based Composite Anodes for Solid Oxide Fuel Cells*. ECS Transactions, (2008). **13**(26): p. 181-194.
198. Ouweltjes JP, Tuel Mv, Sillessen M, and Rietveld G, *Redox Tolerant SOFC Anodes with High Electrochemical Performance*. Fuel Cells, (2009). **9**(6): p. 873-882.
199. Saur G, *Wind-To-Hydrogen Project: Electrolyzer Capital Cost Study*. (2008), National Renewable Energy Laboratory: Golden, Colorado. Technical Report NREL/TP-550-4410.
200. Thijssen JHJS. *The Impact of Scale-Up and Production Volume on SOFC Stack Cost*. in *7th Annual SECA Workshop and Peer Review*. (2006).
201. Thijssen J. *SOFC Stack Operating Strategies*. in *10th Annual Solid State Energy Conversion Alliance (SECA) Workshop*. (2009). Pittsburgh, PA: NETL.
202. Turner J, Sverdrup G, Mann MK, Maness P-C, Kroposki B, Ghirardi M, et al., *Renewable hydrogen production*. International Journal of Energy Research, (2008). **32**(5): p. 379-407.
203. Hashimoto K, Irie H, and Fujishima A, *TiO_2 photocatalysis: A historical overview and future prospects*. Japanese Journal of Applied Physics, (2005). **44**(12): p. 8269-8285.
204. Desai DK, *The Artificial Photosynthesis System: An Engineering Approach*, in *Artificial Photosynthesis: From Basic Biology to Industrial Application*, A.F. Collings and C. Critchley, Editors. (2005), Wiley-VCH Verlag GmbH & Co. KGaA: Weinheim, Germany. p. 291-299.
205. Khaselev O and Turner JA, *A Monolithic Photovoltaic-Photoelectrochemical Device for Hydrogen Production via Water Splitting*. Science, (1998). **280**(5362): p. 425-427.
206. Licht S, Wang B, Mukerji S, Soga T, Umeno M, and Tributsch H, *Efficient solar water splitting, exemplified by RuO_2-catalyzed AlGaAs/Si photoelectrolysis*. Journal of Physical Chemistry B, (2000). **104**(38): p. 8920-8924.

207. Nozik AJ, *Photoelectrochemical Cells*. Philosophical Transactions of the Royal Society of London. Series A, Mathematical and Physical Sciences, (1980). **295**(1414): p. 453-470.
208. Halmann MM and Steinberg M, *Greenhouse Gas Carbon Dioxide Mitigation Science and Technology*. (1999), Boca Raton, Florida: Lewis Publishers.
209. Lehn J-M and Ziessel R, *Photochemical generation of carbon monoxide and hydrogen by reduction of carbon dioxide and water under visible light irradiation*. Proceedings of the National Academy of Sciences of the United States of America, (1982). **79**(2): p. 701-704.
210. Tseng IH, Chang WC, and Wu JCS, *Photoreduction of CO_2 using sol-gel derived titania and titania-supported copper catalysts*. Applied Catalysis B-Environmental, (2002). **37**(1): p. 37-48.
211. Koci K, Obalova L, and Lacny Z, *Photocatalytic reduction of CO_2 over TiO_2 based catalysts*. Chemical Papers, (2008). **62**(1): p. 1-9.
212. Varghese OK, Paulose M, LaTempa TJ, and Grimes CA, *High-Rate Solar Photocatalytic Conversion of CO_2 and Water Vapor to Hydrocarbon Fuels*. Nano Letters, (2009). **9**(2): p. 731-737.
213. Kaneco S, Katsumata H, Suzuki T, and Ohta K, *Photoelectrocatalytic reduction of CO_2 in LiOH/methanol at metal-modified p-InP electrodes*. Applied Catalysis B-Environmental, (2006). **64**(1-2): p. 139-145.
214. Conibeer GJ and Richards BS, *A comparison of PV/electrolyser and photoelectrolytic technologies for use in solar to hydrogen energy storage systems*. International Journal of Hydrogen Energy, (2007). **32**(14): p. 2703-2711.
215. Dry ME, *The Fischer-Tropsch process: 1950-2000*. Catalysis Today, (2002). **71**: p. 227-241.
216. Pruchnik FP, *Organometallic chemistry of the transition elements*, J. John P. Fackler, Editor. (1990), Plenum Press: New York.
217. Zhang YP, Fei JH, Yu YM, and Zheng XM, *Methanol synthesis from CO_2 hydrogenation over Cu based catalyst supported on zirconia modified gamma-Al_2O_3*. Energy Conversion and Management, (2006). **47**(18-19): p. 3360-3367.
218. Gallucci F, Paturzo L, and Basile A, *An experimental study of CO_2 hydrogenation into methanol involving a zeolite membrane reactor*. Chemical Engineering and Processing, (2004). **43**(8): p. 1029-1036.
219. Nakatsuji H and Hu ZM, *Mechanism of methanol synthesis on Cu(100) and Zn/Cu(100) surfaces: Comparative dipped adcluster model study*. International Journal of Quantum Chemistry, (2000). **77**(1): p. 341-349.
220. Kastens ML, Dudley JF, and Troeltzsch J, *Synthetic Methanol Production*. Industrial & Engineering Chemistry, (1948). **40**(12): p. 2230-2240.
221. Chen C-S, Cheng W-H, and Lin S-S, *Study of iron-promoted Cu/SiO_2 catalyst on high temperature reverse water gas shift reaction*. Applied Catalysis A: General, (2004). **257**(1): p. 97-106.
222. Nagai M and Kurakami T, *Reverse water gas shift reaction over molybdenum carbide*. Journal of Chemical Engineering of Japan, (2005). **38**(10): p. 807-812.
223. Joo OS, Jung KD, Moon I, Rozovskii AY, Lin GI, Han SH, et al., *Carbon dioxide hydrogenation to form methanol via a reverse-water-gas-shift reaction (the CAMERE process)*. Industrial & Engineering Chemistry Research, (1999). **38**(5): p. 1808-1812.
224. Inui T, *Highly effective conversion of carbon dioxide to valuable compounds on composite catalysts*. Catalysis Today, (1996). **29**(1-4): p. 329-337.
225. Kieffer R, Fujiwara M, Udron L, and Souma Y, *Hydrogenation of CO and CO_2 toward methanol, alcohols and hydrocarbons on promoted copper rare earth oxides catalysts*. Catalysis Today, (1997). **36**(1): p. 15-24.
226. Tan YS, Fujiwara M, Ando H, Xu Q, and Souma Y, *Syntheses of isobutane and branched higher hydrocarbons from carbon dioxide and hydrogen over composite catalysts*. Industrial & Engineering Chemistry Research, (1999). **38**(9): p. 3225-3229.
227. Kim JS, Lee S, Lee SB, Choi MJ, and Lee KW. *Performance of catalytic reactors for the hydrogenation of CO_2 to hydrocarbons*. (2006): Elsevier Science Bv.
228. Centi G and Perathoner S, *Opportunities and prospects in the chemical recycling of carbon dioxide to fuels*. Catalysis Today, (2009). **148**(3-4): p. 191-205.
229. Takahashi H, Liu LH, Yashiro Y, Ioku K, Bignall G, Yamasaki N, et al., *CO_2 reduction using hydrothermal method for the selective formation of organic compounds*. Journal of Materials Science, (2006). **41**(5): p. 1585-1589.
230. Dry ME, *Fischer–Tropsch Synthesis – Industrial*, in *Encyclopedia of Catalysis*. (2002).
231. Mogensen M, Jensen SH, Hauch A, Chorkendorff I, and Jacobsen T. *Performance of Reversible Solid Oxide Cells: A Review*. in *Proceedings of the 7th European Solid Oxide Fuel Cell Forum*. (2006). Lucerne (CH): European Fuel Cell Forum, Oberrohrdorf, 2006.

232. Atkinson A and Sun B, *Residual stress and thermal cycling of planar solid oxide fuel cells.* Materials Science and Technology, (2007). **23**(10): p. 1135-1143.
233. Michel S, *Methanol production costs, reports on science and technology 61/1999*. (1999), Linde: Munich, Germany.
234. Specht M, Staiss F, Bandi A, and Weimer T, *Comparison of the renewable transportation fuels, liquid hydrogen and methanol, with gasoline-energetic and economic aspects.* International Journal of Hydrogen Energy, (1998). **23**(5): p. 387-396.
235. Williams MC, Strakey J, and Sudoval W, *U.S. DOE fossil energy fuel cells program.* Journal of Power Sources, (2006). **159**(2): p. 1241-1247.
236. Jaramillo P, Griffin WM, and Matthews HS, *Comparative Analysis of the Production Costs and Life-Cycle GHG Emissions of FT Liquid Fuels from Coal and Natural Gas.* Environmental Science & Technology, (2008). **42**(20): p. 7559-7565.
237. Chedid R, Kobrosly M, and Ghajar R, *The potential of gas-to-liquid technology in the energy market: The case of Qatar.* Energy Policy, (2007). **35**(10): p. 4799-4811.
238. Sigurvinsson J and Werkoff F. *On the cost of the hydrogen produced by alkaline electrolysis*. in *International Hydrogen Energy Congress and Exhibition IHEC 2005* (2005). Istanbul, Turkey.
239. Yang C and Ogden J, *Determining the lowest-cost hydrogen delivery mode.* International Journal of Hydrogen Energy, (2007). **32**(2): p. 268-286.
240. *IEA Energy Technology Essentials: Hydrogen Production & Distribution*. (April 2007). ETE 05.
241. van der Zwaan B and Rabl A, *The learning potential of photovoltaics: implications for energy policy.* Energy Policy, (2004). **32**(13): p. 1545-1554.
242. *Energy Prices and Taxes, Volume 2009 Issue 4: Fourth Quarter 2009*, International Energy Agency: Paris, France.

Chapter 4

4. Co-electrolysis of CO_2 and H_2O in Solid Oxide Cells

This chapter[i] examines the initial performance and durability of a solid oxide cell applied for co-electrolysis of CO_2 and H_2O. Such a cell, when powered by renewable/nuclear energy, could be used to recycle CO_2 into sustainable hydrocarbon fuels, as discussed in **Chapter 3**. High initial performance for co-electrolysis was observed, higher than that for CO_2 electrolysis and lower than that for H_2O electrolysis. The internal resistance of the cell for co-electrolysis was closer to that of H_2O electrolysis, which indicated that the reverse water gas shift reaction played a role in the negative-electrode. Polarization curves and electrochemical impedance spectroscopy are employed to break down the cell resistance. Polarization curves and electrochemical impedance spectroscopy were employed to characterize the initial performance and to break down the cell resistance into the resistance for the specific processes occurring during operation. Transformation of the impedance data to the distribution of relaxation times (DRT) and comparison of measurements taken under systematically varied test conditions enabled clear visual identification of five electrode processes that contribute to the cell resistance. The processes could be assigned to each electrode and to gas concentration effects by examining their dependence on gas composition changes and temperature.

This study also introduces the use of the DRT to study cell degradation without relying on a model. The durability was tested at consecutively higher current densities (and corresponding overpotentials) for 200-400 hours at each segment. By analyzing the impedance spectra before and after each segment, it was found that at low current density operation (–0.25 A/cm^2 segment) degradation at the Ni/YSZ electrode was dominant, whereas at higher current densities (–0.5 A/cm^2 and –1.0 A/cm^2), the Ni/YSZ electrode continued to degrade but the serial resistance and degradation at the LSM/YSZ electrode began to also play a major role in the total loss in cell performance. This suggests different degradation mechanisms for high and low current density operation.

[i] This chapter has been published in modified form as: Graves C, Ebbesen S D, and Mogensen M, *Co-electrolysis of CO_2 and H_2O in solid oxide cells: Performance and durability*. Solid State Ionics, 2010. doi:10.1016/j.ssi.2010.06.014.

4.1. Introduction

As discussed in **Chapter 3**, CO_2 and H_2O can be recycled into sustainable hydrocarbon fuels with renewable/nuclear energy in a non-biological process, and a promising means to produce such fuels is by high temperature electrolysis of CO_2 and/or H_2O in solid oxide cells (SOCs) to yield synthesis gas (an energy-rich gas mixture of CO and H_2).

This chapter describes experimental results for co-electrolysis of CO_2 and H_2O in a solid oxide cell. Electrolysis of CO_2 and CO_2/H_2O mixtures was initially investigated in the 1960s as a means to produce O_2 for life support and propulsion in submarines and spacecraft [1-6]. Research on using solid oxide cells for this purpose continues today [7-13]. Recently, there has been a surge of research activity for electrolysis of H_2O [14-24], CO_2 [15, 20, 25-27] and CO_2/H_2O mixtures [28-34] for fuel production purposes, using state-of-the-art cells.

The cell operation is illustrated in **Figure 4-1**. When both H_2O and CO_2 are supplied to the Ni/YSZ electrode for co-electrolysis, the water-gas shift (WGS) equilibrium may play a role in the CO or H_2 production (YSZ = yttria-stabilized zirconia). Since the cell resistance for CO_2 electrolysis is slightly higher than that for H_2O electrolysis [15, 20, 26, 27, 31-34] and at the cell operating temperature of 850 °C the WGS equilibrium favors the reverse reaction, it is expected that part of (possibly most of [32]) the CO produced results from reverse WGS. Co-electrolysis may be advantageous for process simplicity, eliminating the need for a separate reverse WGS reactor to prepare syngas with the H_2/CO ratio needed for catalytic fuel synthesis.

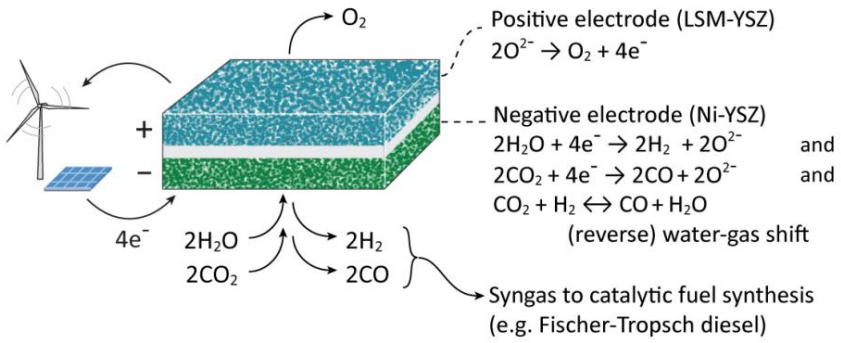

Figure 4-1. Diagram of a solid oxide cell applied for co-electrolysis of CO_2 and H_2O, as part of the renewable fuel cycle discussed in **Chapter 3**. The electrode reactions are also given.

Recently, long-term (>200-hour) durability studies have been reported for H_2O [17, 21, 22, 24, 31, 35-37] and CO_2 [27] electrolysis. The present work, along with a companion paper [34] in which we report the durability for co-electrolysis at low current density, appears to be the first study of co-electrolysis durability. In general, according to literature, degradation at the Ni/YSZ (YSZ = yttria stabilized zirconia) electrode seems to dominate during electrolysis and

apparently involves accumulation of impurities at the three-phase boundary (TPB) between the gas, Ni particles and YSZ particles where the reactions occur [17, 21, 27, 34, 38]. Several mechanisms for degradation have been proposed, and the mechanism might depend heavily on the gas atmosphere—impurities may originate from the test setup [17, 21], from the cell materials [38], and/or from the gasses [27, 34], or the gas atmosphere in combination with high temperature (e.g. 90% steam at 950 °C) may induce mobility of Ni leading to degradation of the electrode microstructure [21]. Characterizing cell durability is complicated by the fact that cell performance sometimes temporarily degrades (passivates) and then recovers (activates), and the real long-term degradation is occurring simultaneously [21, 34]. The magnitude of the cell operating voltage or resulting current density may also affect the durability. Cell durability at high current density (>0.5 A/cm^2 electrolysis) has not been widely reported, although high current density operation may be necessary for an economical synthetic fuel production process (see **Chapter 3**, **section 3.3.2**).

By analyzing the impedance spectra measured at systematically varied test conditions, the cell resistance can be broken down into contributions from the electrodes and electrolyte. Ideally, breaking down resistance can be aided by using a reference electrode that isolates the response of one of the two electrodes (three-electrode set-up). However, using a reference electrode with thin-electrolyte technological solid oxide cells is not possible – proper placement of a reference electrode is difficult and measurements are known to be distorted due to non-uniform current distribution [39-41]. Consequently, breaking down the resistance involves deconvolution of impedance spectra that have overlapping processes (similar characteristic frequencies).

Prior methods of breaking down the cell resistance relied on performing a complex nonlinear least-squares regression to an equivalent circuit composed of an array of serially connected circuit elements (Voigt measurement model) – an inductor (L), a resistor (R), and five serial RQ (resistor in parallel with a constant phase element) subcircuits, or in common equivalent circuit notation, LR(RQ)(RQ)(RQ)(RQ)(RQ) [42, 43]. This equivalent circuit has 17 parameters (one for each L element, one for each R element, and two per Q element) that must be fitted to the impedance data, which requires careful and difficult analysis involving fixing some parameters while fitting others. Alternative methods of breaking down the resistance or at least for providing input data and constraints to the equivalent circuit would be useful. Recently, alternative methods to identify processes have been employed [44], including analysis of differences in impedance spectra (ADIS) [45] and transformation of the impedance data to the distribution of relaxation times (DRT) [46-48]. Both methods increase the resolution of the peaks of the specific processes at their characteristic frequencies, which is helpful for identifying the different processes. In the present study the DRT method is used to analyze the performance and degradation. See **Chapter 1**, **section 1.2** for more information about the DRT and other impedance analysis techniques.

In the present work we examined the co-electrolysis performance of a solid oxide cell and studied the durability during co-electrolysis at consecutively higher current densities. Analysis of the DRT of the impedance spectra measured at various conditions before and after long-term testing segments is also introduced as a way to study the cell degradation mechanisms. In this study, the DRT technique enables identification of the rate-limiting processes that contribute to the cell impedance, their relative resistances, and how they change over time, without relying on a model (equivalent-circuit or otherwise) and the assumptions inherent in a model. The processes that are responsible for changes in cell performance can therefore be identified unambiguously.

4.2. Experimental

A planar Ni/YSZ-supported solid oxide cell produced at Risø DTU was tested as an electrolysis cell. The cell had a 16 cm^2 active area and consisted of a dense thin YSZ electrolyte sandwiched between a porous Ni/YSZ composite negative-electrode and a porous LSM/YSZ (LSM = lanthanum strontium manganite) composite positive-electrode. The cell type and dimensions and the test setup have been described elsewhere [34]. In the present study a Ni wire was used for sealing at the side of the Ni/YSZ electrode (**Figure 4-2**). Initially DC polarization (i-V) curves and AC impedance spectra (IS) were measured at 850, 750 and 800 °C with various gas atmospheres of $H_2/H_2O/CO/CO_2$ mixtures supplied to the Ni/YSZ cathode (always at a total flow rate of 25 L/h) and oxygen or air supplied to the LSM/YSZ anode (50 L/h). The impedance spectra were measured using an external shunt and a Solartron 1255B frequency response analyzer, without DC bias with an AC amplitude of 60 mA in the frequency range of 82451 to 0.082 Hz with 6 or 15 points per frequency decade (15 for use in the DRT transform). The impedance data were corrected using the short-circuit impedance response of the test set-up.

During fuel cell and electrolysis cell polarizations, the cell temperature varied since only the oven temperature was kept constant. During fuel cell polarizations, the ohmic heating of the cell raised the temperature measured at the thermocouple positioned at the center of the cell by up to 6 °C relative to the temperature measured at OCV. During electrolysis polarizations, the cell consumed heat and lowered the measured temperature by up to 1 °C and then at higher cell voltage, approaching the thermoneutral voltage, the temperature slightly increased to up to 1 °C higher than that measured at OCV. The temperature measured by a thermocouple positioned at the corner of the cell was within 1 °C of that measured at the center of the cell, at OCV. During fuel cell polarizations, the corner temperature reached 3 °C lower than the center temperature, and during electrolysis polarizations the difference of the two temperature measurements remained below 1 °C.

After the initial characterization, the cell was operated in galvanostatic mode, with a mixture of 45% CO_2, 45% H_2O, and 10% H_2 with total flow rate of 25 L/h supplied to the

Ni/YSZ cathode and 100% O_2 supplied at 50 L/h to the LSM/YSZ anode, at current densities of –0.25, –0.5, and –1 A/cm^2, operating for 382, 206, and 212 hours respectively at each galvanostatic segment. The same set of electrochemistry measurements as before the galvanostatic test were conducted after each segment, at the same temperatures and gas compositions.

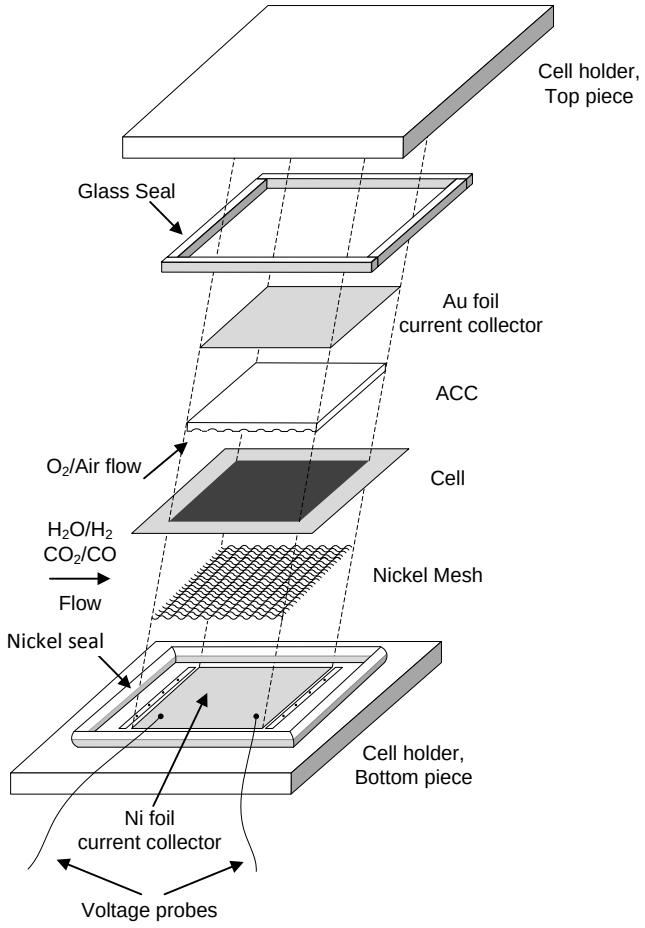

Figure 4-2. Risø-DTU cell assembly in a cross-flow pattern with a nickel seal and a nickel mesh, which provided both current collection and gas flow channels, at the side of the Ni/YSZ electrode, and a glass seal and an LSM/YSZ current collector / gas distributor at the side of the LSM/YSZ electrode, in an alumina housing, after [34].

4.3. Results and Discussion

4.3.1. Performance

Figure 4-3 shows i-V curves for oxidation and reduction in $H_2/H_2O/CO/CO_2$ mixtures at 850 °C. The gas mixtures used were 50% H_2O + 50% H_2, 50% CO_2 + 50% CO, and 25% H_2O + 25% CO_2 + 25% H_2 + 25% CO, and 45% H_2O + 45% CO_2 + 10% H_2. The first three all give 50% reactants for either fuel cell or electrolysis operation, and the last is the composition

that was subsequently used for the electrolysis durability test. Because the free energies of the CO_2 and H_2O dissociation (to yield CO and H_2 respectively) reactions are nearly equivalent at this temperature ([49] and see **section 3.2.2**), the open-circuit voltage (OCV) for the three 50%-reactants compositions are nearly all equivalent, as can be seen in the figure.

The cell exhibited a high performance for co-electrolysis of CO_2/H_2O mixtures, comparable to the performance for steam electrolysis which is known to be high [50]. As has been reported for similar cells [15, 20, 26, 27, 31-34], the cell exhibited slightly higher performance for H_2 oxidation and H_2O reduction than for CO and CO_2 respectively. For the 25%-each composition, co-electrolysis performance was between that of CO_2 and H_2O electrolysis and closer to H_2O. This suggests that besides the CO_2 and H_2O electrolysis reactions, the reverse WGS reaction occurs. The role of the reverse WGS is further studied, using different gas composition variations, in ref. [34]. The degree to which reverse WGS is responsible for CO production cannot be determined from these results. True quantification of the relative amounts of the reactions taking place would require ^{18}O isotope tracing or a similar method. However, whether part of the syngas is produced by the WGS equilibrium has little effect on the energy demand of syngas production in the cell, because the cell's internal resistance can supply the heat needed for either the electrochemical or catalytic reactions.

From **Figure 4-3** it is also observed that at higher current densities the resistance increases for the three 50%-reactants i-V curves. It appears that a limiting current density is approached. This effect is often explained as a gas diffusion limitation of the reactants inside the electrodes [33, 51]. However, it is possible that the increased resistance may arise from effects related to the test set-up instead of the gas transport in the electrode microstructure—gas conversion resistance [52, 53], R_{conv}, and/or gas diffusion resistance due to a volume of stagnant gas outside the porous electrode structure [53, 54], R_{diff}. R_{conv} and R_{diff} are both minimal when the reactant/product ratio is 1. Therefore, when the gasses are supplied at a reactant/product ratio of 1 (the 50%-reactants tests), R_{conv} and R_{diff} are smallest at OCV, and reactant utilization resulting from polarization will reduce this ratio and thereby increase these types of resistance. On the other hand, when the gasses are supplied at a reactant/product ratio of 9 (45% CO_2 + 45% H_2O + 10% H_2), reactant utilization will bring the reactant/product ratio closer to 1, reducing R_{conv} and R_{diff}—hence the relative lack of curvature in that i-V curve. Further study of these effects is important if high reactant utilization is necessary.

The IS measurements at OCV for the same gas compositions (**Figure 4-4**) agree with the i-V curves—the resistance for reduction and oxidation of the co-electrolysis gas composition is higher than for H_2O/H_2 and lower than for CO_2/CO, and closer to that of H_2O/H_2. It can be seen that the serial resistance, R_S, which is almost entirely the ohmic resistance of the electrolyte, contributes 40-50% of the total resistance at OCV at this temperature. From the Nyquist plot, it

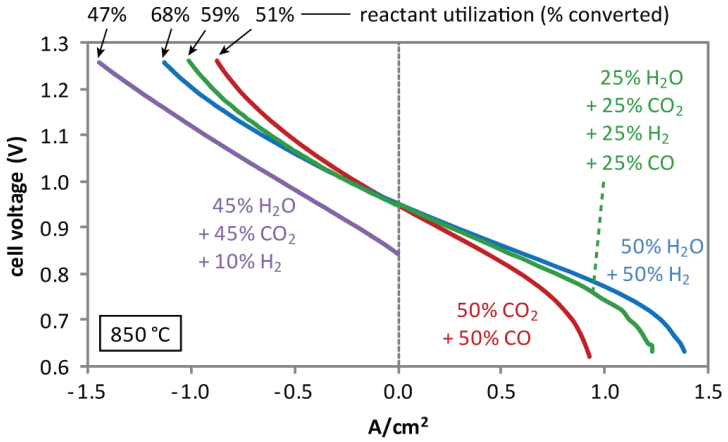

Figure 4-3. DC polarization (i-V) curves for oxidation and reduction of chosen mixtures of H_2, H_2O, CO, CO_2.

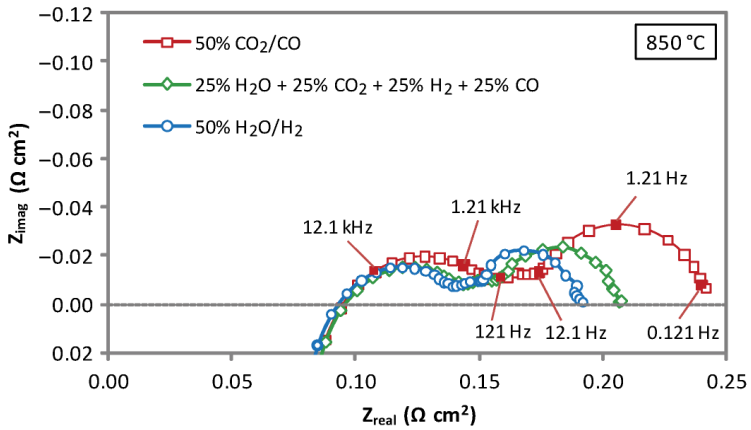

Figure 4-4. Nyquist plot of impedance spectra measured at OCV for the three 50%-reactant gas compositions as in **Figure 4-3**.

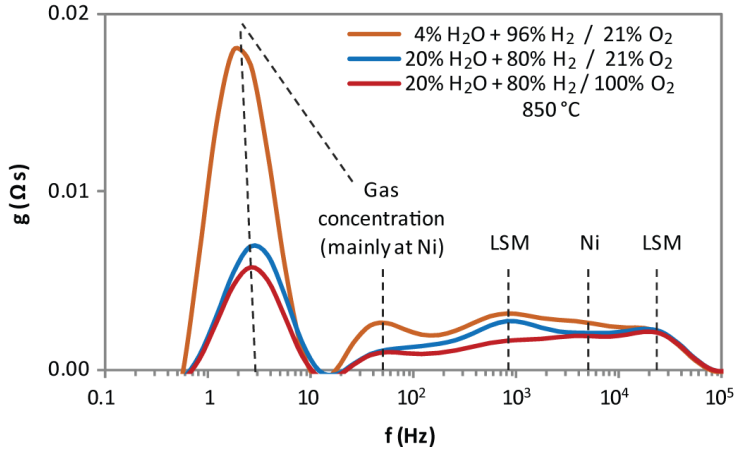

Figure 4-5. Distribution of relaxation times (DRT) for three impedance measurements measured at OCV with various gas compositions supplied to the anode and cathode.

is not clear how much each electrode contributes to the polarization resistance, R_p, and what electrode processes might be contributing. The impedance data, measured at systematically varied temperature and gas compositions at each electrode, were transformed to the DRT and compared to resolve these processes.

Figure 4-5 shows the DRT for three different gas atmospheres at 850 °C. Transforming to the DRT enhances the frequency-domain resolution of the impedance response. By varying the gas composition supplied to the Ni/YSZ electrode, only the Ni/YSZ electrode impedance processes should be affected, and the same goes for the LSM/YSZ electrode. Five rate-limiting processes are visible in the DRT plot—2 LSM/YSZ electrode processes, 1 Ni/YSZ process, and 2 low-frequency processes mainly at the Ni/YSZ side of the cell, which were independent of temperature (not shown) and correspond to gas conversion and gas diffusion impedance [52-54]. The electrode process with the highest characteristic frequency, which is independent of any gas changes, is ascribed to the LSM/YSZ electrode based on the similarities of the summit frequency and gas-independence as found using simplified cells composed of only LSM/YSZ (symmetrical cells) in another study [42, 43]). The summit frequencies are in approximate agreement with the five cell processes found by the equivalent circuit method for this type of cell (described earlier). The DRT therefore enables identification of the rate-limiting processes that contribute to the total impedance of a cell without relying on a model. Modeling would of course still be very useful to study the nature of the processes. The breakdown of the total cell impedance into these processes could at this point be quantified by modeling the DRT (e.g. applying a measurement model by fitting distribution functions to the transformed data to quantify the peaks, or deriving and applying an electrochemical model). However for this study the DRT is used as is, to study the degradation mechanism of the cell by simply identifying which processes are affected by long-term testing.

4.3.2. Durability

During the galvanostatic segments, the cell voltage increased at a faster rate at higher current densities (or correspondingly, higher cell voltages) (**Figure 4-6**). During the low current density (–0.25 A/cm^2) segment, the cell voltage increased initially during the first 100 hours and then leveled off to a slow degradation rate of 0.005-0.008 mV/h during the last 100 hours. The minor passivation and activation of the cell during the first 200 hours was much less pronounced compared with what has been observed for other H_2O [17, 21, 37], CO_2 [27], and co-electrolysis tests [34]. If the previously observed passivation/activation is rooted in impurities, this test illustrates the inconsistency of impurity-related passivation phenomena since the same gasses, same cell type and nearly identical test set-up were used in this test as in some of the others (excluding the tests that used glass sealing, which was believed to contribute to degradation by supplying silica impurities). During the higher current density segments, it is clear that the

degradation rate is significantly faster, on the order of 0.1 mV/h, although the degradation rate was not allowed to fully level off.

The impedance spectra measured before and after each segment (**Figure 4-7**) show an increasing serial resistance (R_S), especially after the final segment at –1 A/cm^2. The high-frequency contributions to the impedance also appear to have enlarged with the consecutively higher current densities. As expected, the low frequency gas concentration impedance arcs do not appear to have noticeably changed. However, not much more can be learned from the Nyquist plot (Figure 4-7). The DRT can be used to reveal more information about which processes were affected during each segment of long-term operation. The DRT does not show R_S (nor changes in R_S). The DRT and the Nyquist plot are therefore complementary for analyzing impedance data. The DRTs of impedance spectra measured before and after the segments (Figure 4-8) clearly show that the impedance contributions related to gas concentration have negligibly changed. The DRTs show that after the –0.25 A/cm^2 segment, the resistance of the Ni/YSZ electrode process has grown, whereas the lower-frequency LSM/YSZ (LSM_{LF}) peak has not been affected. At first glance the high-frequency LSM/YSZ (LSM_{HF}) peak appears to have grown slightly—however since the DRT result is the sum of all the peaks, the growth of the nearby Ni/YSZ peak can visually boost the sum near the LSM_{HF} peak (the inset of **Figure 4-8** illustrates this with example Gaussian peaks that might fit the DRT data). After the –0.5 A/cm^2 segment and especially after the –1 A/cm^2 segment, however, it is clear that the LSM/YSZ electrode has degraded as well; an enlarged Ni/YSZ peak cannot account for the large increases near LSM_{LF} and LSM_{HF} even if the enlarged Ni/YSZ peak is represented by a Gaussian (or any type of) distribution with the maximum width that can fit under the DRT sum.

This analysis suggests different degradation mechanisms for high and low current density operation. At low current density, degradation at the Ni/YSZ electrode dominates, as has been reported for various electrolysis durability tests (discussed earlier), whereas at higher current densities, both serial resistance and LSM/YSZ electrode degradation play a significant role. The Ni/YSZ electrode degradation seems to be related to impurities that accumulate at the TPB, as discussed earlier [17, 21, 27, 34, 38]. Although Ni is a good catalyst for coking reactions, carbon deposition is not thermodynamically favored at any of the conditions that the cell was tested in, and a prior study of pure CO_2 electrolysis [27], which would provide more favorable conditions for carbon formation, determined that carbon formation is not a source of degradation.

Since higher current induces higher potentials across each component of the cell, the different degradation mechanisms might be related to the distribution of the potentials and the magnitude of the potential across each component (the electrodes and electrolyte). When this type of cell has been tested as a fuel cell under similar conditions, far less degradation at high current density has been observed [55], suggesting that the degradation observed here may be specific to electrolysis operation. One possibility is a build-up of oxygen partial pressure in and

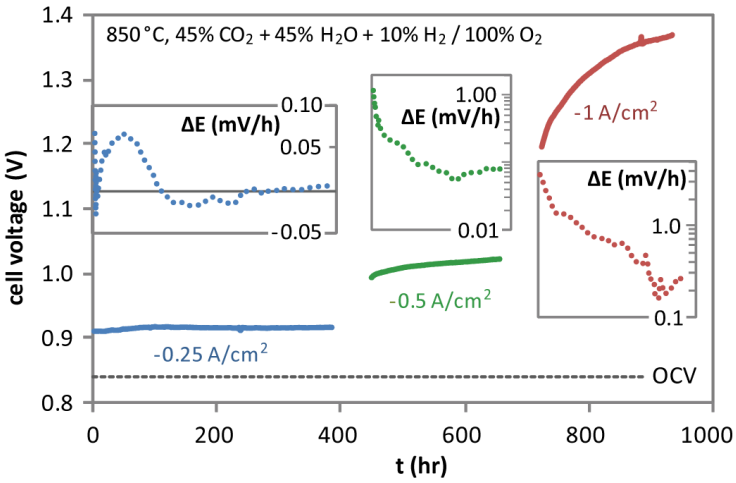

Figure 4-6. The cell voltage and the rate of change of the cell voltage (insets) measured during the 3 consecutive galvanostatic co-electrolysis segments run on the cell.

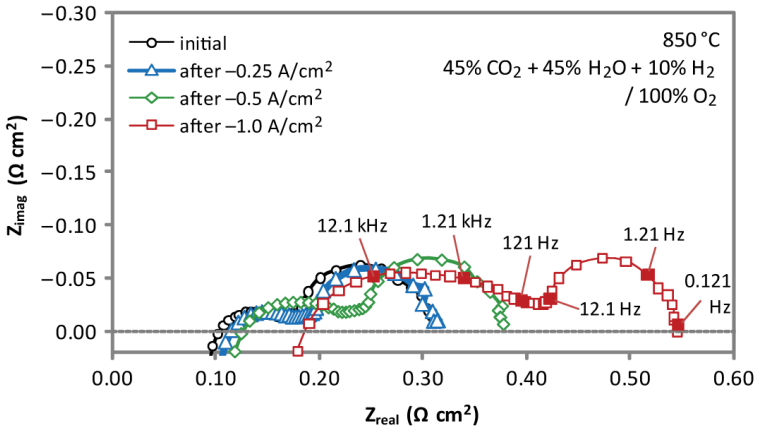

Figure 4-7. Nyquist plot of impedance spectra measured at OCV before and after each galvanostatic test segment.

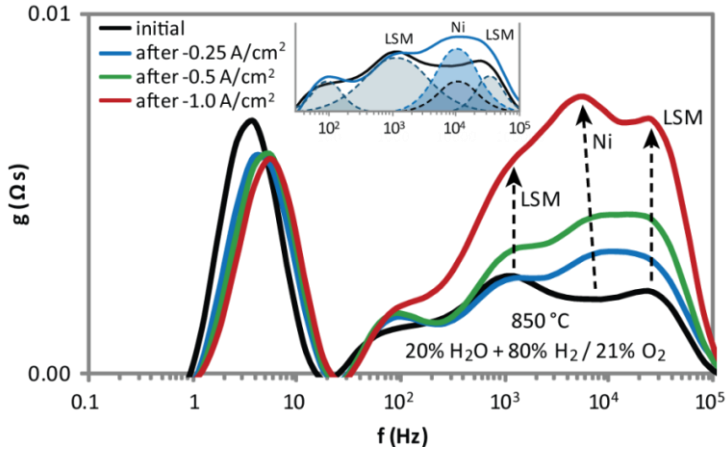

Figure 4-8. DRT of impedance spectra measured at OCV before and after each galvanostatic test segment. Inset: Illustration of example Gaussian peaks fitted to the high-frequency range for "initial" and "after –0.25 A/cm²" measurements.

around the electrolyte due to the potentials applied across the components of the cell [56]. Scanning electron microscope examination of a cell tested at high current density might shed light on the degradation mechanisms—e.g. if delamination of an electrode from the electrolyte, microstructural damage to an electrode, or damage to the electrolyte has taken place, it may be the cause of the serial resistance increase. Therefore, ongoing work includes microscopy, and further testing of electrolysis cells at high current densities.

4.4. Conclusions

Co-electrolysis of CO_2 and H_2O in a solid oxide cell showed a high initial performance, which was higher than for CO_2 electrolysis and slightly lower than for H_2O electrolysis, suggesting that the reverse WGS plays a role during co-electrolysis. Transformation of the impedance data to the distribution of relaxation times (DRT) and comparison of measurements taken under systematically varied test conditions enabled clear visual identification of five electrode processes that contribute to the cell resistance. The processes were assigned to each electrode and to gas concentration effects by examining their dependence on gas composition changes and temperature.

The cell durability for co-electrolysis was examined at consecutively higher current densities and corresponding cell voltage. By analyzing the DRTs of the impedance data measured before and after each segment of operation, it was found that at low current density operation (–0.25 A/cm^2) degradation at the Ni/YSZ electrode dominated, whereas at higher current densities (–0.5 A/cm^2 and –1.0 A/cm^2), the Ni/YSZ electrode continued to degrade but the serial resistance and degradation at the LSM electrode began to play a major role in the total loss in performance. If the electrolyzer is powered by intermittent renewable electricity sources, high current density operation may be necessary for an economical synthetic fuel production process (see **Chapter 3**, **section 3.3.2**). In that case, the durability at high current density needs to be improved. To achieve this, clearer identification of the passivation and degradation mechanisms is important, in order to change the operating conditions, change the cell architecture, modify one or both of the electrodes, or replace one or both of the electrodes with alternative materials. At low current density, the durability may be sufficient for synthetic fuel production using a more constant power supply such as nuclear or hydroelectric power (see **Chapter 3**, **section 3.3.2**).

4.5. References

1. Oser W, *Electrochemical method for conversion of carbon dioxide*. (1967). USPTO 3,316,163.
2. Elikan L and Morris JP, *Solid Electrolyte System for Oxygen Regeneration*. (1969), Westinghouse Electric Corp., for NASA Langley Research Center: Washington, D.C. CR-1359. 181.
3. Weissbart J, Smart WH, Inami SH, McCullough CM, and Ring SA, *Development of a CO_2-H_2O Solid Oxide Electrolysis System: First Annual Report, 29 Mar. 1968 - 29 May 1969*. (1969), NASA Ames Research Center: Moffett Field, California. CR 73358. 65.

4. Elikan L, Morris JP, and Wu CK, *Development of a solid electrolyte carbon dioxide and water reduction system for oxygen recovery*. (1972), Westinghouse Electric Corp., for NASA Langley Research Center: Washington, D.C. CR-2014. 181.
5. Spacil HS and Tedmon JCS, *Electrochemical Dissociation of Water Vapor in Solid Oxide Electrolyte Cells*. Journal of the Electrochemical Society, (1969). **116**(12): p. 1618-1626.
6. Weissbart J and Smart WH, *Study of Electrolytic Dissociation of CO_2-H_2O Using a Solid Oxide Electrolyte*. (1967), NASA Ames Research Center: Moffett Field, California. CR-680.
7. Isenberg AO and Verostko CE, *Carbon Dioxide and Water Vapor High Temperature Electrolysis*. (1989), NASA Research Center. SAE Technical Paper 891506.
8. Isenberg AO and Verostko CE, *Carbon Dioxide Electrolysis With Solid Oxide Electrolyte Cells for Oxygen Recovery in Life Support Systems*. (1988), NASA Research Center SAE Technical Paper 881040.
9. Sridhar KR and Vaniman BT, *Oxygen production on Mars using solid oxide electrolysis*. Solid State Ionics, (1997). **93**(3-4): p. 321-8.
10. Sridhar KR and Iacomini CS, *Combined H_2O/CO_2 Solid Oxide Electrolysis for Mars In Situ Resource Utilization*. Journal of Propulsion and Power, (2004). **20**(5): p. 892-901.
11. Guan J, Doshi R, Lear G, Montgomery K, Ong E, and Minh N, *Ceramic oxygen generators with thin-film zirconia electrolytes*. Journal of the American Ceramic Society, (2002). **85**(11): p. 2651-2654.
12. Tao G, Sridhar KR, and Chan CL, *Study of carbon dioxide electrolysis at electrode/electrolyte interface: part II. pt-YSZ cermet/YSZ interface*. Solid State Ionics, (2004). **175**: p. 621-624.
13. Park JY and Wachsman ED, *Lower temperature electrolytic reduction of CO_2 to O_2 and CO with high-conductivity solid oxide bilayer electrolytes*. Journal of the Electrochemical Society, (2005). **152**(8): p. A1654-A1659.
14. Dönitz W, Schmidberger R, Steinheil E, and Streicher R, *Hydrogen production by high temperature electrolysis of water vapour*. International Journal of Hydrogen Energy, (1980). **5**(1): p. 55-63.
15. Isenberg AO, *Energy-Conversion Via Solid Oxide Electrolyte Electrochemical-Cells at High-Temperatures*. Solid State Ionics, (1981). **3-4**: p. 431-437.
16. Eguchi K, Hatagishi T, and Arai H, *Power generation and steam electrolysis characteristics of an electrochemical cell with a zirconia- or ceria-based electrolyte*. Solid State Ionics, (1996). **86-8**: p. 1245-1249.
17. Hauch A, Jensen SH, Ramousse S, and Mogensen M, *Performance and durability of solid oxide electrolysis cells*. Journal of the Electrochemical Society, (2006). **153**(9): p. 1741-1747.
18. O'Brien JE, Stoots CM, Herring JS, and Hartvigsen J, *Hydrogen production performance of a 10-cell planar solid-oxide electrolysis stack*. Journal of Fuel Cell Science and Technology, (2006). **3**(2): p. 213-219.
19. Herring JS, O'Brien JE, Stoots CM, Hawkes GL, Hartvigsen JJ, and Shahnam M, *Progress in high-temperature electrolysis for hydrogen production using planar SOFC technology*. International Journal of Hydrogen Energy, (2007). **32**(4): p. 440-450.
20. Jensen SH, Larsen PH, and Mogensen M, *Hydrogen and synthetic fuel production from renewable energy sources*. International Journal of Hydrogen Energy, (2007). **32**(15): p. 3253-3257.
21. Hauch A, Ebbesen SD, Jensen SH, and Mogensen M, *Solid Oxide Electrolysis Cells: Microstructure and Degradation of the Ni/YSZ Electrode*. Journal of the Electrochemical Society, (2008). **11**(155): p. B1184-B1193.

22. Stoots CM, O'Brien JE, Condie K, Moore-McAteer L, Housley G, Hartvigsen JJ, et al., *The High-temperature Electrolysis Integrated Laboratory-scale Experiment.* Nuclear Technology, (2009). **166**(1): p. 32-42.
23. Brisse A, Schefold J, and Zahid M, *High temperature water electrolysis in solid oxide cells.* International Journal of Hydrogen Energy, (2008). **33**(20): p. 5375-5382.
24. Schiller G, Ansar A, Lang M, and Patz O, *High temperature water electrolysis using metal supported solid oxide electrolyser cells (SOEC).* Journal of Applied Electrochemistry, (2009). **39**(2): p. 293-301.
25. Green RD, Liu CC, and Adler SB, *Carbon dioxide reduction on gadolinia-doped ceria cathodes.* Solid State Ionics, (2008). **179**(17-18): p. 647-660.
26. Bidrawn F, Kim G, Corre G, Irvine JTS, Vohs JM, and Gorte RJ, *Efficient reduction of CO_2 in a solid oxide electrolyzer.* Electrochemical and Solid-State Letters, (2008). **11**(9): p. B167-B170.
27. Ebbesen SD and Mogensen M, *Electrolysis of carbon dioxide in Solid Oxide Electrolysis Cells.* Journal of Power Sources, (2009). **193**(1): p. 349-358.
28. Jensen SH, Høgh JVT, Barfod R, and Mogensen M. *High Temperature Electrolysis of Steam and Carbon Dioxide.* in *Risø International Energy Conference.* (2003). Risø National Laboratory, Roskilde, Denmark.
29. Stoots CM, O'Brien JE, and Hartvigsen JJ. *Syngas production Via High-Temperature Co-electrolysis of Steam and Carbon Dioxide in a Solid-Oxide Stack.* in *Fuel Cell Science, Engineering & Technology Conference.* (2007).
30. Hartvigsen J, Joshi AV, Elangovan S, Balagopal S, Gordon JH, and Hollist M, *Electrochemical Cell for the production of Synthesis Gas Using Atmospheric Air and Water.* (2007). WIPO WO/2007/025280.
31. Elangovan S and Hartvigsen J, *Efficient Reversible Electrodes for Solid Oxide Electrolyzer Cells.* (2008). WIPO WO/2008/013783.
32. Stoots CM, O'Brien JE, Herring JS, and Hartvigsen JJ, *Syngas production via High-Temperature Coelectrolysis of Steam and Carbon Dioxide.* Journal of Fuel Cell Science and Technology, (2009). **6**(1): p. 011014-12.
33. Zhan Z, Kobsiriphat W, Wilson JR, Pillai M, Kim I, and Barnett SA, *Syngas production By Coelectrolysis of CO_2/H_2O: The Basis for a Renewable Energy Cycle.* Energy & Fuels, (2009). **23**(6): p. 3089-3096.
34. Ebbesen SD, Graves C, and Mogensen M, *Production of Synthetic Fuels by Co-Electrolysis of Steam and Carbon Dioxide.* International Journal of Green Energy, (2009). **6**(6): p. 646 – 660.
35. O'Brien JE, Stoots CM, Herring JS, and Hartvigsen JJ, *Performance of planar high-temperature electrolysis stacks for hydrogen production from nuclear energy.* Nuclear Technology, (2007). **158**: p. 118-131.
36. Hartvigsen J, Elangovan S, O'Brien JE, Stoots CM, Herring JS, and Lessing P. in *6th European Solid Oxide Fuel Cell Forum.* (2004). Lucerne: European Fuel Cell Forum.
37. Jensen SH, Hauch A, Hendriksen PV, and Mogensen M, *Advanced Test Method of Solid Oxide Cells in a plug-Flow Setup.* Journal of the Electrochemical Society, (2009). **156**(6): p. B757-B764.
38. Hauch A, Jensen SH, Bilde-Sorensen JB, and Mogensen M, *Silica segregation in the Ni/YSZ electrode.* Journal of the Electrochemical Society, (2007). **154**(7): p. A619-A626.
39. Winkler J, Hendriksen PV, Bonanos N, and Mogensen M, *Geometric requirements of solid electrolyte cells with a reference electrode.* Journal of the Electrochemical Society, (1998). **145**(4): p. 1184-1192.
40. Chan SH, Chen XJ, and Khor KA, *Reliability and accuracy of measured overpotential in a three-electrode fuel cell system.* Journal of Applied Electrochemistry, (2001). **31**(10): p. 1163-1170.

41. Adler SB, *Reference electrode placement in thin solid electrolytes.* Journal of the Electrochemical Society, (2002). **149**(5): p. E166-E172-E166-E172.
42. Barfod R, Hagen A, Ramousse S, Hendriksen PV, and Mogensen M, *Break down of losses in thin electrolyte SOFCs.* Fuel Cells, (2006). **6**(2): p. 141-145.
43. Barfod R, Mogensen M, Klemenso T, Hagen A, Liu YL, and Hendriksen PV, *Detailed characterization of anode-supported SOFCs by impedance spectroscopy.* Journal of the Electrochemical Society, (2007). **154**(4): p. B371-B378.
44. Jensen SH, Hjelm J, Hagen A, and Mogensen M, *Electrochemical impedance spectroscopy as diagnostic tool*, in *Handbook of Fuel Cells – Fundamentals, Technology and Applications*, W. Vielstich, H. Yokokawa, and H.A. Gasteiger, Editors. (2009), John Wiley & Sons, Ltd.
45. Jensen SH, Hauch A, Hendriksen PV, Mogensen M, Bonanos N, and Jacobsen T, *A method to separate process contributions in impedance spectra by variation of test conditions.* Journal of the Electrochemical Society, (2007). **154**(12): p. B1325-B1330-B1325-B1330.
46. Schichlein H, Müller AC, Voigts M, Krügel A, and Ivers-Tiffée E, *Deconvolution of electrochemical impedance spectra for the identification of electrode reaction mechanisms in solid oxide fuel cells.* Journal of Applied Electrochemistry, (2002). **32**(8): p. 875-882.
47. Leonide A, Sonn V, Weber A, and Ivers-Tiffee E, *Evaluation and modeling of the cell resistance in anode-supported solid oxide fuel cells.* Journal of the Electrochemical Society, (2008). **155**(1): p. B36-B41-B36-B41.
48. Sonn V, Leonide A, and Ivers-Tiffee E, *Combined Deconvolution and CNLS Fitting Approach Applied on the Impedance Response of Technical Ni/8YSZ Cermet Electrodes.* Journal of the Electrochemical Society, (2008). **155**(7): p. B675-B679.
49. Isenberg AO, *Oxygen ion conduction of the oxides of magnesium, calcium, and aluminum by fluoride additions.* Journal of the Electrochemical Society, (2006). **153**(10): p. A1935-A1944.
50. Hauch A, Ebbesen SD, Jensen SH, and Mogensen M, *Highly efficient high temperature electrolysis.* Journal of Materials Chemistry, (2008). **18**(20): p. 2331-2340.
51. Jiang Y and Virkar AV, *Fuel composition and diluent effect on gas transport and performance of anode-supported SOFCs.* Journal of the Electrochemical Society, (2003). **150**(7): p. A942-A951.
52. Primdahl S and Mogensen M, *Gas conversion impedance: A test geometry effect in characterization of solid oxide fuel cell anodes.* Journal of the Electrochemical Society, (1998). **145**(7): p. 2431-2438.
53. Jacobsen T, Hendriksen PV, and Koch S, *Diffusion and conversion impedance in solid oxide fuel cells.* Electrochimica Acta, (2008). **53**(25): p. 7500-7508.
54. Primdahl S and Mogensen M, *Gas diffusion impedance in characterization of solid oxide fuel cell anodes.* Journal of the Electrochemical Society, (1999). **146**(8): p. 2827-2833.
55. Hagen A, Barfod R, Hendriksen PV, Liu YL, and Ramousse S, *Degradation of anode supported SOFCs as a function of temperature and current load.* Journal of the Electrochemical Society, (2006). **153**(6): p. A1165-A1171.
56. Jacobsen T and Mogensen M, *The Course of Oxygen partial pressure and Electric potentials across an Oxide Electrolyte Cell.* ECS Transactions, (2008). **13**(26): p. 259-273.

Chapter 5

5. Aspects of Metal-YSZ Electrode Kinetics

A better understanding of the electrochemistry that takes place at the metal-YSZ electrode-electrolyte interface would help in identifying ways to improve solid oxide cell performance, both from the standpoints of understanding the mechanisms that limit performance and cause it to degrade and of designing new and improved negative-electrodes (YSZ = yttria stabilized zirconia). This chapter[i] presents an experimental study of the electrode kinetics of oxidation and reduction of H_2/H_2O and CO/CO_2 at the metal/YSZ interface in gas compositions relevant to fuel cell and electrolysis cell operation (e.g. including 50% H_2 + 50% H_2O and 50% CO + 50% CO_2), using point-contact metal wire electrodes to form cells with simplified geometry. This simple geometry is useful to obtain a well-defined interface and isolate the true nature of the electrochemistry from the additional properties that arise from a complex three-dimensional microstructure in a porous solid oxide cell electrode.

Impedance spectra were measured at open-circuit voltage and under polarization, and polarization sweeps were performed. Test conditions – the gas composition, the temperature, and the polarization of the electrodes – were varied systematically to examine how the electrochemical measurements varied, to facilitate studying the electrode rate-limiting processes. In addition to applying conditions relevant to electrolysis of H_2O and of CO_2 (e.g. high pH_2O and pCO_2, and cathodic polarization), an additional parameter uncommon in most prior studies was the variation of the metal material itself – by comparing the same reactions using different metals (Ag, Au, Cu, Ni, Pd, and Pt) under identical conditions, the similarities and differences of the electrochemical responses between the different metals revealed more information about the reactions than a single material would have.

Several extreme conditions were also applied to the electrodes causing temporary phase changes, including oxidation by exposure to oxygen followed by re-reduction to metal by hydrogen, and strong cathodic polarization which is known to partially reduce the zirconia – both cases resulted in activation of the electrodes, improving performance by as much as an

[i] Part of this chapter has been published in modified form as: Graves, C., S.D. Ebbesen, and M. Mogensen, *Aspects of Metal-YSZ Electrode Kinetics Studied using Model Electrodes.* ECS Transactions, 2009. 25(2): p. 1945-1955

order of magnitude. The interfaces were examined in the scanning electron microscope after testing and displayed interesting microstructural features resulting from these phenomena.

Possible mechanisms that may explain the electrode kinetics and other details are discussed. Widely different responses of different metals to the same parameter changes were observed, which provides evidence that the same reaction mechanisms are not shared by the different metals, contrary to the conclusions of some recent studies. For all of the metals, the metal-YSZ interface was found to be dynamic. Evidence is found that supports the explanation that impurities segregated to the interface are responsible for the inconsistencies between the electrode kinetics results in different studies. Possible reasons for differences between coarse and fine electrodes, which are interrelated with the reaction mechanisms, are also discussed. Many of the results appear to be quite different or perhaps exaggerated versus a porous electrode; the extent that the model electrode serves as a useful model system is discussed.

5.1. Introduction

It is of great interest for improving the performance and durability of solid oxide cells to gain deeper understanding of the mechanisms that limit performance and cause it to deteriorate. Improving understanding of these phenomena would reveal clear pathways to improving the performance and durability of existing cell designs and/or in designing new cells from the same materials or from alternative materials.

The present work focuses on the reaction mechanisms at the negative-electrode, where the electrochemical reactions, H_2O and CO_2 reduction (in electrolysis operation) and H_2 and CO oxidation (in fuel cell operation) take place in a solid oxide cell. The negative electrode most often used is a porous ceramic-metal (cermet) composite composed of an interpenetrating network of nickel and yttria-stabilized zirconia (Ni/YSZ) particles. As shown in **Chapter 4**, the electrochemical performance of Ni-YSZ electrodes is excellent for both fuel cell and electrolysis operation in both H_2/H_2O and CO/CO_2, and the electrolysis durability is very high at certain conditions. However, the performance (internal resistance of the cells) and/or durability needs to be improved to achieve economic viability for electrolytic synthetic fuel production when powered by intermittent resources (**Chapter 3**).

Regarding durability, cell performance degrades substantially during long-term steady-state electrolysis operation. Recent studies have found that impurities have a major role in limiting the performance and durability, but the nature of this role is still not well understood. Other events such as accidental oxidation by exposure to air at high temperature also cause degradation.

Regarding cell performance, it is important to note that, in light of the economic analysis in **Chapter 3**, cell performance and durability can be traded-off in terms of reducing the cost.

That is, halving the internal resistance of the cell leads to approximately the same capital cost reduction as doubling the durability. With low enough resistance (high enough throughput), electrolysis using solid oxide cells could be economical with only a short (perhaps 1 year) operating life.

A better understanding of metal-YSZ electrode kinetics (oxidation and reduction of H_2/H_2O and CO/CO_2 at metal-YSZ interfaces) could reveal pathways to significantly improving the performance and durability of solid oxide cells. In this chapter the electrochemistry at the metal-YSZ (electrode-electrolyte) interface is studied in detail.

Geometrically simplified "model" metal wire electrodes pressed down upon polished YSZ pellet electrolytes were employed. This point-contact cell geometry is intended to serve as an ideal "model" electrode that represents a single interface of the thousands of ceramic and metal particles that make up the typical three-dimensional composite electrode of a technological solid oxide cell, to isolate the true nature of the electrochemistry (catalytic and electrochemical processes) from the additional properties that arise from a complex three-dimensional microstructure (gas transport and current distribution in porous structures, and heterogeneous interfaces and particle sizes). It also provides a well-defined three-phase boundary (TPB) at the interface.

In the present study, the test conditions – the gas composition, the temperature, and the polarization of the electrodes – were varied systematically to examine how the electrochemical measurements varied, to facilitate studying the electrode rate-limiting processes. A number of workers have studied H_2 oxidation at Ni/YSZ by performing electrochemical impedance spectroscopy and/or polarization sweeps at systematically-varied conditions. This study is unique in the application of test conditions relevant to steam and CO_2 electrolysis (e.g. high partial pressures of H_2O and CO_2 and cathodic polarizations) to point-electrode characterization. In fact, gas atmospheres with high pH_2O and pCO_2 like 50% H_2 + 50% H_2O and 50% CO + 50% CO_2 should be included in fuel cell tests as well because they are relevant to cell operation – with high reactant conversion during either electrolysis or fuel cell operation, the negative-electrode should on average be in a gas atmosphere of something close to 50% fuel + 50% oxidized products (with more fuel near the inlet and more oxidized products near the outlet).

Despite all the work that has been done (reviewed in the next section), the detailed kinetics of the electrode reactions are not well known [1, 2]. Little work has been done comparing the same reactions using different metals, even though this may be a good way to examine the kinetics of reactions occurring at the metal/YSZ interface. Therefore, an additional parameter, which is uncommon in most studies, was the variation of the metal material itself – by comparing the same reactions using different metals (Ag, Au, Cu, Ni, Pd, and Pt) under identical conditions, the similarities and differences of the electrochemical responses between

the different metals revealed more information about the reactions than a single material would have. A comparative characterization of the electrode kinetics of several metals under identical conditions is also useful for addressing recent studies that speculated/concluded that all metals share the same reaction mechanism. In this study the metal electrodes were also subjected to some extreme conditions that cause temporary phase changes, including oxidation by exposure to oxygen followed by re-reduction to metal by hydrogen, and strong cathodic polarization that is known to partially reduce the zirconia.

5.1.1. Prior Work

A number of studies, using a variety of cell geometries, have been carried out with the intention of elucidating the reaction mechanisms. Point-contact electrodes are often a metal wire, either bent or melted to a ball-shaped end. Primarily Ni [3-15], but also sometimes Pt [6, 10, 12, 13], Au [6, 10], and Ag [6], have been used. Others have investigated Ni [16-22] and Pt [23] pattern electrodes and the differences between multiple geometries including patterns, meshes, and porous Ni electrodes (both all-metal porous electrodes and Ni-YSZ cermets) [16, 24-27]. Many different metals (Au, Co, Fe, Mn, Ni, Pd, Pr, Pt, Rh, and Ru) were included in one study that used porous metal electrodes [28]. Most other studies that have included different metals have only done so to assess their relative performance for a given reaction – they did not conduct a systematic test to try to determine the reaction mechanisms as is done in the present study.

The reaction mechanisms have proven very difficult to determine. A number of possibilities have been proposed to explain experimental findings. The proposed mechanisms were recently reviewed in ref. [1]. The only general agreement is that the electrode kinetics are not limited by a single charge-transfer rate-limiting step; the Butler-Volmer equation which is most often used in electrochemistry cannot be used to describe this system [1, 3, 7, 24, 29]. Some studies have derived impedance models from chemical rate equations or created physical models based on first principles and fit them to data [2, 9, 12, 30, 31]. However, these fundamental models are usually applied to a single dataset, often with measurements taken in a limited range of conditions. None of the existing models appear able to describe all (or at least a wider set) of data measured at different conditions and by different studies.

One reason that it may be difficult to put together a clear picture is the lack of consistency in the reported data: contradictory results have been reported for a given geometry and for different geometries. For example, the number of impedance processes that have been identified for simple Ni point electrodes (as well as for Ni pattern electrodes [22]) at similar conditions varies from 1 to 3. The polarization resistance normalized to the three-phase boundary (TPB; the Ni/YSZ/gas interface) length at the same conditions has been reported to vary by 2 orders of magnitude [1, 11, 22]. In some cases Ni and Pt were found to have nearly the same electrochemical activity [6] while in others they were very different [23]. Finally,

oxidation of H_2 on Ni has been reported as many times faster than CO oxidation in some Ni electrode studies [32, 33], while in others they have been reported as nearly equal [34].

While different electrode geometries and test set-ups might be able to explain some cases, it has become clear that impurities accumulated at the TPB may be playing a large role in the inconsistencies, by complicating the interpretation of data and even by changing the reaction mechanism [1, 14, 27, 35-38]. Because of the known presence of impurities at the interface, the purity of the materials used in a study is noted when discussing the literature in the following sections. Specific points from electrode kinetics literature will be further addressed when relevant.

5.2. Experimental

5.2.1. Preparation of cells

Cells with a metal wire electrode contacting a $(Y_2O_3)_{0.08}(ZrO_2)_{0.92}$ (8 mol% YSZ , or 8YSZ) electrolyte pellet (approximately 8 mm diameter and 3 mm thick) with a porous Pt-paste counter electrode were assembled in a single-atmosphere custom test rig. The test set-up was similar to that used in [15]. A pseudo-three-electrode set-up was used, with the relatively large counter electrode expected to contribute negligible resistance and therefore serving as reference electrode.

The YSZ pellets were fabricated from Tosoh TZ-8Y powder. The powder was used as-received and uniaxially pressed (187 MPa) followed by cold isostatic pressing (250 MPa) for 30 s each. The resulting pellets were sintered at 1550 °C for 2 h in air. One side of the pellets was then ground and polished in several steps, ending with 1 μm diamond paste. Finer polishing was also tried on 2 pellets and this showed no effect on the impedance data; the measurements were reproducible with or without the extra polishing. Scanning electron microscope (SEM) and atomic force microscope (AFM) scans of the surface showed a dense, smooth topography with a small concentration of tiny holes that did not extend far into the surface. The other side of each pellet was lightly ground. The pellets were cleaned in ethanol in an ultrasonic bath. The unpolished side was then painted with Pt paste which was subsequently sintered to form the porous Pt counter electrode.

The metal wires had the following diameters and purity: Ni, 0.5 mm, 99.999% (Puratronic, Johnson Matthey); Cu, 0.5 mm, 99.999% (Puratronic, Johnson Matthey); Ag, 0.3 mm, purity unknown; Au, 0.3 mm, purity unknown; Pd, 0.5 mm, 99.95%; Pt, 0.5 mm, 99.95% (Ögussa). Some wires were cut and bent approximately 1 cm from the end, to form a "J" shape (**Figure 5-1**) similar to references [35] [11, 14, 15, 36, 37, 39]. Other wires were melted at the end with a reducing torch flame, to form a bulbous tip (**Figure 5-1**) similar to ref. [6]. Some of the bent wires were annealed and electropolished as described in ref. [15]. These wires had a smooth

surface. However, Ni wires prepared without the electropolishing step showed similar impedance once properly normalized (see **section 5.3.2**). Therefore, and since it would be difficult to similarly smoothen all the other metals by electropolishing (procedures for electropolishing some of the other metals are not well-known and in some cases not as straightforward as for Ni), all metals were simply heat-treated in a reducing atmosphere (9% H_2 + 91 N_2) at 600 °C after bending, to try to clean the surface of organic material. The bulb-tip wires were heat-treated in the same reducing atmosphere at 800 °C after melting the tip, which had caused some oxidation. The prepared wires were cleaned ultrasonically in ethanol and examined in SEM or optical microscope.

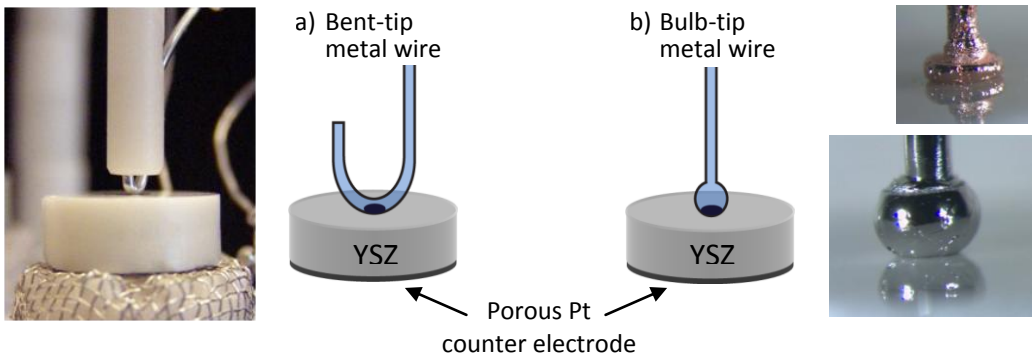

Figure 5-1. Photographs and diagrams of the electrochemical cell set-ups used. (a) Bent metal wire electrode. Photograph: a Pd wire. (b) Melted bulb-tip metal wire electrode. Photographs: a Cu wire (top) and a Pt wire (bottom). All photographs were taken after testing. This Cu wire was stuck after testing and is roughened near the stem as a result of trying to pull it off of the YSZ surface.

5.2.2. Start-up of Electrochemistry Test

The test rig was first cleaned of any stray particles by carefully applying compressed air. Four cells were assembled in the test rig in a laminar air flow chamber to try to avoid contamination. Each wire electrode was inserted into an alumina tube which held it in place and applied pressure downwards from a weight of 210 g attached above. The test set-up was similar to that used previously by Høgh and Schmidt [14, 15, 37, 39]. A Nernst probe (a cell formed on a closed-end tube of YSZ consisting of, internal chamber gasses/Pt/YSZ/Pt/air, where the Pt electrodes are porous and formed by sintering Pt paste) was located near the samples to measure the pO_2.

The test rig was heated to an initial temperature of 1000 °C or 850 °C (for the tests that included silver, to stay below the melting point of silver) in 9% H_2 + 91% N_2 and switched to 97% H_2 + 3% H_2O upon arriving at the initial temperature. For all gas compositions that included H_2O, the H_2O was supplied by flowing the proper amount of O_2 to mix with the H_2 stream which combusted to yield H_2O, upstream of the cells and inside of the furnace. The H_2, CO, and CO_2 gasses were cleaned upstream of the rig. The gas flows during this time and

during the gas variations were set such that the total was 6 L/h. Impedance spectra (IS) were then continuously measured at open-circuit voltage (OCV) for each of the 4 cells. The potentiostatic IS measurements typically used 9 to 13 points per decade, from 1 MHz to 3-100 mHz, with an AC RMS amplitude of 20-30 mV, using a Solartron 1255B+1287 or a Gamry Reference 600. The series resistance (R_S; the high-frequency intercept with the real axis) was monitored during and after heat-up to the initial temperature, while the contact area expanded due to the metal creep.

5.2.3. Systematic Electrochemistry Characterization

The following electrochemistry characterization procedures are the optimized result of an iterative process; it was found that the order of characterizations was important because changing some experimental parameters resulted in either permanent changes in the metal-YSZ interface or temporary changes that took more than a full day to return to steady-state, so these parameters were changed last. It was found that degradation during measurements was not significant, that the impedance was quite stable over days. This is in contrast to some other studies which used Ni pattern electrodes [22] and porous Ni electrodes [24], which may be due to morphological changes of the electrode-electrolyte interface in those tests, or their use of possibly contaminated gasses (here the gasses were cleaned before use).

First, electrochemical impedance spectra were measured at OCV at a variety of conditions. The temperature was varied from 750-1000 °C for three "base" gas compositions: 97% H_2 + 3% H_2O, 50% H_2 + 50% H_2O, and 50% CO + 50% CO_2 (here after referred to as 3% H_2O/H_2, 50% H_2O/H_2, and 50% CO_2/CO respectively). The temperature was varied non-consecutively (for example, 1000–850–750–800 °C rather than 1000–850–800–750 °C) to avoid including any time-varying effects in the trend, e.g. if the electrode performance is degrading with time, the temperature-dependent performance results would incorrectly include this degradation and not only represent temperature dependence. Then, at a fixed temperature (first 1000 °C and then 850 °C), the gas composition was varied systematically in $H_2/H_2O/Ar$ and $CO/CO_2/Ar$ atmospheres. This variation included fixing the pH_2O at 0.5 atm while lowering the pH_2 in steps from 0.5 down to 0.01 atm with the balance supplied as argon. Similarly, the pH_2 was kept constant and pH_2O varied, and then in another variation the pO_2 was kept constant by fixing the pH_2/pH_2O ratio, reducing both the pH_2 and pH_2O equally, together. Finally, the pCO_2 was kept constant while changing the pCO. Time was allowed for the cells to nearly stabilize at each condition by measuring impedance spectra at OCV during the stabilization times. The stabilization times were usually several hours, significantly longer than the time it took for the gas composition to equilibrate according to the pO_2. The "base" conditions were returned to in between some variations to check that the performance had not appreciably changed. An example gas composition variation that included fixed pH_2O, fixed pO_2 and fixed pCO_2 measurements performed at 1000 °C during a test is shown in **Figure 5-2**.

The sequence was repeated at 850 °C thereafter. Other sequences included the fixed pH_2 variation.

Polarization measurements were then performed in at least the 50-50% H_2-H_2O and CO-CO_2 gas atmospheres at one or more temperature points. First, IS was measured at OCV. Then, anodic polarizations were performed: cyclic potential sweeps with consecutively higher upper limits and 3 repeated cycles at the highest upper limit of +300 mV, and IS at +50 or +100 mV increments to +300 mV. Before each IS measurement under polarization, the desired polarization was first held for 5 minutes of DC bias chronoamperometrically to reach near-steady state, and then the impedance measurement was immediately started at that bias. IS were then measured at OCV for at least 12 h during which the impedance response of some electrodes relaxed. The same process was repeated for cathodic polarizations, to –300 mV, followed by at least 12 h relaxation at OCV. Finally, full sweeps in both anodic and cathodic directions, with consecutively higher ranges up to maxima of +300 and –500 mV, were performed.

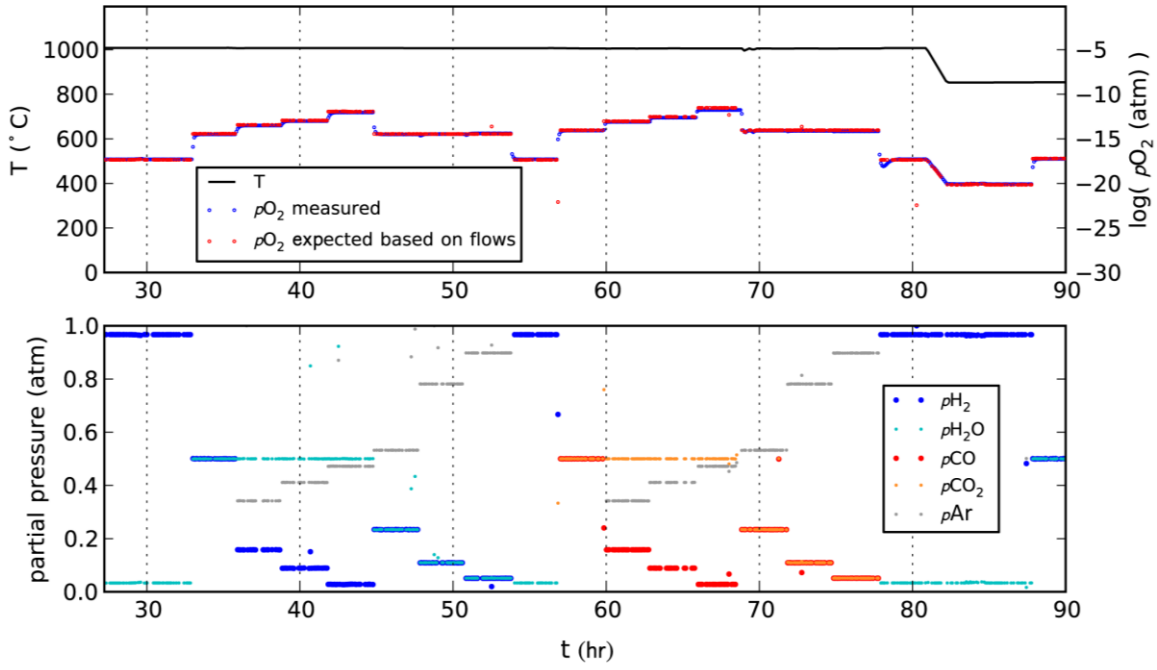

Figure 5-2. Example of a gas variation performed at 1000 °C during a test. "pO_2 expected based on flows" is the pO_2 expected using the Nernst equation (see section 1.1.1) and the set flows of H_2, H_2O, CO, CO_2, and Ar that give the gas partial pressures shown in the lower plot.

In some tests, extreme conditions were applied. In one test with Ni electrodes, the electrodes were oxidized by exposure to air for several hours, at 850 °C and again at 1000 °C,

followed by re-reduction in an H_2-rich atmosphere. In some tests, a strong cathodic polarization was applied to some of the electrodes, based on ref. [14]. The gas atmosphere was set to dry H_2, reaching a pO_2 sensor value of –1370 mV vs air at 850 °C ($pO_2 < 10^{-24}$ atm). Then, the following potential sweeps were performed at 20 mV/s: 0 to –500 mV, 0 to –1000 mV, and –1500 mV. Upon reaching each cathodic voltage, IS were also measured under that voltage. After both extreme conditions, OCV-IS temperature variations and/or polarization characterizations were performed. **Table 5-1** summarizes the parameters that were changed during the tests.

After the test, the cells were disassembled and the electrode was lifted off the electrolyte surface. Both surfaces were examined in the SEM. The final contact area and perimeter (TPB length) were measured from the SEM micrographs using Adobe Photoshop CS4 Extended.

Table 5-1. Summary of the parameters changed during the electrochemical testing.

Metal	Gas composition	Temperature	Polarization	Time
• Ni • Cu • Pd • Pt • Ag • Au	• H_2/H_2O with ranges $0.01 < pH_2 < 1.0$ and $0 < pH_2O < 0.62$ ▪ Fixed pH_2 ▪ Fixed pH_2O ▪ Fixed pO_2 (via dilution by Argon) • CO/CO_2 with ranges $0.03 < pCO < 0.86$ and $0.05 < pCO_2 < 0.5$ ▪ Fixed pCO_2 • Extreme condition: oxidation by air	• 750 °C to 1000 °C	• +300 mV to –500 mV potential sweeps and EIS at 50-100 mV increments of DC bias • Extreme condition: –1500 mV	• At the start, time for stabilization of interface • After changing parameters, waited for steady-state • Tests ran up to 800 hours

5.3. Results and Discussion

In the following sections, the results are presented and specific results are accompanied by discussion. A broader discussion of all the observed phenomena in terms of reaction mechanisms follows in **section 5.4**.

5.3.1. Initial Stabilization of the Interface

Upon arriving at the initial temperature (850-1000 °C), R_S decreased logarithmically for each cell and nearly stabilized within 10-50 h depending on the metal and the temperature (**Figure 5-3**). This was observed for each metal, as has been observed for Ni wire electrodes in the

literature [37]. The time scale was similar to that for Ni wire electrodes in the literature, for this temperature range [11, 37] and much faster than for lower temperature of 500 °C [14]. The Newman relation [40]

$$r = \frac{1}{4 \cdot \sigma_{el} \cdot R_S} \tag{5.1}$$

(where σ_{el} is the electrolyte conductivity) has been shown to approximate the contact radius for point-contact electrodes on solid electrolytes with dimensions on the same order of magnitude as those used in these tests[ii]. The initial decrease in R_S corresponds to an increase in the contact area, which results from the creep of the metal wires at high temperature. The contact area of the Cu wires (**Figure 5-3a**) grew more and for a longer time period than that of the Ni wires (**Figure 5-3b**). The higher creep rate of copper corresponds to the lower melting point of copper. The higher melting point metals Pt and Pd crept similarly to Ni, while the lower melting point metals Ag and Au crept similarly to Cu. Also shown in **Figure 5-3** is the length-specific polarization resistance, LSR_p, as it varies with the varying R_S. The significance of LSR_p is discussed in the next section.

The metal wire electrodes also sometimes "un-crept" when returning to lower temperatures, as can be seen in **Figure 5-4**. At 850 °C, R_S decreased until the temperature was elevated to 1000 °C, at which point R_S decreased further and then stabilized at 63 **Ω**. Upon returning to 850 °C, R_S increased slightly and re-stabilized, indicating that the contact area shrunk slightly.

Whereas Cu, Ni, Pd, and Pt showed a stable contact area at 700-1000 °C, Ag and Au did not at 700-900 °C (the lower maximum temperature due to the melting point of Ag). During a test with Ag and Au electrodes, at one point both showed a quick decrease in R_S (increase in contact area). While the exact reasons and conditions for this were unclear, because of this instability, because Ag and Au had the highest polarization resistance, and because the purity of Ag and Au were unknown, these metals were not studied further. One possibility for the increase in contact area is migration of the metal on the YSZ surface, which might be the case at least for Au according to the SEM micrographs shown in **Figure 5-5**. In the literature, noble metals such as Pt, Pd, and Ag were observed to migrate on YSZ surfaces and form dendritic structures [41 , 42] (although in that study they were in oxidizing atmospheres).

[ii] The Newman relation was derived for an aqueous cell and is valid when the distance between the working and reference electrodes is infinite (large). Newman supported this experimentally by positioning the reference electrode at different distances from the working electrode. Analogous formulas have been derived for heat conduction (pointed out by Newman) and electrical circuits.

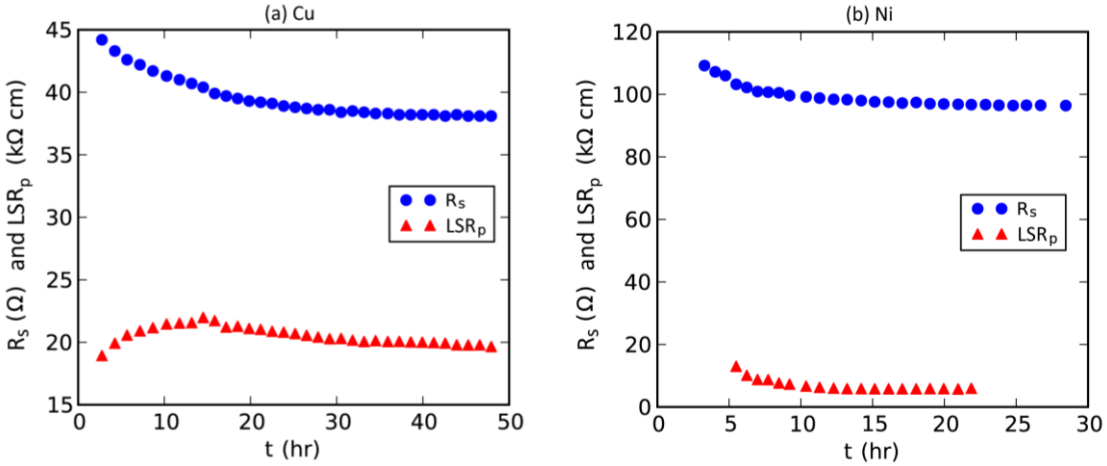

Figure 5-3. Examples of the initial stabilization of the serial resistance (R_S) and length-specific polarization resistance (LSR_P) at the beginning of a test, for (a) a copper wire electrode and (b) a nickel wire electrode. The time is the hour after arriving at 1000 °C. LSR_P is shown when the gas composition was 97% H_2 + 3% H_2O.

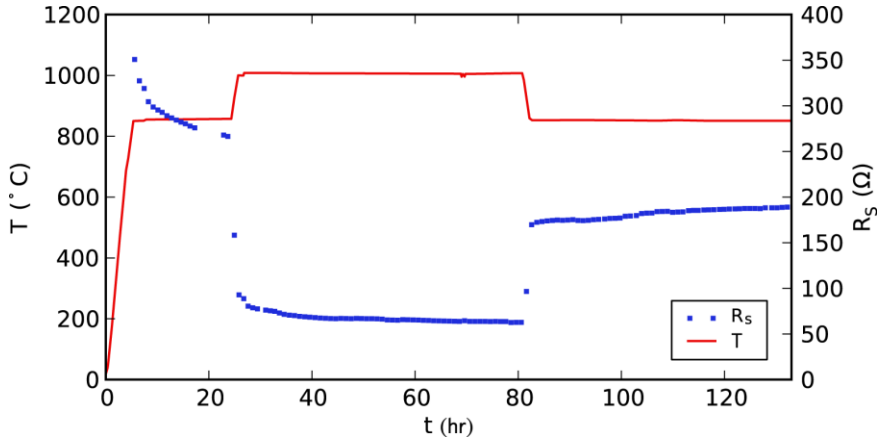

Figure 5-4. Change in R_S for a Ni wire electrode at different operating temperatures at the start of a test.

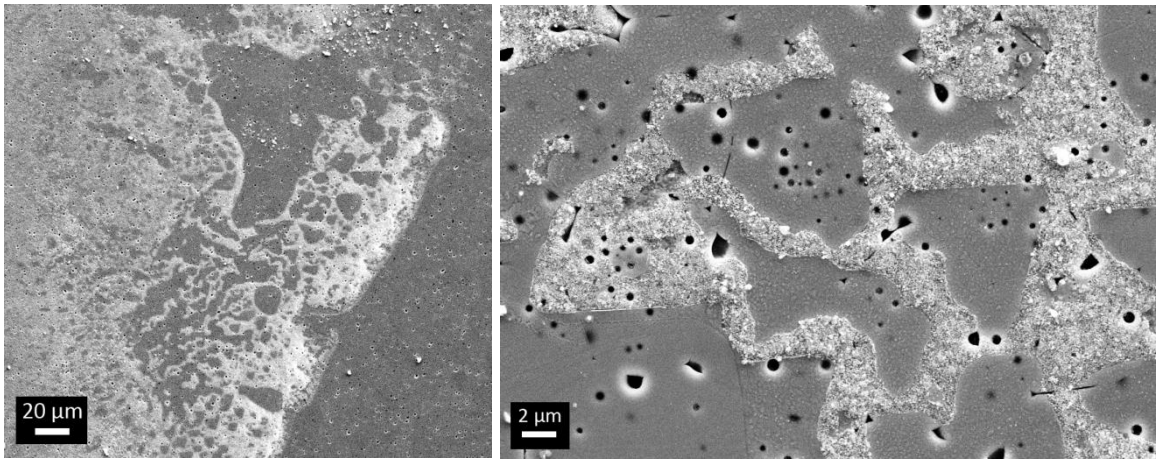

Figure 5-5. SEM micrographs of the YSZ surface where an Au wire electrode had been in contact during testing at up to 900 °C. The lighter areas are Au/YSZ and the darker areas are only YSZ.

5.3.2. Data Normalization and Reproducibility

Ideally, equation (5.1) could simply be used to estimate the size and shape of the metal-YSZ interface. However, there are several possible deviations from ideality:

- The interface does not form a perfect circle, which equation (5.1) is based on
- The conductivity of the electrolyte material must be assumed based on prior measurements
- Measurements of R_S may be larger than expected in an ideal interface due to non-negligible interfacial resistance between the two materials

For some studies, equation (5.1) may be a close enough approximation. However, in this study it was intended to compare the measurements between many electrodes including those of different materials, so a method was developed to manage these non-idealities. After cooling down after a test was complete, the wire electrodes were carefully lifted off of the YSZ surfaces and both surfaces, the flattened metal contact area and the polished YSZ surface where the metal wire had been contacting it, were examined in the SEM. The contact area and perimeter were measured from SEM micrographs of the elliptical flattened area of the metal wire (**Figure 5-6**), and they agreed with the areas on the YSZ surface which exhibited differences in topography relative to the smooth surface outside the contact area (see **Figure 5-7** for the matching "hill-and-valley" topographical patterns on both surfaces and in **Figure 5-15** the smooth surface outside the contact area can be seen). These topographical differences have been studied in literature [11, 14, 35-37, 43]. First, a correction factor for the area $f_{c,area}$ was applied:

$$f_{c,area} = \frac{A_{SEM}}{\pi \cdot {r_N}^2} \tag{5.2}$$

where A_{SEM} is the measured area from the SEM micrograph and r_N is the radius estimated from Newman equation (5.1) using the final R_S and temperature measured at the end of the test (and the YSZ conductivity was estimated at this temperature based on literature [44]). Next, a roughness factor $f_{c,per}$ was applied, to account for the deviation in the perimeter length from a perfect circle:

$$f_{c,per} = \frac{x_{SEM}}{2 \cdot \sqrt{\pi \cdot A_{SEM}}} \tag{5.3}$$

where x_{SEM} is the perimeter length measured from the SEM micrograph and $2 \cdot \sqrt{\pi \cdot A_{SEM}}$ is the perimeter length that corresponds to a perfect circle having the area of A_{SEM}. Note that using these correction factors for times earlier in the test assumes that the overall shape of the contact area did not change by a lot during the slight creep and "un-creep" that occurred after initial stabilization.

A few example calculations of these correction factors are given in **Table 5-2**. One can see that the Newman relation consistently underestimated the contact area by about a factor of 2, and that all of the contact areas had a rough perimeter which was longer than that corresponding to a perfect circle. Electrode Ni-5 stands out from this group – it had a much higher roughness factor of 2.38. The flattened contact area of Ni-5 is shown in **Figure 5-6** (labeled "Ni"). One can see that the perimeter boundary is very rough in comparison with most of the other wires, such as Cu and Pt (also shown in **Figure 5-6**). The other Ni electrodes listed in **Table 5-2**, Ni-1 to Ni-4, were the wires that included electropolishing as a final stage of preparation, so their surfaces were especially smooth and they formed an even smoother contact interface than that of the Pt wire shown in **Figure 5-6**. Without electropolishing, the bent Ni wire Ni-5 had a fractured surface going into the test. The Pd wire shown in Figure 5-6 shows a similar degree of fracture and resulting roughness.

Using these correction factors, the impedance measurements can be normalized to either the contact area or the perimeter of the contact area by multiplying them by $f_{c,area} \cdot \pi \cdot {r_N}^2$ and $f_{c,per} \cdot 2 \cdot \sqrt{f_{c,area}} \cdot \pi \cdot r_N$ respectively, where r_N is the radius estimated by equation (5.1). Since the reaction sites have been linked to the TPB, the TPB length (TPBL), which is the perimeter for these point-contact electrodes, may be a useful metric to normalize resistances [4, 6, 19, 21, 24]. This is illustrated in **Figure 5-8** – the TPBL-normalized impedance measurements are reproducible, whereas the area-normalized impedance measurements are not. The fact that the area-normalized impedance of the rough Ni-5 electrode is the farthest from the others whereas its TPBL-normalized impedance agrees well with that of the smooth, shorter-TPBL electrodes confirms that the TPB is the primary location of the reaction sites. The other metals showed

similarly high reproducibility between electrodes for TPBL-normalized impedance measurements.

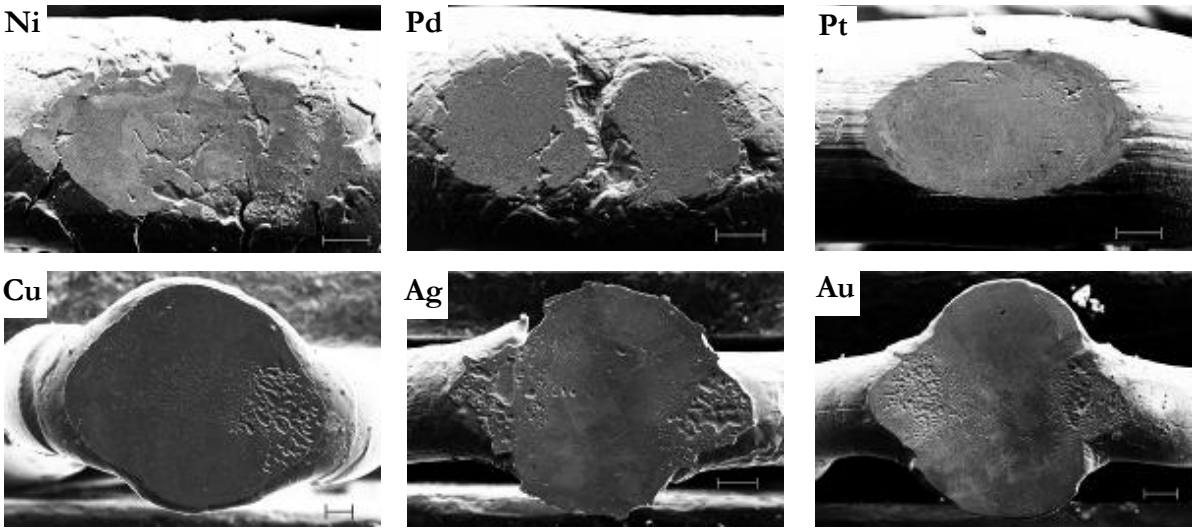

Figure 5-6. SEM micrographs of the flattened contact areas of representative wires of each metal. The scale bar shown in each is 100 microns. The smooth electropolished Ni wires are not shown. Large pieces of YSZ electrolyte were sometimes attached (not shown). The 3 lowest melting point metals (Cu, Ag, Au) crept the most, resulting in the largest contact areas. Some Pd wires such as the one shown formed a crack when bent, which did not heal, resulting in 2 separated contact areas. The bulb-tipped electrodes (not shown) formed a more circular interface rather than the elliptical shape seen here for Ni, Pd, and Pt.

Table 5-2. Examples of the normalization process. The shaded columns are measurements. The two factors $f_{c,area}$ and $f_{c,per}$ are obtained by dividing A_{SEM}/A_N and $x_{SEM}/2\sqrt{\pi\, A_{SEM}}$ respectively.

Electrode	Final R_S (Ω)	Final T (°C)	r_N (mm)	A_N (mm^2)	A_{SEM} (mm^2)	$f_{c,area}$	$2\sqrt{\pi\, A_{SEM}}$ (mm)	x_{SEM} (mm)	$f_{c,per}$
Ni-1	235	849	0.158	0.079	0.181	2.30	1.51	1.84	1.22
Ni-2	249	849	0.149	0.070	0.149	2.13	1.37	1.91	1.39
Ni-3	206	849	0.181	0.103	0.213	2.07	1.64	2.02	1.24
Ni-4	249	849	0.149	0.070	0.161	2.30	1.42	1.81	1.27
Ni-5	189	854	0.168	0.089	0.153	1.73	1.39	3.30	2.38
Cu-1	107	854	0.296	0.275	0.536	1.95	2.59	2.98	1.15
Cu-2	108	854	0.294	0.272	0.510	1.88	2.53	2.94	1.16

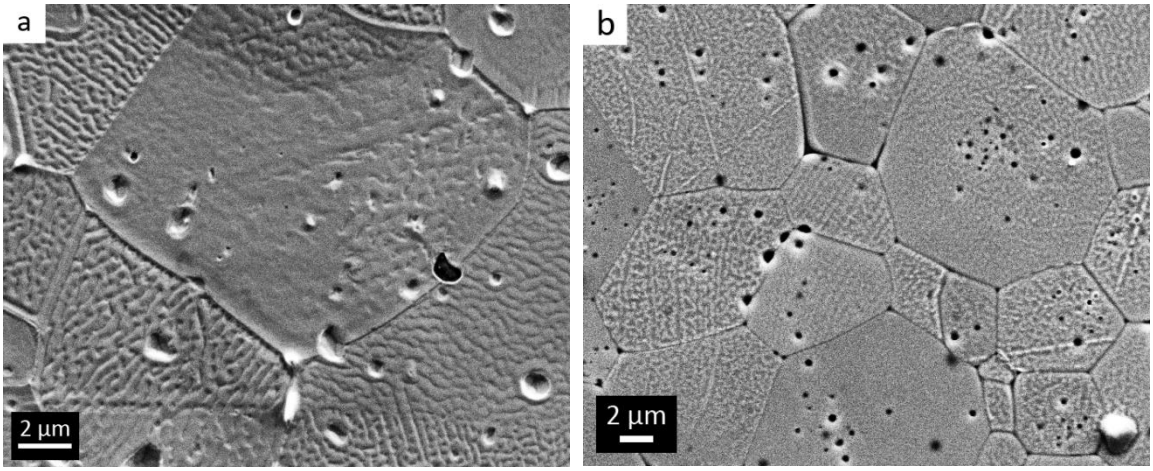

Figure 5-7. SEM micrographs showing the matching topographical patterns within the metal-YSZ interface on (a) the metal surface (Ni wire in this case), and (b) the YSZ surface.

Strictly speaking, if any morphological changes happen at the TPB during a test, this method may not accurately estimate the TPB length for those times in the test. For example, both of the extreme conditions of oxidation and strong cathodic polarization (**section 5.3.5**) seem to change the TPB length either by inducing the formation of a finer microstructure (perhaps temporarily) or freeing the TPB from segregated impurities that were blocking it. Therefore, the normalized data from after those events most likely underestimates the TPB length, but since the contact area did not change and a zoomed-out view of the TPB most likely looks the same, it is still useful as an indication of the degree of activation that occurred as a result of those phenomena.

Note that the contact area has a different meaning than the nominal area usually discussed in regards to three-dimensional porous electrodes. For porous electrodes, the TPB length cannot be accurately determined, so the nominal geometric area of the porous structure is used for normalization, keeping in mind that only a small fraction of this area comprises the active reaction sites. For the point-contact cell geometry, while the contact area is clearly not useful for normalizing the polarization resistance, it is still useful for normalizing the capacitance across the metal-YSZ contact [6].

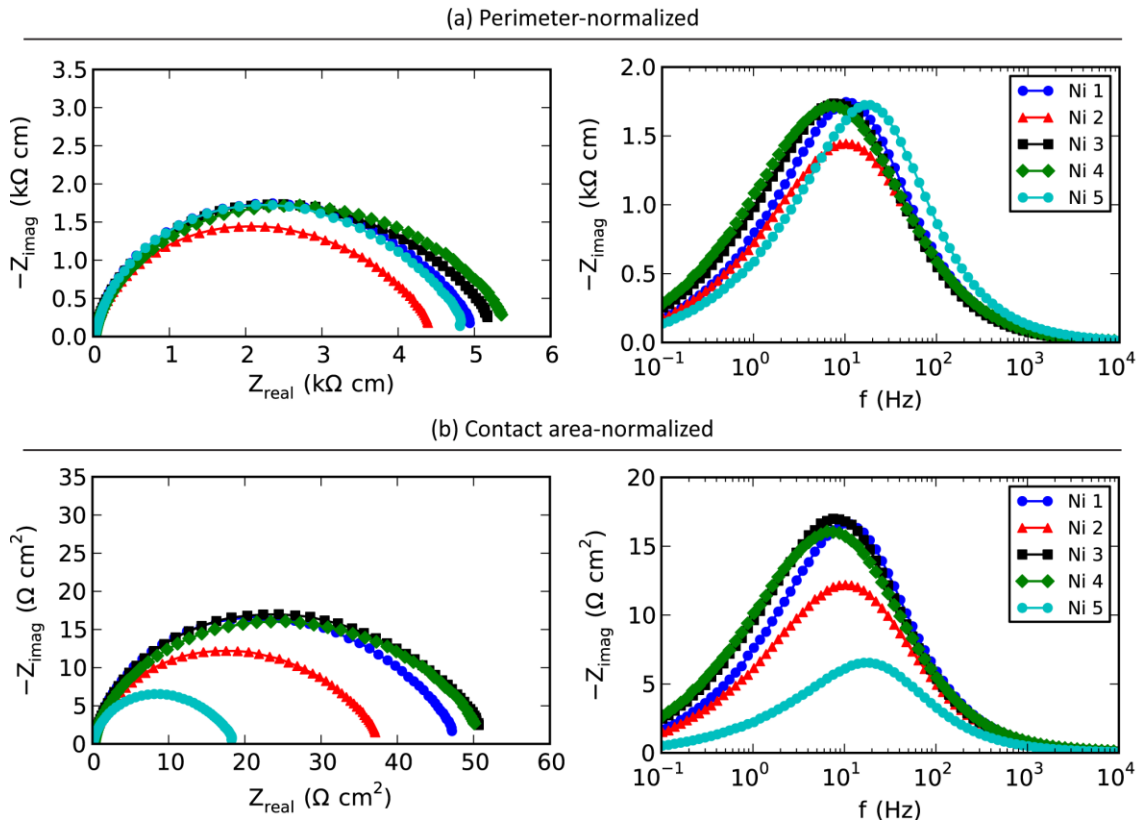

Figure 5-8. Impedance spectra measured on five Ni wire electrodes in 97% H_2 + 3% H_2O at 1000 °C at the start of a test shortly after heat-up, (a) normalized to the TPBL, and (b) normalized to the contact area.

5.3.3. Impedance Spectroscopy at OCV

5.3.3.1. Number of Rate-limiting Processes

IS were measured at open circuit voltage at systematically varied gas compositions and operating temperature. Analysis of IS employed the method of condensing the impedance data by representing it with an equivalent circuit model. This is a useful way to reduce the data and attempt to identify the processes contributing to the impedance data without knowing the nature of the physical and/or chemical processes, before attempting to construct a true physical/electrochemical model of the system. Simple equivalent circuits composed of serial RQ elements were used, where R is a resistor and Q is a constant phase element [45].

The IS could be fit with low error to an equivalent circuit model composed of up to 3 serially-connected RQ elements, $LR_S(RQ)_1(RQ)_2(RQ)_3$. The inductance L, usually associated with artifacts of the test set-up, was minor in comparison to the magnitudes of the cell impedance, so most fits were performed without L and by discarding the high frequency range at which L contributed (>100 kHz, which was much higher frequency than any contributions from the cell response). Using the Kramers-Kronig transform, this high frequency data was

found to include greater measurement error. Some IS and fitting results are shown in **Figure 5-9**. $R^2 > 0.96$ for all of the fits shown.

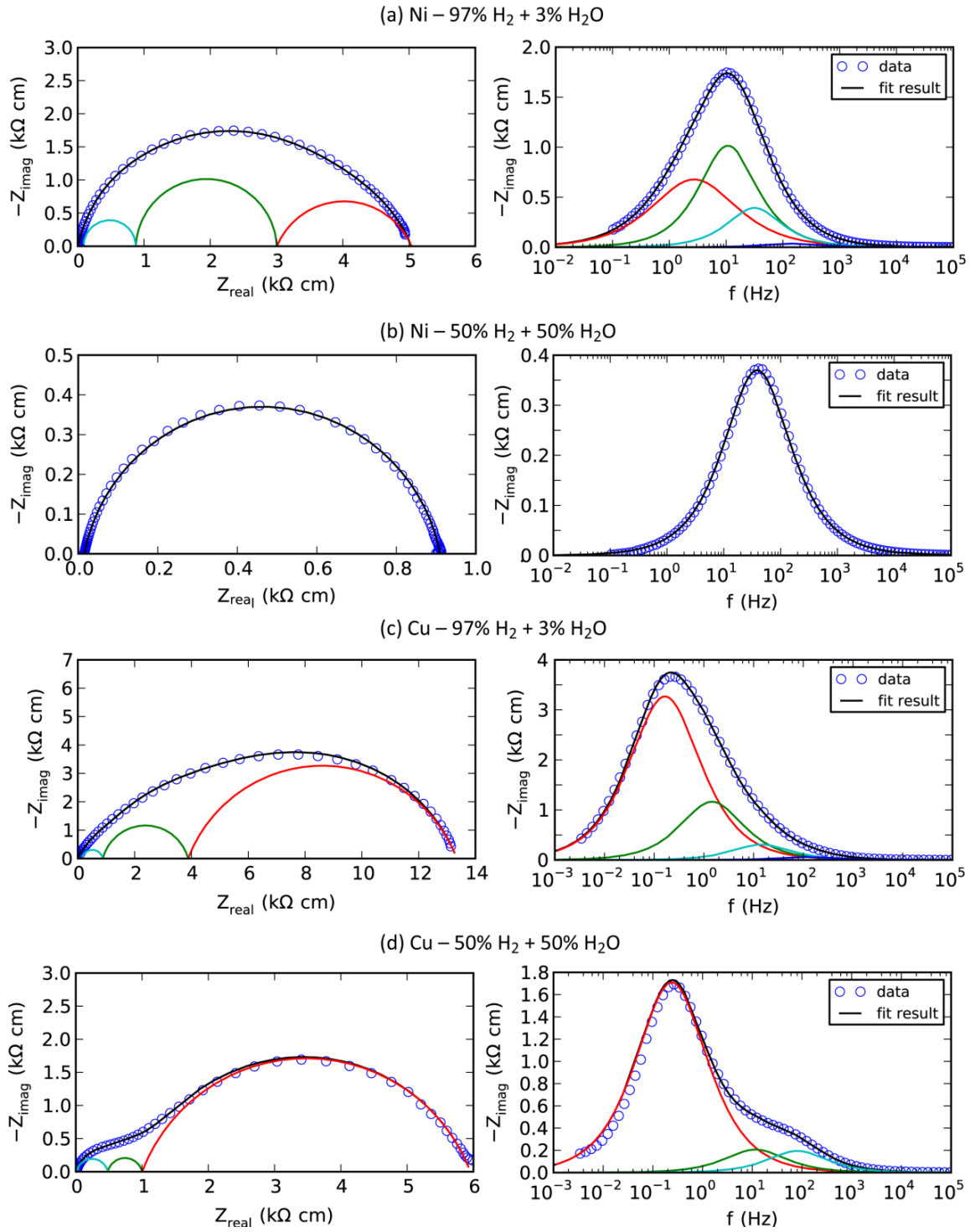

Figure 5-9. Some impedance spectra measured at OCV at 1000 °C in H_2/H_2O atmospheres on (a) a Ni electrode, and (b) a Cu electrode. The non-linear least squares fitting results using equivalent circuits composed of 1-3 serially connected RQ elements are also shown along with the impedance of the individual RQ elements.

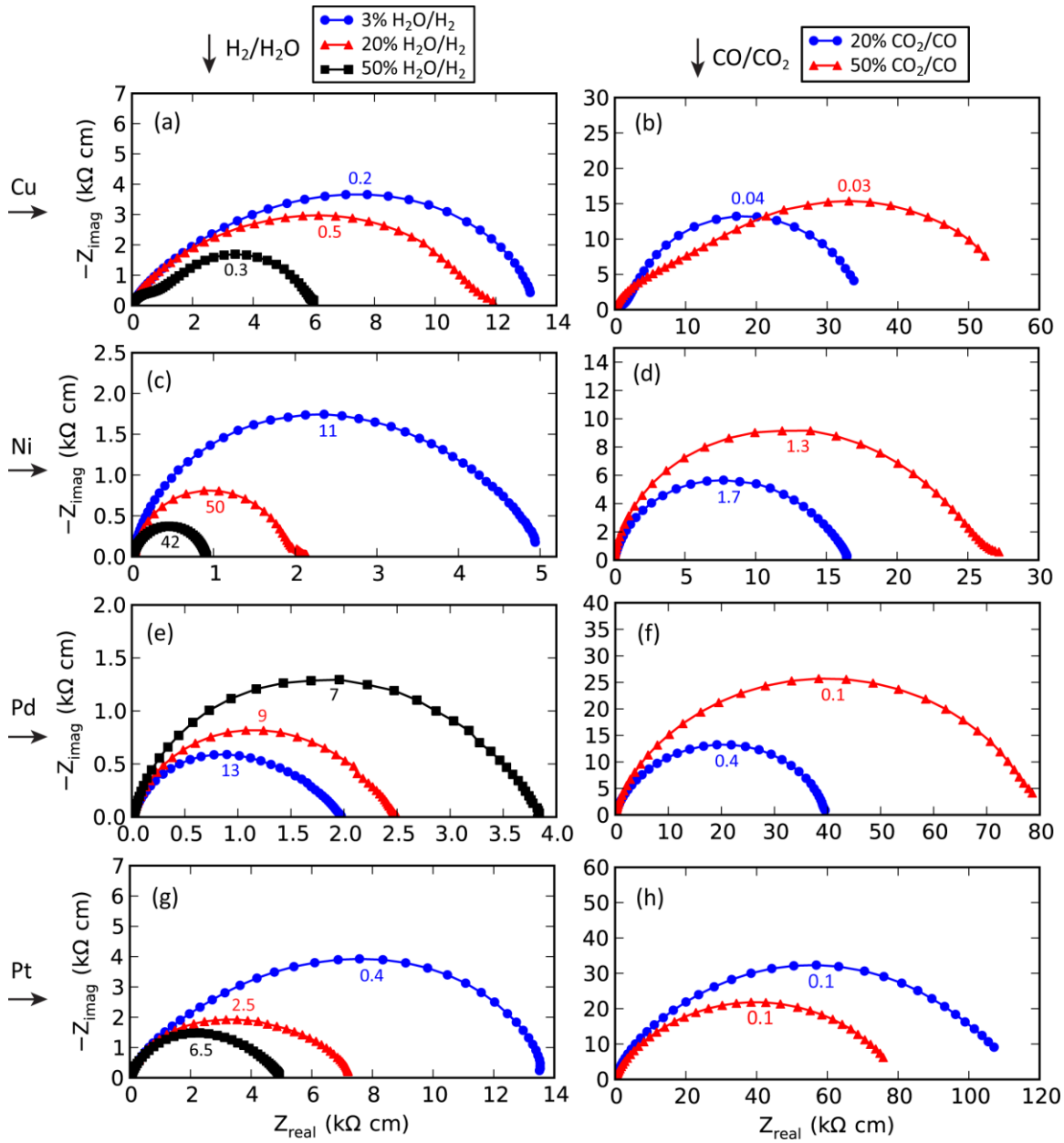

Figure 5-10. Impedance spectra measured at OCV at 1000 °C at Cu, Ni, Pd and Pt electrodes (one metal per row) in various H_2/H_2O atmospheres and CO/CO_2 atmospheres (columns). The numbers shown next to each spectra are the approximately summit frequency. Some of the spectra shown for Ni and Cu are the same as those shown in **Figure 5-9**. The low-frequency "tails" are true reproducible measurements and not the results of drifting conditions.

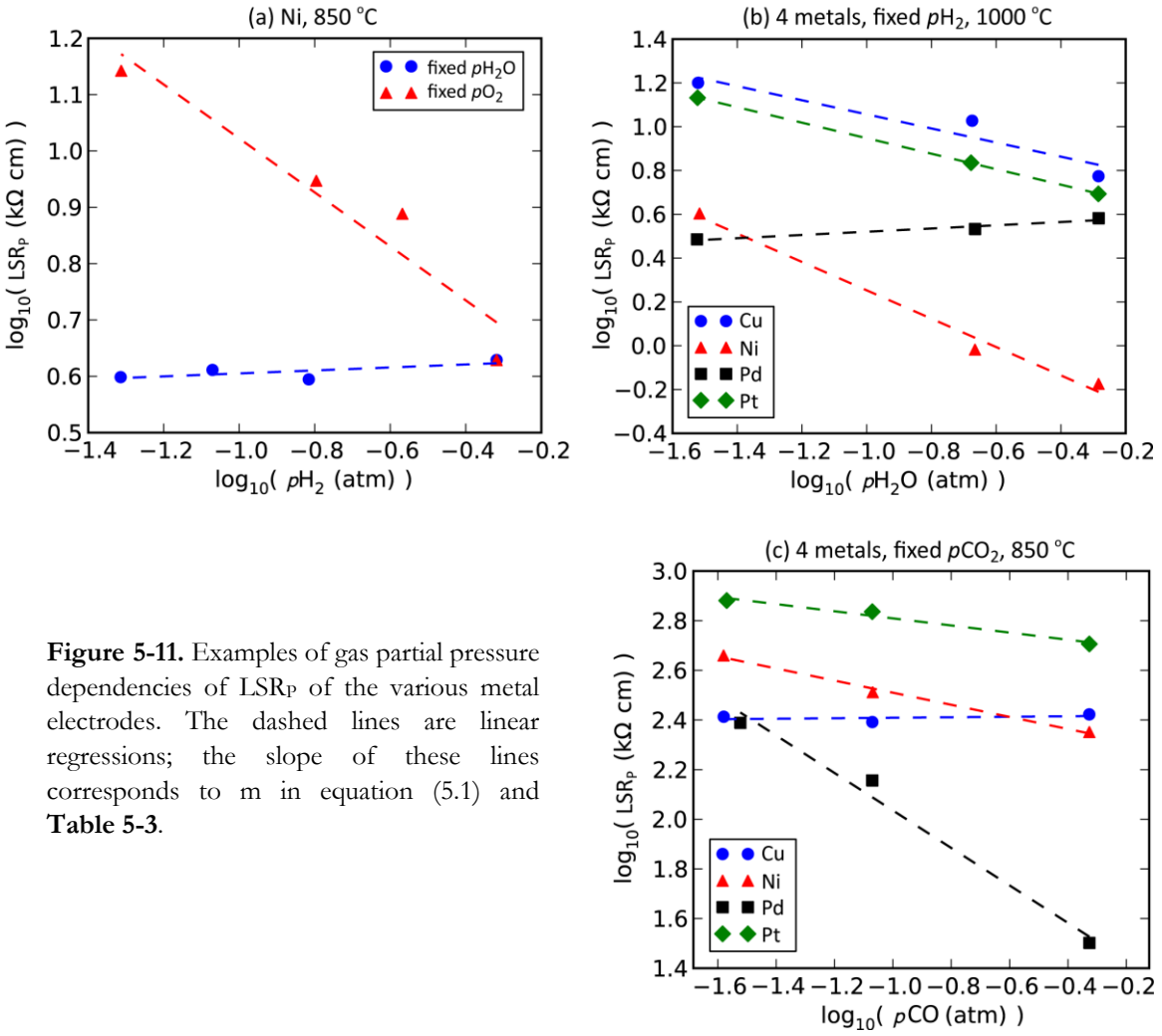

Figure 5-11. Examples of gas partial pressure dependencies of LSR_P of the various metal electrodes. The dashed lines are linear regressions; the slope of these lines corresponds to m in equation (5.1) and **Table 5-3**.

Table 5-3. Gas partial pressure dependencies of LSR_P at 850 °C, using equation (5.1). The pO_2 dependences for the fixed pH_2O and fixed pH_2 variations are equal to the m values listed for pH_2^m and pH_2O^m multiplied by factors of -1 and ½ respectively. Since R^2 regression coefficients for near-zero slopes (m values) are meaningless, they are not shown. Some of the gas variations included only 3 data points, so the statistical significance may not be as high as implied by the high R^2 values.

Metal	Cu	Ni	Pd	Pt
Fixed pO_2: m, in pH_2O^m and pH_2^m	-0.45	-0.61	-0.46	-0.54
R^2	1.000	0.969	0.983	1.000
Fixed pH_2O: m, in pH_2^m	0.17	0.02	-0.10	0.00
R^2	0.967	-	0.998	-
Fixed pH_2: m, in pH_2O^m	-0.46	-0.63	0.07	-0.57
R^2	0.963	0.997	0.947	0.994
Fixed pCO_2: m, in pCO^m	0.01	-0.24	-0.76	-0.14
R^2	-	0.993	0.984	0.974

For the Ni electrodes at 1000 °C in 97% H_2 + 3% H_2O, 3 processes were evident (**Figure 5-9a**). The high-frequency arc 1 had n-values (for the constant phase element) close to unity (>0.97). For the mid-frequency arc 2, n was around 0.95. For the low-frequency arc 3, n was around 0.73. Sometimes a fourth small high-frequency arc was found (barely visible in the Bode plot in **Figure 5-9a**), which consistently contributed <2% to the total impedance. This can likely be ascribed to the porous Pt counter electrode: a symmetrical cell with this electrode painted on both sides of an 8YSZ pellet was tested and the magnitudes and the high summit frequency of the impedance response agrees well with this minor arc. All of the processes were found to be temperature-activated by approximately the same amount, and there was little to no change in shape of the IS with change in temperature. The shape of the IS in **Figure 5-9a** compares well with that found in literature for similar conditions with similar Ni wire electrodes contacting non-high-purity stabilized zirconia [11, 37, 43].

On the Ni electrode, it appears that an increase in pH_2O causes a decrease in the impedance of the lower-frequency RQ elements, so much so that they become negligible and only one process remains (**Figure 5-9b**). The Cu electrode also needed 3 RQ elements for a low-error fit, and the impedance of these processes was also reduced with increasing pH_2O (**Figure 5-9c+d**). One might consider that gas concentration effects can result in reduced R_P with higher pH_2O for solid oxide cells [46-48]. However, such contributions are expected to be negligible for point electrode tests [46, 47]. Furthermore, such processes should not be thermally activated, but for the measurements obtained here all three processes appear to have a strong and similar temperature dependence. Finally, the same effect was not seen with increased pCO_2 in CO/CO_2 atmospheres, and some of the point electrodes showed the opposite response in H_2/H_2O – both of these results are described below. This confirms that there are no gas concentration processes contributing to the IS.

5.3.3.2. Effects of Gas Composition

The IS from the first set of gas variations – 3%, 20%, and 50% H_2O with balance H_2, and 20% and 50% CO_2 with balance CO – at 1000 °C are shown in **Figure 5-10**. The fitted spectra for Ni shown in **Figure 5-9** and discussed in the prior section are part of the variation shown in **Figure 5-10c**. The single-arc impedance observed at 50% H_2O / H_2 is further reduced by about 25% when continuing the variation to 62% H_2O / H_2 (not shown).

The effects of the gas composition were further examined by gas variations with fixed pH_2, fixed pH_2O, fixed pO_2 and fixed pCO_2. The dependencies of LSR_P on the partial pressure of a gas can be correlated by equation (5.1). This empirical correlation is discussed in references [1, 20, 49].

$$log\ (LSR_P) = m \cdot \log\ (p\mathrm{X}) \tag{5.1}$$

Results of the gas variations at 850 °C and the linear regression of equation (5.1) using the results are shown in **Figure 5-11** and **Table 5-3** respectively. The same gas variations (but a less complete set) were performed at 1000 °C and the trends were nearly the same, but with usually somewhat shallower slopes (m values).

Some trends in the dependence of the impedance on the gas composition can be clearly seen.

—*All of the metals showed better performance in 50% H_2O/H_2 than in 50% CO_2/CO, by a factor of 10-25 at this temperature* (**Figure 5-10**). In the literature, for Ni similarly large differences have been sometimes reported for porous Ni-YSZ cermet electrodes [32, 33]. On the other hand, other results have shown only 25-50% higher resistance for oxidation/reduction of CO/CO_2 versus H_2/H_2O for porous Ni-YSZ cermet based cells [34, 50-52] (and see Chapter 4).

—*One can distinguish the relative electrocatalytic performance of the metals in different atmospheres* (**Figure 5-10**). For the different metals, the relative electrocatalytic activities clearly vary with gas composition. The gas partial pressure dependencies identified below further describe this effect. The relative performance is further examined in the following section in regards to temperature dependency, and in regards to polarization in **section 5.3.4**.

—*Trends in the shapes of the impedance spectra are also observed* (**Figure 5-10**). In 3% H_2O/H_2, Ni and Pd have nearly identical shape, and Cu and Pt have a different, nearly identical shape. Ni and Pd also have significantly higher performance than Cu and Pt in 3% H_2O/H_2, which might be due to the large low-frequency process that defines the shape of the Cu and Pt IS (e.g. see **Figure 5-9c** for Cu). It is worth noting also that only Ni seems to approach a single semicircle shape at any conditions.

—*Different pH_2O, pH_2, and pCO_2 dependencies are observed for the different metals* (**Figure 5-10**, **Figure 5-11** and **Table 5-3**). Notably, when shifting to higher pH_2O, Cu, Ni and Pt are all activated (LSR_P is reduced), whereas Pd has the opposite response. In CO/CO_2 atmospheres on the other hand, it is Pt that shows a different response than the rest, being activated by increased pCO_2 whereas Cu, Ni, and Pd all show higher impedance. The "fixed" gas variations reveal more information about these trends:

- In H_2/H_2O atmospheres, Ni and Pt show similar responses, LSR_P having minor or negligible pH_2 dependency and strong pH_2O dependency (**Figure 5-11a** and **Table 5-3**). The dependency of LSR_P on pH_2O for Ni, m = –0.63, is within the range found in literature, –0.35 to –0.87 (and most often close to –0.5), for simple-geometry Ni electrodes [4, 7, 21, 22, 24, 25]. The lack of pH_2 dependency also agrees with most literature (same references). While the LSR_P of Cu also shows a similar trend, it does have a pH_2 dependency and it has a somewhat weaker pH_2O dependency. Pd shows anomalous behavior, with inverse dependencies on pH_2 and pH_2O compared with the other metals. This can be attributed to the Pd-H system (discussed further in following sections).

- In CO/CO_2, Cu is the metal with the anomalous impedance responses, having negligible pCO dependence (**Figure 5-11c** and **Table 5-3**). Since the LSR_P of Cu significantly increased when changing both CO and CO_2 – from 20% CO_2/CO to 50% CO_2/CO (**Figure 5-10b**) – it may be dependent on pCO_2. The CO/CO_2 behavior of Pt in **Figure 5-10h** is not evident in the fixed pCO_2 gas variation (**Figure 5-11c** and **Table 5-3**), suggesting that Pt may be activated by higher pCO_2 and not by lower pCO.

5.3.3.3. Effects of Temperature

The temperature dependence of the electrode impedance also provides information about the electrode kinetics. Using the Arrhenius relation, the activation energy can be obtained by multiplying k in equation (5.2) with the ideal gas constant.

$$\ln\left(1/\mathrm{LSR_P}\right) = k \cdot (1/\mathrm{T}) \tag{5.2}$$

Figure 5-12 shows the results of the temperature variation from 750-1000 °C in 3% H_2O/H_2, 50% H_2O/H_2, and 50% CO_2/CO, along with the linear regression of the results in equation (5.2). The impedance closely follows this relation. As mentioned earlier, the shape of the IS did not appreciably change at different temperatures – all of the processes contributing to the impedance appear to have similar temperature activation.

The activation energy (E_A) of LSR_P was quite similar for all of the metals:

- In 3% H_2O/H_2, it was in the range 1.4-1.7 eVfor Ni, Pd, and Pt, while for Cu it was about 2.0 eV.
- In 50% H_2O/H_2, all were in the range 1.3-1.6 eV.
- In 50% CO_2/CO, all were in the range 1.8-2.0 eV.
- The E_A for R_S was 0.85 eV for 850-1000 °C or 0.8-0.9 eV in the 750-1000 °C range (not shown), which corresponds well with literature for the oxide ion conductivity of YSZ [49].

The E_A for Ni, 1.4 and 1.6 eV in 3% H_2O/H_2 and 50% H_2O/H_2 respectively, agrees well with most results for Ni point electrodes in literature [1, 6, 7] as well as some Ni pattern electrodes [24]. On the other hand, a Ni point electrode prepared on high-purity single-crystal stabilized zirconia had a much lower E_A of 0.9 eV [14] albeit at a lower temperature range, 500-750 °C, and many finer-structure (pattern, porous, and cermet) electrodes have a similarly low E_A [21, 25, 26]. Baker et al reported an E_A for Pd of ~1.2 eV in 5% H_2 + 5% H_2O + 90% N_2 in the 600-800 °C range [6], which is not far from the 1.3 eV found here in 50% H_2O/H_2 (same H_2/H_2O ratio). However, that same study reported only 0.8 eV for Pt, and here it is 1.5 eV in 50% H_2O/H_2.

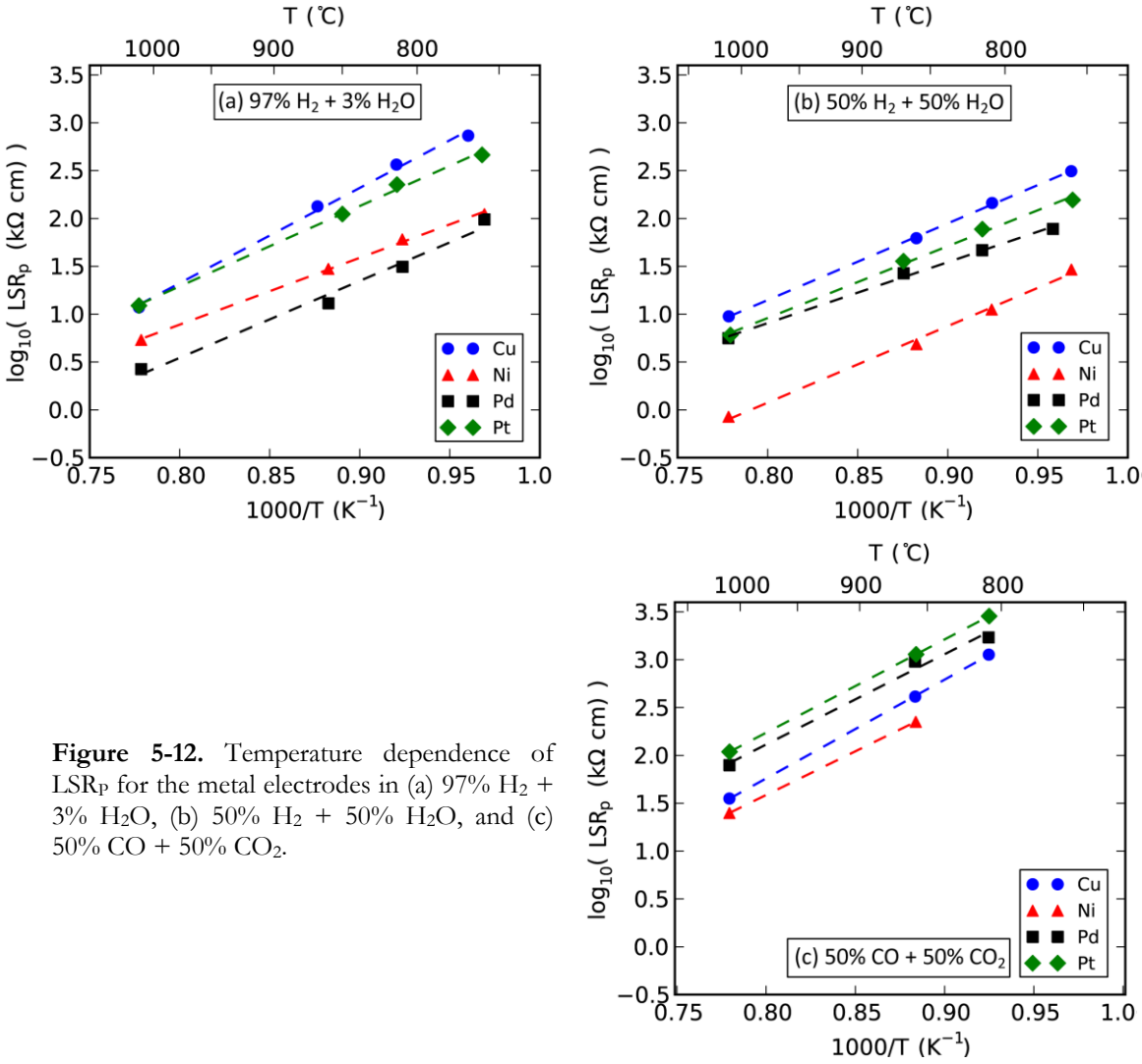

Figure 5-12. Temperature dependence of LSR_P for the metal electrodes in (a) 97% H_2 + 3% H_2O, (b) 50% H_2 + 50% H_2O, and (c) 50% CO + 50% CO_2.

The relative performance of the metals at OCV in the three different gas compositions observed at 1000 °C (**Figure 5-10**) holds throughout this temperature range, due to the similar activation energies.

- In 3% H_2O/H_2, Pd shows the lowest LSR_P, followed by Ni, and then Cu and Pt which have nearly the same LSR_P (Pd > Ni > Pt/Cu).
- In 50% H_2O/H_2, the order is different: Ni > Pd > Pt > Cu. Pd is less active than it was in the higher H_2/H_2O ratio. The results from literature do not consistently agree with these results (although they are also not generally available for the same gas compositions). In the Baker et al study mentioned above, LSR_P went Pt > Ni > Pd at 800 °C. If their 5% H_2 + 5% H_2O + 90% N_2 atmosphere can be compared to 50% H_2O/H_2 because the H_2/H_2O ratio is the same, then Pt was simply much more active in that study than it was here. As mentioned above, the E_A was also much lower than

observed here, so this is a likely possibility. Possible reasons will be discussed in section 5.4.

- In 50% CO_2/CO, the order is Ni > Cu > Pd/Pt. In CO/CO_2, Cu is more active than Pd and Pt. Cu is known to be a good catalyst for CO/CO_2 reactions such as methanol synthesis by CO_2 hydrogenation ($CO_2 + 3H_2 \rightarrow CH_3OH + H_2O$, see Chapter 3). Pt has the lowest performance in 20% CO_2/CO, which might be due to the blocking of Pt electrodes by CO, as proposed to explain the poor performance of Nernst probe oxygen sensors with Pt electrodes in dry CO/CO_2 atmospheres [53]. SOFCs with Pt electrodes were also shown to have poor performance in dry CO/CO_2 compared with H_2/H_2O atmospheres [34].

In regards to the magnitudes of LSR_P found in this study, for Ni at 1000 °C in 3% H_2O/H_2 the LSR_P is around 5 kΩ cm, which is within the wide range of ~0.2-20 kΩ cm found in the literature for these same conditions for Ni point electrodes [1, 11]. At 800 °C in 3% H_2O/H_2, the LSR_P for Ni is approximately 60 kΩ cm which is within the wide range reported for point and porous electrodes at similar conditions [1, 11].

5.3.4. Effects of Applied Potentials

5.3.4.1. DC Polarization Curves

Cyclic polarization curves (also known as cyclic voltammograms, or potential sweeps) were performed on all of the electrodes in 50% H_2O/H_2 and 50% CO_2/CO at 1-2 mV/s.

For Ni, the polarization curves show higher activity for H_2 oxidation than for H_2O reduction (**Figure 5-13**). High anodic potentials sometimes resulted in instability in both H_2/H_2O and CO/CO_2 which became apparently more regular oscillations in H_2/H_2O (**Figure 5-13**). Such oscillations were observed by Schmidt et al [15] for Ni point electrodes in H_2/H_2O (also in very different conditions – air – oscillations were observed for Pt [41] and Pd [42]). The instabilities appear to begin at approximately +190 mV for 50% H_2O/H_2 at 1000 °C and +150 mV for 50% CO_2/CO at 1000 °C, which is –690 mV vs air for both. In 3% H_2O/H_2, the instabilities appear to be absent, even at +300 mV (–760 mV vs air). At 850 °C in 50% H_2O/H_2, the instabilities begin at about +250 mV (–672 mV vs air). The instabilities seem to consistently begin when the local pO_2 becomes higher than a certain value (around 10^{-12} and 10^{-13} atm at 1000 °C and 850 °C respectively), independent of H_2/H_2O and CO/CO_2 atmospheres. It is near these values that Ni oxidizes to NiO, according to thermodynamics [54]. Therefore, because the instability is observed in both H_2/H_2O and CO/CO_2 atmospheres, this is clear evidence that at least part of the instability is caused by Ni oxidizing to NiO (after which it would be reduced again by incoming H_2 or CO). Both H_2 oxidation and CO oxidation are significantly activated by the instability phenomena, evident in the hysteresis in the polarization

curves that have instability (**Figure 5-13**). This observation is related to phenomena that will be discussed **section 5.3.5.1** (related to Ni/NiO phase changes).

This Ni-NiO transition was considered by Schmidt et al [15]. However CO/CO_2 tests were not performed and it was noted that NiO formation should not begin quite so soon (but also noted that surfaces can oxidize sooner than bulk). Instead, the explanation proposed was that a passivating film of $Ni(OH)_2$ was temporarily formed on the Ni, causing a slowing of the current, which was then reduced back to Ni by incoming H_2, causing a jump in the measured current, resulting in the sawtooth oscillation. The $Ni(OH)_2$ film is proposed to be passivating by assuming that the H_2 oxidation reaction mechanism is proton diffusion through Ni and the diffusion path grows longer as the passivating film grows. In addition, it was proposed that the H_2O formed at the TPB during anodic current reacts with impurities that are present at the TPB and mobilizes them (e.g. $SiO_2(s) + 2H_2O(g) \rightarrow Si(OH)_4(g)$), resulting in activation.

Because the oscillations are more periodic in H_2/H_2O than in CO/CO_2 (**Figure 5-13**), Ni-NiO may only explain part of the instability. A mechanism that involves $Ni(OH)_2$ might still be possible. During high anodic polarization, H_2 is consumed producing H_2O, and the potentials vs air mentioned above correspond to high local pH_2O/pH_2 ratios of >95/1. Thermodynamics indicates that volatile $Ni(OH)_2$ forms to an appreciable extent under such conditions [54], and literature studies of Ni/YSZ point electrodes and cermets have speculated that is the cause of observed morphological changes of Ni [8, 15, 55-57]. Alternatively, the formation of and surface transport of Ni_2–OH complexes might explain observed morphological changes [58]. Indeed, in the present study the Ni morphology was changed by anodic polarizations – submicron-sized Ni particles were present on the YSZ surface as a belt around where the interface had been (**Figure 5-15**), as has been sometimes observed in literature for Ni point electrodes [8, 15, 25] and even in Ni cermets [57]. It is believed that as the hydroxylated Ni species move away from the TPB to a lower pH_2O region, they reduce back to Ni metal and deposit as particles. Verification that the particle belt does not also form in CO/CO_2 would further support this mechanism, however no tests with anodic polarizations only in CO/CO_2 were conducted in this study. It seems plausible that the oscillations could be the result of the same mechanism that forms the particle belt and may not involve a passivating $Ni(OH)_2$ film. Activation could occur if parts of the belt temporarily become connected, increasing the TPB length, and then slow deactivation could occur if the particles slowly agglomerate and disconnect (or even reincorporate into the bulk Ni electrode) due to the high temperature. Similar phenomena have been speculated to explain similar sawtooth oscillations in the study mentioned in **section 5.3.1** about Pt migration in oxidizing atmosphere [41]. Alternatively, even if the particles never become connected, the presence of nanoparticles could improve adsorption or desorption kinetics and cause periodic activation if they were formed periodically, which could result from a number of accumulation mechanisms. Finally, it is also feasible that

the mobilization of impurities at the TPB (e.g. the abovementioned $Si(OH)_4$ reaction) could contribute to the activation and oscillations.

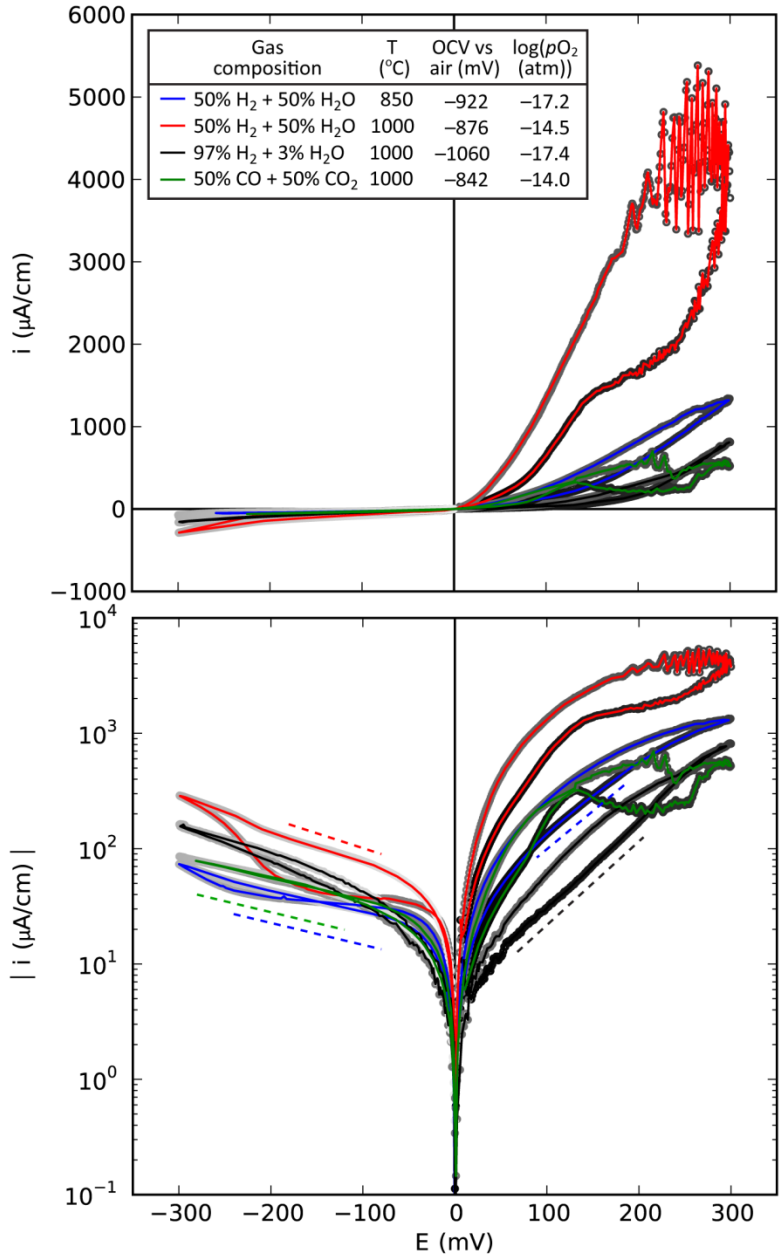

Figure 5-13. Potential sweeps of H_2 oxidation (positive voltage) and H_2O reduction (negative voltage) at Ni/YSZ at different temperatures and gas compositions, measured in the order listed in the legend. The current is normalized to the TPBL. The OCV corresponds to a different potential versus air (a different pO_2) for each curve, as labeled in the legend. The shading of the points behind the curves changes from black to light gray with time. The sweep rate for each was 1 mV/s. Possible linear regions in the log current plot are marked with dashed lines. Note: the noise near OCV for the black curve is measurement noise due to the low currents measured – unlike the oscillations seen at the higher voltages.

At overpotentials below the unstable regimes, the shapes of the curves in H_2/H_2O atmospheres are generally consistent with those performed on simplified Ni geometries in H_2/H_2O atmospheres in literature [7, 18, 20, 24]. It seems likely that the large hysteresis in the cathodic curve measured at 1000 °C in 50% H_2O/H_2 is related to the unstable anodic curve that had taken place just beforehand. In the log current plot, some linear regions indicative of Tafel kinetics might be present, but they are not easy to identify. Such linear regions seem to be present at the start of the polarization curves, when sweeping in the anodic direction below the unstable regime. After reaching +300 mV the electrodes seem to be activated during the downwards sweep, resulting in hysteresis. In cathodic sweep that followed, linear regions seem to sometimes be present but often only during the downwards sweep back to OCV. For CO oxidation at 1000 °C there is clearly no linear region, whereas for CO_2 reduction there does seem to be one.

Polarization curves performed on the Ni electrode later in the test at 850 °C in 50% H_2O/H_2 and 50% CO_2/CO are shown in **Figure 5-14**. The possible linear regions are more evident in 50% CO_2/CO, especially in the cathodic sweep, however for 50% H_2O/H_2 there is again curvature throughout the anodic sweep and only at the end of the cathodic sweep returning to OCV can a possible linear region be identified. However, the general slopes are nearly the same as for CO/CO_2. Assuming Tafel kinetics describe the curves, the anodic and cathodic charge transfer coefficients corresponding to the labeled slopes are approximately 1.40 and 0.56 respectively, indicative of a multi-step reaction as rate limiting. The anodic slope of the 50% H_2O/H_2 curve at 1000 °C, however, is much steeper and would give a very high anodic transfer coefficient. It is possible that the reactions are single-step charge-transfer limited at some potentials but the interface seems to be dynamic even ignoring the unstable anodic regime. Adsorbed intermediate species might accumulate on the Ni or YSZ surface at some potentials. This will be further discussed in the next section. Sweeps with lower limits of +200 and –200 mV did not reveal clearer linear regions; the continuous curvature for H_2 oxidation on Ni was still present.

Polarization curves for all of the metals at 850 °C are shown in **Figure 5-16** and **Figure 5-17**. Although one curve is shown at each condition, multiple were performed at different polarization ranges up to the maximum range shown (+300 mV to –500 mV). The shapes of the sweeps were generally reproducible at consecutively larger overpotentials, usually with slight activation after each sweep that reached high positive or negative overpotentials (see also **section 5.3.4.3**). In some cases, hysteresis was observed. In the cases of hysteresis, nearly the same hysteresis curve was followed when scanning to lower overpotentials (e.g. +200 mV and –300 mV). For example, the large hysteresis observed for Pt in 50% H_2O/H_2 in the cathodic direction was also reproducible through sweeps with lower cathodic overpotential limits, as well as the hysteresis observed for anodic polarization of Ni in CO/CO_2. The magnitude and shapes of the curves were also generally reproducible between different electrodes of the same metals.

Apparent linear slopes can be seen in some of the log-current polarization curves (CO/CO_2 more often than H_2/H_2O), which suggests the electrochemistry might be defined by Tafel kinetics for some of the metals in some conditions (in other cases, adsorbed species might be playing a role, as discussed later). For Pd, no linear regions can be identified, suggesting more complex phenomena take place on the Pd electrode. It is not expected that the curvature and hysteresis of the curves is the result of performing the scans too quickly, because the same results were obtained at both 1 and 2 mV/s and because some curves are linear in the log-plot and without hysteresis.

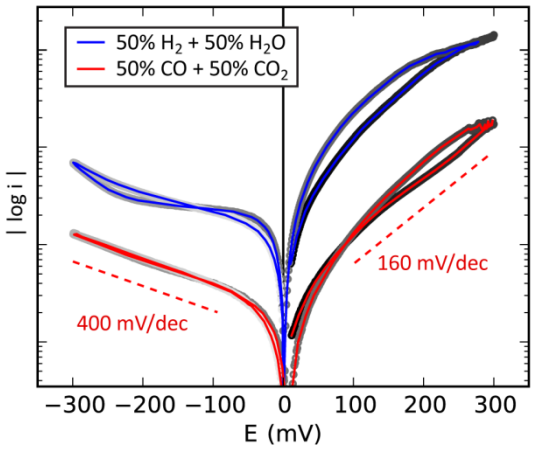

Figure 5-14. Example polarization curves on a Ni electrode at 850 °C.

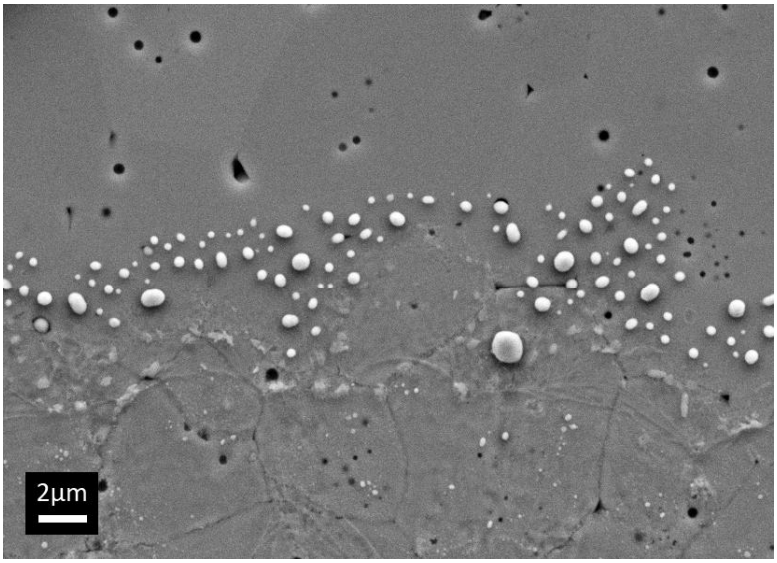

Figure 5-15. SEM micrograph of the belt of Ni particles found on the smooth YSZ surface outside of the contact area after tests with anodic polarizations, apparently linked to the oscillating currents shown in **Figure 5-13**.

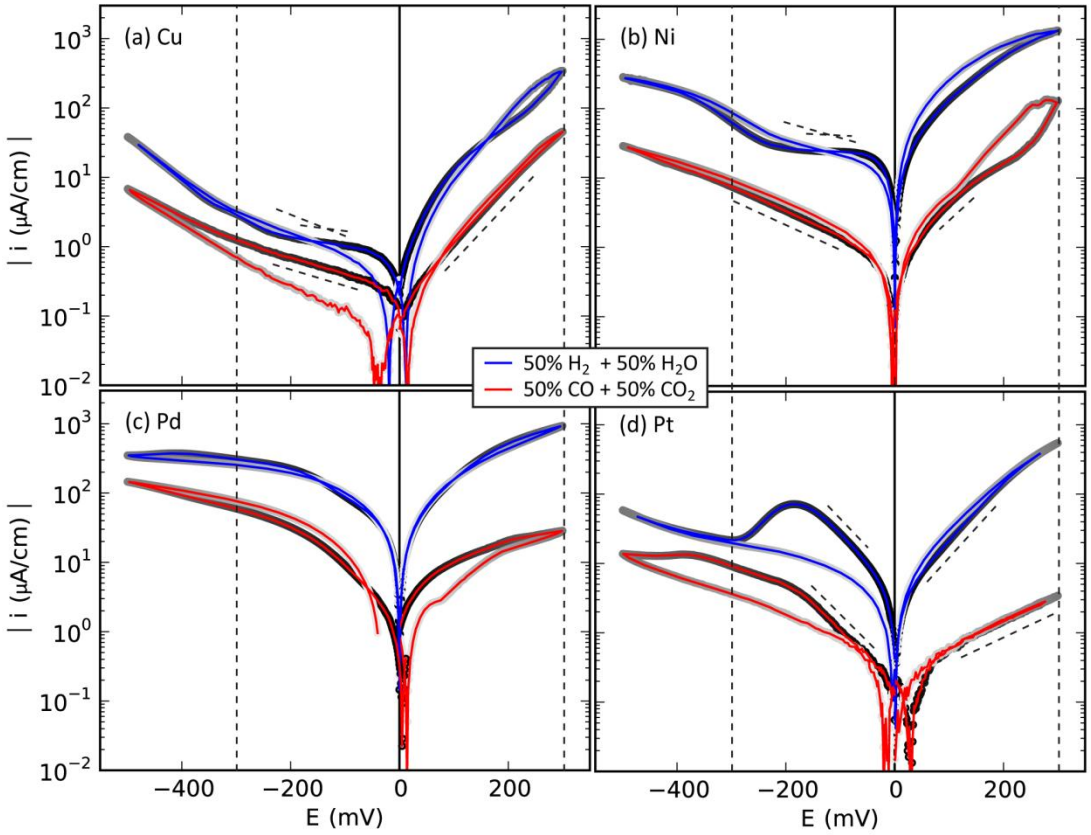

Figure 5-16. Polarization curves performed at 1-2 mV/s at 850 °C in 50% H_2O/H_2 (blue curves) and 50% CO_2/CO (red curves), on (a) Cu, (b) Ni, (c), Pd, and (d) Pt wire electrodes. The shading of the points behind the curves changes from black to light gray with time, first for the anodic sweep and then for the cathodic sweep. The dashed vertical lines mark +300 and –300 mV. The other dashed lines identify linear regions.

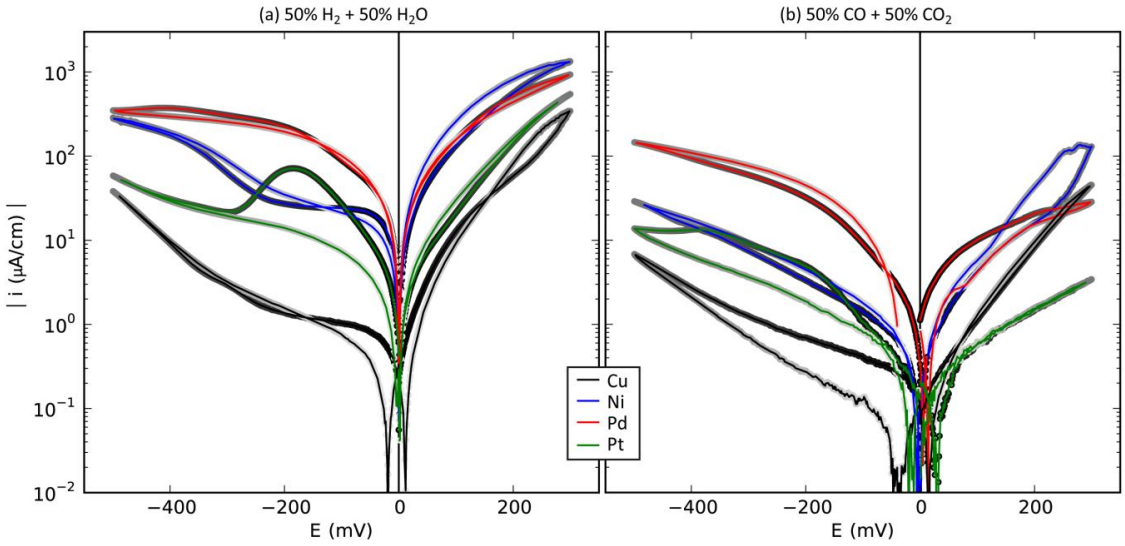

Figure 5-17. The same potential sweeps as in **Figure 5-16**, now with the results for the different metals overlaid at the same experimental conditions. The shading of the points behind the curves changes from black to light gray with time, first for the anodic sweep and then for the cathodic sweep.

Like the AC measurements, DC polarizations revealed interesting and different behavior of the metal electrodes. The relative performance between H_2/H_2O and CO/CO_2 for each metal, based on the polarization curves of **Figure 5-16**, is similar to that observed in OCV measurements earlier. However, notably, whereas Cu and Ni have similar curve shapes with much greater anodic than cathodic activity[iii], both Pd and Pt show nearly equal anodic-cathodic activity or even the opposite response in CO/CO_2 (greater activity for CO_2 reduction than CO oxidation). In H_2/H_2O, the OCV measurements described above which showed that R_P was lower for lower $p$$H_2O$ for Pd may be linked to the reason why the activity increased more so during cathodic than anodic polarization. The possible blocking of Pt by CO mentioned earlier (**section 5.3.3.2**) does not seem to be detrimental to CO_2 reduction on Pt. According to the comparison of the different metals in the same conditions (**Figure 5-17**), Cu is the least active for all conditions except CO oxidation, and Pd is generally the most active, more than Ni except at high anodic overpotentials, and especially the most active for electrolysis of H_2O and of CO_2.

5.3.4.2. Impedance Spectroscopy under DC Bias

Impedance spectra were measured potentiostatically under anodic and cathodic DC bias. A set of spectra for Ni at 1000 °C in 3% H_2O/H_2 is shown in **Figure 5-18**. These measurements were taken immediately after the polarization curve shown in **Figure 5-13** measured at the same conditions. The total LSR_P of these spectra agree with the instantaneous slopes of the polarization curve at each 150 mV increment. The electrode is activated (LSR_P reduced) both for anodic and cathodic polarizations, more so for anodic, by more than a factor of 20 at +130 mV. For cathodic polarizations, the summit frequency does not appear to change, whereas for anodic polarizations it increases with increasing polarization. Under +150 mV anodic polarization, the IS appears to be a single depressed semicircle, suggesting that the polarization eliminates two of the possibly-three processes identified at OCV, similarly to changing to 50% H_2O/H_2 (see **section 5.3.3.1** and **Figure 5-9**).

Some of the polarized spectra show a low-frequency inductive loop (most likely for +150 mV as well, but the +150 mV measurement did not go to as low frequency). Such loops have been observed in the literature for Ni point and pattern electrodes [8, 13, 24]. These loops are also present in other measurements on the other metals and are further discussed below.

[iii] Both are significantly activated by anodic reactions. For Ni, +300 mV yield an order of magnitude higher current density than at –300 mV in both H_2/H_2O and CO/CO_2 atmospheres. For Cu, a similar trend but with 2 orders of magnitude higher current density is observed.

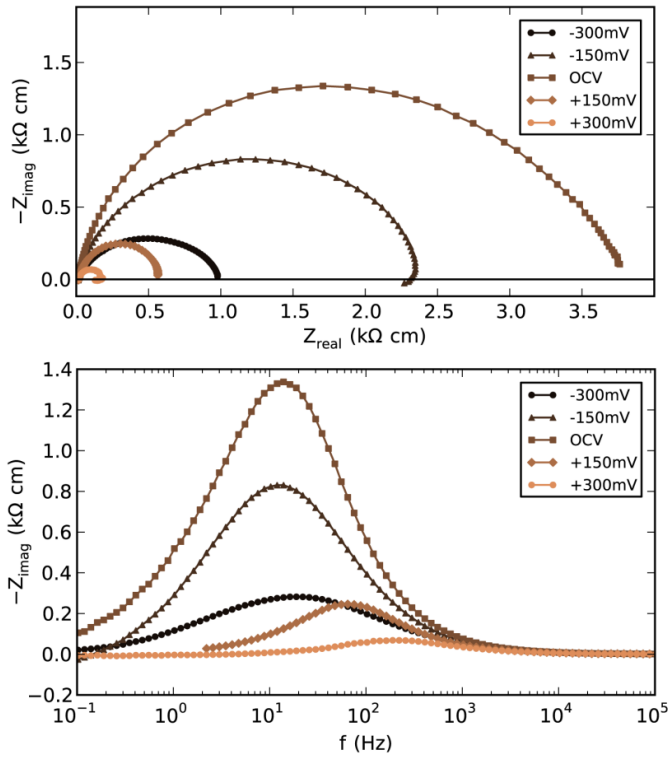

Figure 5-18. Impedance spectra measured under DC bias from +300 to –300 mV in 150 mV increments on a Ni electrode at 1000 °C in 3% H_2O/H_2. The order was +150, +300, –150, –300 mV, and then OCV 6 hours later. The impedance at OCV is somewhat less than that measured before the polarizations; see the next section.

Impedance spectra measured under DC bias in the range of +300 to –300 mV in 100 mV increments at 850 °C for both 50% H_2O/H_2 and 50% CO_2/CO atmospheres are shown in **Figure 5-19**, **Figure 5-20**, **Figure 5-21**, and **Figure 5-22** for Cu, Ni, Pd, and Pt electrodes respectively. The spectra are consistent with the polarization curves of **Figure 5-16** and provide more detail. Cu and Ni have higher anodic than cathodic activity in both atmospheres (**Figure 5-19** and **Figure 5-20**). Pt has higher anodic activity in H_2/H_2O, but lower anodic than cathodic activity in CO/CO_2 (**Figure 5-22**). Pd has higher cathodic than anodic activity in both atmospheres except at high anodic overpotential in H_2/H_2O (**Figure 5-21**). Pd is more active under both directions of polarization than at OCV in both atmospheres, whereas Cu, Ni, and Pt are all more active at OCV than under cathodic bias in H_2/H_2O. Since charge transfer resistance decreases with increasing overpotential, this higher resistance at cathodic overpotentials than at OCV suggests that charge transfer is not limiting.

The shapes and apparent number of processes contributing to the impedance spectra change under polarization. For Cu, Ni and Pt in H_2/H_2O and Cu and Ni in CO/CO_2, the anodic polarized spectra exhibit low-frequency inductive loops. These loops are also observed for some cathodic polarized spectra – Ni in H_2/H_2O and Pd in both H_2/H_2O and CO/CO_2.

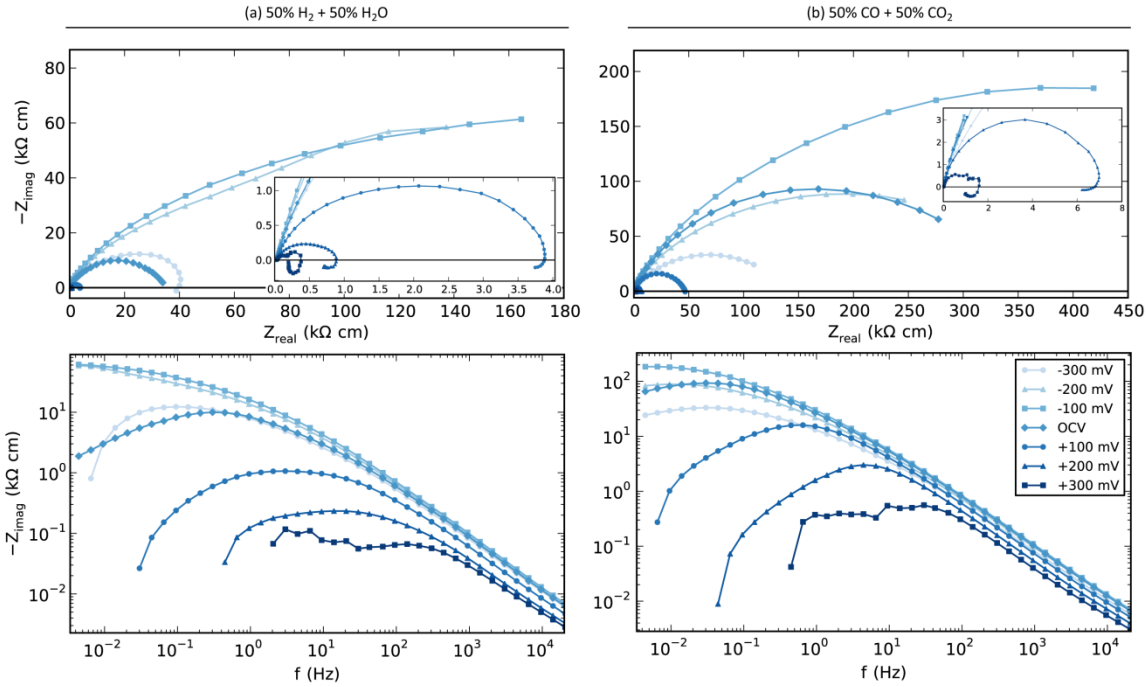

Figure 5-19. Impedance spectra measured on a Cu electrode under DC bias at 850 °C in (a) 50% H_2O/H_2 and (b) 50% CO_2/CO. The order was: OCV, anodic, cathodic, first for CO/CO_2, then H_2/H_2O. Note: positive Z_{imag} values are missing from the log-scale Bode plots.

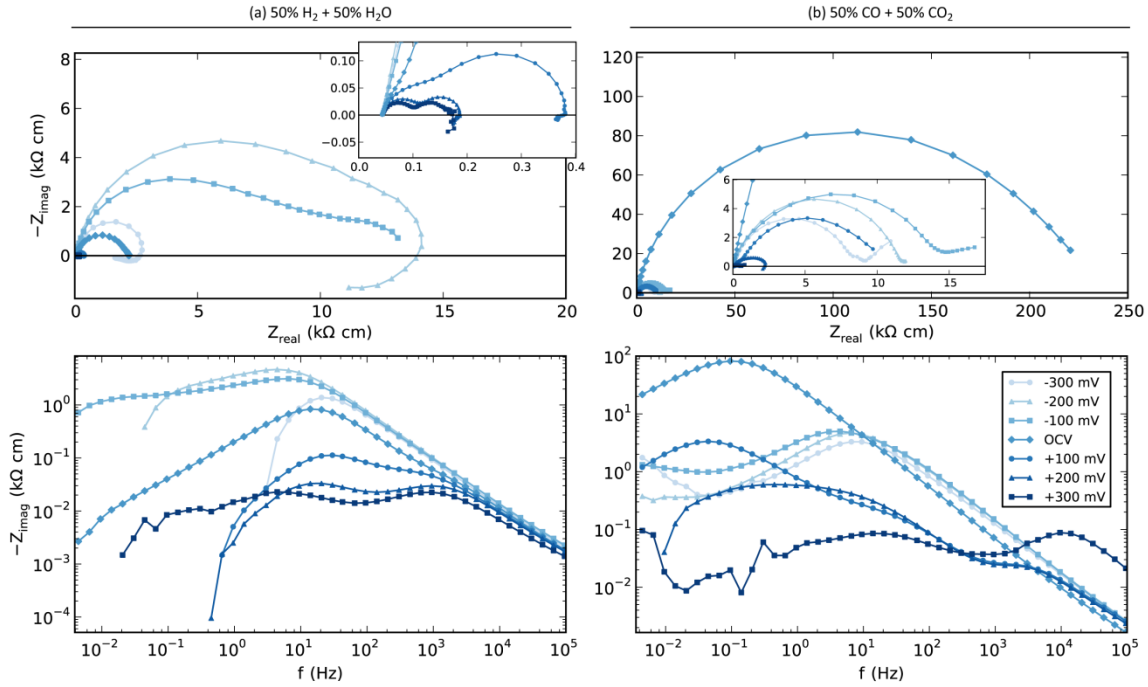

Figure 5-20. Impedance spectra measured on a Ni electrode under DC bias at 850 °C in (a) 50% H_2O/H_2 and (b) 50% CO_2/CO. The order was: OCV, anodic, cathodic, first for CO/CO_2, then H_2/H_2O. Note: positive imagine impedance values are missing from the log-scale Bode plots.

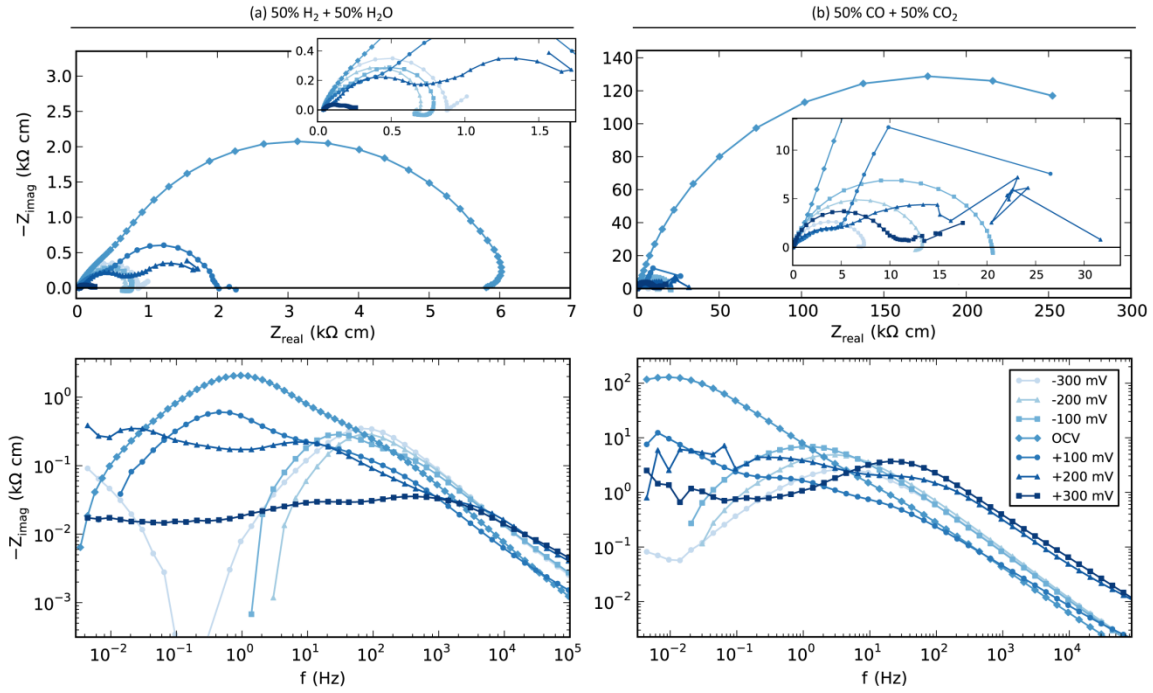

Figure 5-21. Impedance spectra measured on a Pd electrode under DC bias at 850 °C in (a) 50% H_2O/H_2 and (b) 50% CO_2/CO. The order was: OCV, anodic, cathodic, first for CO/CO_2, then H_2/H_2O. Note: positive imagine impedance values are missing from the log-scale Bode plots.

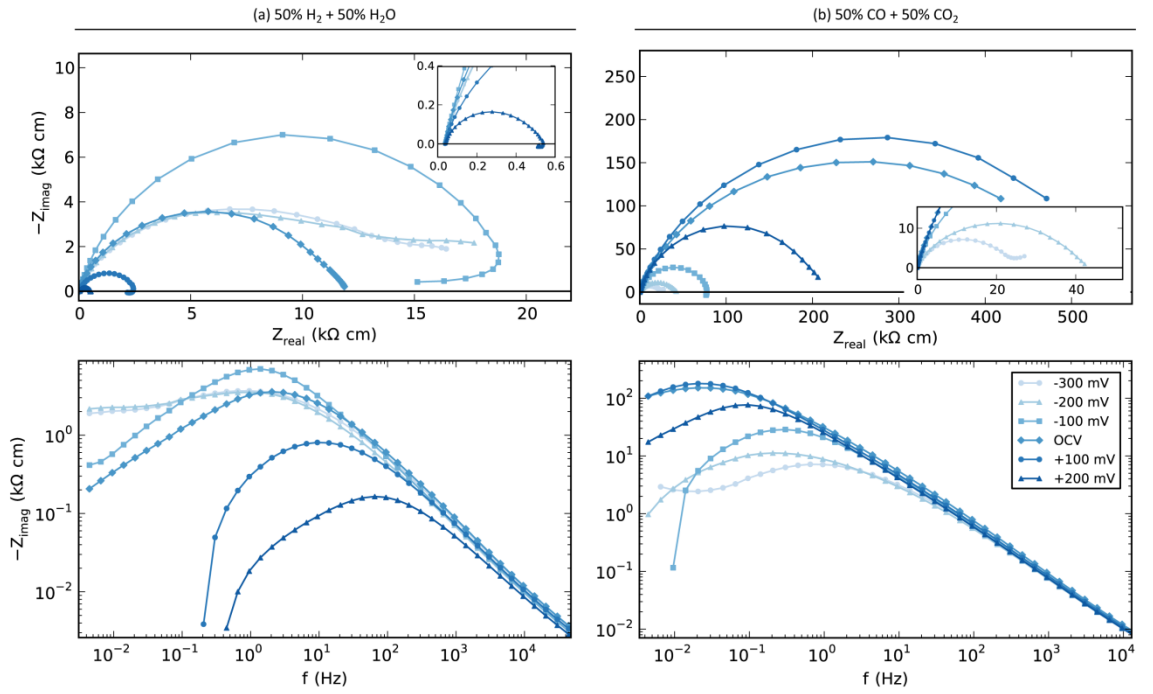

Figure 5-22. Impedance spectra measured on a Pt electrode under DC bias at 850 °C in (a) 50% H_2O/H_2 and (b) 50% CO_2/CO. The order was: OCV, anodic, cathodic, first for CO/CO_2, then H_2/H_2O. Note: positive imagine impedance values are missing from the log-scale Bode plots.

Under increasing anodic polarization, the spectra for Ni and Pd (and perhaps Cu as well, though it is less clear) transition into two distinct arcs. This is not observed under cathodic polarization for any of the metals in either atmosphere. Instead, under cathodic polarization, apparent Warburg-like diffusion limitations are sometimes seen (**Figure 5-20b**, **Figure 5-21a**, and **Figure 5-22a+b**). In some cases, the low-frequency impedance switches between inductive loops and diffusion-limitation type response at different cathodic overpotentials, e.g. for Pd in H_2/H_2O (**Figure 5-21a**) and Pt in CO/CO_2 (**Figure 5-22b**). Under high anodic polarization for some metals, instability is seen in the measurements. This is expected for Ni, as observed in the polarization curves and described in the prior **section 5.3.4.1**. In the impedance measurements it is also observed for Cu and Pd. Ni oxidizes well before Cu and Pd, so the oxidation-reduction mechanism mentioned in the prior **section 5.3.4.1** is not likely responsible for the instability for Cu and Pd. The hydroxide film oscillation mechanism mentioned in the prior section might be occurring. More tests would be necessary to try to determine the source of the instability.

Low frequency inductive loops can arise in reactions involving adsorbed intermediates [12, 13, 59-62]. More specifically, these authors have shown via modeling that inductive effects may occur under applied potential due to the potential dependence of the adsorbed intermediates in the reaction mechanism:

> "*Inductive effects may occur whenever a stepwise electron transfer takes place towards adsorbed intermediates. Whether the inductive effect appears in the impedance diagram will depend on the value of the rate constants and hence on the potential dependence of the fraction of coverage of the adsorbed intermediates.*" [60]

On the other hand, an inductive loop might be the result of an increase of the electrode surface area by injection of electrons into the YSZ subsurface, resulting in enhanced electronic conductivity and spreading of the reaction zone during anodic polarization [60, 63]. However, if the YSZ surface has electronic conductivity and the effective contact area is larger, this should show up as a lower R_S during polarization, and in the measurements presented here the R_S varied only +/- 2% during anodic or cathodic bias relative to OCV and most often increased, not decreased. It is worth considering whether other activation phenomena (e.g. other changes in morphology) could also cause the inductive loops observed here. It is very important that measurements are made at steady-state, which was the reason for the 5-minute fixed DC bias (chronoamperometry) immediately before each impedance measurement as the same bias. As a test, some measurements were taken without chronoamperometry, and activation (or deactivation, depending on the metal and the applied potential) would sometimes take place during the impedance measurement, lowering impedance and causing a drift in the direction of the origin in Nyquist plots. Since the impedance was measured from high to low frequency and the majority of measurement time is spent on the low-frequency data points, this drift creates a shape similar to the inductive loops. Similarly, deactivation during measurement could result in the diffusion-limited shape. However, in these tests the resulting curve was not inductive – it did not extend into the positive imaginary regime – and it did not curl back upwards.

Furthermore, inspecting the chronoamperometry measurements before and the current measured during the potentiostatic IS measurement revealed no correlation between the direction of current drift (if there was any) and the shapes or the impedance spectra (inductive loops or Warburg-like diffusion limitation, including the apparent drift seen for H_2O reduction on Pt in **Figure 5-22a**). Finally, the Kramers-Kronig transform showed very little residual error for nearly all of the impedance measurements (except when there is clearly instability during measurement at high anodic overpotentials). Therefore it is believed that the polarized impedance data, including the inductive loops and diffusion-limitation type responses, is valid. This suggests that adsorbed intermediates play a role in the reaction mechanism for all of the metals and may participate in the rate-limiting step during polarization.

5.3.4.3. Relaxation after Applied Potentials

After each set of anodic and cathodic polarized impedance measurements presented in the prior section, the electrode was allowed to rest at OCV and the impedance was monitored (**Figure 5-23**). In many cases the electrodes were activated (LSR_P was decreased) by polarization and a slow relaxation process was observed.

- *Cu.* In both H_2O/H_2O and CO/CO_2, the OCV LSR_P for Cu was basically unaffected by either anodic or cathodic polarizations (**Figure 5-23a+b**).
- *Ni.* Ni, on the other hand, was activated by anodic polarization in H_2/H_2O and it took at least 24 hours for the LSR_P to relax and return back to near the value before polarization (**Figure 5-23c**). Activation followed by similar relaxation time constants have been observed for Ni point-contact electrodes [35], as well as porous Ni electrodes [24] and Ni pattern electrodes [22], however the porous and pattern electrodes activated only by <20%, whereas the Ni point electrodes here activated by an order of magnitude. In CO/CO_2, Ni was similarly strongly activated (LSR_P decreased by more than a factor of 10), however the activation appeared to be more permanent (**Figure 5-23d**). Returning to H_2/H_2O seemed to return the LSR_P for Ni back to near its "normal" value (not shown). Ni was not significantly affected by cathodic polarization in either atmosphere (**Figure 5-23c+d**).
- *Pd.* In H_2/H_2O, Pd was strongly activated (LSR_P was decreased) by anodic polarization and did not relax much at all and very slowly (**Figure 5-23e**), similar to Ni in CO/CO_2. Cathodic polarization had little effect and even appeared to accelerate the relaxation back to "normal" performance. In CO/CO_2, Pd was activated by anodic polarization and fully relaxed after about 24 hours, whereas cathodic polarization caused a more permanent activation, though less than observed for anodic bias of Ni in CO/CO_2 and for anodic bias of Pd in H_2/H_2O.
- *Pt.* The anodic polarizations for Pt were only conducted up to +200 mV which may lessen their effects relative to those performed on the other metals which included +300

mV. In H_2/H_2O, Pt was activated by anodic polarization and mostly relaxed within about 10 hours, whereas cathodic polarization, which had a higher LSR_P during measurement, did not cause any activation – but after the measurement it slowly activated. In CO/CO_2, Pt was unaffected by anodic polarization but significantly activated by cathodic polarization, after which it did not fully relax even after 50 hours.

The above observations are summarized in **Table 5-4**.

For all of the different metals, there is generally a correlation between the degree of activation during the +300 mV or –300 mV measurement and the rate of relaxation, except for Cu where even strong activation during measurement is followed by almost immediate relaxation.

The anodic activation of Ni coincides with the activation at high anodic overpotentials discussed in **section 5.3.4.1** and evident in the hysteresis of the polarization curves. However, the seemingly more permanent anodic activation in CO/CO_2 is not reflected in the polarization curves. It is also surprising that Pd is so strongly and more permanently activated by anodic bias in H_2/H_2O and by cathodic bias in CO/CO_2 considering the lack of hysteresis in the corresponding polarization curves (**Figure 5-16c**).

Activation is most likely the result of either accumulation of reactive species or changes in morphology (such as an increase in the TPBL).

—*Accumulated species*. One possible explanation for the seemingly permanent activations and their apparent non-existence in the polarization curves is that abruptly stopping the polarization leaves the interface is a more activated state than when the overpotential is gradually reduced. Species might have accumulated and are left to accelerate the much slower OCV reactions for a long time, whereas when the potential is ramped down these species are consumed with less and less being added. These species could be:

- adsorbed intermediates on the metal or YSZ surface
- absorbed intermediates in the metal or YSZ bulk
- holes injected into the YSZ subsurface, as discussed in the prior section. However, as already discussed, this seems unlikely since a decrease in R_S was not observed.

The fact that the long-term activation was only present for some metals suggests that if accumulated species are responsible, they are present in or on the metal, not the YSZ. Whether they are adsorbed or adsorbed probably depends on the metal. The Pd–H system is well known – during H_2 oxidation the Pd electrode might store a significant amount of hydrogen atoms. The activation of the Pd electrode after CO_2 electrolysis seems to indicate that Pd and carbon oxides have some kind of affinity as well. Ni–C is also well known, in that Ni is a good

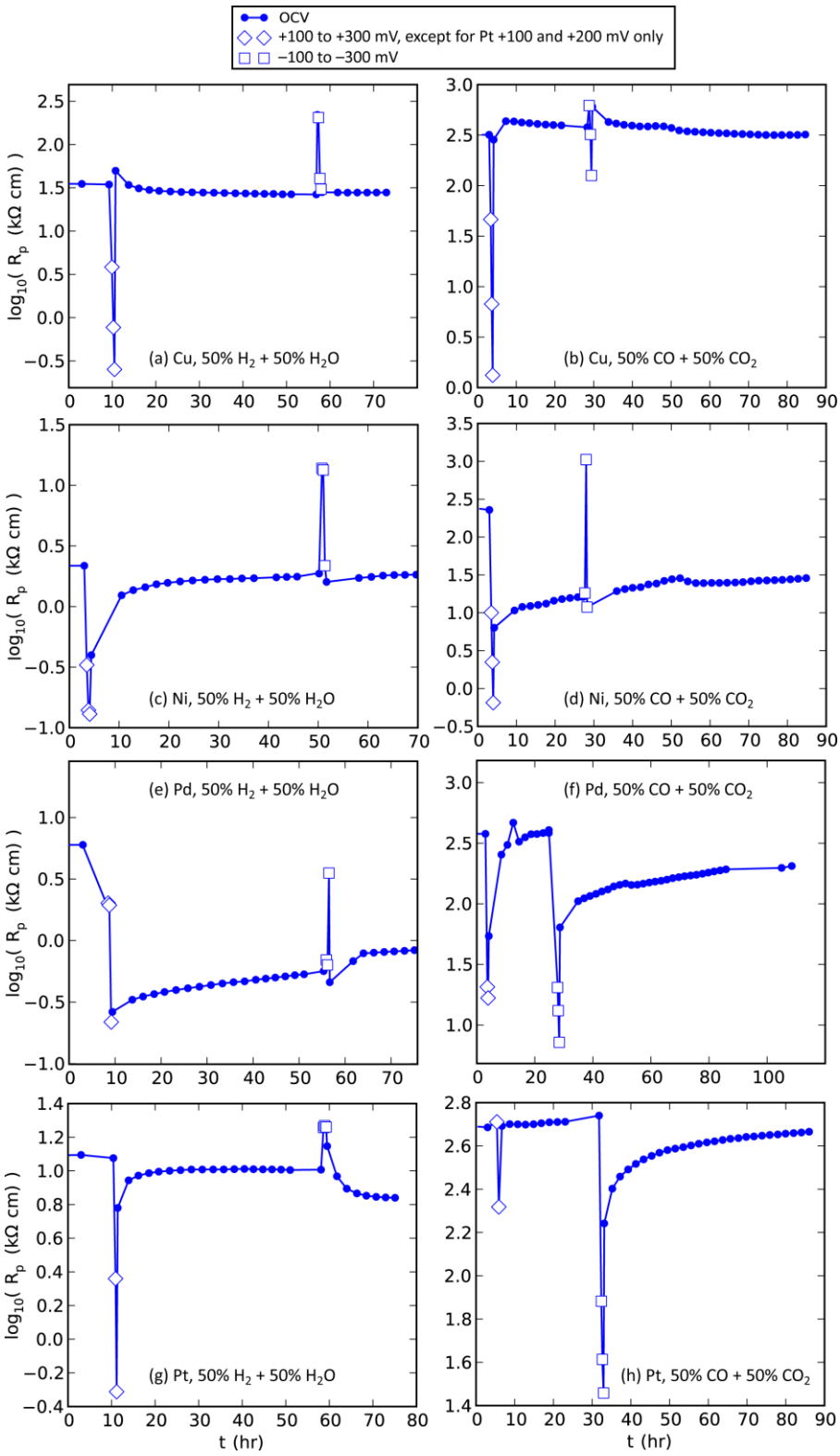

Figure 5-23. LSR_P at OCV before and after the polarizations, for each metal. The polarized data points are the same measurements as those shown in **Figure 5-19**, **Figure 5-20**, **Figure 5-21**, and **Figure 5-22**.

Table 5-4. Summary of post-bias relaxation for the metals. "-" signifies little or no effect, "X" signifies significant activation of LSR_P followed by relaxation to near the value prior to polarization, and "XX" signifies significant activation from which the electrode does not relax over an extended time.

Metal	Cu		Ni		Pd		Pt	
Atmosphere	H_2/H_2O	CO/CO_2	H_2/H_2O	CO/CO_2	H_2/H_2O	CO/CO_2	H_2/H_2O	CO/CO_2
Anodic activation	-	-	X	XX	XX	X	X[a]	-[a]
Cathodic activation	-	-	-	-[b]	-[b]	XX	X	X

[a] Uncertain; the +300 mV polarization was not included as for the other metals. Most likely "-" would be "X".

[b] The electrode was still activated when these cathodic polarizations were conducted, so these cathodic polarizations might be more activating than they seem.

catalyst for carbon deposition. However, carbon deposition is usually expected to deactivate, not activate, Ni electrodes and it should not occur as CO is consumed and CO_2 produced since any deposited carbon should be removed by the Boudouard equilibrium reaction ($CO_2 + C \rightarrow 2\ CO$).

—*Morphological changes*. It is also conceivable that morphological changes at the interface that lengthen the TPB could produce similar lasting activation effects. For Ni, if structural rearrangements via Ni-NiO occurred and roughened the Ni perimeter at high anodic polarization, as discussed in **section 5.3.4.1** and as will be discussed further in section 5.3.5.1, the 850 °C steam in the 50% H_2O/H_2 atmosphere might accelerate smoothing it back out (see the discussion about Ni transport via Ni hydroxide species in **section 5.3.4.1**) and reducing the TPBL back to normal, whereas the 50% CO_2/CO atmosphere would not. Alternatively, mobilization and removal of impurities from the TPB, thereby lengthening the TPB, might be occurring (see **section 5.3.4.1**). However, that mechanism is based on the impurities reacting with water, which is consistent with activation by H_2 oxidation but would not explain the activations in CO/CO_2 which are observed to be just as common.

5.3.5. Effects of Extreme Gas Conditions and Applied Potentials

5.3.5.1. Oxidation

One of the smooth electropolished Ni electrodes was oxidized by exposure to air for 2 hours at 850 °C. The impedance spectra measured in 3% H_2O/H_2 before and after oxidation are shown in **Figure 5-24**. The LSR_P decreased by a factor of 10 (from 22 kΩ cm to 2.3 kΩ cm at 850 °C) as a result of the oxidation. R_S, and therefore the contact area, did not change. During the next 4 hours at 850 °C, the LSR_P did not change. However, upon increasing the temperature to 1000 °C, the first IS showed an LSR_P of 3 kΩ cm, larger than the measurements

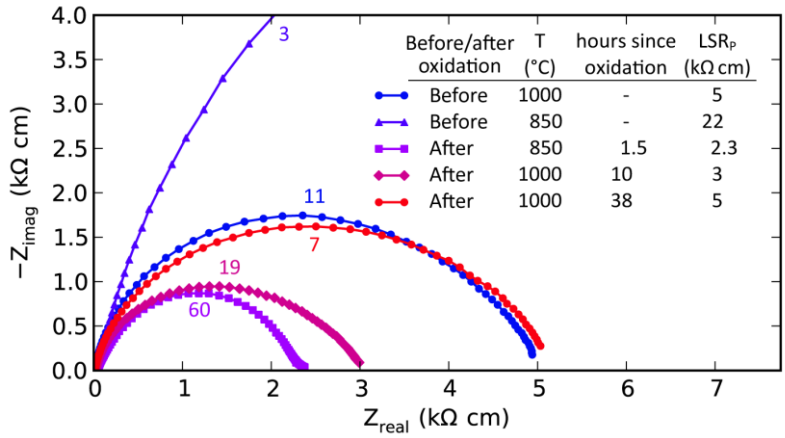

Figure 5-24. Impedance spectra measured at OCV in 3% H_2O/H_2 before and after oxidation at 850 °C. The numbers next to each arc give the approximate summit frequency in Hz.

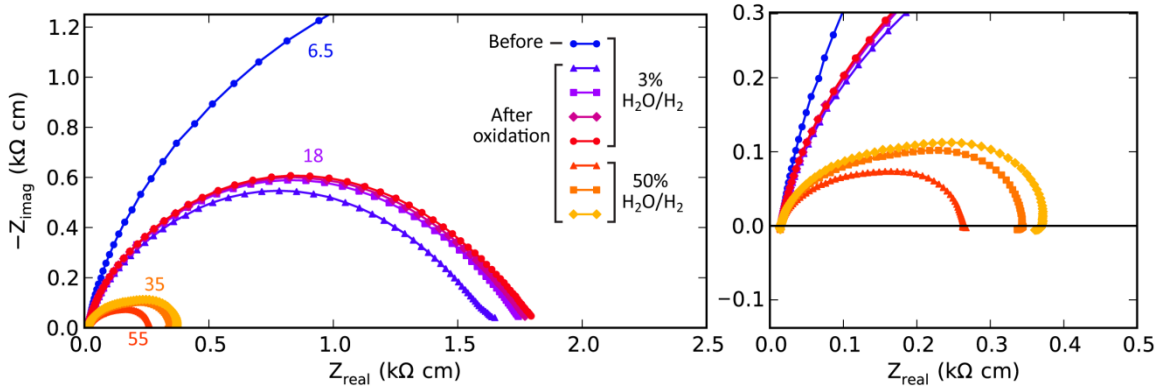

Figure 5-25. Impedance spectra measured at OCV before and after oxidation at 1000 °C. The numbers next to each arc give the approximate summit frequency in Hz.

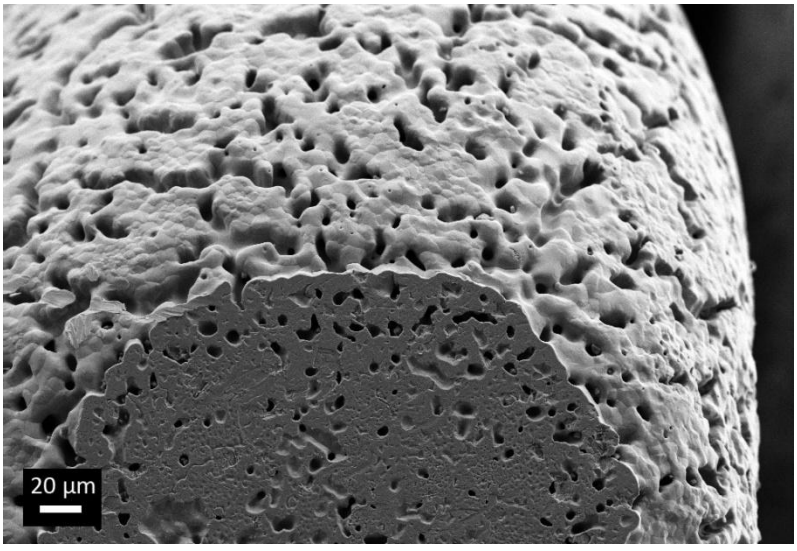

Figure 5-26. Scanning electron micrograph of the Ni wire that was oxidized twice during testing.

just taken at 850 °C which clearly contradicts the temperature-activated nature of the electrochemical reactions. The LSR_P was increasing at 1000 °C – after another 28 hours the LSR_P had returned to the value from before the oxidation (5 $k\Omega\,cm$).

The electrode was oxidized again for 30 h at 1000 °C (**Figure 5-25**). The LSR_P reduced by a factor of 3 for 3% H_2O/H_2 and began to increase. The gas composition was changed to 50% H_2O/H_2. The LSR_P was ~0.3 $k\Omega\,cm$ and continued to increase.

Examining the Ni wire electrode in the SEM after testing revealed a porous surface (**Figure 5-26**). After the second oxidation, the electrode was tested in a variety of H_2/H_2O and CO/CO_2 atmospheres for 110 h more at 1000 °C followed by 130 h more at 850 °C before cooling down. The porosity is the result of the oxidation and it is believed to have smoothened by sintering over time. The smoothening would explain the increasing LSR_P after oxidation events – immediately after oxidation, the NiO of the electrode surface is reduced back to Ni metal producing a rough microstructure with high surface area, and the high temperature causes the surface area to slowly decrease. The formation of the NiO during oxidation and/or the reduction back to Ni must have occurred non-homogenously to yield the rough microstructure with high surface area and longer TPB than before oxidation. At 850 °C, the new high-surface-area microstructure was preserved, at least for the few hours of measurements. At 1000 °C, the microstructure smoothened and LSR_P increased dramatically. Upon oxidizing the electrode again at the higher temperature, a new higher surface area microstructure was again formed yielding a longer TPB, which also began to smoothen. The final result is the TPB shown in the SEM micrograph. If the TPB length was enhanced like this, the data normalization procedure does not account for this and is not exactly correct, but is still useful to compare the degree of activation that occurred, as discussed at the end of **section 5.3.2**.

It is interesting that oxidizing the Ni electrode greatly enhances the electrochemical activity. However, such treatment on a Ni-YSZ cermet may not be practical because the Ni is structural, and the microstructural changes and expansion resulting from oxidizing Ni to NiO and reducing back again to Ni ("redox cycles") are known to severely damage the structure, and in the case of Ni-YSZ electrode supported cells, redox cycles can crack the adhered electrolyte layer as well, destroying the cell [64, 65]. In addition, cermets are in fact prepared as NiO-YSZ composites and the NiO is most often reduced to Ni *in situ* at the start of cell operation, so the enhanced microstructure is most likely already present (and because the Ni and YSZ are intermixed fine particles, the YSZ prevents the Ni from sintering too much even at high temperatures). However, at low temperatures around 650 °C where Ni is less prone to rapid oxidation, the redox expansion-contraction is less severe and the Ni-YSZ cermet electrode was found to remain intact as well as activate somewhat [66], though to a much lesser extent than observed here but most likely due to similar microstructural enhancements as observed here.

After the second oxidation, further characterization was performed. This high-resolution impedance data is included as Appendix 1. It contributes to the description of the original mechanisms (or close to the original mechanisms) of the Ni electrode before oxidation and may be useful for modeling purposes.

5.3.5.2. Strong Cathodic Polarization

Strong cathodic polarization (SCP) was performed on the metal electrodes in dry H_2. With very little H_2O available, the cathodic current reduces other species. For example, it has been reported by a number of workers that zirconia can be electrochemically reduced at high cathodic overpotentials; SCP is also known to increase the electrocatalytic activity of metal/stabilized zirconia electrodes [14, 67-69].

Figure 5-27 shows strong cathodic polarization curves performed on one of the Ni electrodes. When each cathodic overpotential limit was reached (–500 mV, –1000 mV, and then –1500 mV), potentiostatic EIS was performed at that cathodic bias for a few minutes. The "to –1000 mV" curve exactly overlays the "to –500 mV" curve, so the –500 mV polarization did not noticeably affect the interface, the electrode or electrolyte materials. After the application of –1000 mV, however, the following curve "to –1500 mV" follows a different current-voltage path, suggesting that –1000 mV has had some effect. The responses of the other metals are shown in **Figure 5-28**. Cu and Pt show a similar response. Pd, on the other hand, is already activated after the –500 mV sweep and has a different curvature with the current temporarily dropping from about –500 to –550 mV. This might have to do with hydrogen storage properties of Pd. Then the behavior in this range may indicate that in this overpotential range the small amount of steam present is being used up (more quickly than it is supplied) and other species begin to be reduced.

The IS measured after each polarization curve, under each strong cathodic bias, are shown for the Ni electrode in **Figure 5-29a**. The other metals had very similar results. During the stronger polarizations (–1000 mV and –1500 mV), the R_S decreased. The R_S changed from 195 **Ω** at OCV to 35 **Ω** at –1500 mV, and appeared to be decreasing during the –1000 mV and –1500 mV impedance scans based on the decreasing impedance at high frequencies. Indeed, the magnitude of the current measured during the –1500 mV potentiostatic IS (not shown) increased linearly by about 70% during the IS measurement. The spectra were not at all measured at steady-state and their shapes are significantly distorted, so they are used only to determine the approximate R_S. The apparent low-frequency loop is also the result of the decreasing R_S.

The IS measured at OCV immediately before the polarizations and in between each are shown for the Ni electrode in **Figure 5-29b**. All of the metals appeared to be activated (LSR_P

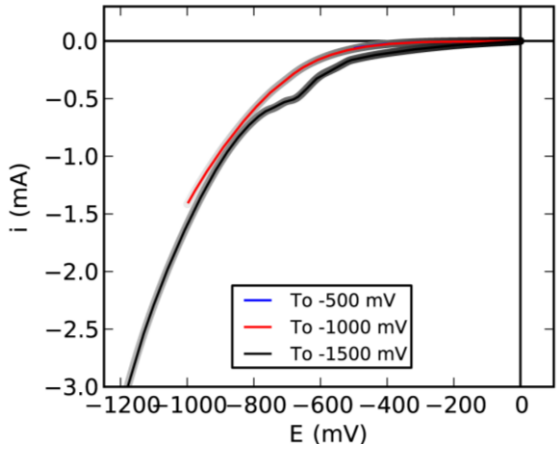

Figure 5-27. Strong cathodic polarization curves performed on a Ni electrode at 850 °C in dry H_2. The red "to –1000 mV" curve overlays the blue "to –500 mV" curve. The full "to –1500 mV" curve is shown in **Figure 5-28**b. The shading of the points behind the curves changes from black to light gray with time

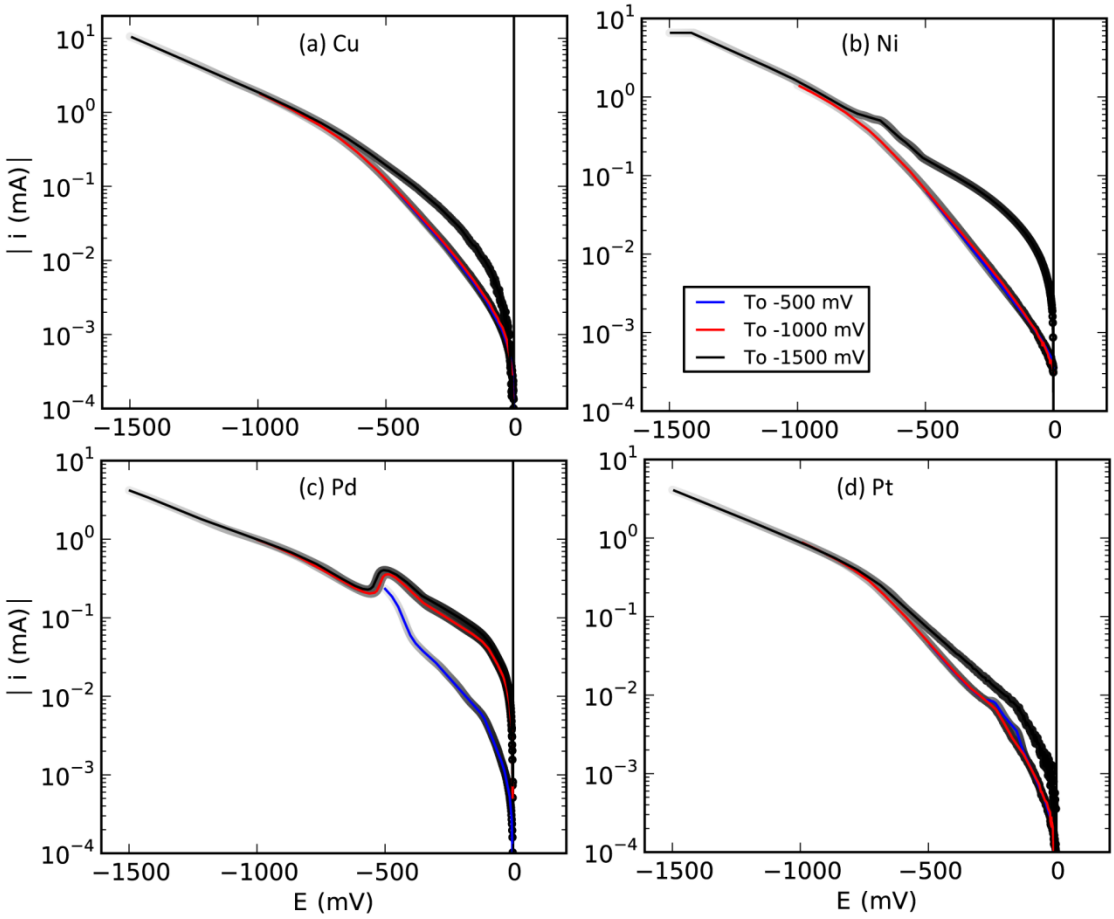

Figure 5-28. Strong cathodic polarization curves performed at 850 °C in dry H_2 on (a) Cu, (b) Ni, (c) Pd, and (d) Pt electrodes. The curve shown in (b) is the same curve as that shown in **Figure 5-27**. The shading of the points behind the curves changes from black to light gray with time

was decreased) by a factor of 20-40 by the cathodic polarization. For the first part of the measurements, R_S is rapidly increasing. By the end of the measurements, such drift appears to have mostly stopped, as it would otherwise be even more prominent in the low frequency data. Indeed, in subsequent OCV measurements in dry H_2 the R_S had returned to 180 **Ω**, close to that measured before the cathodic polarizations, and 6 hours later in 50% H_2O/H_2 the R_S was back to normal at 195 **Ω**. The evolution of R_S is summarized in **Table 5-5**.

After the SCPs, the atmosphere was changed to 50% H_2O/H_2 and 50% CO_2/CO. The IS measured in these conditions for each metal are shown in **Figure 5-30** along with the IS measured at the same conditions before the SCPs. The SCP clearly activated all of the electrodes. In H_2/H_2O, the LSR_P decreased by a factor of 5, 10, and 20 for Ni, Pt, and Cu respectively. In CO/CO_2, the LSR_P decreased by a factor of 50-60 for those same metals. For Pd, the decreases were somewhat less, about a factor of 5 in both atmospheres. However, but the measurements shown before the SCP were taken after some of the electrodes had been activated by the normal anodic/cathodic polarizations, e.g. the Pd electrode was still activated by more than an order of magnitude after H_2 oxidation (see **Figure 5-23e** and **section 5.3.4.3**). In comparison with the first measurements at 850 °C in 50% H_2O/H_2 and 50% CO_2/CO (see **Figure 5-12**), the electrodes were at this point activated by up to a factor of 150 depending on the metal and atmosphere (**Figure 5-31**). In general, it can be concluded that the SCP caused a decrease in LSR_P by 1 to 2 orders of magnitude. In terms of the relative magnitudes of the LSR_P, after the SCPs, Pd, Ni and Pt had the lowest values and were quite similar, with Pd slightly more active than Ni and Pt, and the LSR_P for Cu was about a factor of 2-3 higher.

The shapes of the IS consistently show, for all of the metals, 2 rate-limiting processes after the SCP. Assuming that the IS measured before the treatment in the same 50% H_2O/H_2 atmosphere also represent 2 processes (which overlap and are more difficult to distinguish visually), the high-frequency process has been activated the most. There is no shift in the summit frequency towards higher frequency as observed when other Ni electrodes were activated by oxidation (**Figure 5-25** and **section 5.3.5.1**).

The IS measured at OCV before and after the SCP for an Ni electrode, in 3% H_2O/H_2, is shown in **Figure 5-32**. In this gas composition, before the SCP, up to 3 impedance processes were identified (**Figure 5-9a**), whereas now the IS show a single semicircle, similar to impedance measured in 50% H_2O/H_2 (**Figure 5-9b**) and under anodic polarization in 3% H_2O/H_2 (**Figure 5-18**).

The temperature dependence of LSR_P in 50% H_2O/H_2 after the SCPs was measured from 850 to 750 °C. The activation energies were 1.1, 0.8, 1.1, and 1.1 eV for Cu, Ni, Pd, and Pt respectively, whereas earlier they were all in the range of 1.3-1.6 eV (**section 5.3.3.3**). The activation energy of Ni especially had decreased as a result of the SCP, halving from 1.6 to 0.8

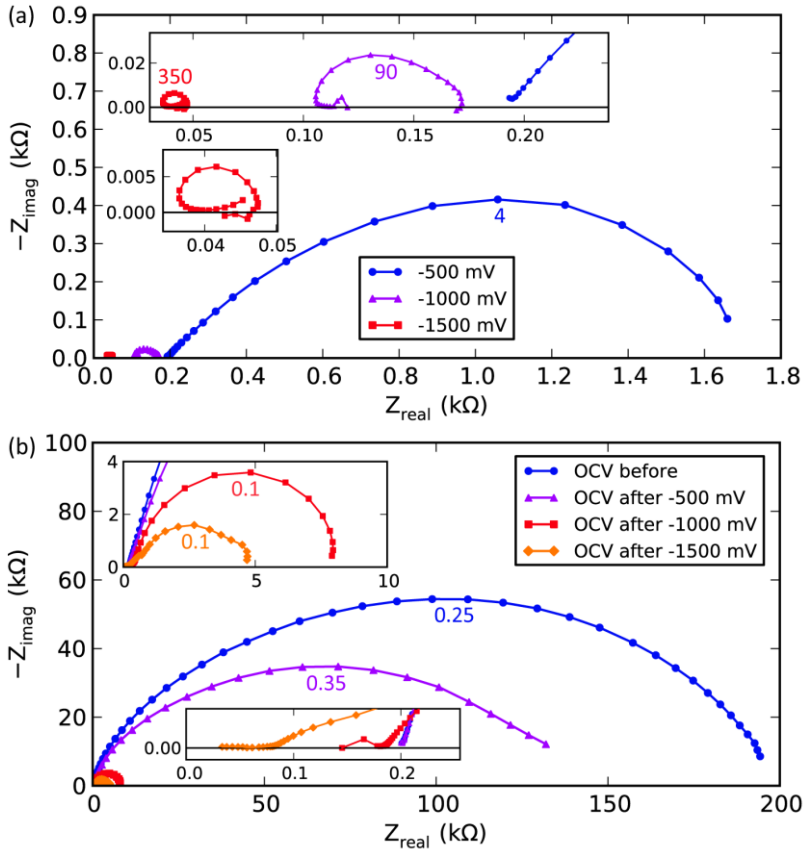

Figure 5-29. Impedance measurements made at 850 °C in dry H_2 in the Ni electrode (a) during the strong cathodic polarizations at each applied bias and (b) before and after the polarizations at OCV.

Table 5-5. R_S before, during and after cathodic biased impedance measurements, in dry H_2 except for the last data point, at 850 °C.

Condition	R_S (Ω)
OCV	195
During –500 mV	190
OCV immediately after –500 mV	195
During –1000 mV	107
OCV immediately after –1000 mV	184
During –1500 mV	35
OCV immediately after –1500 mV	78
OCV 10 minutes later	180
OCV in 50% H_2O/H_2, 6 hours later	195

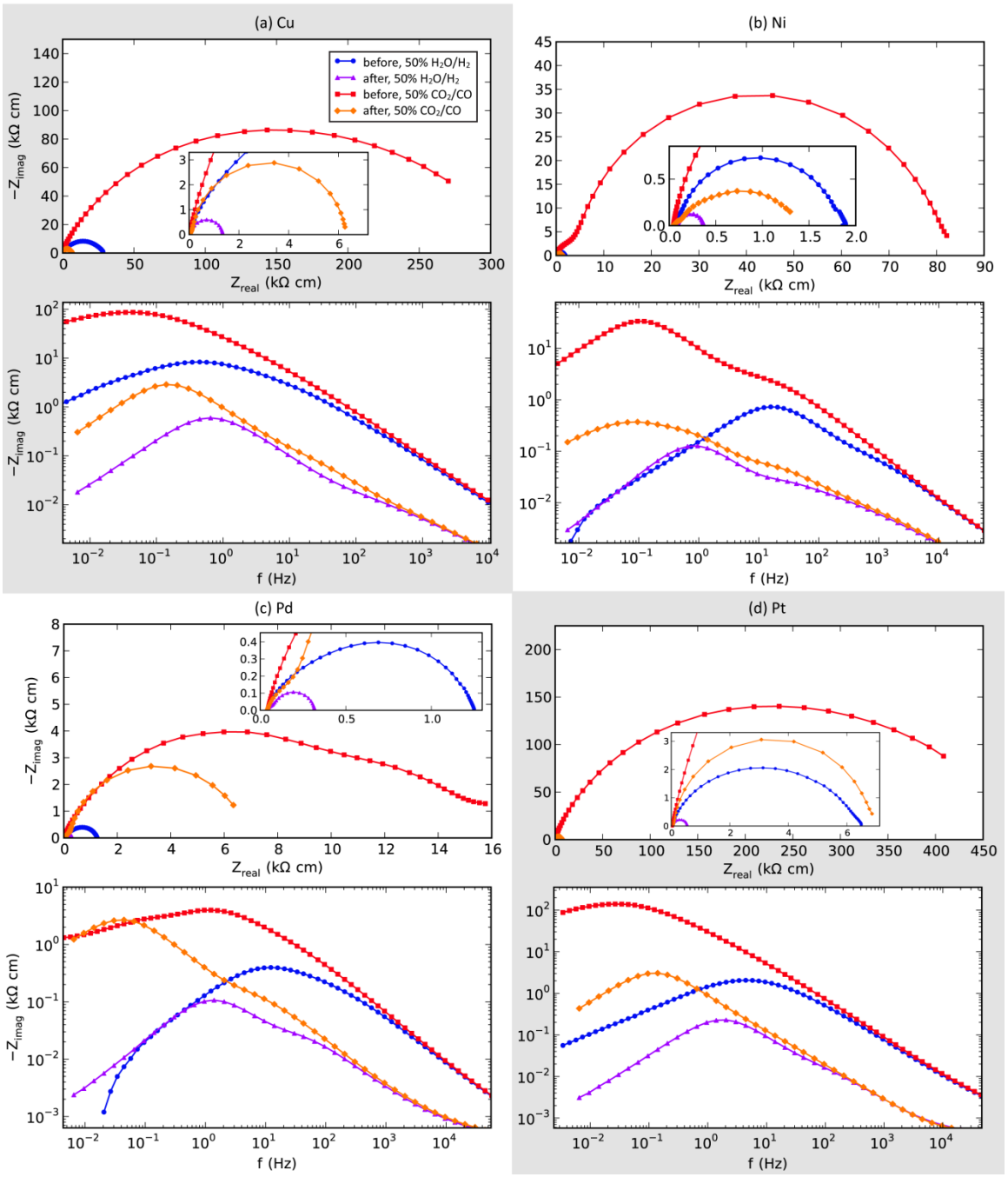

Figure 5-30. Impedance spectra measured at OCV before and after the strong cathodic polarization, at 850 °C in 50% H_2O/H_2 and in 50% CO_2/CO, for the (a) Cu, (b) Ni, (c) Pd, and (d) Pt electrodes.

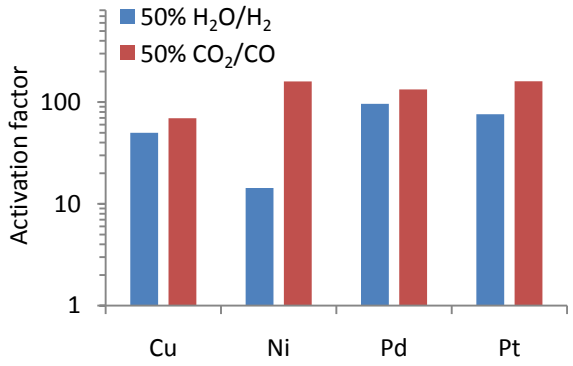

Figure 5-31. Activation factors for the LSR_P of the electrodes between the first measurements in the test and after the strong cathodic polarization.

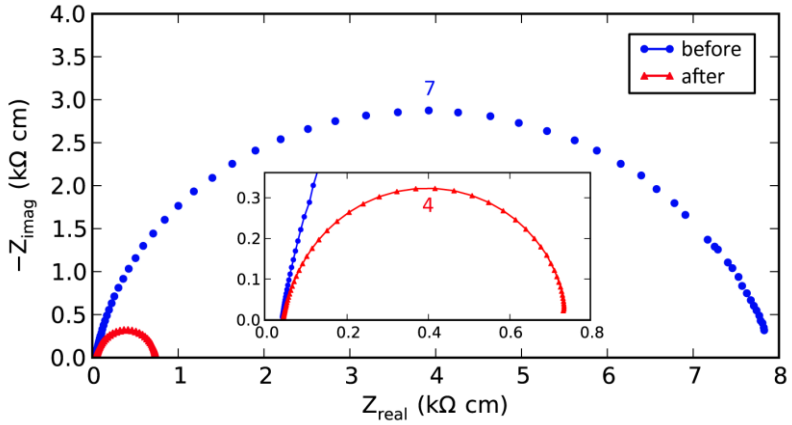

Figure 5-32. Impedance spectra measured on a Ni electrode at OCV at 850 °C in 3% H_2O/H_2 before and after the strong cathodic polarization.

eV. In literature, for Ni point electrodes subjected to a stronger cathodic polarization, an extremely low activation energy of 0.4-0.65 eV was measured at a lower temperature range than here [14]. In terms of the relative magnitudes of the LSR_P, at higher temperature the value for Pt became lower than that for Ni.

Polarization curves were also performed on the electrodes after the SCPs. **Figure 5-33** shows these sweeps along with the sweeps measured earlier (+300 to –300 mV bound sweeps measured just before the larger-ranged sweeps shown in **Figure 5-16**). Remarkably, most of the polarization curves are now close to linear, especially for H_2 oxidation. Most likely the high frequency process that was apparently activated (based on the impedance spectra, **Figure 5-30**)

was a potential-dependent process and since it no longer dominates the polarization resistance, the polarization resistance is now nearly independent of potential. The activation of all of the electrodes is evident in the polarization curves. CO oxidation curves for all of the metals reach several times higher current density (Pt in fact has improved by more than an order of magintude), as well as all cathodic curves (both H_2O reduction and CO_2 reduction). At high anodic overpotentials of H_2 oxidation for Cu and Ni, however (**Figure 5-33a+b**), the earlier curves meet the new curves, and for Pd they nearly meet.

The relative performance of the metals for oxidation and reduction of $H_2/H_2O/CO/CO_2$, at 200-300 mV anodic and cathodic overpotentials, is shown in **Figure 5-34** and summarized in **Table 5-6** in comparison with **Figure 5-17.** The relative performance has not changed. With the "straightened" curves, Ni is more active at the full range of anodic overpotentials whereas before Pd was more active at lower overpotentials. Pd is still by far the most active for H_2O and CO_2 reduction. The relative activity of Pt seems to have somewhat increased (but not enough to move up in ranking).

One of the Ni electrodes that had been oxidized (and had subsequently lost its resulting improved performance due to 1000 °C heat treatment for many hours, see **section 5.3.5.1**) was also subjected to SCP under the same conditions but to a more negative limit of –2000 mV. The polarization curves measured before and after are shown in **Figure 5-35**. This stronger cathodic polarization activated the electrode even more – the maximum currents are much higher and the polarization curves are even more linear.

Explaining what occurred during the SCPs must address at least the temporary decrease of R_S and the more lasting decrease of LSR_P (generally, that the electrodes activated), and ideally the change in the shape of the impedance spectra and the change in the shape of the polarization curves as well. The test was not continued for long after the SCP to see if the LSR_P approached its earlier values – in the literature it was observed that some Ni point electrodes relaxed (LSR_P increased to near the value before the SCP) after the activation over the course of 2 weeks in 3% H_2O/H_2 at 700 °C whereas others were more permanently activated, with LSR_P still lower by more than a factor of 5-10 after 1 month [14].

—*Changes in* R_S. Electrochemical reduction (as well as reduction by very dry H_2 at high temperature) of yttria- or scandia-stabilized zirconia removes oxygen from the crystal lattice and visibly blackens the zirconia [68-73]. The mechanism by which the zirconia is reduced is a valence change either of Zr^{4+} to Zr^{3+} or of a point defect (a dissolved chemical impurity or a structural defect such as an oxygen vacancy). The outcome of reduction is (a) a variation in the stoichiometry due to oxygen release, e.g. ZrO_{2-x}, (b) a change in the ionic and electronic conductivities of the stabilized zirconia, and (c) a coloration due to trapped electrons which can be excited to higher energy levels [74]. The electrons are trapped at oxygen vacancies [75].

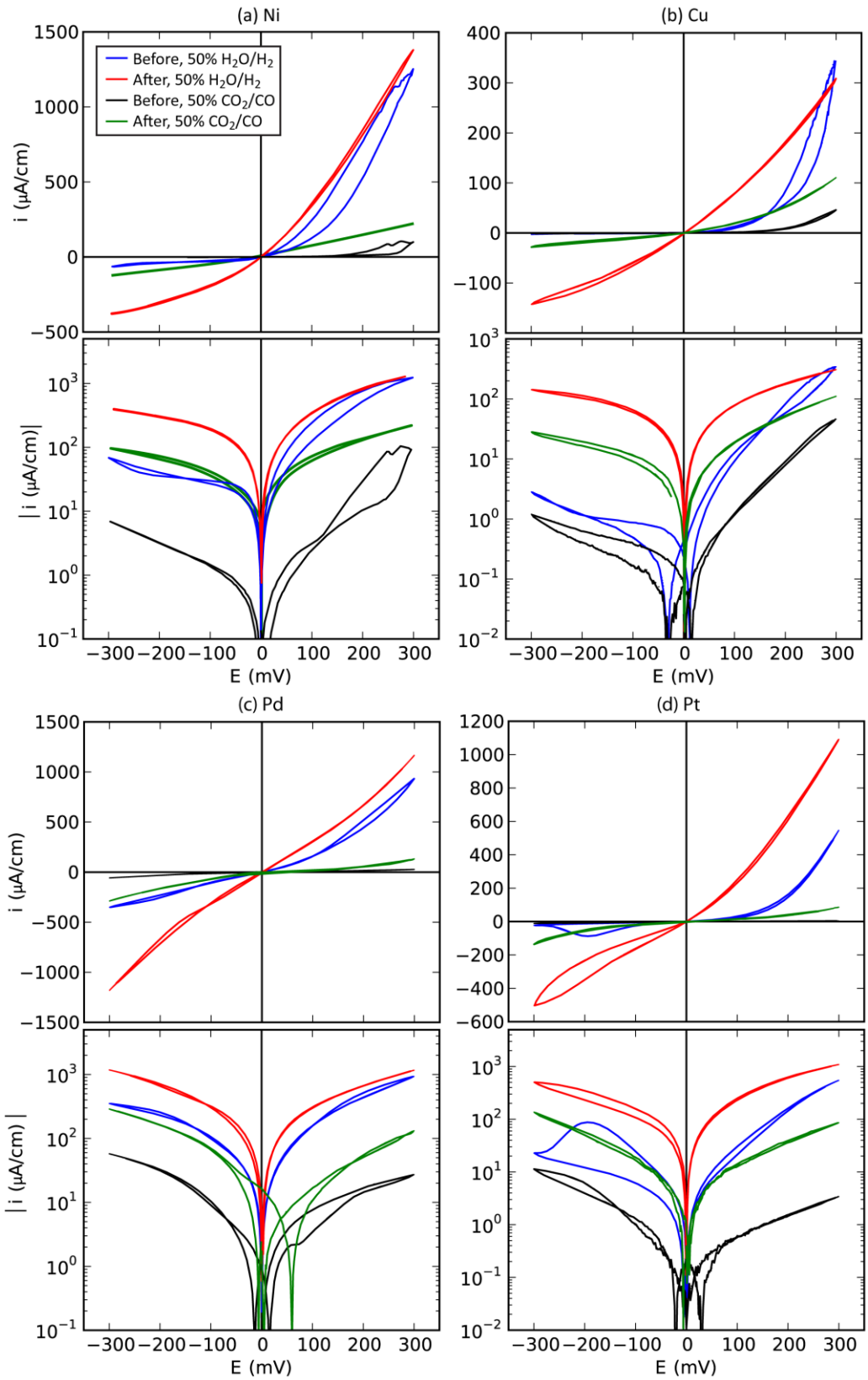

Figure 5-33. Polarization curves before and after the strong cathodic polarizations for the (a) Cu, (b) Ni, (c) Pd, and (Pt) electrodes. The directions of the "before" sweeps are the same as in **Figure 5-16**.

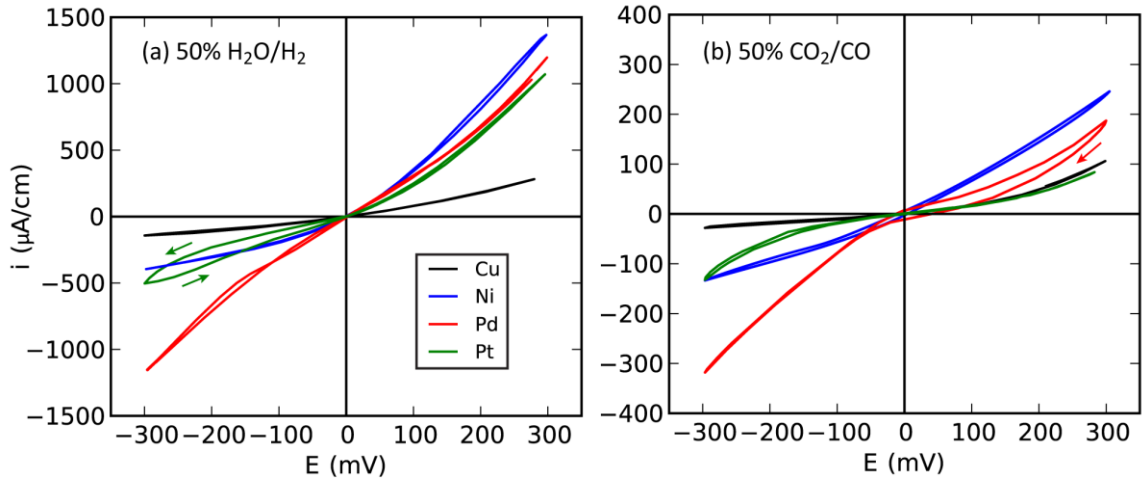

Figure 5-34. Polarization curves after the strong cathodic polarizations for all of the metals overlaid, in (a) 50% H_2O/H_2 and (b) 50% CO_2/CO.

Table 5-6. Relative performance of the metals for fuel cell and electrolysis electrode reactions at 100-300 mV anodic and cathodic overpotentials before (based on **Figure 5-17**) and after (based on **Figure 5-34**) the strong cathodic polarizations.

Polarization	Ranking of activity before	Ranking of activity after
H_2 oxidation	Ni > Pd > Pt > Cu	Ni > Pd > Pt > Cu
H_2O reduction	Pd > Ni/Pt > Cu	Pd > Pt/Ni > Cu
CO oxidation	Ni > Pd/Cu > Pt	Ni/Pd > Cu/Pt
CO_2 reduction	Pd > Ni/Pt > Cu	Pd > Ni > Pt > Cu

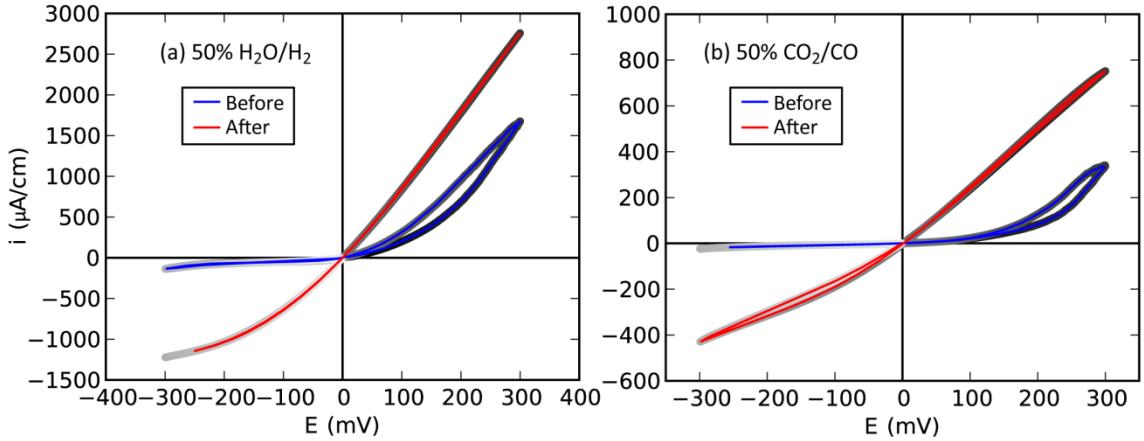

Figure 5-35. Polarization curves performed at 850 °C on a Ni electrode that had been oxidized.

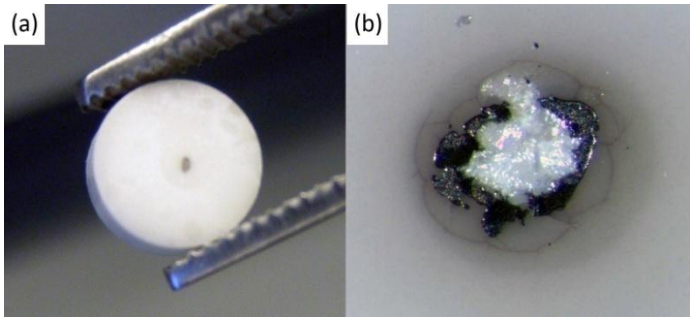

Figure 5-36. YSZ electrolyte pellets after tests in which strong cathodic polarizations were performed. (a) Photograph after a –2000 mV polarization. (b) Optical micrograph after a –1500 mV polarization. The metal electrode was strongly adhered to the YSZ and difficult to remove (the white in (b) is where fresh YSZ is exposed because the top layer was pulled off during removal of the electrode). The YSZ surface outside of the interface sometimes showed cracking as in (b).

Blackening is believed to be the result of these trapped electrons in the YSZ subsurface, forming color centers. After the SCPs in the present tests, the electrolyte surface near the interface was visibly blackened (**Figure 5-36**). Reducing zirconia is known to increase the electronic conductivity [76, 77]. The decreasing R_S in the impedance data indicates that electronic conductivity was induced in the YSZ during the SCPs. The increasing R_S thereafter indicates loss of the electronic conductivity in the YSZ as it re-oxidizes. The R_S seemed to increase more quickly in 50% H_2O/H_2 than in dry H_2, which is consistent with re-oxidation because the pO_2 is much greater in 50% H_2O/H_2. Re-oxidation of electrochemically reduced YSZ has been studied in the literature [78]. The blackened coloration seems to last much longer through oxidation than the electronic conductivity.

—*Lasting activation (decrease in LSR_P).* The activation could be the result of a few different mechanisms.

- The electrons that were trapped in the electrolyte surface might enhance the catalytic activity, proposed by ref. [67].
- Impurities such as SiO_2 that were blocking parts of the TPB might be reduced to metal and unblock parts of the TPB, proposed by ref. [14]. In the present study, polarization at between –500 and –1000 mV provided the first activation effects. The polarization was applied in dry H_2 atmosphere (–1370 mV vs air at 850 °C). Therefore, this corresponds to an oxygen activity of –1870 to –2370 mV vs air (10^{-35} to 10^{-44} atm O_2 at 850 °C). The maximum polarizations of –1500 and –2000 mV correspond to –2870 and –3370 mV vs air (10^{-53} to 10^{-62} atm O_2 at 850 °C). According to thermodynamic data, silica is favored to reduce to Si at oxygen activities less than 10^{-33} atm at 850 °C [54]. ZrO_2 is favored to reduce to Zr metal at 10^{-41} atm. The segregated impurities are known to be comprised of glassy Na-K-Ca-Mg-Al-Si phases which segregate as a "rim ridge" at the perimeter of the interface [11, 14, 35-37, 39, 43, 79]. In the present study such phases were found as particles embedded in or attached to the metal wire in some locations, as well as on the

YSZ surface inside the interface. The glassy phases probably can be reduced in a similar range as their oxide constituents. Oxides of Al, Mg, and Ca, are reduced to metal at similar or slightly lower oxygen activities than Zr. In fact, according to the thermodynamic data these metals are liquid in these conditions. The SCP clearly provides the conditions to reduce the impurity phases (as well as the YSZ) and the reduced impurities may become mobile and rearrange such that when they re-oxidize upon releasing the strong cathodic bias, the TPB may be relatively unblocked and freshened. This mechanism seems very possible. The electrodes would likely slowly deactivate again after releasing the SCP.

- Changes in the microstructure of the metal-YSZ interface could occur. If the ZrO_2 is reduced to Zr metal during the SCP (and possibly also the yttria to Y metal, which should occur at lower oxygen activity than 10^{-49} atm), the metal electrode might alloy with the metallic phases. Upon releasing the polarization, the Zr metal is favored to re-oxidize and a metal-Zr-O composite phase with a rough micro- or nanostructure could form. Sub-oxides of ZrO_2, ZrO_{2-x}, might also be reactive with the metal electrode. Both Zr metal and nano-crystallites of ZrO_{2-x} [72] have been reportedly found along the grain boundaries of electrochemically reduced YSZ. Nano-sized grains of tetragonal YSZ were also found after re-oxidation of electrochemically reduced YSZ [75]. After tests that included SCP, most metal electrodes were strongly adhered to the YSZ surface (whereas usually the electrodes are easily lifted off), which supports the idea of alloying or reactivity between the reduced YSZ and the metal electrode. Indeed, SEM micrographs of the interface after pulling off the electrode revealed a complex microstructure composed of metal and YSZ inside the contact area and at the perimeter (**Figure 5-37** and **Figure 5-38**). The metal wire also had a corresponding nanostructured surface where it had been in contact with the YSZ surface (**Figure 5-38c**), which is very different than the relatively smooth and flat surface observed when strong cathodic polarization had not been applied (**Figure 5-7**). The YSZ surface adjacent to the interface with an Ni electrode which had formed a belt of Ni particles earlier in the test (see **Figure 5-15**) exhibited Ni-YSZ nanostructures surrounding most of the Ni particles in the belt (**Figure 5-38a+b+d**). Probably the Ni particles were not connected to the bulk electrode, so the current path was through the reduced YSZ. Since R_S decreased it is expected that the surface YSZ reduced outwards from the electrode. The YSZ probably also reduced downwards from the electrode, but if it had only reduced downwards R_S would not increase until a large portion of the thickness of the YSZ pellet had been reduced, which is unlikely.

Thus it seems likely that both reduction of impurities and reaction of the metal electrode with reduced zirconia, resulting in the formation of a fine microstructure, are responsible for the observed activation. In fact, both mechanisms would increase the TPB length, one un-blocking the TPB and the other roughening it. It would be interesting to see if exposure to high temperature coarsened the fine microstructure as was observed for the oxidized Ni electrodes

(**section 5.3.5.1**), however the impurities would also likely re-accumulate more quickly at higher temperature obscuring any increasing in LSR_p that might be observed. It is important to note that, in light of the observed fine microstructured TPB after strong cathodic polarization, the normalization to the TPB length to obtain LSR_p is no longer accurate because the TPB length has increased. However it is still useful to compare the degree of activation, as discussed at the end of **section 5.3.2**.

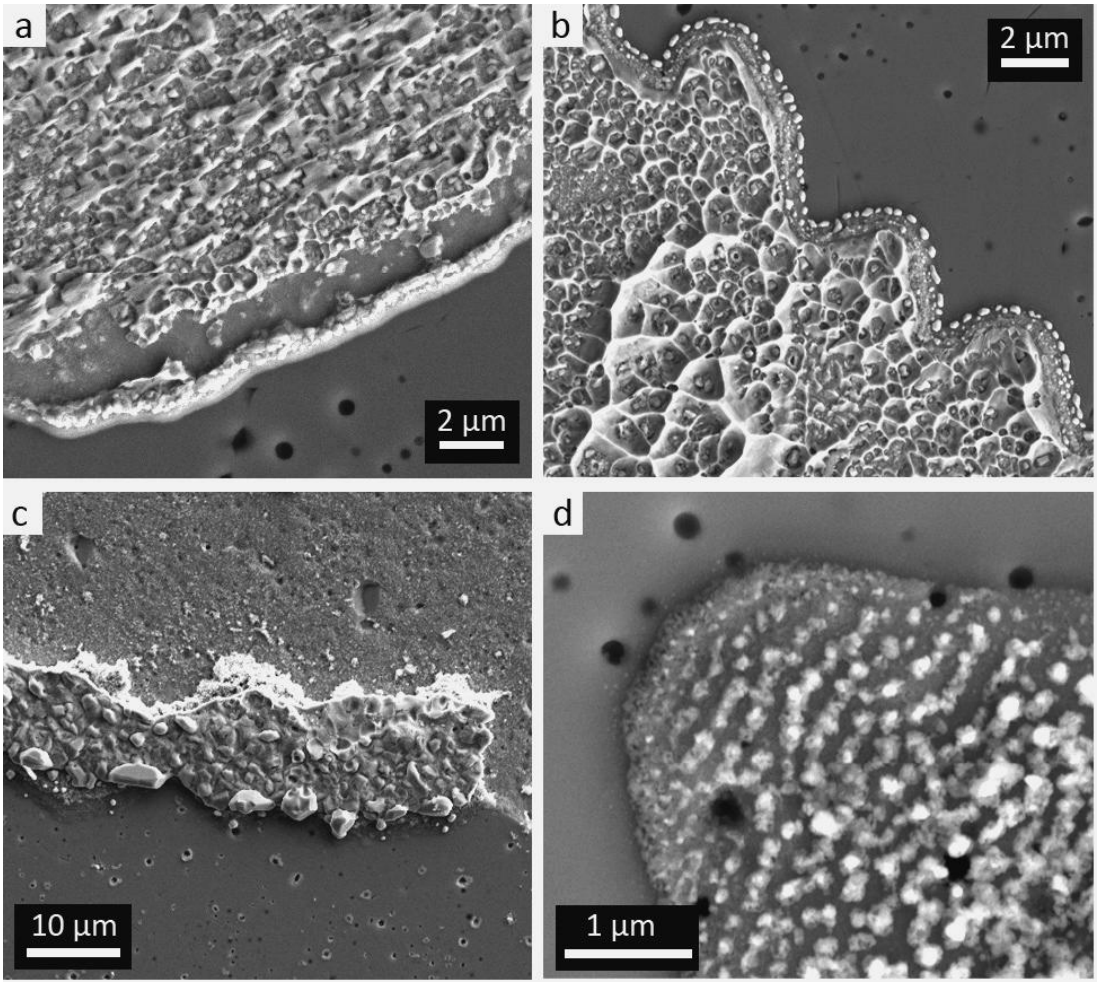

Figure 5-37. SEM micrographs of the YSZ surface at the edge of where the metal-YSZ interface had been during testing, for (a) a Pt electrode, (b) the same Pt electrode elsewhere on the perimeter, (c) a Pd electrode, (d) a Ni electrode (not the same electrode as shown in **Figure 5-38**). In (c) a layer of the YSZ surface had pulled off when removing the adhered electrode, except in some parts of the perimeter part of the electrode remained.

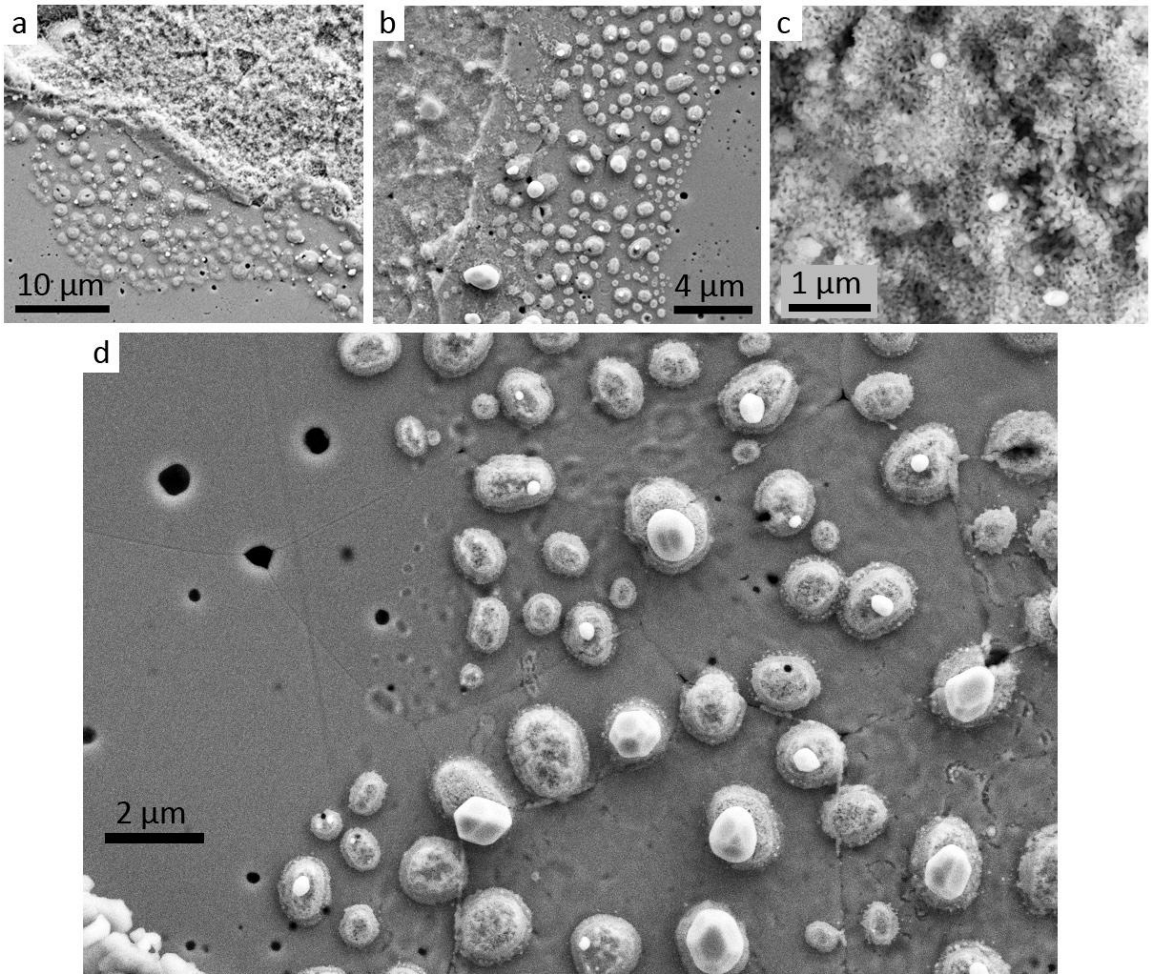

Figure 5-38. SEM micrographs of the (a, b and d) YSZ surface at the edge of the contact area of a Ni electrode which had been subjected to a strong cathodic polarization. (c) The surface of the Ni wire that had been in contact with the YSZ surface. The Ni particle belt described previously had formed on the smooth polished YSZ surface outside the contact area, and the subsequent SCP formed Ni-zirconia composite nanostructures.

Altogether the effects of strong cathodic polarization seem to make the point-contact electrodes more similar to cermet electrodes with fine microstructure – the nearly linear polarization curves are observed for fine-structured Ni-YSZ cermets, and the activation energy observed after strong cathodic polarization of the Ni point electrode is similar to that of fine Ni-YSZ cermets as well. However, the nanostructures resulting from reactivity between the metal and the reduced YSZ should not be present in cermets that were not subjected to strong cathodic polarization, so one possibility for the linearity for fine cermets is that there are fewer impurities. This will be further discussed in the next **section 5.4**. In regards to the nanostructures, during this study another research group performed strong cathodic polarization –2000 mV on a full cell with a Ni-YSZ cermet negative electrode and observed a decrease in the polarization resistance [80]. That study is still underway, but according to the

authors they observed fine Ni-YSZ nanostructures as a result of the treatment (not yet published).

5.4. Discussion of Reaction Mechanisms

Widely different responses of different metals to the same parameter changes were observed. The gas partial pressure dependencies of LSR_p were different between the different metals, and shapes of the polarization curves and impedance spectra were different. These observations provide evidence that the different metals do not generally share the same reaction mechanisms, contrary to recent studies that suggested that the relative electrochemical activity of various metals, including those studied here, is simply correlated to metal oxide formation enthalpy [28] or the stability of surface-adsorbed atomic oxygen [81]. The electrocatalytic activities may be more complicated than a single correlated property of the metals could describe. Those studies were based on a more limited set of measurements – only anodic polarization in dry H_2 (a single experimental condition). Also, the purities of the different metals used were not specified.

Based on the phenomena observed in this study, the reaction mechanisms that take place for oxidation and reduction of H_2/H_2O and CO/CO_2 at metal-YSZ interfaces must be able to explain the following:

—*Inconsistencies between studies*:

For the different metals:

1. The differences in relative performance between different studies

For a given metal:

2. The variability of the magnitude of LSR_p in the same conditions in different studies
3. The differences in the activation energies in different studies

For Ni electrodes specifically (they have been the most studied in literature):

4. The different number of rate-limiting processes identified in different studies based on impedance spectra measured at the same conditions
5. The large difference, usually around an order of magnitude, of LSR_p between H_2/H_2O and CO/CO_2 observed for all metals in this study and in other studies versus the relatively little difference in other studies
6. The differences in the degree of gas partial pressure dependencies in different studies (the trends are generally consistent but the degree of the dependency differs)
7. The differences in the bias dependency of the LSR_p in different studies

—*The responses of the different metals observed in this study*:

8. The gas partial pressure dependencies of the impedance of the different metals (section 5.3.3.1 and 5.3.3.2) including the shapes of the impedance data

9. The shapes of the polarization curves of the different metals (section 5.3.4.1)
10. The evolution of the impedance spectra under applied potential (section 5.3.4.2) including the inductive loops and apparent diffusion-limited reponses
11. The activation effects of polarization and relaxation thereafter (section 5.3.4.1, 5.3.4.2, and 5.3.4.3)
12. The activation effects of strong cathodic polarization on the magnitude of the LSR_P, on the shape of the OCV impedance spectra and on the shape of the polarization curves (section 5.3.5.2).

Fully determining the reaction mechanisms for all of the metals for H_2 oxidation, H_2O reduction, CO oxidation, and CO_2 reduction is outside of the scope of this study. An electrochemical model could be derived to try to describe the impedance data, which is a topic of future work. First, however, a hypothesis must be formed, for which it is useful to examine the trends.

Some trends were already discussed in the earlier sections for the results presented here. There also seems to be a trend running through literature and this study that might be able to explain the inconsistencies between studies. The different results seem to correlate with the purity of the starting materials and/or the fineness of the microstructure (outlined in **Figure 5-39**). For example, for Ni the activation energies range from 1.4-1.6 eV for point-contact electrodes [6, 7, 82], pattern and porous electrodes [24], felt electrodes and coarse cermets [25], to 0.7-1.0 eV for fine cermets [24-26] and for pattern [19, 21, 26], porous [26], and point-contact [14] electrodes prepared on high-purity single-crystal YSZ. Both fine cermets and coarse electrodes prepared with high-purity materials clearly correlate with lower activation energy.

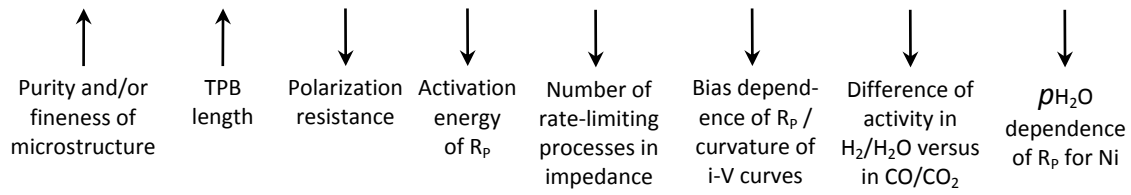

Figure 5-39. Proposed correlation of inconsistencies between different studies based on trends observed. Arrows pointing upwards signify an increase and arrows pointing downwards signify a decrease.

In the last 8 years clear evidence that impurities segregate and accumulate the TPB has been found, as discussed earlier. These impurities might be responsible for all of the observed inconsistencies. Finer microstructures might improve performance by a different mechanism, however in a fine three-dimensional structure the large number of reaction sites (very long TPB and surface area) might not be as significantly affected by impurities. In other words, since the impurities segregate from the YSZ and from the metal, with a much longer TPB length per

quantity of material (and corresponding quantity of impurities) as a result of fine microstructure, the reaction sites at the TPB would become relatively less blocked by impurities as they segregate during heat treatment.

With different starting purity of the materials, different studies would observe very different performance for the same metals even if they used the exact same electrode geometry or microstructure because their cells have different available TPB lengths. The effect of impurities on increasing the polarization resistance was clearly demonstrated for Ni point electrodes by several authors [11, 14, 36, 37, 39, 43, 79]. This can explain items 1 and 2 above. How could the higher activation energies (item 3 above) be explained by the TPB being simply partly blocked? There appears to be a correlation between LSR_P and activation energy for Ni electrodes [1, 11] [38]. A possible explanation is that with fewer available reaction sites due to impurities, a different rate-limiting step with a higher activation energy dominates, such as diffusion around or through the impurities. This would also explain the different number of rate-limiting processes (item 4 above) reported on Ni electrodes and assuming that strong cathodic polarization reduces impurities as proposed this would explain the apparent disappearance of rate-limiting processes as a result of strong cathodic polarization observed here (**Figure 5-32**). Microstructural differences alone might also be able to explain some of these inconsistencies. In the study mentioned earlier which correlated electrocatalytic activity of various metals with the metal oxide formation enthalpy [28], it was noted that the grain sizes of the porous electrodes tested varied by more than a factor of 2. However, Pd was found to be more than an order of magnitude less active for H_2 oxidation than Ni, which cannot reconcile the results with those found here.

Some of the inconsistencies seem to be more related to microstructure than impurities. In terms of the different relative activities of Ni in H_2/H_2O versus CO/CO_2 (item 5), after the strong cathodic polarization the activity was still around an order of magnitude lower for CO/CO_2 than for H_2/H_2O for all metals (**Figure 5-30** and **Figure 5-33**). The strong cathodic polarization, which likely reduces impurities, did not help reduce the gap in performance between H_2/H_2O and CO/CO_2. A fine three-dimensional microstructure in a porous cermet might provide enough reaction sites that the relatively slower adsorption and surface diffusion of CO/CO_2 intermediates than H_2/H_2O intermediates has less effect. The gas partial pressure dependencies (namely the pH_2O dependency) and the bias dependency of the polarization resistance of Ni (items 6 and 7 above) seem to be higher for coarser microstructures [25, 26]. Bieberle and Gauckler [26] observed stronger activation with bias for smaller-TPB Ni electrodes and this seems to be independent of purity because they used high-purity single-crystal YSZ for all cells. The results of Brown et al [25] along with their tabulation of prior work show an apparent correlation between fineness of microstructure and pH_2O dependence of the polarization resistance for various Ni electrode geometries, ranging from 0.5-0.6 for wire, paste, felt, and pattern electrodes to 0.4 for the coarse cermet they tested and only 0.2-0.3 for fine

cermets. The first report from a study currently being carried out by Utz et al [22] on Ni pattern electrodes provides a good review of other $p\mathrm{H_2O}$ dependencies found in literature, and is consistent with the above.

The greater bias dependence with coarser microstructure might be related to the possible activation by accumulation of adsorbed intermediate species discussed in **section 5.3.4.2** and **section 5.3.4.3**. The species would accumulate on either the metal surface, the YSZ surface, or both. Coarser structures have more surface per TPB than finer structures, providing more area for accumulation. The inductive loops observed in some impedance spectra measured under bias are consistent with adsorbed intermediates (**sections 5.3.4.2** and **5.3.5.1**). Based on the discussion above, it does not seem likely that the previously proposed [15] mobilization of impurities by their reaction with product H_2O during anodic bias plays a major role in the bias dependence (or $p\mathrm{H_2O}$ dependence), although that might also be occurring to some extent.

Several mechanisms have been proposed for the $p\mathrm{H_2O}$ dependence of the polarization resistance for Ni. One is that it can be simply explained by "equilibrium-potential effects alone, without the necessity of assuming any additional kinetic or catalytic effect" [83]. In light of the results of the present study – increasing R_p with higher $p\mathrm{CO_2}$ in $\mathrm{CO/CO_2}$ atmospheres for Ni, and an opposite response in $\mathrm{H_2/H_2O}$ (increasing R_p with higher $p\mathrm{H_2O}$) for Pd versus Ni – this explanation seems unlikely. Another proposed mechanism is based on the higher $p\mathrm{H_2O}$ leading to a hydroxylated YSZ surface which allows the migration of H^+ on the YSZ [21]. Presumably this mechanism would be independent of the metal electrode material, however in the present study Pd exhibits the opposite $p\mathrm{H_2O}$ dependency. That does not rule out the YSZ-hydroxyl mechanism for Ni, though, because the mechanism may be different for Pd. For Pd, the increase in $p\mathrm{H_2O}$ might bring about a competing phenomena that is more detrimental to performance than any improvements the adsorbed hydroxyls on YSZ might bring. For example, the increase in $p\mathrm{H_2O}$ might block adsorbed/absorbed hydrogen on Pd.

There is no reason that the same adsorbed intermediates that might be accumulating during polarization are not also more available in higher $p\mathrm{H_2O}$. The magnitude of the capacitance is worth considering. For the impedance spectra shown in **Figure 5-9** and **Figure 5-10**, the change from 3% $\mathrm{H_2O/H_2}$ to 50% $\mathrm{H_2O/H_2}$ results in a ~50% increase in the capacitance, which is calculated according to equation (**5.3**).

$$C = \frac{1}{2 \cdot \pi \cdot f \cdot R_P} \tag{5.3}$$

The capacitance changes from about 8×10^3 to 12×10^3 $\mu F/cm^2$. This magnitude is characteristic of a chemical capacitance, not a double-layer capacitance. Adsorbed intermediate species are known to cause such a pseudo-capacitance. An increase in the capacitance could simply be due to the adsorption of more of the species that cause it. Compared with this 3%

H_2O/H_2 to 50% H_2O/H_2 change in capacitance, the impedance spectra measured under bias shown in **Figure 5-18** exhibit a similar increase in capacitance between OCV and +150 mV anodic bias and similar magnitudes. As discussed in ref. [30], at high temperature H_2O was found to adsorb onto Pt by $H_2O \rightarrow OH + H$ and hydroxyl coverage is promoted on the surface [84, 85]. It is also sensible to assume that in higher $p$$H_2O$ there would be more OH adsorbed on the surface whereas in higher $p$$H_2$ there would be more H adsorbed on the surface. Since Ni, Cu and Pt share a similar response to $p$$H_2O$ and only Pd is different, we propose that hydroxyl species adsorbed on the metal surface are the source of activation for Ni, Cu, and Pt. The apparent higher activity of Pd in the presence of more H_2 can probably be explained by the Pd–H system. It is well-known that hydrogen is soluble in Pd. In fact Pd-hydride has been considered as a means of hydrogen storage. At standard temperature and pressure, Pd can absorb up to 900 times its own volume of hydrogen. On a H^+ conducting electrolyte, a dense Pd film electrode was observed to have higher performance for H_2 oxidation than a porous Pd electrode [86] – the H_2 transports through the Pd film and the entire film surface is reactive. This might explain some of the anomalous behavior of Pd in H_2/H_2O. However, it does not explain the higher electrolysis performance for CO_2 than for CO oxidation. Recently, Vogler et al [31] showed via modeling that, besides a hydroxyl transfer mechanism between Ni and YSZ, a double hydrogen transfer mechanism might be able to explain the $p$$H_2O$ dependency of the polarization resistance, and that the double hydrogen transfer mechanism seems to be more consistent with the lack of $p$$H_2$ dependence. The adsorption of hydroxyl species on metal surfaces at high temperature does not appear to be well known in surface science, whereas dissociative adsorption is well known and known to be fast and can result in high H_{ad} coverage [87]. In addition to the uncertainty of which species accumulates, it is also not known which surface, the Ni or YSZ (or both), hosts the accumulated species. Clearly, more modeling efforts will be needed to determine which adsorbed species are part of the rate-limiting step.

Nearly linear polarization curves, which are indicative of a very high exchange current density, were obtained after strong cathodic polarization, most likely due to the longer TPB that resulted from either the fine microstructure that formed or the removed impurities that no longer blocked the TPB. This type of polarization curves are typically measured only on fine cermet electrodes. Before strong cathodic polarization, many i-V curves could possibly be described by Tafel kinetics. The impedance spectra also indicate that the strong cathodic polarization seems to have eliminated one or more rate limiting processes.

Finally, it is worth considering the magnitude of the length-specific polarization resistance values measured here and measurements reported in literature and how it relates to porous cermet electrodes. A few recent studies have provided estimates of the TPB length per unit volume of a porous Ni-YSZ cermet electrode, of around 2-6 $\mu m/\mu m^3$ [88-91]. It is also known that a good Ni-YSZ cermet electrode can have an OCV polarization resistance of about 0.1 Ω cm^2 at 850 °C in H_2/H_2O and that the physical thickness of the electrode that contains active

TPB sites is about 10 μm [82]. From these values, a simple calculation can be done to estimate the LSR_p in a porous electrode and compare it to the point electrode measurements. This gives a LSR_p value in the range of 20-60 kΩ cm for the porous cermet (of course this would be on average, since there is a gradient in the porous electrode with more reactions occurring at the TPB regions closer to the electrolyte). In the present work, LSR_p values of approximately 6 and 30 kΩ cm were measured on the point electrode (with a TPB presumably blocked by impurities) at 850 °C in 50% H_2O/H_2 and 3% H_2O/H_2 respectively. Since the activating effect of H_2O is much less significant in a fine cermet, presumably the 3% H_2O/H_2 value can be compared. That the order of magnitude agrees so well is remarkable, and if such a simple calculation is correct, it suggests that perhaps equal concentrations of impurities are segregated to the TPB in the cermet electrode. In that case, the fine microstructure itself would be solely responsible for the different electrochemical properties of coarse and fine microstructured electrodes (such as the different activation energies).

5.5. Conclusions

Metal wires contacting YSZ were systematically characterized as model electrodes for solid oxide cells. A number of important observations about the electrode kinetics of metal-YSZ interfaces were made:

- Widely different impedance responses of the different metals to the same parameter changes (such as gas composition and applied potential) were observed, which provides evidence that the different metals do not generally share the same reaction mechanisms, contrary to some recent studies that tried to correlate electrocatalytic activity of metals for H_2 oxidation with a single other property of the metals. Trends in the responses were observed, indicating that some metals do share the same reaction mechanism in some conditions.

- The relative performance of the metals was Ni > Pd > Pt > Cu for H_2 oxidation, Pd > Ni > Pt > Cu for H_2O reduction, Ni > Pd > Cu > Pt for CO oxidation, and Pd > Ni > Pt > Cu for CO_2 reduction. Pd was especially more active for the reduction reactions than for the oxidation reactions whereas Cu and Ni behaved oppositely. Pt was more active for oxidation of H_2 than reduction of H_2O, but in CO/CO_2 it was more active for CO_2 reduction than CO oxidation.

- Oxidation of Ni electrodes followed by re-reduction apparently induced formation of a fine microstructure of the Ni electrode and improved the electrode performance by an order of magnitude, but at high temperature (>850 °C) the effect was subsequently undone, most likely due to coarsening back to a smooth TPB.

- Strong cathodic polarization was also found to improve performance by as much as an order of magnitude, for all of the metals. The activation energies of the metals also significantly decreased. Based on the impedance spectra, one or more rate-limiting processes appeared to have been eliminated. The interfaces were examined in the scanning electron microscope after testing and displayed interesting microstructural features resulting from this treatment. It is believed that the TPB length was enhanced by reducing impurities that were segregated at the TPB, unblocking the TPB, and by reaction of Ni with reduced YSZ during the treatment, which formed a fine microstructure at the TPB. Further studies of the effects of cathodic polarization might reveal more information about the exact mechanism.

- The results – the length-specific polarization resistance at OCV, the activation energy, the dependence of R_P on different gas partial pressures, the bias dependence of the impedance (and corresponding shape of polarization curves), and the relative performance between H_2/H_2O and CO/CO_2 for each metal – were compared with results in literature, and reasons for inconsistencies between different studies were proposed. Trends were identified and discussed. Evidence supports the explanation that impurities segregated to the TPB are responsible for the inconsistencies between the results in different electrode kinetics studies. The impurities are more detrimental to the performance of coarse metal-YSZ electrodes (with large electrode and electrolyte surface area and volume – e.g. sources of the impurities – per TPB length) than electrodes with fine microstructure (e.g. cermets) most likely because they block a greater fraction of the total TPB.

5.6. References

1. Mogensen M, Hogh J, Hansen KV, and Jacobsen T, *A Critical Review of Models of the $H_2/H_2O/Ni/SZ$ Electrode Kinetics*. ECS Transactions, (2007). **7**(1): p. 1329-1338.
2. Goodwin DG, Zhu H, Colclasure AM, and Kee RJ, *Modeling Electrochemical Oxidation of Hydrogen on Ni--YSZ pattern Anodes*. Journal of the Electrochemical Society, (2009). **156**(9): p. B1004-B1021.
3. Guindet J, Roux C, and Hammou A. *Hydrogen oxidation at the Ni/zirconia electrode*. in *Proc. of the 2nd International Symposium on SOFC*. (1991). Athens, Greece.
4. Norby T, Velle OJ, Leth-Olsen H, and Tunold R, *Reaction resistance in relation to three phase boundary length of Ni-YSZ electrodes*. Proc. of the 3rd International Symposium on SOFC, (1993). **93-4**: p. 473-478.
5. Norby T. *Electrochemical behaviour of Ni-YSZ electrodes*. in *Proc. of the 2nd European Solid Oxide Fuel Cell Forum*. (1996). Oslo, Norway.
6. Baker R, Guindet J, and Kleitz M, *Classification criteria for solid oxide fuel cell electrode materials*. Journal of the Electrochemical Society, (1997). **144**(7): p. 2427-2432.
7. Mohamedi-Boulenouar FZ, Guindet J, and Hammou A. *Influence of water on electrochemical oxidation of H_2 at the nickel-YSZ interface*. in *Proc. of the 5th International Symposium on SOFC (SOFC-V)*. (1997). Pennington, NJ.
8. Aaberg RJ, Tunold R, Mogensen M, Berg RW, and Odegard R, *Morphological Changes at the Interface of the Nickel-Yttria Stabilized Zirconia point Electrode*. Journal of the Electrochemical Society, (1998). **145**(7): p. 2244-2252.

9. Aaberg RJ, Tunold R, and Ødegård R, *On the electrochemistry of metal-YSZ single contact electrodes.* Solid State Ionics, (2000). **136-137**: p. 707-712.
10. Kek D, Mogensen M, and Pejovnik S, *A study of metal (Ni, pt, Au)/yttria-stabilized zirconia interface in hydrogen atmosphere at elevated temperature.* Journal of the Electrochemical Society, (2001). **148**(8): p. A878-A886.
11. Vels Jensen K, *The Ni-YSZ interface: Structure, composition and electrochemical properties at 1000°C*, Ph.D. thesis in *Materials Research Department*. (2002), Risø National Laboratory: Roskilde, Denmark. p. 111.
12. Lauvstad GO, Tunold R, and Sunde S, *Electrochemical oxidation of CO on pt and Ni point electrodes in contact with an yttria-stabilized zirconia electrolyte - I. Modeling of steady-state and impedance behavior.* Journal of the Electrochemical Society, (2002). **149**(12): p. E497-E505.
13. Lauvstad GO, Tunold R, and Sunde S, *Electrochemical oxidation of CO on pt and Ni point electrodes in contact with an yttria-stabilized zirconia electrolyte - II. Steady-state and impedance measurements.* Journal of the Electrochemical Society, (2002). **149**(12): p. E506-E514.
14. Høgh J, *Influence of impurities on the $H_2/H_2O/Ni/YSZ$ electrode*, Ph.D. thesis in *Materials Research Department / Department of Chemistry*. (2005), Risø National Laboratory / The Technical University of Denmark: Roskilde, Denmark. p. 127.
15. Schmidt MS, Vels Hansen K, Norrman K, and Mogensen M, *Three-phase-boundary dynamics at the Ni/ScYSZ interface.* Solid State Ionics, (2009). **180**(4-5): p. 431-438.
16. Bieberle A, *The electrochemistry of solid oxide fuel cell anodes: Experiments, modelling, and simulations*, thesis. (2000), Swiss Federal Institute of Technology,: Switzerland.
17. Habibzadeh B, Sukeshini AM, Becker B, and Jackson GS, *CO Electrochemical Oxidation on Ni patterned Anodes for Assessing Solid Oxide Fuel Cell Kinetics.* ECS Transactions, (2008). **11**(33): p. 53-61.
18. Mizusaki J, Tagawa H, Saito T, Yamamura T, Kamitani K, Hirano K, et al., *Kinetic studies of the reaction at the nickel pattern electrode on YSZ in H_2---H_2O atmospheres.* Solid State Ionics, (1994). **70-71**(Part 1): p. 52-58.
19. Yamamura T, Yoshitake H, Tagawa H, Mori N, Hirano K, Mizusaki J, et al. *Experimental Evidence for Three phase Boundary as Active Site on Nickel/YSZ System*. in *2nd Euro. Solid Oxide Fuel Cell Forum*. (1996).
20. Yamamura T, Tagawa H, Saito T, Mizusaki J, Kamitani K, Hirano K, et al. *Reaction Kinetics at the Nickel pattern Electrode on YSZ and its Dependence on Temperature*. in *4th Int. Sympo. Solid Oxide Fuel Cells*. (1995).
21. Bieberle A, Meier LP, and Gauckler LJ, *The Electrochemistry of Ni pattern Anodes Used as Solid Oxide Fuel Cell Model Electrodes.* Journal of the Electrochemical Society, (2001). **148**(6): p. A646-A656.
22. Utz A, Stormer H, Leonide A, Weber A, and Ivers-Tiffee E, *Degradation Effects of Ni patterned Anodes in H_2/H_2O Atmosphere.* ECS Transactions, (2009). **25**(2): p. 2013-2021.
23. Mizusaki J, Tagawa H, Saito T, Kamitani K, Yamamura T, Hirano K, et al., *Preparation of Nickel pattern Electrodes on YSZ and Their Electrochemical properties in H_2-H_2O Atmospheres.* Journal of the Electrochemical Society, (1994). **141**(8): p. 2129-2134.
24. de Boer A, *Hydrogen oxidation at porous nickel and nickel/yttria-stabilised zirconia cermet electrodes*, Ph.D. thesis. (1998), University of Twente: The Netherlands.
25. Brown M, Primdahl S, and Mogensen M, *Structure/Performance Relations for Ni/Yttria-Stabilized Zirconia Anodes for Solid Oxide Fuel Cells.* Journal of the Electrochemical Society, (2000). **147**(2): p. 475-485.
26. Bieberle A and Gauckler LJ, *Ni-based SOFC anodes: Microstructure and electrochemistry.* Zeitschrift Fur Metallkunde, (2001). **92**(7): p. 796-802.
27. Mogensen M, Jensen KV, Jorgensen MJ, and Primdahl S, *Progress in understanding SOFC electrodes.* Solid State Ionics, (2002). **150**(1-2): p. 123-129.
28. Setoguchi T, Okamoto K, Eguchi K, and Arai H, *Effects of Anode Material and Fuel on Anodic Reaction of Solid Oxide Fuel Cells.* Journal of the Electrochemical Society, (1992). **139**(10): p. 2875-2880.
29. Bessler WG, Gewies S, and Vogler M, *A new framework for physically based modeling of solid oxide fuel cells.* ELECTROCHIMICA ACTA, (2007). **53**(4): p. 1782-1800.
30. Bieberle A and Gauckler LJ, *State-space modeling of the anodic SOFC system Ni, H_2-H_2O|YSZ.* Solid State Ionics, (2002). **146**(1-2): p. 23-41.

31. Vogler M, Bieberle-Hutter A, Gauckler L, Warnatz J, and Bessler WG, *Modelling Study of Surface Reactions, Diffusion, and Spillover at a Ni/YSZ patterned Anode*. Journal of the Electrochemical Society, (2009). **156**(5): p. B663-B672.
32. Matsuzaki Y, Hishinuma M, and Yasuda I. *Electrochemical Characteristics of a Ni-YSZ Cermet Electrode on YSZ in a H_2-H_2O-CO-CO_2 System*. in *Sixth Intl Symp. on Solid Oxide Fuel Cells (SOFC-VI)*. (1999). Honolulu, Hawaii: Electrochemical Society.
33. Holtappels P, De Haart LGJ, Stimming U, Vinke IC, and Mogensen M, *Reaction of CO/CO_2 gas mixtures on Ni-YSZ cermet electrodes*. Journal of Applied Electrochemistry, (1999). **29**(5): p. 561-568.
34. Eguchi K, Setoguchi T, Okamoto K, and Arai H. *An Investigation of Anode Material and Anodic Reaction for Solid Oxide Fuel Cell*. in *Third International Symposium on Solid Oxide Fuel Cells (SOFC III)*. (1993). Honolulu, Hawaii: Electrochemical Society.
35. Vels Jensen K, Primdahl S, Chorkendorff I, and Mogensen M, *Microstructural and chemical changes at the Ni/YSZ interface*. Solid State Ionics, (2001). **144**(3-4): p. 197-209.
36. Vels Jensen K, Wallenberg R, Chorkendorff I, and Mogensen M, *Effect of impurities on structural and electrochemical properties of the Ni-YSZ interface*. Solid State Ionics, (2003). **160**(1-2): p. 27-37.
37. Schmidt MS, Hansen KV, Norrman K, and Mogensen M, *Characterisation of the Ni/ScYSZ interface in a model solid oxide fuel cell anode*. Solid State Ionics, (2008). **179**(39): p. 2290-2298.
38. Mogensen M and Hansen KV, *Impact of impurities and interface reaction on electrochemical activity*, in *Handbook of Fuel Cells – Fundamentals, Technology and Applications*, W. Vielstich, H. Yokokawa, and H.A. Gasteiger, Editors. (2009), John Wiley & Songs, Ltd.
39. Schmidt MS, *Effects of dopants and trace elements at the Ni / ScYSZ interface*, PhD thesis. (2008), University of Southern Denmark.
40. Newman J, *Resistance for Flow of Current to a Disk*. Journal of the Electrochemical Society, (1966). **113**(5): p. 501-502.
41. Nielsen J and Jacobsen T, *Three-phase-boundary dynamics at pt/YSZ microelectrodes*. Solid State Ionics, (2007). **178**(13-14): p. 1001-1009.
42. Nielsen J and Jacobsen T, *Three-Phase-Boundary dynamics at metal/YSZ microelectrodes*. Solid State Ionics, (2008). **178**(33-34): p. 1769-1776.
43. Schmidt MS, Hansen KV, Norrman K, and Mogensen M, *Effects of trace elements at the Ni/ScYSZ interface in a model solid oxide fuel cell anode*. Solid State Ionics, (2008). **179**(27-32): p. 1436-1441.
44. Appel CC, Bonanos N, Horsewell A, and Linderoth S, *Ageing behaviour of zirconia stabilised by yttria and manganese oxide*. Journal of Materials Science, (2001). **36**(18): p. 4493-4501.
45. Barsoukov E and Macdonald JR, *Impedance Spectroscopy: Theory, Experiment, and Applications*. 2 ed. (2005): Wiley-Interscience. 616.
46. Primdahl S and Mogensen M, *Gas conversion impedance: A test geometry effect in characterization of solid oxide fuel cell anodes*. Journal of the Electrochemical Society, (1998). **145**(7): p. 2431-2438.
47. Primdahl S and Mogensen M, *Gas diffusion impedance in characterization of solid oxide fuel cell anodes*. Journal of the Electrochemical Society, (1999). **146**(8): p. 2827-2833.
48. Jacobsen T, Hendriksen PV, and Koch S, *Diffusion and conversion impedance in solid oxide fuel cells*. Electrochimica Acta, (2008). **53**(25): p. 7500-7508.
49. Geyer J, Kohlmuller H, Landes H, and Stubner R, *Investigations into the Kinetics of the Ni-YSZ-cermet-anode of a Solid Oxide Fuel Cell*. Electrochemical Proceedings, (1997). **97-18**: p. 585-594.
50. Jensen SH, Larsen PH, and Mogensen M, *Hydrogen and synthetic fuel production from renewable energy sources*. International Journal of Hydrogen Energy, (2007). **32**(15): p. 3253-3257.
51. Ebbesen SD and Mogensen M, *Electrolysis of carbon dioxide in Solid Oxide Electrolysis Cells*. Journal of Power Sources, (2009). **193**(1): p. 349-358.
52. Ebbesen SD, Graves C, and Mogensen M, *Production of Synthetic Fuels by Co-Electrolysis of Steam and Carbon Dioxide*. International Journal of Green Energy, (2009). **6**(6): p. 646 – 660.
53. Guth U and Zosel J, *Electrochemical solid electrolyte gas sensors - Hydrocarbon and NOx analysis in exhaust gases*. Ionics, (2004). **10**(5-6): p. 366-377.
54. *FactSage 5.5 software*.

55. Gubner A, Landes H, Metzger J, Seeg H, and Stübner R, in *Proceedings of 5th International Symposium on Solid Oxide Fuel Cells (SOFC-V)*, U. Stimming, et al., Editors. (1997): Pennington, NJ. p. 884.
56. Hauch A, Ebbesen SD, Jensen SH, and Mogensen M, *Solid Oxide Electrolysis Cells: Microstructure and Degradation of the Ni/YSZ Electrode.* Journal of the Electrochemical Society, (2008). **11**(155): p. B1184-B1193.
57. Du K, Ernst F, Garrels M, and Payer J, *Formation of nickel nanoparticles in nickel-ceramic anodes during operation of solid-oxide fuel cells.* International Journal of Materials Research, (2008). **99**(5): p. 548-552.
58. Sehested J, Gelten JAP, Remediakis IN, Bengaard H, and Norskov JK, *Sintering of nickel steam-reforming catalysts: effects of temperature and steam and hydrogen pressures.* Journal of Catalysis, (2004). **223**(2): p. 432-443.
59. van Hassel BA, Boukamp BA, and Burggraaf AJ, *Electrode polarization at the Au, O_2(g)/yttria stabilized zirconia interface. part I: Theoretical considerations of reaction model.* Solid State Ionics, (1991). **48**(1-2): p. 139-154.
60. van Hassel BA, Boukamp BA, and Burggraaf AJ, *Electrode polarization at the Au, O_2 (g) / yttria stabilized zirconia interface. part II: electrochemical measurements and analysis.* Solid State Ionics, (1991). **48**(1-2): p. 155-171.
61. Bai L and Conway BE, *AC Impedance of Faradaic Reactions Involving Electrosorbed Intermediates: Examination of Conditions Leading to pseudoinductive Behavior Represented in Three-Dimensional Impedance Spectroscopy Diagrams.* Journal of the Electrochemical Society, (1991). **138**(10): p. 2897-2907.
62. Bai L and Conway BE, *Three-dimensional impedance spectroscopy diagrams for processes involving electrosorbed intermediates, introducing the third electrode-potential variable--examination of conditions leading to pseudo-inductive behavior.* Electrochimica Acta, (1993). **38**(14): p. 1803-1815.
63. Schouler EJL and Kleitz M, *Electrocatalysis and Inductive Effects at the Gas, pt/Stabilized Zirconia Interface.* Journal of the Electrochemical Society, (1987). **134**(5): p. 1045-1050.
64. Klemensø T and Mogensen M, *Ni-YSZ solid oxide fuel cell anode behavior upon redox cycling based on electrical characterization.* Journal of the American Ceramic Society, (2007). **90**(11): p. 3582-3588.
65. Sarantaridis D and Atkinson A, *Redox cycling of Ni-based solid oxide fuel cell anodes: A review.* Fuel Cells, (2007). **7**(3): p. 246-258.
66. Pihlatie M, Ramos T, and Kaiser A, *Testing and improving the redox stability of Ni-based solid oxide fuel cells.* Journal of Power Sources, (2009). **193**(1): p. 322-330.
67. Nguyen BC and Mason DM, *Mechanisms of catalytic oxidation of hydrocarbons in a solid-electrolyte fuel cell*, in *Other Information: In Brookhaven National Lab., proceedings of the conference on high temperature solid oxide electrolytes, Volume 1, 331-347, N--84-21342 11-76*. (1983). Medium: X; Size: Pages: 17.
68. Mason DM, *Method for producing Electricity from a Fuel Cell Having Solid-oxide Ionic Electrolyte.* (1984). USPTO 4,459,340.
69. Stevenson DA and Frank CW, *Electrochemical abatement of pollutants NO_x and SO_x in combustion exhaust gases employing a solid-oxide electrolyte.* (1989). Medium: ED; Size: Pages: (3 p).
70. Thorp JS, Aypar A, and Ross JS, *Electron spin resonance in single crystal yttria stabilized zirconia.* Journal of Materials Science, (1972). **7**(7): p. 729-734.
71. Farley J, Thorp J, Ross J, and Saunders G, *Effect of current-blackening on the elastic constants of yttria-stabilised zirconia.* Journal of Materials Science, (1972). **7**(4): p. 475-476.
72. Moghadam FK, Yamashita T, and Stevenson DA, *Characterization of the current-blackening phenomena in scandia stabilized zirconia using transmission electron microscopy.* Journal of Materials Science, (1983). **18**(8): p. 2255-2259.
73. Wright DA, Thorp JS, Aypar A, and Buckley HP, *Optical absorption in current-blackened yttria-stabilized zirconia.* Journal of Materials Science, (1973). **8**(6): p. 876-882.
74. Kleitz M, Levy M, Fouletier J, and Fabry P, in *Science and Technology of Zirconia vol. 3*, A.H. Heuer and L.W. Hobbs, Editors. (1981), The Am. Ceram. Soc.: Columbus p. 337.
75. Boulfrad S, Djurado E, and Fouletier J, *Electrochemical characterization of nanostructured zirconias.* Solid State Ionics, (2009). **180**(14-16): p. 978-983.

76. Saburo S, Michihito H, Takuma E, Akihiro T, and Kiichi O, *Electric Conductivity of Solid-state Electrochemically Reduced Yttria partially Stabilized Zirconia.* Journal of the Japan Society of Powder and Powder Metallurgy, (2004). **51**(12): p. 847-851.
77. Eder D and Kramer R, *The stoichiometry of hydrogen reduced zirconia and its influence on catalytic activity - part 1: Volumetric and conductivity studies.* Physical Chemistry Chemical Physics, (2002). **4**(5): p. 795-801.
78. Ben-Michael R and Tannhauser DS, *Visual observation of chemical diffusion in stabilized zirconia.* Applied Physics A: Materials Science & Processing, (1991). **53**(3): p. 185-188.
79. Høgh J, Hansen KV, Chorkendorff I, Jacobsen T, and Mogensen M, *The $H_2/H_2O/Ni/Zirconia$ point Electrode: Effects of Impurities on the Zirconia Surface*. (2006).
80. Klotz D, Leonide A, and Ivers-Tiffee E, *Recovery of Anode performance by Reverse Current Treatment.* ECS Transactions, (2009). **25**(2): p. 2049-2056.
81. Rossmeisl J and Bessler WG, *Trends in catalytic activity for SOFC anode materials.* Solid State Ionics, (2008). **178**(31-32): p. 1694-1700.
82. Primdahl S, *Nickel/yttria-stabilised zirconia cermet anodes for solid oxide fuel cells*, PhD thesis. (1999), University of Twente, Faculty of Chemical Technology, The Netherlands.
83. Bessler WG, Warnatz J, and Goodwin DG, *The influence of equilibrium potential on the hydrogen oxidation kinetics of SOFC anodes.* Solid State Ionics, (2007). **177**(39-40): p. 3371-3383.
84. Hellsing B, Kasemo B, and Zhdanov VP, *Kinetics of the hydrogen-oxygen reaction on platinum.* Journal of Catalysis, (1991). **132**(1): p. 210-228.
85. Fridell E, Rosen A, and Kasemo B, *A Laser-Induced Fluorescence Study of OH Desorption from pt in H_2O/O_2 and H_2O/H_2 Mixtures.* Langmuir, (1994). **10**(3): p. 699-708.
86. Asano K, Tominaga Y, Mugikura Y, and Watanabe T, *Anodic reaction of dense pd film in SOFC using Y-doped $BaCeO_3$-- Effect of mixed ionic conduction of electrolyte.* Solid State Ionics. **181**(3-4): p. 236-239.
87. Mogensen M and Skaarup S, *Kinetic and geometric aspects of solid oxide fuel cell electrodes.* Solid State Ionics, (1996). **86-88**(Part 2): p. 1151-1160.
88. Wilson JR, Kobsiriphat W, Mendoza R, Chen HY, Hiller JM, Miller DJ, et al., *Three-dimensional reconstruction of a solid-oxide fuel-cell anode.* Nature Materials, (2006). **5**(7): p. 541-544.
89. Lanzini A, Leone P, and Asinari P, *Microstructural characterization of solid oxide fuel cell electrodes by image analysis technique.* Journal of Power Sources, (2009). **194**(1): p. 408-422.
90. Wilson JR, Duong AT, Gameiro M, Chen H-Y, Thornton K, Mumm DR, et al., *Quantitative three-dimensional microstructure of a solid oxide fuel cell cathode.* Electrochemistry Communications, (2009). **11**(5): p. 1052-1056.
91. Shikazono N, Kanno D, Matsuzaki K, Teshima H, Sumino S, and Kasagi N, *Numerical Assessment of SOFC Anode polarization Based on Three-Dimensional Model Microstructure Reconstructed from FIB-SEM Images.* Journal of the Electrochemical Society. **157**(5): p. B665-B672.

Chapter 6

6. Molybdate Based Ceramic Electrode Materials

Ceramic materials offer a number of potential advantages over metals for solid oxide cell electrode applications. Developing a high performance ceramic electrode could significantly improve the economics of electrolysis.

This chapter[i] presents a study of fundamental properties of a number of molybdate ceramic materials which might be useful as components of negative-electrodes in solid oxide cells, as alternatives to the common Ni-YSZ electrode studied in previous chapters. The molybdate family is relatively unexplored for solid oxide cell applications. A few of the materials examined in the present study had been studied as fuel cell anodes in prior work and others are new materials from related families that have not been tested as solid oxide cell electrodes. None of the materials, including those that have been studied as fuel cell anodes, have been tested for electrolysis.

The composition of the materials was systematically varied within the molybdate family. Other elements, based on their ionic radii and properties of potential stability and electrochemical activity, were introduced alongside Mo on the B-site of the ceramic crystals. The electrical conductivity, phase (and phase stability in different atmospheres) and microstructure of the materials was investigated. These properties could be linked to the composition – the stability could be mostly explained by thermodynamic data of the constituent oxides and the conductivity was related to the valence states of the ions and the defect chemistry of the ceramic crystals. The conductivity of all the materials depended significantly on the thermal history.

The electrochemical activity for reduction of H_2O and CO_2 and oxidation of H_2 and CO was investigated using simplified geometry point-contact electrodes similar to those used to study the metals in **Chapter 5**. Several of the materials studied in this work were found to have

[i] Part of this chapter has been published in modified form as: Graves C, Sudireddy B R, and Mogensen M, *Molybdate Based Ceramic Negative-electrode Materials for Solid Oxide Cells*. ECS Transactions, 2010. Vol. 28. In press.

very high performance. Some of the materials were found to have much higher performance in reducing H_2O/CO_2 than in oxidizing H_2/CO, which is especially interesting for application as electrolysis electrodes. The results show that the high performance is attained sometimes by very different and unique mechanisms among different members of the materials families.

$SrTiO_3$, $SrMoO_3$, and $SrVO_3$ were found to form a solid solution. Without dopants, $SrTiO_3$ is an insulator. On the other hand, $SrMoO_3$ and doped variants have the highest electronic conductivity of all known oxides (higher than many metals), but are only phase stable in a narrow pO_2 range, oxidizing to $SrMoO_4$ and reducing to Mo and SrO. For the solid solutions, conductivity was gained from $SrMoO_3$ and stability was gained from $SrTiO_3$ and $SrVO_3$. The electrochemical performance of these materials was high but not as high as that of the double perovskites.

The double-perovskites were more stable than $SrMoO_3$ and the solid solution. The double perovskite lattice allows Mo to be fully oxidized as Mo^{6+} (and therefore can be sintered in air) and tends to stabilize against strong reduction (but can still decompose if strong enough reducing conditions are applied). The double-perovskites, with 50 at% Mo on the B-site, had a lower conductivity than the solid solutions.

Some of the double-perovskites exhibited much higher electrical conductivity than would be expected by the mechanism proposed for Sr_2MgMoO_6. Previously unreported phenomena were observed for the molybdates Sr_2NiMoO_6 and Sr_2CoMoO_6 which can explain the high electrical conductivity observed here as well as discrepancies in literature. At 800 °C in 9% H_2/N_2, Sr_2NiMoO_6 gradually decomposed to a multi-phase composite with enhanced electronic conductivity. Most notably, the decomposition resulted in the precipitation of nanoparticles of Ni and Mo-Ni alloy (and apparently other Sr-Mo-O phases) which lined the grain boundaries, forming chains. The surface of the decomposed materials was nanostructured and these nanoparticles were also present on all surfaces. Preparing a material and then performing controlled decomposition to form multiple desirable phases and a desirable microstructure (which can take place *in situ*) from these materials is considered as an interesting new way to prepare potentially high-performance electrode materials.

The electrochemical activity of the decomposed Sr_2NiMoO_6 was very high for H_2O/CO_2 reduction and H_2/CO oxidation, higher than any of the metal electrodes from **Chapter 5** and comparable to the Ni metal electrode that had been activated by strong cathodic polarization. Sr_2FeMoO_6 did not decompose yet exhibited even slightly higher performance, due to a different mechanism most likely related to the defect chemistry of this material (possibly high mixed ionic-electronic conductivity) and/or the mixed valency of the Fe and Mo ions. The addition of Ti to the B-site, e.g. $SrTi_{0.5}Ni_{0.25}Mo_{0.25}O_3$, was found to prevent the decomposition.

The polarization resistances of the best molybdate materials were two orders of magnitude lower than that of donor-doped strontium titanates. Many of the molybdate materials were

significantly activated by cathodic polarization, and they exhibited higher performance for cathodic (electrolysis) polarization than anodic (fuel cell) polarization, which makes them especially interesting for use in electrolysis electrodes. Whereas nearly all of the molybdates showed higher performance for H_2O electrolysis than CO_2 electrolysis, one with vanadium showed nearly equal performance, and a non-molybdate which exhibits some complementary properties to the best molybdates, Gd-doped ceria in nanoparticle form, was found to be an excellent electrocatalyst for CO_2 electrolysis and CO oxidation (moreso than for H_2O/H_2 for which it is known to be good).

6.1. Introduction

As discussed in **Chapter 3**, the economics of electrolysis is dominated by the capital cost. This holds for any electrolyzers, both high temperature and low temperature, and applies to fuel cells as well. It was shown that several properties of the electrolysis cell contribute to affordability by lowering the capital cost:

1. *Lower internal resistance*—leading to higher current density at a given efficiency
2. *Lower degradation*—maintaining the internal resistance over time during operation and through unexpected events
3. *Lower manufacturing cost*—for which it was noted that the raw materials are only a fraction of the total cost of producing the electrolyzer system, with the rest of the cost in processing, the balance of the system, etc.

It was also noted that these can be traded off. This was also mentioned in terms of the negative-electrode in **Section 5.1**. For example, with a low enough internal resistance, the electrode does not need to be as durable. This may be especially relevant for intermittent electrolysis operation, where the cell is only used during a fraction of its life. A cell with a lower internal resistance will produce more fuel sooner, whereas the capital cost of a cell that has higher internal resistance may become higher from depreciation, even if it is more durable and ultimately has a longer operating life.

The traditional Ni-YSZ ceramic-metal (cermet) negative-electrode of solid oxide cells has been optimized (in terms of microstructure) over the years to provide high performance for fuel cell and electrolysis operation (YSZ = yttria-stabilized zirconia). In **Chapter 4** it was shown to have high performance for co-electrolysis of CO_2 and H_2O. However, Ni is susceptible to degradation by sulphur poisoning, segregation of other impurities at the three-phase boundary (TPB), and can be severely damaged by reduction-oxidation (redox) cycles due to the Ni-NiO phase transitions and because the Ni is structural in these electrodes. These issues were examined and discussed in **Chapters 4** and **5**.

It is also possible to produce electrodes composed entirely of ceramic oxides. The typical positive-electrode (oxygen electrode) composed of lanthanum strontium manganite and

YSZ is such an electrode. Other commonly studied positive-electrodes are ferrites and cobaltites. Because the negative-electrode has more stringent requirements, it has been more difficult to obtain a good ceramic material. The more stringent requirements include stability at extremely low oxygen partial pressure and preferably redox stability (the positive-electrode need only be stable in air or pure oxygen type atmospheres so the materials are never reduced and need not be, and are not, redox stable). In terms of electrocatalytic activity, it is also important to note that, whereas at the positive-electrode (oxygen electrode) the electrode kinetics are closely related to the oxygen surface exchange rate, this is not necessarily the case for the negative-electrode since the reaction mechanisms are more complex, involving hydrogen and carbon atoms in addition to oxygen atoms (see also **Chapter 5**).

All-ceramic negative-electrodes have been actively studied since about 1990 [1]. Several recent review articles have provided excellent overviews of the current state-of-the-art of ceramic negative-electrode material development [2-6]. Ceramics offer a number of possible advantages over metals, depending on the composition and preparation methods:

- *Mixed ionic-electronic conductivity (MIEC)*—This leads to a reactive surface with the reaction zone not only at the TPB. This can enhance the electrochemical performance, leading to lower internal resistance (**1**, in the above list). A mixed conductor is also likely more tolerant to impurities that collect at the TPBs, improving durability (**2**).
- *Fine microstructures*—Whereas metal particles agglomerate and creep, ceramic oxides do not (however they do still sinter leading to increased grain size). Fine microstructures lead to higher surface area and number of reaction sites, lowering the area-specific and material-quantity-specific polarization resistance (**1**).
- *Redox stability*—This improves the durability (**2**)
- *Composed mostly of oxygen and alkaline/rare earths*—More expensive transition metals typically make up 20 at% or less of the crystal lattice (typically <33 wt%), potentially improving the manufacturing cost (**3**).

Most of the ceramic materials that have been found to offer some of these properties have the fluorite or perovskite crystal structures. Fluorites offer mixed conductivity, but the electronic conductivity is not sufficient. Fluorites like doped ceria and YSZ exhibit sufficient oxide ion conductivity for use as electrolyte materials. Doped ceria is also useful as a surface catalyst [7-11]. Perovskites can offer very high electronic conductivity, and some compositions also show good ionic conductivity [12]. For both fluorites and perovskites, mixed conductivity is the result of defects in the crystal lattice. The defect chemistry is sometimes complex, but it is often driven by reduction of the ceramic material by a low oxygen partial pressure, leading to free positively-charged oxygen vacancies ($V_O^{\bullet\bullet}$) and negatively-charged electrons (e'), as expressed in Kroger-Vink notation in equation (6.1).

$$O_O^x \rightarrow V_O^{\bullet\bullet} + \frac{1}{2}\mathrm{O}_2(g) + 2\mathrm{e}' \tag{6.1}$$

The additional requirements of any solid oxide cell electrode (which are applicable to ceramic electrodes as well) include:

- Thermodynamic stability in operating conditions (gas atmospheres and temperature range)
- Dimensional stability in operating conditions
- Thermal expansion compatibility with the electrolyte material
- Chemical compatibility with the electrolyte and other materials during operation, e.g. the electrode and electrolyte do not react and form undesirable phases
- Chemical compatibility with the electrolyte and other materials during fabrication

Finally, it is important to note that recently developed methods of preparing electrodes with new types of microstructures can effectively bypass some of the criteria of the two lists above. For example, a porous backbone structure can be formed that is stable (redox stable, thermodynamically stable, and dimensionally stable) and compatible (thermal expansion compatible and chemically non-reactive during operation and fabrication) with the electrolyte material. The backbone can provide ionic and/or electronic conductivity (if ionic, then usually the backbone is made of the same material as the electrolyte material and they are sintered together). Then the backbone structure can be coated with the electrochemically active phase (and also provide ionic and/or electronic conductivity if the backbone does not provide one). The coating can be formed by infiltrating a solution of nitrate precursors of the desired phase into the pre-sintered backbone structure and heat-treating at lower temperature than is needed to fully sinter a structurally-sound electrode. The backbone structure provides the structural stability. In prior work, such coating-type negative-electrodes have been comprised of: an interconnected network of Cu metal with dispersed doped ceria particles on a YSZ scaffold [7], an interconnected network of Ni metal particles on a YSZ scaffold [13, 14], interconnected network of chromate or titanate ceramics with low electronic conductivity on a YSZ scaffold [15, 16], and an interconnected network of doped ceria with dispersed Ni particles on an electron conducting backbone made of Nb-doped strontium titanate [9, 10] or FeCr [11]. An illustration of these type of coated backbone structures is shown in **Figure 6-1**.

With this type of electrode, the active material does not need to be redox stable, dimensionally stable, thermal expansion compatible with the electrolyte, or chemically compatible with the electrolyte at the high sintering temperatures that would normally be required for fabrication. It only needs to be chemically compatible with the backbone material during operation and thermodynamically stable during operation.

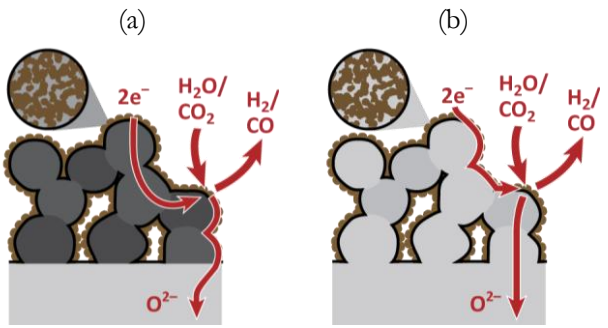

Figure 6-1. Illustration of solid oxide cell electrodes comprised of an electrocatalytic coating of networked particles (a) which also provides ionic conductivity and is coated onto an electron-conducting backbone, and (b) which also provides electronic conductivity and is coated onto an ionic conducting backbone.

The purpose of this work was study some fundamental properties of a variety of molybdate based materials and to test them for electrolysis of H_2O and CO_2 (as well as oxidation of H_2 and CO). A few of the materials have been studied as fuel cell anodes in prior work and others are new materials from related families that have not been tested as solid oxide cell electrodes. None of the materials, including those that have been studied as fuel cell anodes, have been tested for electrolysis. Furthermore, the prior anode studies used porous electrodes, and most of them only reported the performance of the full cell (not isolating the performance of the electrode). In the present study, simplified geometry electrodes are employed, similar to that used for metal materials in **Chapter 5**. The electrodes contact YSZ with a well-defined three-phase boundary, enabling study of the electrochemical properties and relative electrocatalytic performance of the materials without the effects of a complex microstructure of porous electrodes. Using such point-contact electrodes is generally less straightforward for ceramics than for metals because the electrode materials are not soft like metals and do not creep and form a well-defined interface and TPB. In the present study, methods were developed to successfully measure the TPB for ceramic materials, improving upon prior point-contact ceramic electrodes studies. This will be briefly discussed in **section 6.2** and reported in more detail in the future.

In the following sections, the prior studies of molybdate materials in solid oxide cells are reviewed, followed by a discussion about designing a molybdenum-based ceramic electrode.

6.1.1. Prior Work with Mo Based Ceramics in Solid Oxide Cells

The first major material based on Mo that was studied for use in solid oxide cells was the oxide ion conductor, $La_2Mo_2O_9$ [17]. This material was found to have higher O^{2-} ion conductivity than YSZ at temperatures above 600 °C, suggesting that it could be a good electrolyte material. However, it is unstable in reducing atmospheres in this temperature range, limiting its practical applicability.

The pyrochlore $Gd_2Ti_yMo_{1-y}O_7$ was considered as a potential solid oxide fuel cell (SOFC) anode material due to its high electronic conductivity in reducing atmospheres as well as its ionic conductivity, making it a mixed conductor [18]. At first, the stability in the pO_2 range relevant to operating conditions was not sufficient [19], but by tuning the composition it was made more stable and tested as an anode [20]. It was still certainly not redox-stable. The oxidation performance was notable, with an area-specific polarization resistance (ASR_p) of 0.2 Ω cm^2 at 950 °C at OCV. This material exhibited high sulfur tolerance. In fact, remarkably, this anode had almost as high performance in H_2S as in H_2.

Recently, the double perovskite Sr_2MgMoO_6 (SMM) was reported as an excellent SOFC anode material [21, 22]. In fact, a variant with some La substituted for Sr is the highest performing single-phase anode material reported for H_2 and CH_4 oxidation to date [23]. Replacing Mn with Mg was also tested but had slightly lower performance [21, 22]. With a lanthanum-doped ceria (LDC) layer between the SMM anode and a electrolyte to prevent undesirable reaction and interdiffusion, an ASR_p of 0.1-0.15 Ω cm^2 (for 0 to 0.5-1 A/cm_2 on a polarization curve) was reported at 800 °C in H_2. Up to at least 50 ppm H_2S tolerance, with minimal impact on performance, was reported. An anode made of SMM is also believed to be redox-stable (although that is not the case with the La-substituted variant). The electrochemical activity is believed to be related to the mixed ionic-electronic conductivity of the material. The mechanism that leads to the mixed conductivity will be further discussed in the next section and later in the Results sections of this chapter. The conductivity of 4-9 S/cm in reducing atmospheres is sufficient, although there have been a wider range of conductivity values reported since the initial study (discussed further in **section 6.3.2**). This material and some related double perovskites are studied further in the present work. Some studies of the related double perovskites were reported while the present work was carried out, and will be discussed and compared to the results obtained here in the Results sections. The results are able to explain some of the inconsistencies in this recent literature.

Finally, an amorphous lanthanum molybdate (LaMoO) was recently reported as a high performance SOFC anode material. This material was in fact prepared by reducing the oxide-ion conductor mentioned above, $La_2Mo_2O_9$, which decomposed it to an amorphous phase. For a full cell with an LDC buffer layer, similar performance was reported [24] as the full cell performance reported for SMM [21, 22]. 20 ppm sulfur tolerance was also reported. This material is also included in the present study.

6.1.2. Designing an Mo-based Electrode

The elements molybdenum and tungsten have interesting properties. They are the only elements that prefer the +6 valence state at normal oxidized conditions. MoO_3 and WO_3 are perovskites with all vacancies for the A-sites. They have a large valence range of 0 to 6, rivaled only by Mn and the more expensive elements Ru, Os, Rh, and Ir. The tungsten bronze

$(Na/K)_xWO_3$ and the perovskite $SrMoO_3$ have applications in electrochromics (the color can be changed by slight modifications to the material that change the valence, e.g. Na_xWO_3 [25, 26]), very high conductivity oxides (conductivities reaching 10^5 S/cm at room temperature [27-32], see also **section 6.3.2**), and catalysis (oxidation of hydrocarbons [33-35]). Ni-Mo and Ni-W alloy electrodes with fine micro- or nano-structures have been reported as highly electrocatalytic negative-electrodes for alkaline electrolysis cells, improving upon the performance of Ni electrodes [36-39].

In the perovskite $SrMoO_3$, the Mo valence is 4+. One may consider the ionic radius and the Goldschmidt tolerance factor, **Table 6-1** and **equation (6.2)**.

$$t = \frac{r_A + r_O}{\sqrt{2} \cdot (r_B + r_O)} \tag{6.2}$$

If the dimensionless value of the tolerance factor t is close to 1, the ions are the ideal size for fitting into their cavities in the perovskite structure and the structure is expected to adopt the ideal cubic symmetry. Note that the tolerance factor is very close to 1 for $SrMoO_3$ (Mo^{4+}), as well as for $SrTiO_3$ (Ti^{4+}). This will be revisited in **section 6.3.1**.

In double perovskites, Mo is also on the B site, but Mo^{6+} or Mo^{5+} is paired with a 2+ or 3+ valence ion respectively. The differences in charge and ionic radii result in 6+/2+ or 5+/3+ ordering and a superlattice structure (see **Table 6-1** for the relevant ionic radii). Of the 2+ ions, Mg is the most stable against reduction, according to thermodynamics [40]. The mechanism for high electrochemical performance proposed by Huang et al for the double perovskite anode Sr_2MgMoO_6 is mixed conductivity. When the material is reduced, oxygen is lost from the crystal structure, resulting in the formation of oxygen vacancies and electrons, see equation (6.1). A fraction of the Mo^{6+} ions accept the electrons and become Mo^{5+}. Both the 6+ and 2+ ions in the double perovskite must have coordination flexibility to allow release of oxygen from the crystal lattice [22]. The electromagnetic properties of double perovskites vary significantly depending on the partner 2+/3+ ion [41-43]. For double perovskites, a "fitness factor" has also been proposed to more exactly discriminate crystal systems than the Goldschmidt tolerance factor [44].

Table 6-1. Ionic radii (Å) for VI-fold coordination [45]. ls = low spin; hs = high spin.

Valence	Mo	W	Ti	Nb	Valence	Mg	Mn	Ni	Fe	Co
+4	0.65	0.66	0.605	0.68	+2	0.72	0.67(ls)	0.69	0.61(ls)	0.65(ls)
+5	0.61	0.62		0.64			0.83(hs)		0.78(hs)	0.745(hs)
+6	0.59	0.60			+3		0.58(ls)	0.56(ls)	0.55(ls)	0.545(ls)
							0.645(hs)	0.60(hs)	0.645(hs)	0.61(hs)

One must also consider the thermodynamic stability of the valence states of the ions during synthesis and operation. Diagrams of phase stability versus temperature and pO_2 for the Mo-O and W-O systems are shown in **Figure 6-2**. These are the constituent oxides of the perovskites, e.g. $SrO + MoO_2 \rightarrow SrMoO_3$. Knowledge of the preferred valence state based on the constituent oxides is useful as a guideline for synthesis parameters and as an indication of possible stability ranges during operation. Also marked on the diagram are typical operating conditions, 700-900 °C and 3%, 50%, and 90% H_2O / H_2. The 3% and 90% H_2O conditions represent SOFC and SOEC starting conditions, and the 50% H_2O condition represents the average gas compositions that would be seen across an operating cell (in either mode, fuel cell or electrolysis) run at high reactant utilization – as mentioned in **section 5.1**. As a simple test to briefly examine the Mo-O phase transitions, a bent Mo metal wire point electrode was used as with the other metal point electrodes described in **Chapter 5**. The Mo metal wire easily oxidized to MoO_2 upon exposure to 50% H_2O/H_2, in agreement with the thermodynamic data. This was evident in the impedance measurements – MoO_2 is still electron conductive but has lower electrochemical activity. Upon re-exposure to 3% H_2O/H_2, the electrode reduced back to metal. **Figure 6-3** shows SEM micrographs of the surface of the wire that had been smooth before the experiment. After re-reduction the surface "bloomed" into interesting nanostructures. The surface area increased, similar to the Ni electrode after oxidation (see **section 5.3.5.1**). One could say that the Mo metal wire was redox cycled between 3% H_2O/H_2 and 50% H_2O/H_2.

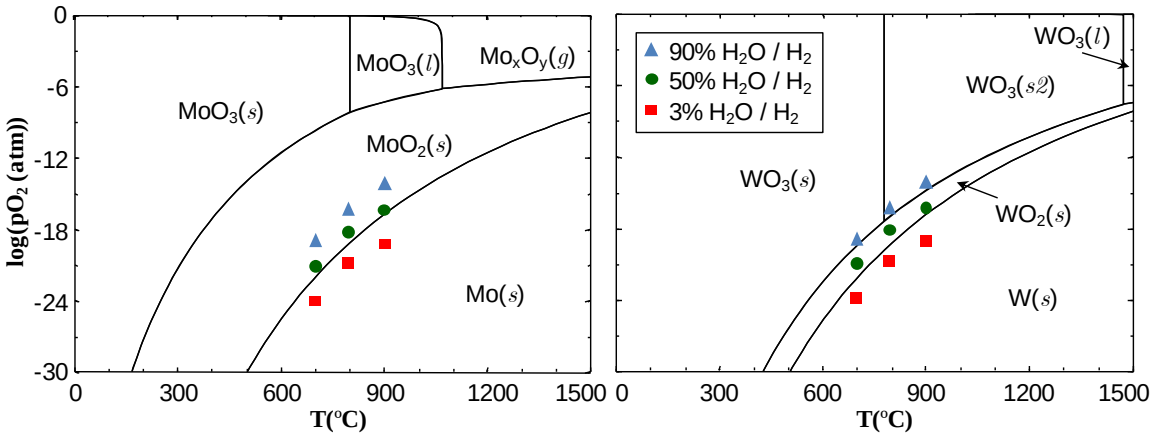

Figure 6-2. Phase stability for the Mo-O and W-O systems, according to thermodynamic data [40].

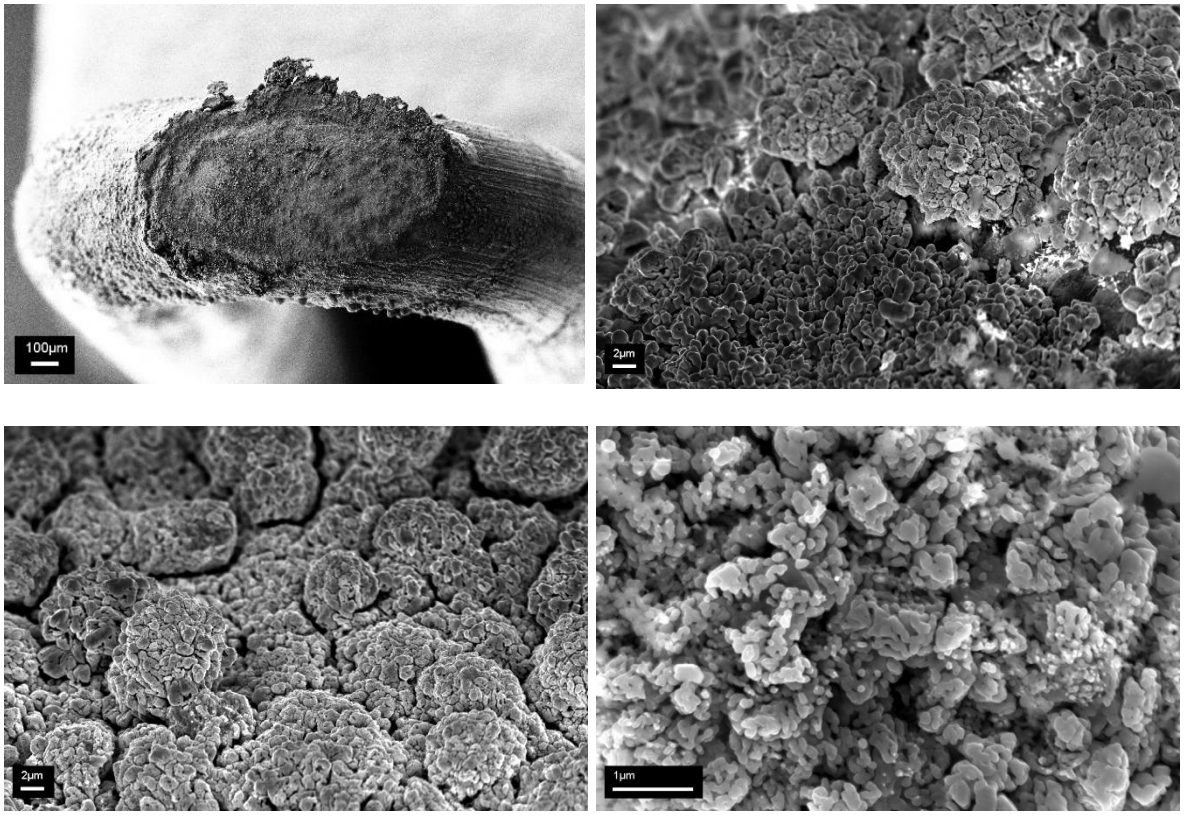

Figure 6-3. SEM micrographs of a Mo wire that had been subjected to 3% H_2O/H_2, then 50% H_2O/H_2 which caused oxidation to MoO_2, then 3% H_2O/H_2 again which reduced it back to metal.

6.2. Experimental

A variety of molybdate-based materials were studied. The compositions were systematically varied with 12.5-100 at% Mo or W on the B site in related "families": $SrMoO_3$, amorphous LaMoO, Sr_2CoMoO_6, Sr_2FeMoO_6, Sr_2MgMoO_6, Sr_2MgWO_6, Sr_2NiMoO_6, Sr_2NiWO_6, $SrTi_{0.5}Mo_{0.5}O_3$, $SrTi_{0.5}Ni_{0.25}Mo_{0.25}O_3$, and $Sr_2V_{0.5}Mo_{0.5}O_3$. The compositions, B-site valences, crystal structures, and tolerance factors are given in **Table 6-2**. Polycrystalline samples were synthesized by solid state reaction (e.g. for Sr_2MgMoO_6: $2\,SrCO_3 + MgO + MoO_3 \rightarrow Sr_2MgMoO_6 + CO_2$). Oxide and carbonate powders were mixed in stoichiometric quantities with ethanol and roll milled with YSZ balls for 12-24 h. The purities of the precursor powders are given in **Table 6-3**. The slurry was dried, hand-ground in an agate mortar and pestle, and the powder was heat treated to form the desired phase. Some heat treatments were in air and others were in 9% H_2/Ar, room-temperature humidified 9% H_2/Ar (adding ~3% H_2O), or humidified 9% H_2/Ar through a bubbler that was refrigerated (adding about 1.3% H_2O). All heat treatments used heating and cooling rates of 2 °C/min. The powders were pressed into bars and pellets to prepare for sintering dense bodies. They were uniaxially pressed for 30 s at 50-100 MPa and then isostatically pressed for 30 s at 250 MPa. The green bodies were sintered in air or

humidified 9% H_2/Ar depending on the composition. After each heat treatment and sintering, the phase of the powders or sintered bodies was examined by XRD using a STOE Diffractometer with Cu-Kα radiation. After sintering, some samples of each material were polished down to 1 μm diamond paste and examined in the SEM/EDX (a Zeiss Supra 35 FE-SEM equipped with a Noran System SIX X-ray microanalysis system). The heat treatment conditions for successful phase formation and sintering for each material are reported and discussed in **section 6.3.1**.

Table 6-2. The molybdate materials that were synthesized and studied in the present work. The tolerance factors were calculated using the low-spin ionic radii

Composition	B site composition	Acronym	Crystal structure	Tol. factor
$SrMoO_3$	Mo^{4+}	SM	Perovskite	0.98
LaMoO	$Mo^{various+}$	LM	Amorphous	-
Sr_2CoMoO_6	Mo^{6+} Co^{2+}	SCM	Double perovskite	0.99
Sr_2FeMoO_6	$Mo^{5+/6+}$ $Fe^{2+/3+}$	SFM	Double perovskite	1.00[a]
Sr_2MgMoO_6	Mo^{6+} Mg^{2+}	SMM_1	Double perovskite	0.98
$Sr_2MgMoO_{6-\delta}$[b]	$Mo^{5+/6+}$ Mg^{2+}	SMM_2	Double perovskite	0.98
Sr_2MgWO_6	W^{6+} Mg^{2+}	SMW	Double perovskite	0.97
Sr_2NiMoO_6	Mo^{6+} Ni^{2+}	SNM	Double perovskite	0.98
Sr_2NiWO_6	W^{6+} Ni^{2+}	SNW	Double perovskite	0.98
$SrTi_{0.5}Mo_{0.5}O_3$	Mo^{4+} Ti^{4+}	STM	Perovskite	0.99
$SrTi_{0.5}Ni_{0.25}Mo_{0.25}O_3$	Mo^{6+} Ni^{2+} Ti^{4+}	STNM502525	(Double?) perovskite	0.99
$SrV_{0.5}Mo_{0.5}O_3$	Mo^{4+} V^{4+}	SVM	Perovskite	1.00

[a] Tolerance factor for Fe^{2+} and Mo^{6+} or Mo^{5+}. The exact amounts of Fe^{2+}, Fe^{3+}, Mo^{5+}, and Mo^{6+} are not known. With both ions fully reduced (Fe^{3+} and Mo^{5+}), the tolerance factor is slightly higher, 1.01.

[b] Synthesized in reducing atmosphere (see **Table 6-4**).

Table 6-3. Purities (wt%) and suppliers of the oxide and carbonate precursor compounds used to prepare the molybdates and titanates.

Precursor compound	Purity	Supplier
Co_3O_4	99.7%	Alfa Aesar
Fe_2O_3	99.9%	Alfa Aesar
La_2O_3	99.99%	Alfa Aesar
MgO	99.5%	Alfa Aesar
$MnCO_3$	99.99%	Johnson Matthey
MoO_3	99.95%	Alfa Aesar
Nb_2O_5	99.9%	Alfa Aesar
NiO	99%	Alfa Aesar
$SrCO_3$	99.9%	Sigma Aldrich
TiO_2	99.8%	Sigma Aldrich
WO_3	99.8%	Alfa Aesar
V_2O_5	99.6%	Alfa Aesar
Y_2O_3	99.9%	Johnson Matthey

Conventional 4-point DC conductivity tests were performed on the sintered bars. First, #320 SiC grinding paper was used to remove a few microns from all surfaces of the bars. Pt wire and Pt paste were used to form the current leads at each end of a bar. Pt wire voltage probes with a fixed separation distance (built into the test set-up) were contacted to the surface.

Electrochemistry tests were performed on most of the materials using a similar set-up as that described in **Chapter 5**. The cells consisted of pointed ceramic electrodes contacting a smooth polished YSZ pellet surface (prepared the same as in **Chapter 5**), with a much larger porous Pt counter electrode acting as a reference electrode (pseudo 3-electrode setup, see **Figure 6-4**), similar to the metal point electrode tests of **Chapter 5**. The pointed electrodes were prepared from the sintered pellets by grinding the pellets to a cone-like shape, as has been used in prior work [46-53]. In the present study, however, the pointed electrodes were made by hand-grinding on SiC paper affixed to a grinding wheel, with the grinding direction away from the tip so as to avoid getting SiC particles lodged in the electrode, which would contaminate the electrode with impurities (it was also verified by SEM on some electrodes that no SiC particles were present on the pointed tip nor anywhere on the electrode surface). This resulted in "pyramid" rather than cone shaped electrodes. It was found that equivalent results could be obtained by machining the pellets into a cone versus the hand-grinding method. In fact, a number of electrode geometries using the same material were tested, as it was desired to find a standard platform to quickly test the electrochemical properties of different materials without going through the entire cell development process. The advantages and disadvantages of the different geometries will be reported in the future. The point-contact geometry is a very useful geometry, especially if the TPB can be measured after testing and used to apply correction factors to the Newman relation as done for the metal point electrode study of **Chapter 5**. For the materials studied here, given the sintering conditions used, it was possible to observe the TPB in the SEM after testing and measure its length.

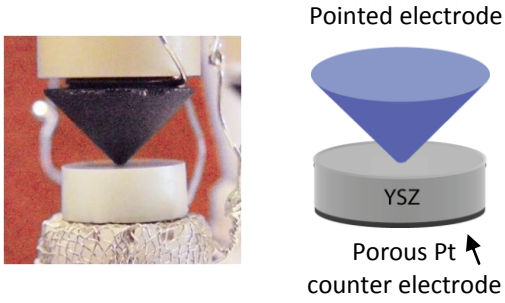

Figure 6-4. Photograph and diagram of ceramic cone-type point electrode used in the electrochemistry tests.

Some donor-doped strontium titanate based materials known from literature were also included here for comparison, including $Sr_{0.94}Ti_{0.9}Nb_{0.1}O_3$ [10, 53, 54], $La_{0.35}Sr_{0.65}TiO_3$ [55, 56], $Y_{0.08}Sr_{0.92}TiO_3$ [57, 58], and $Y_{0.08}Sr_{0.88}TiO_3$ [59-62]. These materials were also prepared by solid

state reaction. It was found that the titanates with compositions that were not charge-compensated, $Y_{0.08}Sr_{0.92}TiO_3$ and $La_{0.35}Sr_{0.65}TiO_3$, needed to be sintered in a very reducing atmosphere (dry 9% H_2/Ar) at high temperature (1450 °C) to eliminate impurity phases such as the pyrochlores $Y_2Ti_2O_7$ and $La_2Ti_2O_7$. All of the sintered titanates were generally harder than the molybdates. Since they were harder, the contact area did not develop into a well-defined interface and was more difficult to determine. An additional method to determine the contact area was developed. At the end of a test, a strong cathodic polarization was applied (as for the metal point electrodes, **Chapter 5**, but for a different purpose). This is known to blacken the YSZ at the interface within the contact area, which made an "imprint" of the cone-tip contact area. The cells were cooled immediately afterwards and the YSZ surface was examined by optical microscope to estimate the contact area by the area that had been blackened.

The tip of one $Sr_{0.94}Ti_{0.9}Nb_{0.1}O_3$ (STN) cone-shaped electrode was coated with Gd-doped ceria ($Ce_{0.8}Gd_{0.2}O_2$; CGO) particles by vacuum infiltrating a single drop of an aqueous solution composed of precursor nitrates and ethanol. The preparation procedure for the infiltration solution followed that of a recent study that found CGO-infiltrated porous STN backbone electrodes to have remarkably high performance [10]. That concept was applied here to the cone-shaped electrode. In the present study, the CGO precursors loaded into the electrode tip were decomposed to form the CGO phase *in situ* in the reducing atmosphere, forming submicron-sized CGO particles.

The electrochemistry tests were similar to those described in **Chapter 5** but included a less extensive characterization. Simpler tests were used to more rapidly test the materials and get an idea of their relative performance, without attempting to understand their possible reaction mechanisms. After assembling the cells, they were heated up to 850 °C in dry 9% H_2/Ar (or 9% H_2/Ar that was humidified with 1% H_2O for some of the samples). The gas atmosphere was switched to 3% H_2O/H_2 and impedance spectra (IS) were measured constantly at OCV while the interface stabilized, usually 12-24 h but in some cases up to 100 h to allow time to reduce the ceramic electrode material if it was not pre-reduced. The potentiostatic IS measurements typically used 6 to 9 points per decade, from 1 MHz to 3 mHz, with an AC RMS amplitude of 10 mV, using a Gamry Reference 600. OCV IS were measured at different temperatures from 850 to 700 °C, repeating a set-point more than once to check if the electrode performance had changed during the temperature variation. The gas atmosphere was changed to 50% H_2O/H_2 and to 50% CO_2/CO and the temperature variation was repeated for each. In 50% H_2O/H_2 and 50% CO_2/CO, cyclic potential sweeps were performed from OCV to +300 mV to –300 mV to OCV for at least 3 cycles. Finally, IS were measured under polarization in 100 mV increments, in the order OCV, +100 mV, +200 mV, +300 mV, –100 mV, –200 mV, –300 mV, with 5 minutes of fixed DC bias (chronoamperometry) at each given applied potential before the IS measurement. 2 or 3 electrodes of the same material were tested for 4 of the

materials (SFM, SMM, SNM, and STM50), and 1 electrode was tested for the remaining materials.

6.3. Results and Discussion

6.3.1. Materials Synthesis

The optimized synthesis parameters that were found are given for each material in **Table 6-4**. In some cases, Heating #1 was an initial heat treatment in air which was used to decompose the $SrCO_3$ (otherwise it might remain as a carbonaceous material, since the pO_2 is so low). For other materials Heating #1 was used to form an intermediate phase: for SM synthesis, the first heat treatment was 1000 °C for 8 h in air to form the oxidized phase, $SrMoO_4$. The $SrMoO_4$ was subsequently reduced in the listed Heating #2. According to literature [32, 35, 63-66] (and trials conducted in the present study), this is the most reliable way to obtain $SrMoO_3$. Similarly, for LaMoO an initial heat treatment of 950 °C for 10 h in air was used to obtain $La_2Mo_2O_9$. As in ref [24], the $La_2Mo_2O_9$ was subsequently reduced to decompose it to an amorphous phase. The sintered densities were >90% theoretical for 1400 °C sintered samples and >66% for the 1300 °C sintered samples.

Successful synthesis of the desired phase was often pO_2 dependent – to obtain a reduced Mo valence, a reducing atmosphere was needed. Over-reduction can yield Mo metal, however, so careful control of the pO_2 is necessary. Of the double perovskites, all that have 2+/6+ ordering when oxidized were possible to synthesize in air. In the literature, SMM produced by sol-gel synthesis is often sintered in reducing atmosphere [21], so a different sample, SMM_2, was sintered in reducing atmosphere – this will be further discussed in the following **section 6.3.2**. SFM had a narrower window of suitable pO_2 required to form the phase and could not be synthesized in air – one or both of $Fe^{2+/3+}$ and Mo^{6+} needed to be reduced. Synthesis in air yielded segregation of $SrMoO_4$, and over-reduction yielded the Ruddleston-Popper phase $Sr_3FeMoO_{6.88}$ as has been reported in literature [67].

High phase purity was obtained for all materials except the reducing-sintered SMM_2, in which a few % MgO, $SrMoO_4$, and Sr_3MoO_6 were present. These impurity phases were not present in the reducing-sintered SMM reported in literature [21], however in that study the powder was prepared by sol-gel synthesis, yielding a finer particle size, and the sintering temperature was only 1200 °C with a more strongly reducing atmosphere of dry 5% H_2/Ar. In that study the intent was to sinter a porous electrode microstructure, not a dense sample. Here, on the other hand, solid state reaction was used and a dense sample was desired, so a higher sintering temperature was required. A stronger reducing atmosphere was found to result in the

Table 6-4. Optimized synthesis parameters for the molybdate materials. "H" stands for dry 9% H_2/Ar. "w" stands for "wet" (room-temperature humidified ~3% H_2O); "cw" stands for "cold-wet" (~1.3% H_2O).

			Heating #1 (powder)			Heating #2 (form phase, powder)			Sinter dense sample		
Composition	B site composition	Acronym	°C	hr	gas	°C	hr	gas	°C	hr	gas
$SrMoO_3$	Mo^{4+}	SM	1000	8	air	800	26	H	1300	12	cw-H
LaMoO	$Mo^{various+}$	LM	950	10	air	900	10	H	1200	10	w-H
Sr_2CoMoO_6	Mo^{6+} Co^{2+}	SCM	-	-	-	1300	12	air	1400	12	air
Sr_2FeMoO_6	$Mo^{5+/6+}$ $Fe^{2+/3+}$	SFM	900	4	air	1250	12	w-H	1400	12	w-H
Sr_2MgMoO_6	Mo^{6+} Mg^{2+}	SMM_1	-	-	-	1300	12	air	1400	12	air
$Sr_2MgMoO_{6-\delta}$	$Mo^{5+/6+}$ Mg^{2+}	SMM_2	850	12	air	1200	24	H	1350	18	w-H
Sr_2MgWO_6	W^{6+} Mg^{2+}	SMW	900	12	air	1200	24	H	1350	18	w-H
Sr_2NiMoO_6	Mo^{6+} Ni^{2+}	SNM	-	-	-	1300	12	air	1400	12	air
Sr_2NiWO_6	W^{6+} Ni^{2+}	SNW	-	-	-	1300	12	air	1400	12	air
$SrTi_{0.5}Mo_{0.5}O_3$	Mo^{4+} Ti^{4+}	STM	1200	12	w-H	1200	10	cw-H	1440	12	cw-H
$SrTi_{0.5}Ni_{0.25}Mo_{0.25}O_3$	Mo^{6+} Ni^{2+} Ti^{4+}	STNM502525	-	-	-	1300	12	air	1400	12	air
$SrV_{0.5}Mo_{0.5}O_3$	Mo^{4+} V^{4+}	SVM	-	-	-	900	10	cw-H	1300	12	cw-H

formation of Mo metal, so the humidified 9% H_2/Ar atmosphere was used. For the air-sintered samples, the compositions and synthesis conditions were optimized to eliminate $SrMoO_4$ and $SrWO_4$ impurities, which are commonly reported in literature to form during sintering in air (and found in the present study before optimization). Part of the optimization consisted of adding 2% excess NiO/MgO/etc. It did not seem to be a matter of there being insufficient NiO/MgO/etc in the precursors (for example, if some of the NiO had turned to carbonate over time, when measuring the weight of NiO to mix stoichiometric SNM, less Ni metal than expected would be present). It was found afterwards that another group recently reported needing to add 5 wt% excess NiO when preparing Sr_2NiMoO_6 by solid state reaction [68]. It is also worth noting that any remaining $SrMoO_4$ will reduce to $SrMoO_3$ in operating conditions – as mentioned above, this is in fact how $SrMoO_3$ was prepared in the present study, and the $SrMoO_3$ + ½ O_2 ↔ $SrMoO_4$ phase transition is reversible. Sr_3MoO_6 might also disappear during reduction. XRD data from a few of the compositions is shown in **Figure 6-5**.

$SrMoO_3$ and $SrTiO_3$ appear to form a solid solution in $SrTi_{0.5}Mo_{0.5}O_3$ – the peaks measured for $SrTi_{0.5}Mo_{0.5}O_3$ fell directly between those of $SrMoO_3$ and $SrTiO_3$ (**Figure 6-5a**). A solid solution was also found for $SrMo_{0.5}V_{0.5}O_3$. Based on the similar ionic radii, solid solutions are not unexpected and a literature search showed that they have been reported [69-71].

The double perovskites are all tetragonal at room temperature, evident by their peak splitting as shown for Sr_2NiMoO_6 (**Figure 6-5b**). They typically transition to cubic at 200-300 °C [68, 72-78]. The double-perovskite titanate hybrid, $SrTi_{0.5}Ni_{0.25}Mo_{0.25}O_3$, showed peaks between that of Sr_2NiMoO_6 and $SrTiO_3$ (evident by the slight 2θ offset between Sr_2NiMoO_6 and $SrTi_{0.5}Ni_{0.25}Mo_{0.25}O_3$) – similar to $SrTi_{0.5}Mo_{0.5}O_3$ in that both exhibited peaks in between their component oxides. Other XRD peaks that are indicative of double perovskites were present for $SrTi_{0.5}Ni_{0.25}Mo_{0.25}O_3$, but they were much smaller than those visible for Sr_2NiMoO_6.

This could be the results of either some long-range ordering on the B-site, e.g. a pseudo-double perovskite with a new type of $Ni^{2+}/Ti^{4+}/Mo^{6+}$ ordering, or the material might just be a composite of the two phases. Further crystallographic and microstructural studies are needed to determine if it is single-phase or a composite.

Finally, the XRD data showing the reduction of $La_2Mo_2O_9$ to amorphous LaMoO is presented in **Figure 6-5c** and compares well with that presented in the prior work [24].

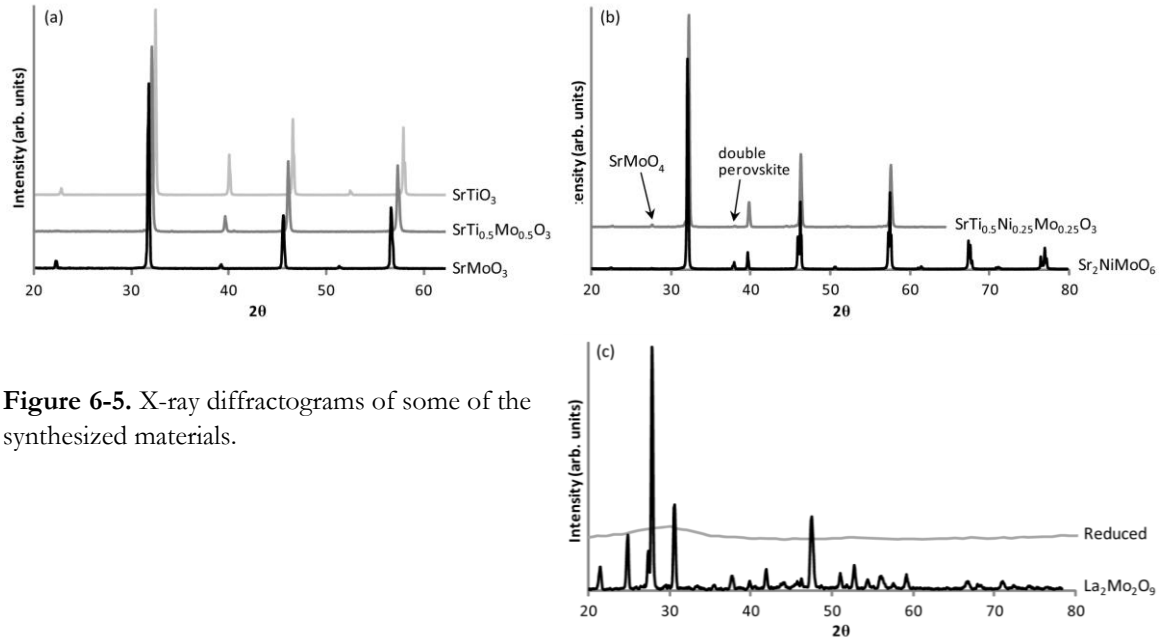

Figure 6-5. X-ray diffractograms of some of the synthesized materials.

6.3.2. Electrical Conductivity

The electrical conductivity was measured versus temperature and pO_2. The measurements for the 100% B-site Mo (SM and LM) and solid solutions (STM and SVM) are shown in **Figure 6-6**. SM clearly has extremely high conductivity (**Figure 6-6a**), near 10^4 S/cm at room temperature, which is consistent with literature [31, 32, 64, 79-81]. Its conductivity had not previously been reported for this high temperature range and pO_2. At 800 °C the conductivity was just under 2000 S/cm and the pO_2 was 10^{-22} atm. However, when increasing the pO_2 only slightly, to 10-20 atm, the conductivity decreased to <0.01 S/cm. The material oxidized and became the insulating $SrMoO_4$ phase, at least on the surface where the voltage probes made contact. This is roughly consistent with the reported narrow pO_2 window for stability of SM at the higher temperature of 1200 °C [63].

SVM (**Figure 6-6b**) and STM (**Figure 6-6e**) also exhibited very high conductivity, around 400 S/cm at 800 °C in 10^{-20} atm O_2. Similar values have been reported in literature for

SVM [70, 71] and the similar $CaV_{0.5}Mo_{0.5}O_3$, [71, 82], as well as STM [69]. These materials are much more stable than SM at higher pO_2, retaining high conductivity at pO_2 as high as 10^{-17} atm, which corresponds to H_2O-rich electrolysis type conditions with a pH_2O/pH_2 ratio of 9 (**Figure 6-6c** and **Figure 6-6f**). It appears that conductivity was gained from $SrMoO_3$ and some stability gained from $SrTiO_3$ and $SrVO_3$. Whereas $SrTiO_3$ is an insulator, $SrVO_3$ has been reported to have high metallic electronic conductivity [83, 84].

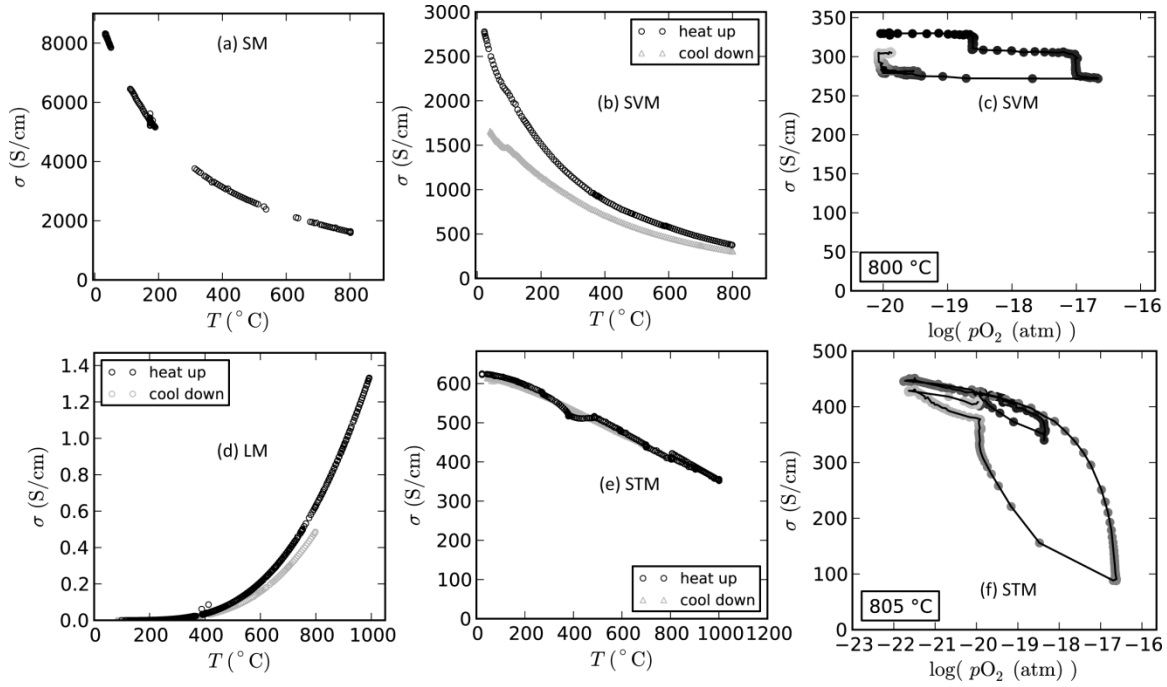

Figure 6-6. Electrical conductivity versus temperature or pO_2 for (a) SM, (b,c) SVM, (d) LM, and (e,f) STM. In the pO_2 graphs (c,f), one point was measured every 3 minutes and the shading of the points changes from black to light gray with time.

The amorphous lanthanum molybdate LM, on the other hand, exhibited low conductivity with semiconductor behavior – around 0.6 S/cm at 800 °C in 10^{-20} atm O_2 and slightly lower at 0.5 S/cm with higher pO_2 (**Figure 6-6d**). The log conductivity was linear with 1/T (not shown). The conductivity had not been reported in the LM anode study [24]. This low conductivity is only sufficient for a thin active layer of an electrode, not a current collecting layer [2, 85].

The conductivity measurements for the air-sintered double perovskite sample SMM_1 are shown in **Figure 6-7**. At 800 °C in the very reducing dry 9% H_2/Ar atmosphere (pO_2=10^{-24} atm), it took more than 600 hours to fully reduce the material. The final value was about 3.5 S/cm. On the other hand, the reducing-sintered sample SMM_2 did not need further reduction and reached a higher conductivity of 8.1 S/cm at 800 °C in 10^{-20} atm O_2 (**Figure 6-8**). The

conductivity increased to 12 S/cm in $10^{-22.5}$ atm O_2 and decreased to 4 S/cm in $10^{-17.5}$ atm O_2, with an apparent linear log slope.

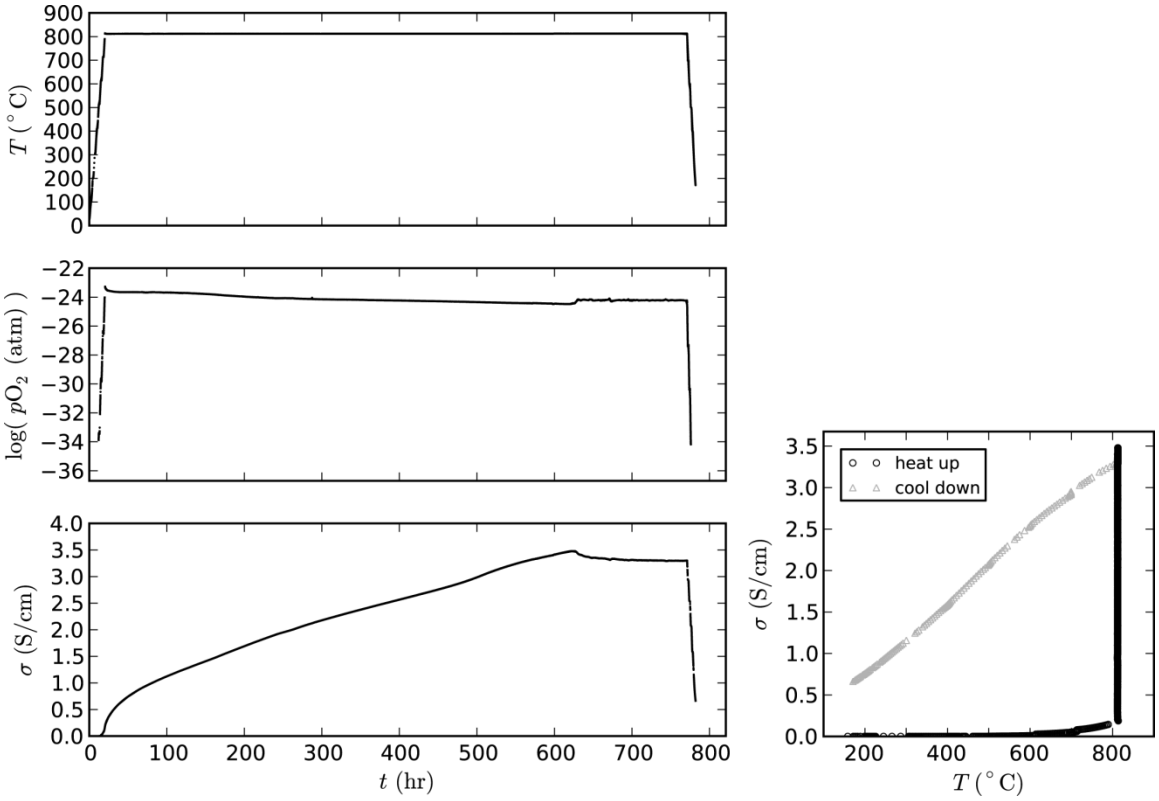

Figure 6-7. Electrical conductivity measurements of the air-sintered Sr_2MgMoO_6 sample SMM_1.

Clearly, the conductivity is a function of the pO_2 during measurement and during sintering. The SMM_2 values are in agreement with those measured in the original study by Huang et al which synthesized the material via a reducing-sinter [21]. Thus it seems that the minor impurities phases present in the reducing-sintered sample were not detrimental to the conductivity. As mentioned earlier, many of these impurity phases will become reduced to more electron-conductive phases *in situ*. Also, impurity phases like Sr_3MoO_6 were found in a prior study of the related material SFM, present as islands that that did not affect the bulk material properties [86].

The widely varying conductivity values reported in literature for SMM can most likely be explained by the extent of reduction. The reported conductivity of air-sintered samples at 800 °C ranges from 0.3 S/cm in 5% H_2/Ar [87], 1.6 S/cm in 10^{-17} atm O_2 [78], and 8.6 S/cm in 5% H_2/Ar [88]. These are all lower than the value reached after 600 h in the present study, except for the 8.6 S/cm measurement. However, that study reported that their sample had a significant amount of $SrMoO_4$ impurity. As discussed above, $SrMoO_4$ will reduce to $SrMoO_3$ in reducing atmosphere, during the test, which could enhance the conductivity since $SrMoO_3$ has such high

conductivity. The reported conductivity of reducing-sintered samples ranges from 0.8 S/cm in 5% H_2/Ar [87] to 8.6 S/cm in 10^{-21} atm O_2 [21]. The latter is very close to the value obtained here in the similar pO_2 of 10^{-20} atm. The 0.8 S/cm value may have been obtained on a sample that was sintered at a lower temperature or in a less reducing atmosphere. Alternatively, the pO_2 during measurement was not specified and may be higher than expected. It is important that workers measure and report the pO_2, because with dry "5% H_2/Ar", the pO_2 depends largely on the seal-tightness of the set-up and how much O_2 leaks in (plus any trace O_2 in the feed gasses). There remains the question of the large difference between the equilibrium conductivity values of the air-sintered and reducing-sintered samples – 3.5 S/cm and 12 S/cm at 10^{-24} and 10^{-23} atm O_2 respectively. It seems very possible that the 3.5 S/cm is the "true" conductivity for the material Sr_2MgMoO_6 at equilibrium with the 800 °C reducing atmosphere, whereas the higher value may be a result of the formation of $SrMoO_3$, perhaps on the surface – any $SrMoO_4$ impurities might not incorporate into the crystal lattice and simply become reduced to the high-conductivity $SrMoO_3$ phase during the reducing-sinter, enhancing the conductivity.

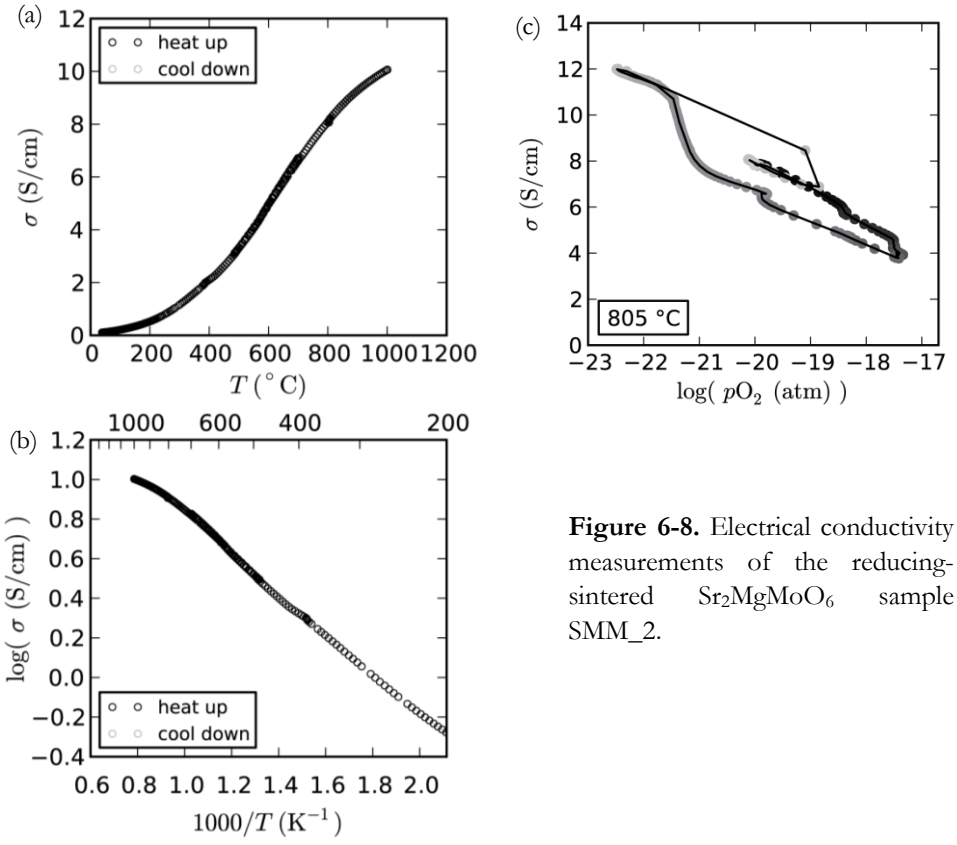

Figure 6-8. Electrical conductivity measurements of the reducing-sintered Sr_2MgMoO_6 sample SMM_2.

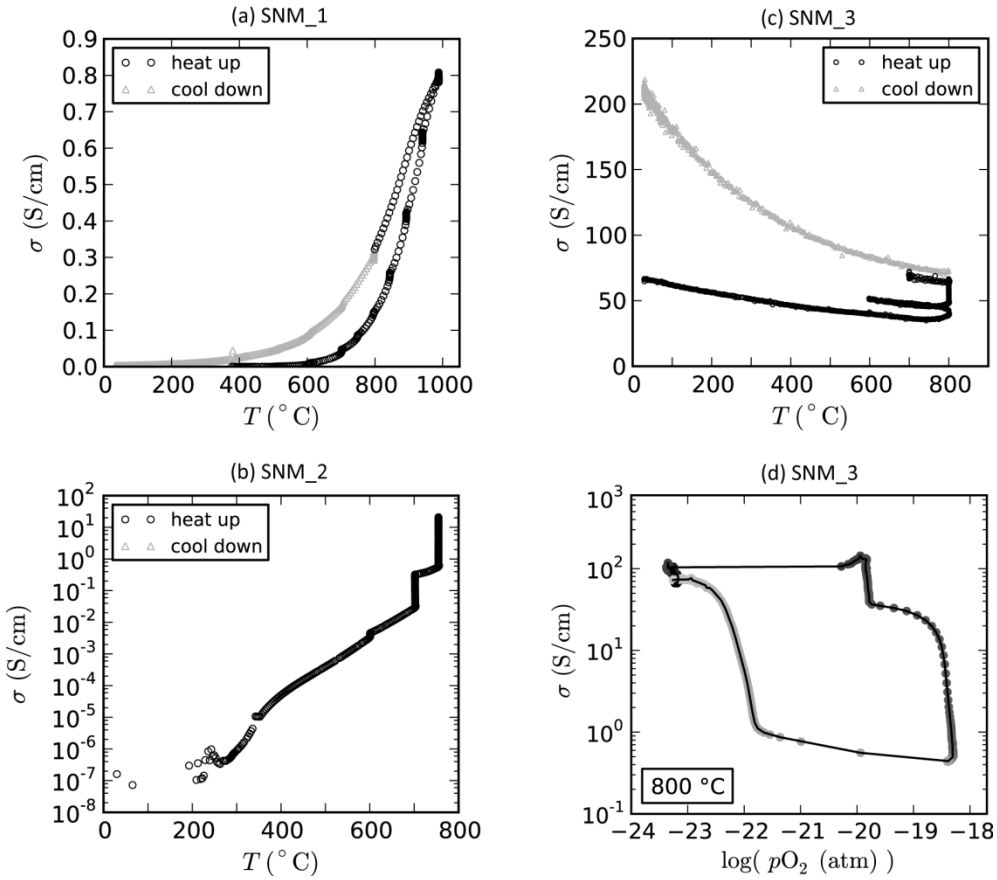

Figure 6-9. Electrical conductivity measurements made on 3 different SNM samples, with the differences described in the text.

The conductivity measurements for three air-sintered double perovskite Sr_2NiMoO_6 (SNM) samples are shown in **Figure 6-9**. SNM_1 was sintered in air and tested in 1.3%H_2O/9%H_2/90%N_2 (cold-humidified), which had a pO_2 of 10^{-20} atm at 800 °C. The conductivity reached about 0.3 S/cm at 800 °C and was slightly enhanced at temperatures above 800 °C, evident from the vertical regions during which conductivity increased at a fixed temperature (**Figure 6-9a**). SNM_2 was also sintered in air but tested in a more reducing atmosphere, dry 9% H_2/N_2 (pO_2=10^{-26} atm at 750 °C). Its conductivity reached 45 S/cm at 750 °C and seemed to continually increase during the test (**Figure 6-9b**). SNM_3 was pre-reduced before measurement at 800 °C in dry 9% H_2/Ar for 24 h, and tested in dry 9% H_2/N_2. Unlike the others, the measurements show that this sample began the test with metallic conductivity (**Figure 6-9c**). Upon reaching 800 °C and holding this temperature, the conductivity began to increase with time. Upon reducing the temperature to 600 °C, the conductivity was stable. The temperature was again increased to 800 °C and the conductivity continually increased, reaching about 70 S/cm. At this point, the pO_2 variation was carried out (**Figure 6-9d**) and at a slightly different pO_2 the conductivity increased further, to >100 S/cm. However, at a pO_2 higher than 10^{-19}-10^{-18}, the conductivity dropped sharply to about 0.4 S/cm – about the same as that

measured on SNM_1. Decreasing the pO_2 again returned the conductivity to its high value; it seemed the changes taking place were nearly reversible.

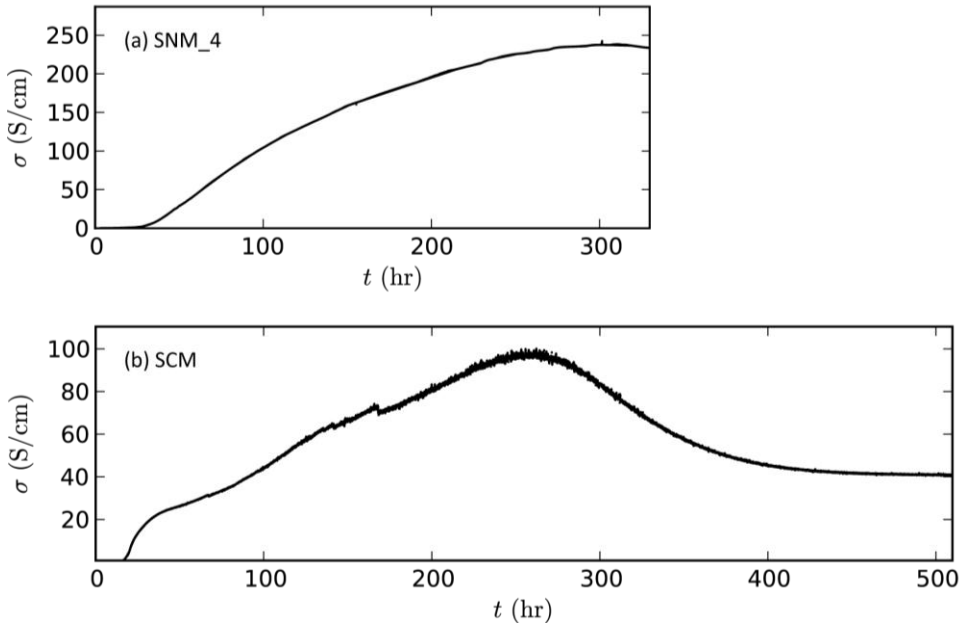

Figure 6-10. Long-term electrical conductivity measurements of air-sintered samples (a) SNM_4, tested at 800 °C in 10^{-23} atm O_2, and (b) SCM, tested at 800 °C in 10^{-24} atm O_2. The temperature and pO_2 profile for (b) was the same as that in Figure 6-7 (this SCM sample and that SMM sample were tested simultaneously), and the conditions for (a) were similar (but with the slightly higher pO_2).

Finally, a fourth SNM sample, SNM_4, was tested for a long time at 800 °C in 10^{-23} atm O_2 (**Figure 6-10a**). This sample was not pre-reduced before testing. After about 300 h, the conductivity had reached 240 S/cm at which point it reached a plateau. This plateau was in fact due to a slight variation in the pO_2 – the pO_2 slightly decreased throughout the test until this point. The test was continued and the conductivity remained near this level, gradually increasing to 270 S/cm during the next 100 h, but the pO_2 was slightly unstable so it is not shown here. During the continuation of this test the pO_2 was purposely varied as well, and these results are described in the next **section 6.3.3**. A similar test was conducted with the Co-bearing variant, SCM (**Figure 6-10b**). The conductivity similarly increased for around 260 hours, after which it reached a plateau at close to 100 S/cm and then decreased over the next 160 hours and stabilized at 40 S/cm. These two materials show similar reduction profiles, based on their conductivity. The pO_2 was slightly lower for the SCM sample than for the SNM sample, 10^{-24} atm, which might explain the slightly faster increase and peaking in the conductivity. The question arises: How can an order of magnitude greater conductivity than SMM (>100 S/cm vs 10 S/cm) be possible with the same oxygen-vacancy $Mo^{5+}/^{6+}$ conduction mechanism? Why is there a continuous increase of σ in dry H_2/N_2? Is the phase stable or is it the result of decomposition?

These questions are answered below, but first, it is important to note that, while working on this, Wei et al [89] and Huang et al [90] published results for Sr_2NiMoO_6 – but did not explain them. Again, the values were widely different – 67 S/cm at 850 °C in H_2 [89] and ~1 S/cm at 850 °C in H_2 [90]. Like SMM, the values must depend on the extent of reduction before or during measurement, but to a much greater degree. Overall, the conductivity of the molybdates clearly depends significantly on the thermal history, the pO_2 during sintering and during measurement, and on the length of time allowed for equilibration during the measurement.

Wei et al did provide an explanation for their high values:

> "After being reduced in H_2 at 1123 K for more than 2 h, the sample's conductivity increases greatly, because reduction in H_2 leads to the formation of oxygen vacancies in the double-perovskite structure." [89]

However, we will show in the next section that this mechanism, which seems to be accurate for SMM, is clearly not the mechanism for such high conductivity in SNM.

The conductivity of the Fe-variant SFM was higher than any of the other double-perovskites (**Figure 6-11**), in agreement with reports in literature [43, 91]. Its conductivity was metallic type, and stable up to 1000 °C (800 °C with $pO_2=10^{-23}$ atm was held for 68 h, and 1000 °C $pO_2=10^{-18.5}$ atm was held for 3 h), suggesting that the conductivity mechanism is not the same as that for SMM, SNM and SCM. SFM has different properties because the Fe-Mo ion couple is mixed-valent for both ions, according to literature [42, 92 subref 26] and as shown in **Table 6-4** ($Fe^{2+/3+}$ and $Mo^{5+/6+}$). This mixed-valency enhances the electronic conductivity [93]. It has been proposed that metallic conductivity in a double perovskite depends on the 3+/5+ couple [94]. On the other hand, SNM and SCM are expected to show semiconductor type conductivity [95], not metallic as was observed in the present study.

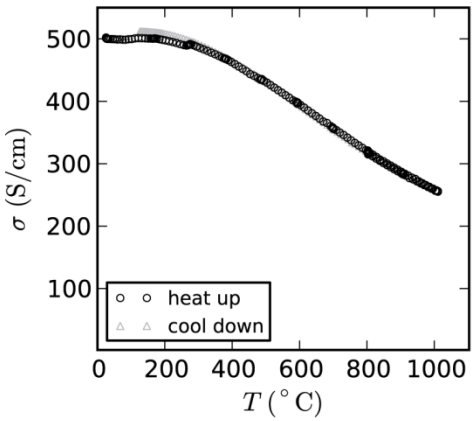

Figure 6-11. Electricity conductivity of Sr_2FeMoO_6 in dry 9% H_2/Ar.

Finally, the conductivity of the tungstates was measured and was found to be <0.01 S/cm for both materials, SMW and SNW. In literature, the Fe-variant SFW, has been reported as an insulator [96, 97]. The insulating nature of W versus Mo can be explained by the relatively higher stability of Mo^{5+} versus W^{5+} [91]. This most likely relates to the narrow region of stability of W^{4+} as well, seen in the phase diagram earlier (**Figure 6-2**). Due to such a low conductivity, the tungstates could not be further studied as electrode materials.

6.3.3. Phase Stability and Microstructure

The phases of all of the materials were examined by XRD before and after the conductivity tests. The microstructure of smooth polished surfaces was studied by SEM, as well. It was found that SNM exhibited the most remarkable changes, so SNM is the focus of this section. SCM exhibited similar behavior but was not studied in as much detail. The other materials, except for SM, were generally stable.

Before testing, SNM was dense and its polished surface was smooth, with large 5-10 μm grains visible and sintered together. After all of the conductivity tests, as well as some additional heat treatments in reducing atmospheres, one surface of each sample was again polished and in the SEM the grain boundaries were clearly visible. However, it was not thermal etching – magnifying the areas revealed chains of nanoparticles lining the grain boundaries for the moderately-reduced sample SNM_2 (**Figure 6-12** through **Figure 6-15**). The SEM micrograph taken with the backscatter detector (**Figure 6-14**) shows that the brightly-shaded nanoparticles are most likely metallic and electron-conductive, suggesting that they might be at least partly responsible for the enhanced electronic conductivity. On the polished surface of SNM_3, which has been exposed to a more reducing atmosphere for a longer time and exhibited higher conductivity, the apparent decomposition extended further into the grains (**Figure 6-16**). The polished surface of SNM_4, which had been reduced for several hundred hours, was almost completely decomposed – the grains were nearly gone and replaced with an remarkable topography with seemingly linear rows of the nanoparticles (**Figure 6-17**). We considered whether the nanoparticles might have aligned due to the electric field applied during conductivity testing, however similar features were observed on samples that were only reduced in a furnace without conductivity measurements and the orientation of the lines seem to be more related to the geometry of the grains that had been there than the direction of the electric field. In **Figure 6-18**, the polished surface of a sample that had been reduced by heat treatment without conductivity testing is shown. An apparent reaction front, from the upper left to the lower right, is visible. The edge of the sample was beyond the upper left of the image, and the center is beyond the lower right. It seems that, at least for this sample, the decomposition reactions took place at the surface and as the material was reduced at the grain boundaries, pathways were created for small amounts of the reducing gas to continue infiltrating the sample and continue the decomposition towards the bulk of the sample.

An EDX map was performed on the particles in a grain boundary of sample SNM_2 (**Figure 6-19**). This clearly shows that the nanoparticles are Ni-rich, however they appear to not simply be Ni metal particles because the Mo signal does not drop within the scan area of the nanoparticles. Therefore they might be Ni-Mo alloy particles. XRD data of these surfaces completed the picture and revealed more phases besides the precipitated nanoparticles. According to the XRD data, within a few hours at 800 °C in dry 9% H_2/Ar, SNM completely decomposes. First, Sr_3MoO_6 dominates and is accompanied by some $SrMoO_3$ and $Ni/MoNi_4$ nanoparticles. As reduction continues, the fraction of $SrMoO_3$ and $Ni/MoNi_4$ increases until there is nearly as much $SrMoO_3$ as Sr_3MoO_6 after 300 h (for the 300-h conductivity tested sample, **Figure 6-10a**). A small fraction of Sr_2MoO_4 also sometimes accompanies the decomposed phases.

We are therefore able to propose a decomposition mechanism, or two mechanisms that seem to be occurring and interplaying to different extents:

1. $Sr_2NiMoO_6 \rightarrow \frac{1}{2}\ SrMoO_3 + \frac{1}{2}\ Sr_3MoO_6 + Ni + \frac{3}{4}\ O_2$
2. $Sr_2NiMoO_6 \rightarrow \frac{1}{4}\ Sr_2MoO_4 + \frac{1}{2}\ Sr_3MoO_6 + \frac{1}{4}\ MoNi_4 + O_2$

From these reactions we can also surmise the source of the enhanced electronic conductivity based on the product phases. As shown earlier, $SrMoO_3$ exhibits very high metallic conductivity. Sr_2MoO_4 has also been reported to have metallic conductivity [98] or perhaps even superconductivity [99]. The Sr_3MoO_6 strontium molybdate phase was found to be a mixed ionic-electronic conductor with oxygen ion transference numbers of 0.2–0.4 in the temperature range from 800 to 1050°C [100, 101]. The metallic nanoparticles may also enhance electronic conductivity, but since they appear to be largely disconnected they may not enhance it as much as would first appear.

The observed decomposition can explain the increasing conductivity observed during measurement as well as the wide range of conductivity results in literature that were thought to be due only to the formation of oxygen vacancies and corresponding partial reduction of Mo^{6+} to Mo^{5+}. It can also provide an alternative explanation for the high oxygen vacancy values that have been reported for SCM ($\delta = 0.14\text{-}0.17$ in $Sr_2CoMoO_{6-\delta}$) [42, 93], whereas a value of only 0.05 has been reported for SMM [87, 102, 103].

From an application standpoint this decomposition is not necessarily disadvantageous. The resulting composite material may provide excellent electrocatalytic activity. The nanostructures were observed all over the unpolished surfaces of the various samples (**Figure 6-20** through **Figure 6-23**). Precipitation of Ni or Pd metal particles from titanate ceramics in a reducing atmosphere has been exploited in catalysis [104-107][108], and precipitation of Ni or Ru metal particles from chromite ceramic solid oxide cell anodes has been observed [109, 110],

but not decomposition to this extent to form a composite of multiple useful phases with an entirely nanostructured surface.

The apparent reversibility of the conductivity measurements seen in **Figure 6-9d** when increasing and then decreasing the pO_2 suggests interesting behavior – potentially reversible phase changes between SNM and the decomposed phases. To investigate this, an SNM sample that had been reduced at 800 °C in dry 9% H_2/Ar for 10 h was re-oxidized in air at 800 °C for 10 h. One can clear see from the X-ray diffractograms (**Figure 6-24**) that the material completely decomposed into Sr_3MoO_6, $SrMoO_3$, and Ni/$MoNi_4$ particles upon reduction, and upon re-oxidation the double-perovskite phase was almost entirely recovered, accompanied by small fractions of $SrMoO_4$ and NiO. The long-term SNM conductivity test described earlier (**Figure 6-10a**) was continued with pO_2 variations including oxidation in air and re-reduction (**Figure 6-25**). After 24 h exposure to air at 800 °C, during which the conductivity dropped to about 0.1 S/cm, the high conductivity was mostly recovered within 24 h upon re-exposure to dry 9% H_2/Ar. The quickness with which the high conductivity was recovered, in comparison with the 300 h that were needed for the initial reduction-decomposition, suggests that the "extra" $SrMoO_4$ and NiO phases observed in the XRD are quickly reduced back to $SrMoO_3$ and Ni. As a layer in an electrode this could be quite advantageous, providing the ability to refresh or regenerate the nanostructured surface by oxidizing and then re-reducing it, which might restore the surface's high electrocatalytic activity that might have been lost over time as the nanostructures coarsened or impurities accumulated.

Adding Ti to the B-site, as $SrTi_{0.5}Ni_{0.25}Mo_{0.25}O_3$, prevented decomposition and reduced the total conductivity that could be attained, which shows that the extent of decomposition can be controlled by modifying the composition.

In the next section, the electrocatalytic activity of this decomposed material and some of the other materials are investigated.

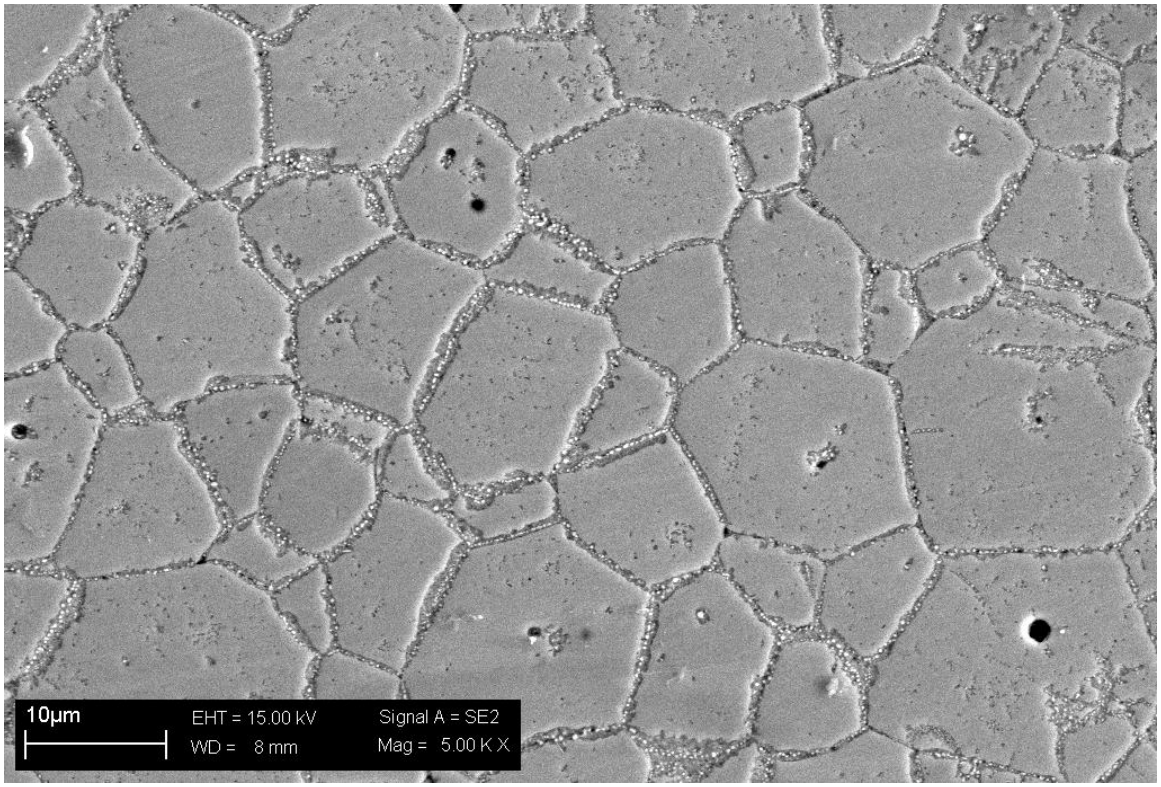

Figure 6-12. SEM micrograph of the SNM_2 polished surface after the conductivity test.

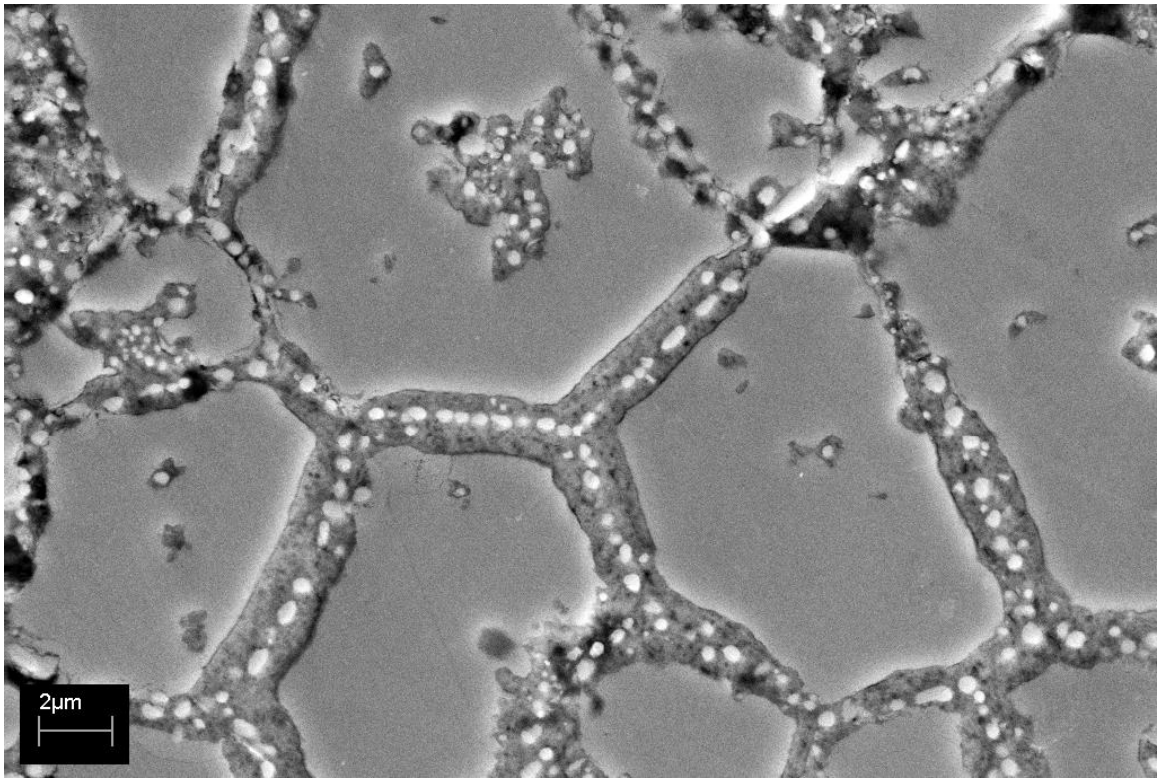

Figure 6-13. SEM micrograph of the SNM_2 polished surface after the conductivity test.

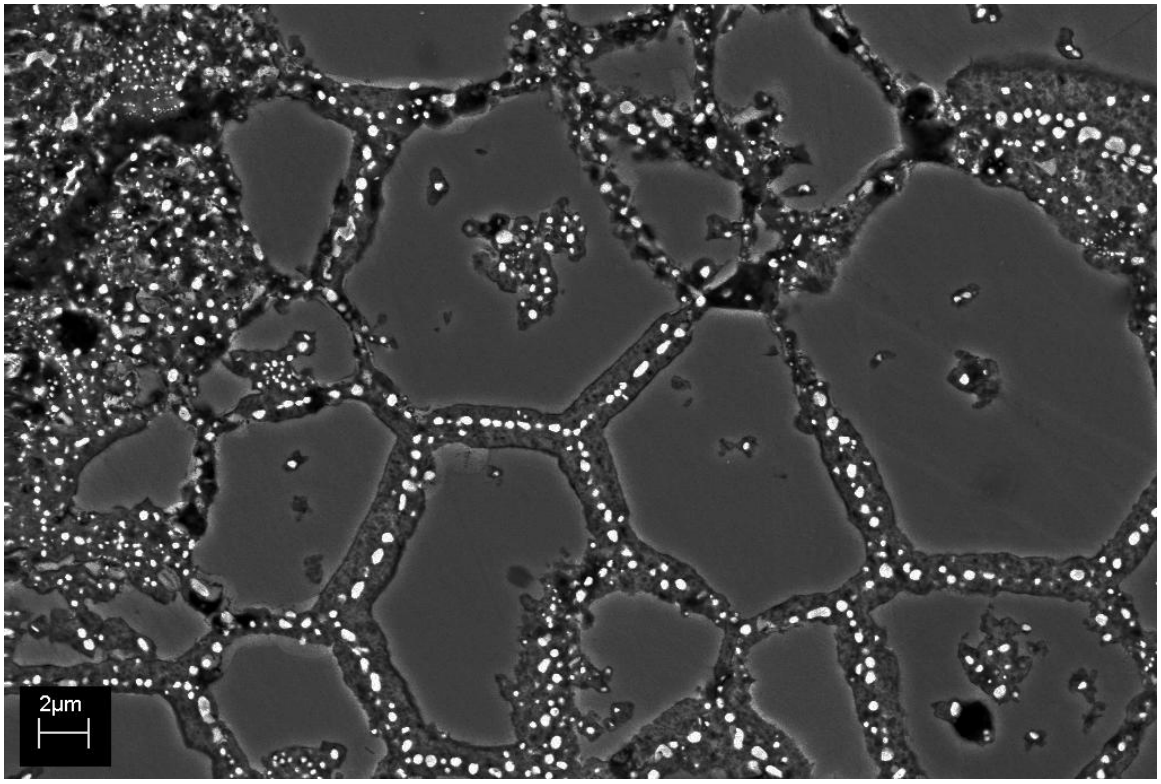

Figure 6-14. SEM micrograph of the SNM_2 polished surface after the conductivity test, with the backscatter detector.

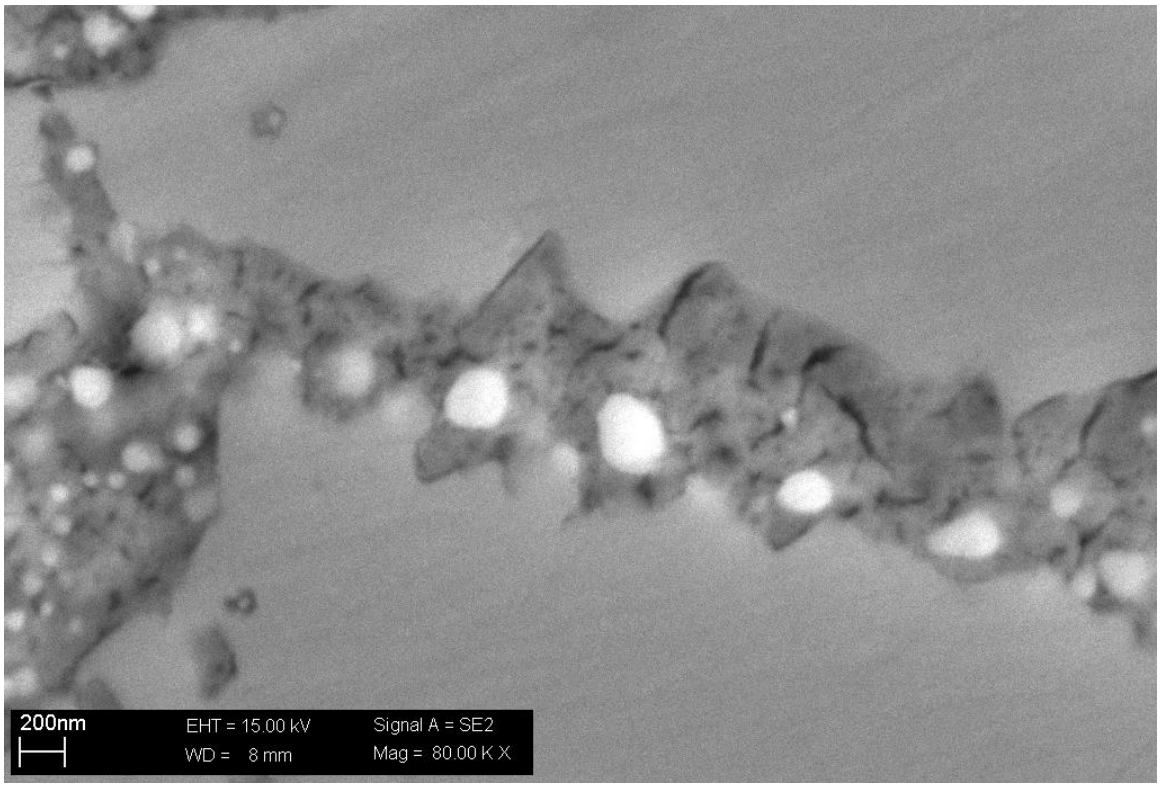

Figure 6-15. SEM micrograph of the SNM_2 polished surface after the conductivity test.

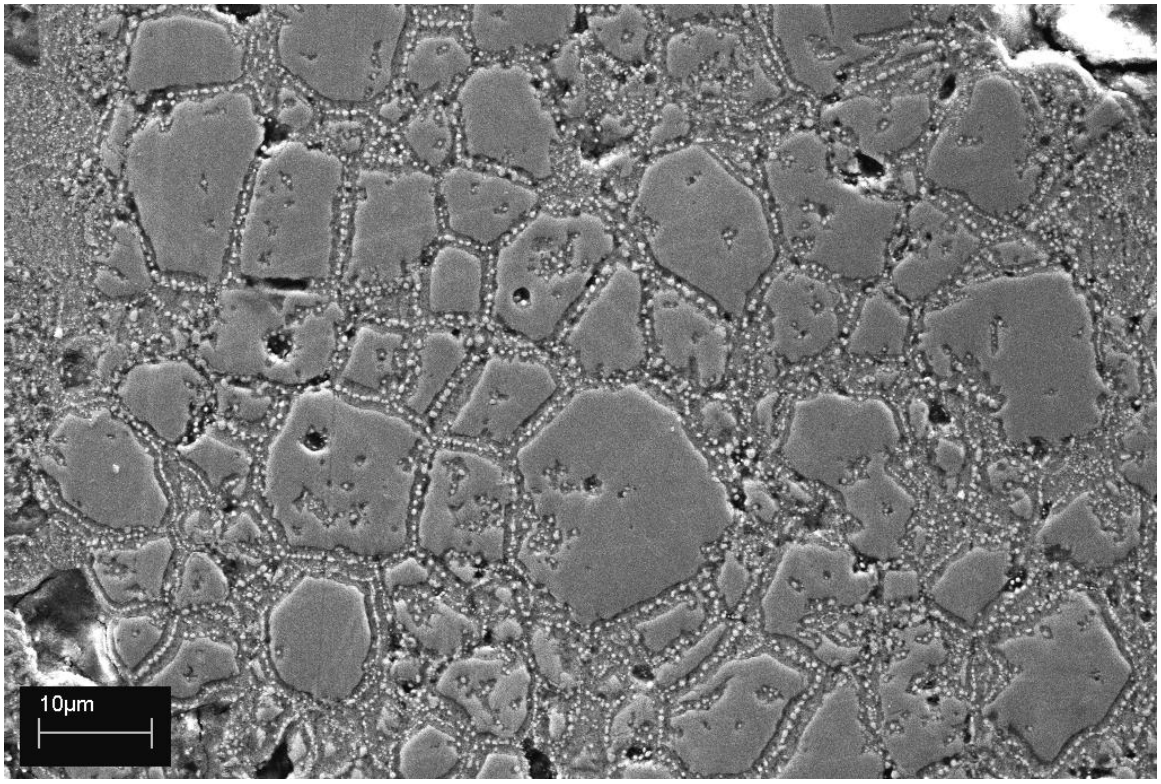

Figure 6-16. SEM micrograph of the SNM_3 polished surface after the conductivity test. SNM_3 had been exposed to a more reducing atmosphere and for a longer time.

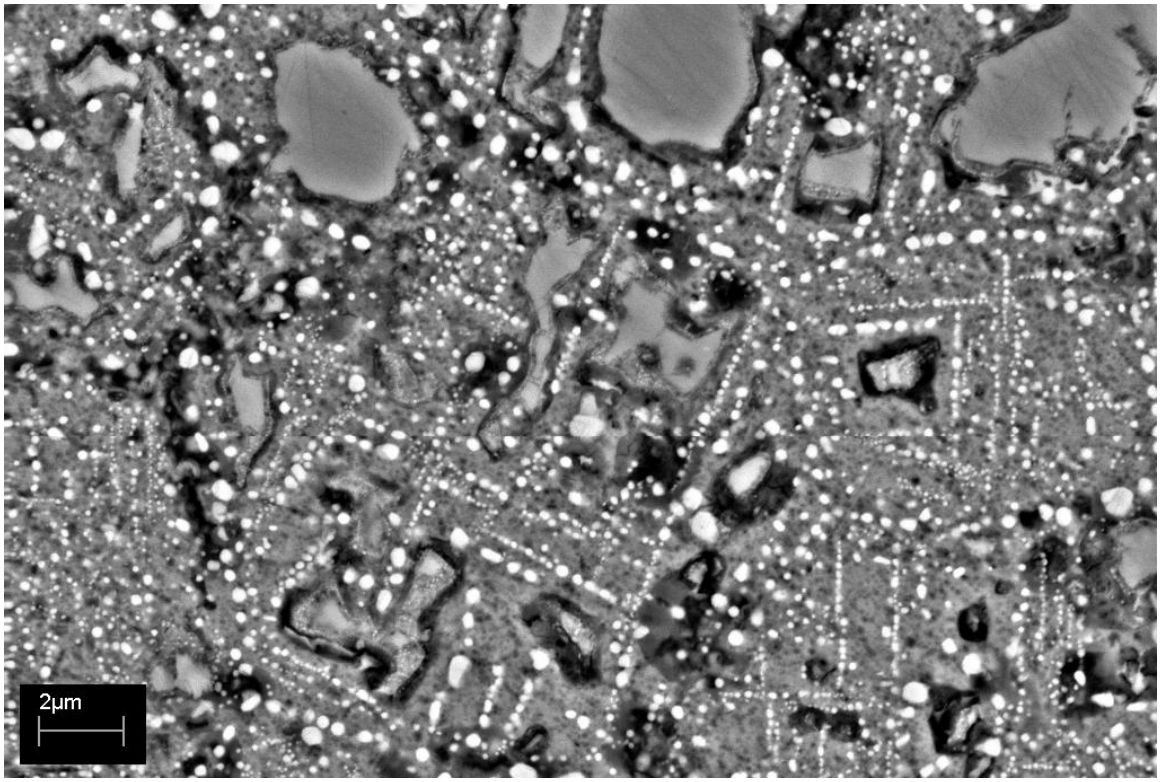

Figure 6-17. SEM micrograph of the SNM_4 polished surface after the conductivity test.

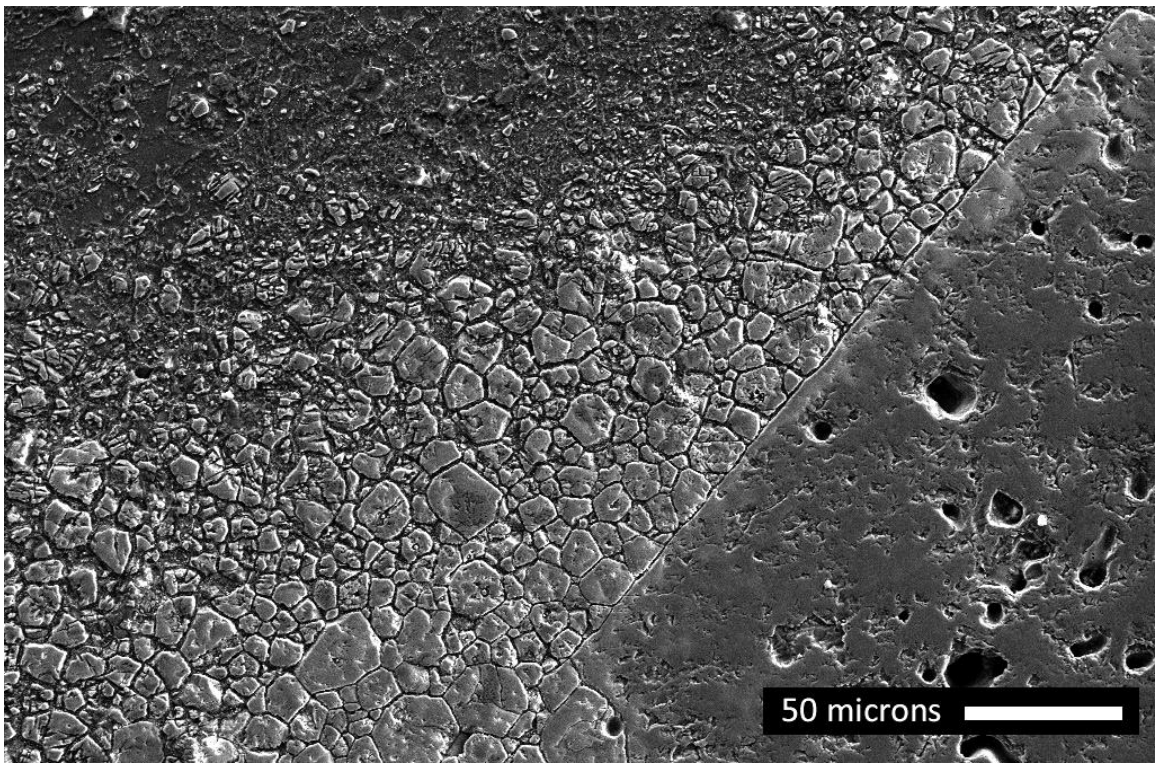

Figure 6-18. SEM micrograph of the polished surface of another SNM sample that had not been used in a conductivity test but only heat treated in a reducing atmosphere.

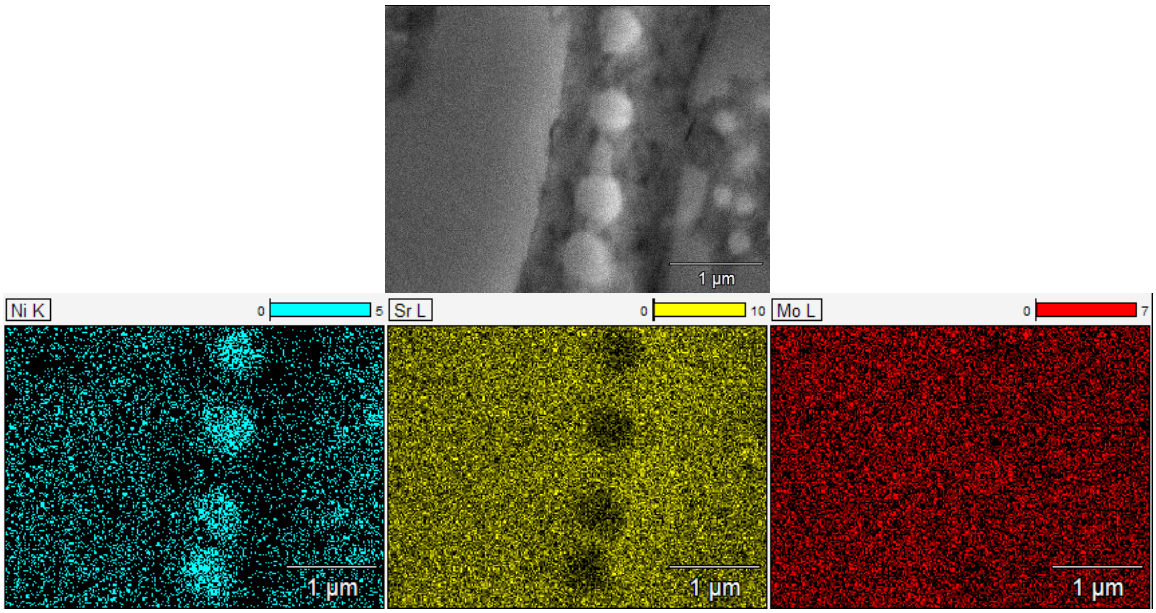

Figure 6-19. EDX spectral map of the grain boundary particles of sample SNM_2.

Figure 6-20. SEM micrograph of an unpolished surface of one of the reduced SNM samples.

Figure 6-21. SEM micrograph of an unpolished surface of one of the reduced SNM samples.

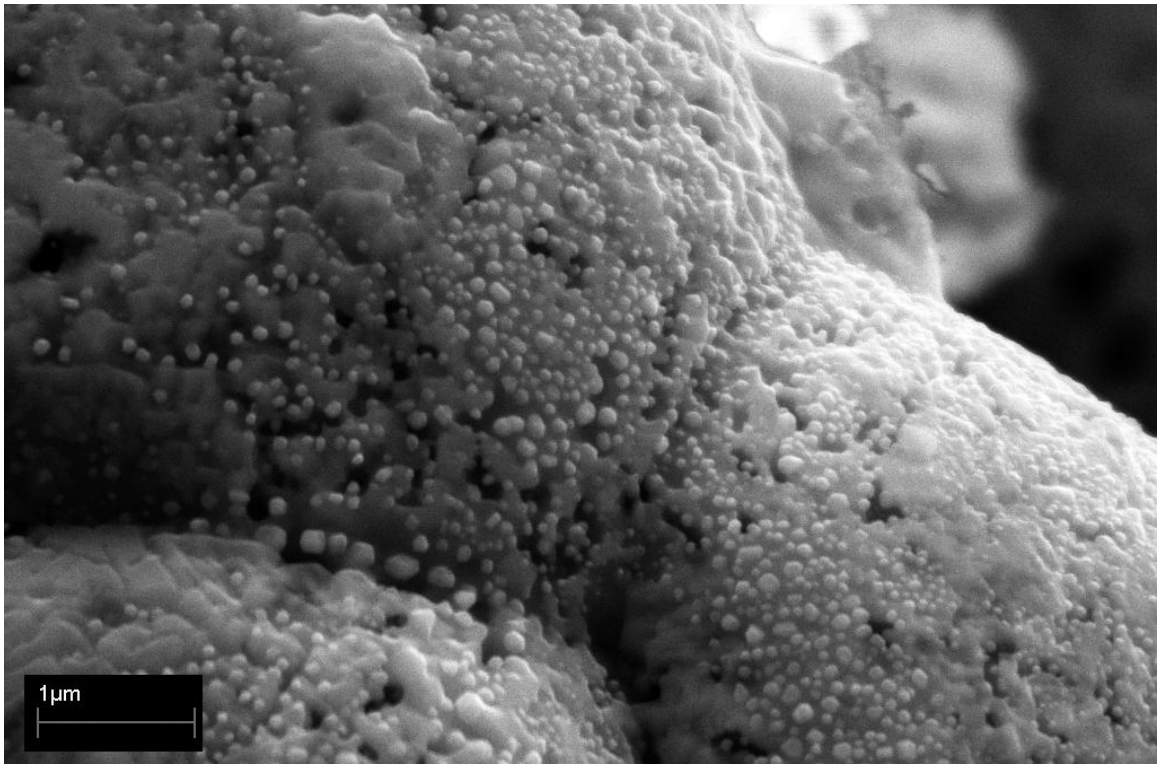

Figure 6-22. SEM micrograph of an unpolished surface of one of the reduced SNM samples.

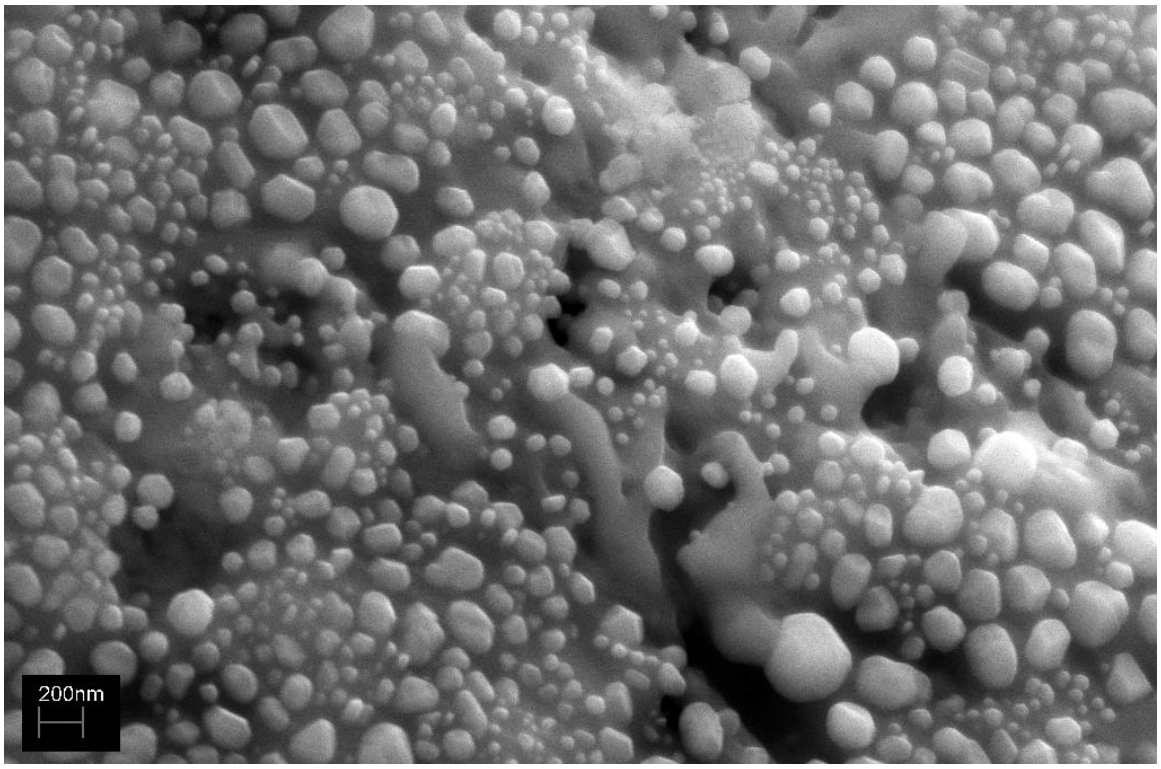

Figure 6-23. SEM micrograph of an unpolished surface of one of the reduced SNM samples.

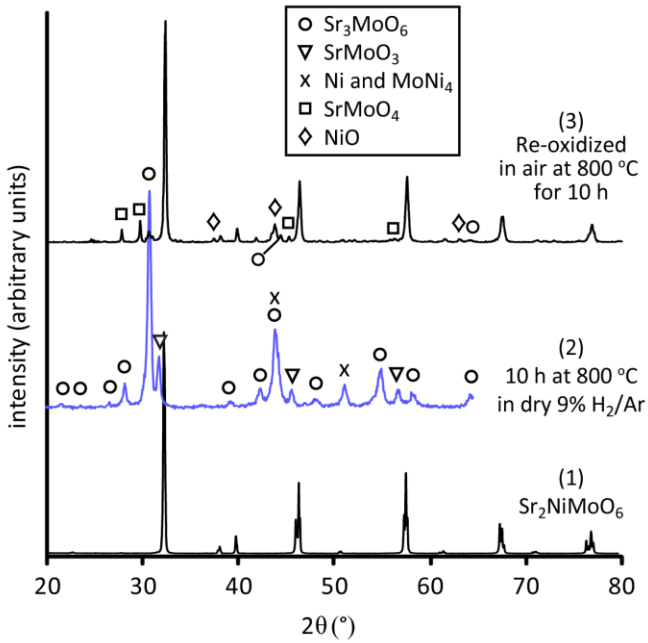

Figure 6-24. X-ray diffractograms of an SNM sample that was subjected to reduction and re-oxidation.

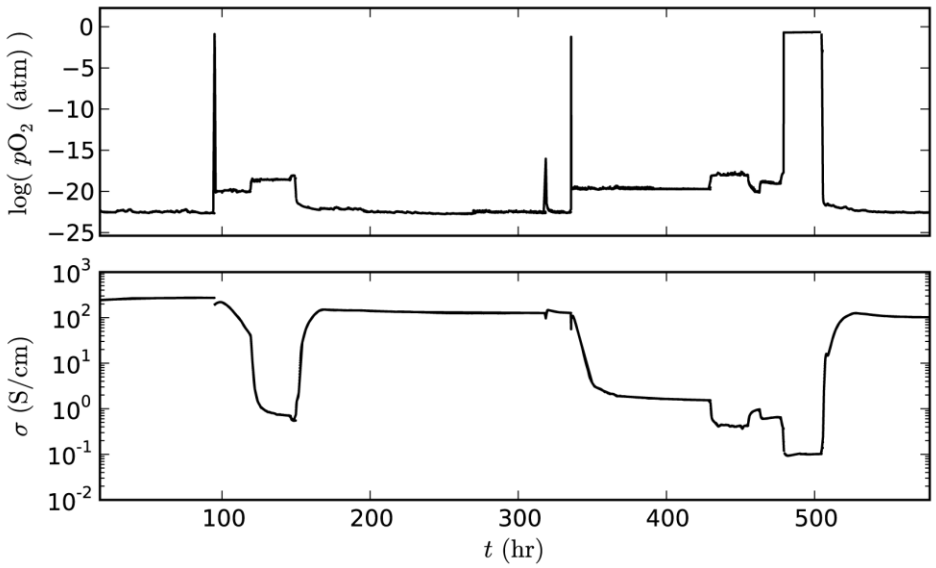

Figure 6-25. Continuation of the 300-h SNM conductivity test shown in **Figure 6-10a**, with pO_2 variations include oxidation in air and re-reduction in dry 9% H_2/Ar. The prior test was shut down, the sample was removed and analyzed by XRD, and then the sample was placed back into the conductivity test set-up and heated up again to 800 °C in dry 9% H_2/Ar. Metallic-type conductivity was observed during heat-up and the conductivity measured at 800 °C was the same as before cool-down.

6.3.4. Electrochemical Activity for H_2O/CO_2 Electrolysis and H_2/CO Oxidation

The electrochemical activity of the molybdate materials was investigated using point-contact electrodes. A series of experiments were performed to determine the best geometry and method to estimate the TPB length. Even if some of the materials exhibit mixed conductivity, the TPB length is still the most useful normalization parameter. In the end, the normalization method was as successful as the metal point contact electrode methods described in **Chapter 5**. An example of the contact area for one of the electrodes is shown in **Figure 6-26**. The area and perimeter were measured. Then the same method as for the metals – applying correction factors to the area and TPB estimated by the Newman relation (from the serial resistance R_S) – was used. The measurements on different electrodes of the same material were reproducible within ~50%, which is sufficient for this quick test and considering that the performance of the different materials spans orders of magnitude. Since none of the electrodes exhibited a rapidly and/or constantly increasing R_S which would be indicative of the formation of an insulating layer, none of the electrodes were strongly reactive with YSZ at the operating conditions (700-850 °C). SMM has been reported to react with YSZ at higher temperatures [103].

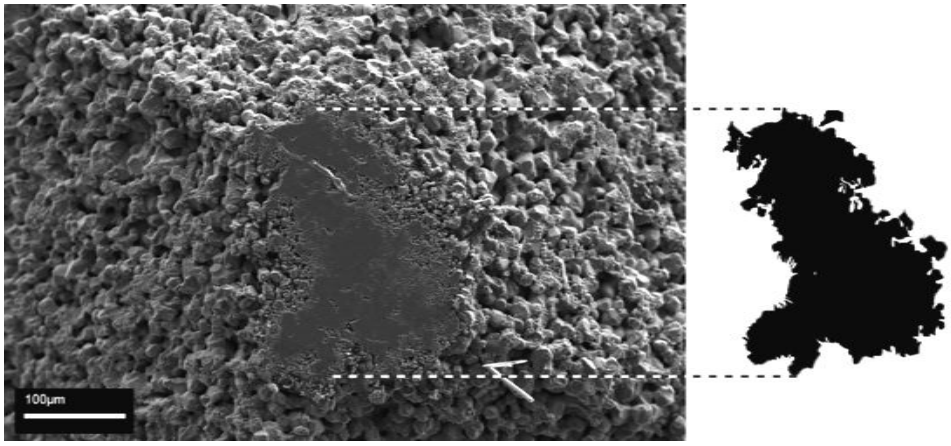

Figure 6-26. Contact area of the tip of an SFM cone type electrode that had been in contact with the smooth polished YSZ surface. The outline of the measured contact area is shown at the right.

Example impedance spectra measured at OCV are shown in **Figure 6-27**. A detailed analysis of the IS was not carried out in the present study. The IS were used only to determine R_S and R_P to assess the relative performance of the materials. From these spectra one can see that SFM has much higher performance than STM for all atmospheres. Furthermore, the difference in performance in CO/CO_2 vs H_2/H_2O is much greater for STM than for SFM.

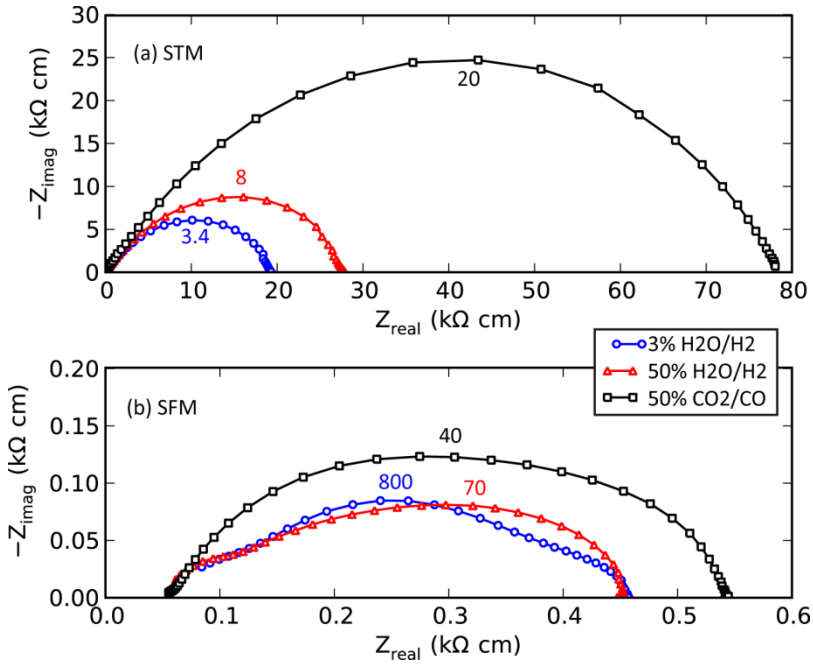

Figure 6-27. Example impedance spectra measured at OCV at 850 °C on (a) one of the STM electrodes, and (b) one of the SFM electrodes. The numbers near each peak are the approximate summit frequency in Hz.

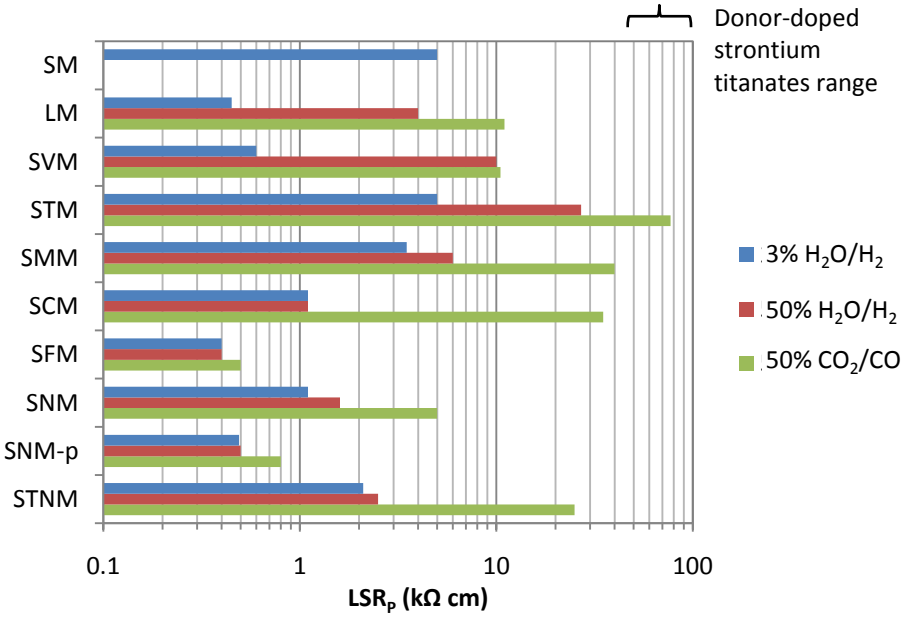

Figure 6-28. Relative electrochemical performance of the tested materials, in terms of the LSR_P at OCV in 3% H_2O/H_2, 50% H_2O/H_2, and 50% CO_2/CO. SNM-p = pre-reduced SNM.

The relative performance, as the length-specific polarization resistance (LSR_P) measured at OCV, of all of the materials tested, is shown in **Figure 6-28**. The LSR_P values are averages between multiple electrodes when multiple electrodes of a single material were tested. For SM,

only the LSR_P in 3% H_2O/H_2 is given, because the material oxidized to $SrMoO_4$ upon switching to 50% H_2O/H_2. From the rest of the results, one can see that SFM and the pre-reduced SNM materials have the highest electrocatalytic activity in the OCV measurements. The SMM electrode was made of the air-sintered material, so even though it was pre-reduced at 800 °C in dry 9% H_2/Ar, its electrochemical performance was most likely lower than it would be for a reducing-sintered sample (see discussion about SMM in **section 6.3.2**). For all of the electrodes, LSR_P in 3% H_2O/H_2 is lower than or equal to LSR_P in 50% H_2/H_2. Most likely this can be attributed to the fact that 3% H_2O/H_2 is a more reducing atmosphere, which more strongly reduces the ceramic materials at least at the surfaces, leading to oxygen loss and a higher concentration of electrons and oxygen vacancies.

Another noteworthy observation is that, whereas most of the materials have significantly lower performance in 50% CO_2/CO than in 50% H_2O/H_2, SVM has almost the exact same performance, which suggests that V may be a good catalyst for the CO/CO_2 reactions. At the other extreme, the much lower performance of SCM in CO/CO_2 than in H_2/H_2O suggests that Co may not be a desirable catalyst for CO/CO_2 reactions. Finally, also marked on the plot is the LSR_P range obtained for the donor-doped strontium titanates. Although these titanates are known to provide poor performance as electrode materials, the fact that the new materials have 2 orders of magnitude lower LSR_P values suggests that they are very promising electrocatalysts.

SEM inspection of the electrode surfaces after testing showed the nanostructured surfaces described in the last section, for SNM and SCM. In fact, for the SNM electrode that was not pre-reduced, the decomposition was apparent in the sequence of impedance spectra measured during the electrochemistry test (**Figure 6-29**). At around hour 35 of the test, which was about 30 hours after having reached 850 °C and switched to 3% H_2O/H_2, the shape and magnitude of the impedance spectra suddenly changed. This change most likely indicates that the decomposition reached a threshold, at least at the surface. Perhaps the newly formed materials and nanostructured surface defined the interface region near the TPB at that point.

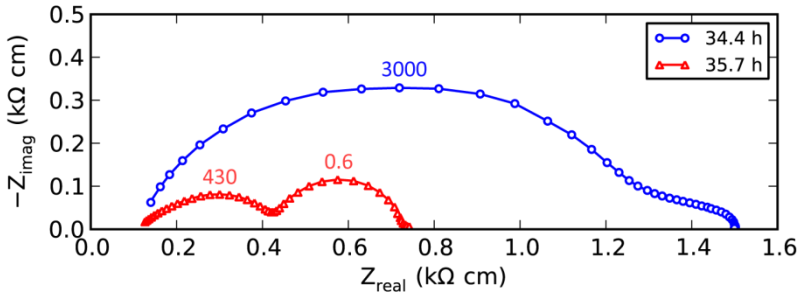

Figure 6-29. Impedance spectra measured at OCV on the non-pre-reduced SNM electrode in 3% H_2O/H_2 at 850 °C. The numbers above each peak are the approximate summit frequency in Hz.

Potential sweeps were performed on all of the electrodes in 50% H_2O/H_2. Only one is shown as an example – that for SVM (**Figure 6-30**). Cathodic polarization (H_2O electrolysis, in this case) significantly activates the electrode relative to OCV. The instantaneous slope of the polarization curve at –200 mV vs at OCV, determined by IS measured under bias, was about 0.8 kΩ cm vs 10 kΩ cm, or a factor of 12 lower LSR_P. –200 mV is chosen because this magnitude of cathodic bias is relevant for electrolysis cell operation – the total overpotential, including the potential drop at the positive-electrode and the ohmic drop across the electrolyte, should be 500-700 mV for electrolysis at 850 °C if operating at the thermoneutral voltage (see sections **1.1.2**, **3.2.2.3**, and **4.3.1**). Clearly, OCV R_P values are not always indicative of the true performance of these molybdates (as well as some other ceramics e.g. titanates [8, 53]). Some ceramic materials activate during reduction, most likely because reducing them leads to defect chemistry changes on the surface of the material, such as oxygen loss and an increase in surface oxygen vacancy concentration.

Not all of the electrodes activated so significantly during cathodic polarization; for others the potential sweeps were more linear. The activation or deactivation of the electrodes with anodic or cathodic overpotentials is summarized in **Figure 6-31**. In **Figure 6-31a**, an "activation factor" for anodic and cathodic bias is presented for each electrode. This is the ratio of the LSR_P at the given overpotential (+200 mV or –200 mV) versus the LSR_P at OCV, determined from impedance measurements. An activation factor value below 1 indicates that the OCV LSR_P was lower than at the applied potential. Clearly, SVM is not the only material that activates by cathodic polarization. STM and LM activate to a similar degree (by a factor of 7 to 11). Many of the double-perovskites are activated as well, but only slightly by comparison. Most of the materials have lower anodic than cathodic performance, in contrast to some of the metals, such as Ni, studied in **Chapter 5**. The exception is LM, for which the anodic performance is even higher than the cathodic performance, both relative to the OCV performance. To assess the relative performance of the different materials for oxidation and reduction, the i-V curves must be used. **Figure 6-31b** shows the absolute length-specific current measured at overpotentials of +200 mV and –200 mV. SFM and the pre-reduced SNM-p show some of the best performance, as indicated by the OCV measurements earlier. However, LM now shows similarly high performance due to its strong activation with anodic and cathodic bias. It should also be noted that the potential sweeps were reversible and repeatable. That is, none of the electrodes remained activated or deactivated after applying potentials. Further study of the observed cathodic activation phenomena of these electrodes will be important for application in electrolysis cell cathodes.

The high performance of SNM is most likely due to the nanostructured surface and precipitated nanoparticles discussed earlier. SFM, on the other hand, does not seem to decompose in such a way, yet has even higher performance. The stability can be attributed to the greater stability of Fe against reduction to metal than Ni and Co, and the high performance

may be related to the defect chemistry of SFM. A higher concentration of oxygen vacancies may be present in the material. In catalysis, SFM was observed to provide high catalytic performance for CH_4 oxidation and this high performance was attributed to a high concentration of oxygen vacancies [111]. As discussed earlier, oxygen vacancies form in reduced SMM as a result of some of the Mo^{6+} ions accepting an electron and becoming Mo^{5+}. In SFM, the Fe ions most likely are mixed-valent as well ($Fe^{2+/3+}$), which might allow for yet more oxygen vacancies in the crystal lattice.

The LSR_P values can be compared with those measured on the metal point electrodes in **Chapter 5**. The best molybdate electrodes have significantly higher performance than any of the metals. Only by subjecting the metals to extreme conditions of oxidation or strong cathodic polarization, both of which enhanced the performance, could the performance of the metals approach that of these molybdates. However, for the metals, how long the enhanced performance will last, and to what degree the treatments can be used on porous electrodes, is unclear.

Finally, the non-molybdate STN-CGO electrode exhibited interesting characteristics that are relevant to the discussions above regarding activity for CO/CO_2 versus H_2/H_2O reactions and regarding cathodic activation. **Figure 6-32a** shows impedance spectra measured at OCV. As with the molybdates, the performance in 3% H_2O/H_2 was higher than in 50% H_2O/H_2. In this case, however, the performance was significantly higher – the LSR_P was about a factor of 8 lower. Remarkably, this electrode showed higher performance in CO/CO_2 than in H_2/H_2O – the LSR_P was more than a factor of 2.5 lower in 50% CO_2/CO than in 50% H_2O/H_2. Potential sweeps were also measured in the same gas atmospheres (**Figure 6-32b**). As with many of the molybdates, this electrode activates under cathodic polarization in H_2/H_2O atmospheres. However, in CO/CO_2, the activation is only minor and the polarization curve for both anodic and cathodic directions is nearly linear, which means that either the cathodic activation phenomena is linked to H_2/H_2O or for this specific electrode composition a different reaction mechanism takes over in CO/CO_2. For an STN electrode without the CGO particles, the shape of the potential sweep in CO/CO_2 was the same as in H_2/H_2O, suggesting that CGO is a good catalyst for CO oxidation and CO_2 reduction. The relatively higher performance in 50% CO_2/CO than in 50% H_2O/H_2 holds for the entire range of overpotentials from –300 to +300 mV. The difference in performance becomes much larger in the anodic regime and much smaller at higher cathodic overpotentials due to the different shapes of the sweeps in 50% CO_2/CO and 50% H_2O/H_2.

Note that the measurements are not normalized to the TPB nor the contact area. This is because it was observed in the SEM after the test that the CGO particles spread out on the YSZ surface and on the electrode tip; the interface was not well-defined. Still, a rough estimate could be made which indicated that the polarization resistance was 1-2 orders of magnitude lower for the CGO-coated STN electrode than for an STN electrode without CGO, in both

H_2/H_2O and CO/CO_2 atmospheres, in agreement with prior work done using porous STN backbones coated with CGO particles [10].

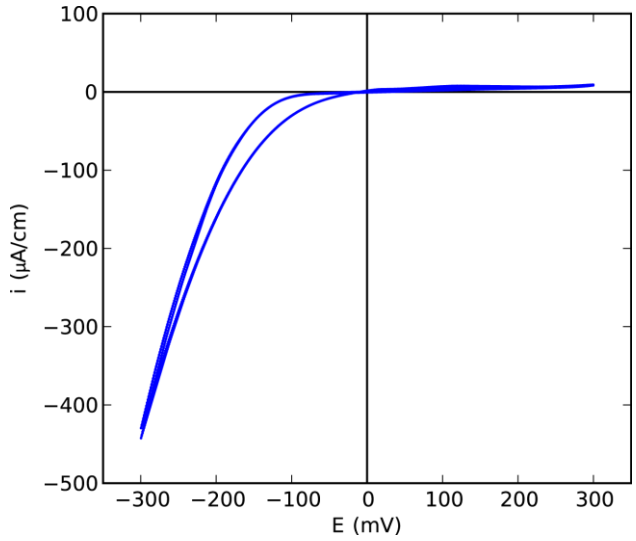

Figure 6-30. Potential sweep on the SVM electrode, at 2 mV/s at 850 °C in 50% H_2O/H_2. The sweep was repeated 3 times. The 3 cycles nearly overlaid each other.

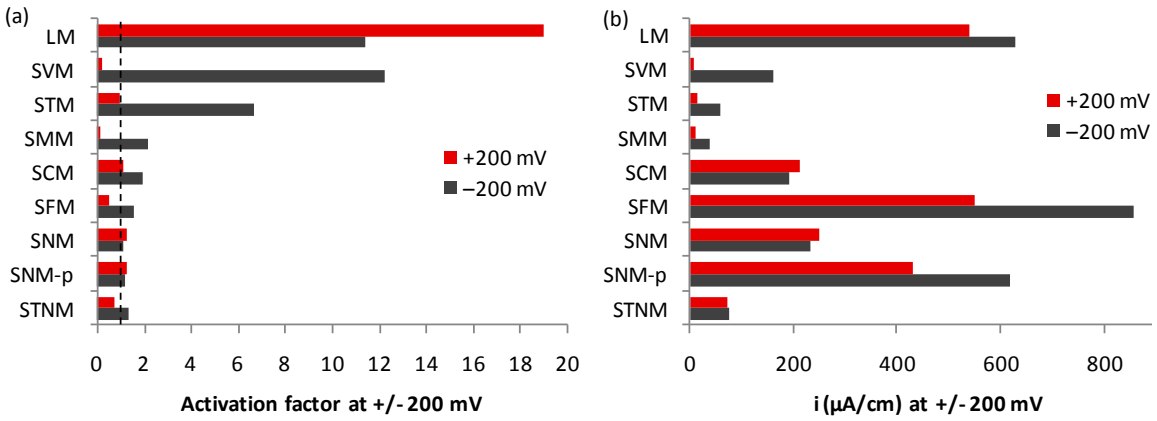

Figure 6-31. (a) Activation factors of LSR_P measured under bias relative to OCV LSR_P and (b) TPB-length-specific currents, obtained at anodic (+200 mV) and cathodic (–200 mV) overpotentials at 850 °C in 50% H_2O/H_2. The dashed vertical line at Activation factor = 1 indicates activation (above 1) vs deactivation (below 1).

Overall, it appears that CGO is an especially promising electrode material for CO_2 electrolysis and for a fuel cell running on CO. Since CGO has insufficient electronic conductivity to serve as an electrode on its own, it can be coated onto an electron-conducting backbone like STN. CGO has some complementary properties to the best molybdates – high ionic conductivity and moderate electronic conductivity in the reducing atmospheres present at

the negative-electrode, whereas the best molybdates have high electronic conductivity and most likely moderate ionic conductivity.

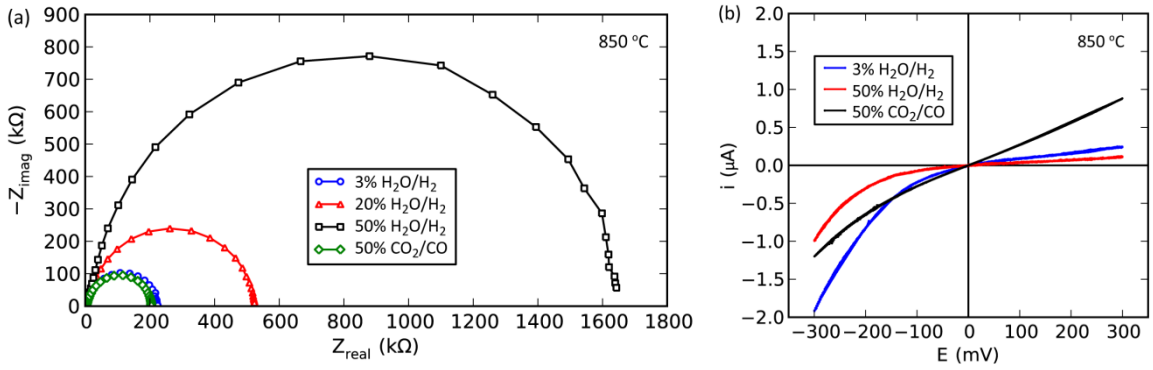

Figure 6-32. Electrochemistry measurements made on the STN-CGO cone-shaped electrode contacting the polished YSZ surface: (a) Impedance spectra measured at OCV, (b) Potential sweeps measured at 2 mV/s.

6.4. Conclusions

In this study, a number of Mo-based ceramics were studied for their fundamental properties of phase, microstructure and electronic conductivity, and they were tested as solid oxide cell negative-electrodes. The results show that molybdenum can be used on the B-site of a variety of ceramic materials that have high electrochemical performance for H_2O/CO_2 reduction and H_2/CO oxidation. These materials are therefore very promising as electrodes or as components of electrodes. Most of the rich properties that Mo-based ceramics have to offer seem to be related to the valence flexibility of the Mo ion. These Mo-based ceramics can provide high electronic conductivity, high electrocatalytic activity, and mixed ionic-electronic conductivity via oxygen vacancies (which also often enhances the electrocatalytic activity). Many of the materials were significantly activated by cathodic polarization, and they exhibited much higher performance for cathodic (electrolysis) polarization than anodic (fuel cell) polarization, which makes them especially interesting for electrolysis electrodes.

For some materials such as the double-perovskites Sr_2NiMoO_6 and Sr_2CoMoO_6, a decomposition phenomenon that leads to a unique nanostructured surface and multiple desirable electrocatalytic and electron-conductive phases was observed under operating conditions (certain reducing atmospheres). The material was reduced and decomposed in a beneficial way, precipitating Ni and Ni-Mo nanoparticles to the surface and grain boundaries and forming other ceramic phases with high electronic conductivity. This phenomenon explains the wide range of electrical conductivity results reported in literature. The decomposition might be performed *in situ* and controlled by temperature and pO_2 (and possibly even applied potential) to obtain desired properties.

By modifying the composition (adding Ti to the B-site), it was possible to prevent decomposition. Another member of the double-perovskite molybdate family, Sr_2FeMoO_6, exhibited similarly high electronic conductivity and electrocatalytic activity but did not decompose. The high activity was the result of a different mechanism (besides a nanostructured surface), probably related to the defect chemistry of the material (possibly high mixed ionic-electronic conductivity) and/or the mixed valency of the Fe and Mo ions.

The polarization resistances of the best molybdate materials were two orders of magnitude lower than that of donor-doped strontium titanates. Whereas nearly all of the molybdates showed higher performance for H_2O electrolysis than CO_2 electrolysis, one with vanadium showed nearly equal performance, and a non-molybdate which exhibits some complementary properties to the best molybdates, Gd-doped ceria in nanoparticle form, was found to be an excellent electrocatalyst for CO_2 electrolysis and CO oxidation (moreso than for H_2O/H_2 for which it is known to be good).

In terms of the stability of molybdate based materials, Mo needs a partner. If a redox-stable or near-redox-stable material is desired, one must allow the fully oxidized valence of 6+. Alternatively, if one can deal with reversible phase changes accompanied by large volume expansion and contraction (as with Ni-NiO in conventional electrodes), one can use Mo with 4+ valence.

In terms of cost, Mo is a somewhat more expensive metal than Ni – currently just less than twice as expensive per unit mass. However, it is important to note that in these ceramic materials Mo comprises only half of the B site – it makes up only $1/10^{th}$ of the atoms in the crystal lattice of a double perovskite (~25 wt% depending on the other elements). Although Mo is an order of magnitude scarcer than Ni is the Earth's crust, it is 2-3 orders of magnitude more abundant than Pt, Pd and other expensive metals that are considered for low-temperature fuel cell catalysts, so there does not appear to be a resource limitation for Mo especially if it is used in a thin layer. Finally, according to cost estimates of solid oxide cell systems, the total manufacturing cost is dominated not by the raw materials but by the fabrication process and balance of system [112, 113]. Therefore, the use of these molybdate materials is not expected to be economically prohibitive. On the contrary, if in a porous technological electrode they can provide the exceptional level of electrocatalytic activity observed in the present study, they would most likely improve the economics of solid oxide cells.

6.5. References

1. Steele BCH, *Survey of materials selection for ceramic fuel cells II. Cathodes and anodes.* Solid State Ionics, (1996). **86-88**(Part 2): p. 1223-1234.
2. Atkinson A, Barnett S, Gorte RJ, Irvine JTS, McEvoy AJ, Mogensen M, et al., *Advanced anodes for high-temperature fuel cells.* Nature Materials, (2004). **3**(1): p. 17-27.

3. Fergus JW, *Oxide anode materials for solid oxide fuel cells.* Solid State Ionics, (2006). **177**(17-18): p. 1529-1541.
4. Goodenough JB and Huang YH, *Alternative anode materials for solid oxide fuel cells.* Journal of Power Sources, (2007). **173**(1): p. 1-10.
5. Sun CW and Stimming U, *Recent anode advances in solid oxide fuel cells.* Journal of Power Sources, (2007). **171**(2): p. 247-260.
6. Irvine JTS, *Perovskite Oxide Anodes for SOFCs*, in *Perovskite Oxide for Solid Oxide Fuel Cells*, T. Ishihara, Editor. (2009). p. 167-182.
7. Park S, Vohs JM, and Gorte RJ, *Direct oxidation of hydrocarbons in a solid-oxide fuel cell.* Nature, (2000). **404**(6775): p. 265-7.
8. Marina OA, Pederson LR, Williams MC, Coffey GW, Meinhardt KD, Nguyen CD, et al., *Electrode performance in reversible solid oxide fuel cells.* Journal of the Electrochemical Society, (2007). **154**(5): p. B452-B459.
9. Blennow P, *Strontium Titanate-based Anodes for Solid Oxide Fuel Cells*, Ph.D. thesis. (2007), Lund University. p. 209.
10. Blennow P, Hansen KK, Wallenberg LR, and Mogensen M, *Strontium Titanate-based Composite Anodes for Solid Oxide Fuel Cells.* ECS Transactions, (2008). **13**(26): p. 181-194.
11. Blennow P, Hjelm J, Klemenso T, Persson A, Brodersen K, Srivastava A, et al., *Development of planar Metal Supported SOFC with Novel Cermet Anode.* ECS Transactions, (2009). **25**(2): p. 701-710.
12. Goodenough JB, *Electronic and ionic transport properties and other physical aspects of perovskites.* Reports on Progress in Physics, (2004). **67**(11): p. 1915-1993.
13. Jiang SP, *A review of wet impregnation - An alternative method for the fabrication of high performance and nano-structured electrodes of solid oxide fuel cells.* Materials Science and Engineering a-Structural Materials Properties Microstructure and Processing, (2006). **418**(1-2): p. 199-210.
14. Sholklapper TZ, Kurokawa H, Jacobson CP, Visco SJ, and De Jonghe LC, *Nanostructured Solid Oxide Fuel Cell Electrodes.* Nano Letters, (2007). **7**(7): p. 2136-2141.
15. Kim G, Corre G, Irvine JTS, Vohs JM, and Gorte RJ, *Engineering composite oxide SOFC anodes for efficient oxidation of methane.* Electrochemical and Solid State Letters, (2008). **11**(2): p. B16-B19.
16. Kim G, Lee S, Shin JY, Corre G, Irvine JTS, Vohs JM, et al., *Investigation of the Structural and Catalytic Requirements for High-Performance SOFC Anodes Formed by Infiltration of LSCM.* Electrochemical and Solid-State Letters, (2009). **12**(3): p. B48-B52.
17. Lacorre P, Goutenoire F, Bohnke O, Retoux R, and Laligant Y, *Designing fast oxide-ion conductors based on $La_2Mo_2O_9$.* Nature, (2000). **404**(6780): p. 856-858.
18. Porat O, Heremans C, and Tuller HL, *Stability and mixed ionic electronic conduction in $Gd_2(Ti_{1-x}Mo_x)_2O_7$ under anodic conditions.* Solid State Ionics, (1997). **94**(1-4): p. 75-83.
19. Holtappels P, Poulsen FW, and Mogensen M, *Electrical conductivities and chemical stabilities of mixed conducting pyrochlores for SOFC applications.* Solid State Ionics, (2000). **135**(1-4): p. 675-679.
20. Zha S, Cheng Z, and Liu M, *A Sulfur-Tolerant Anode Material for SOFCs.* Electrochemical and Solid-State Letters, (2005). **8**(8): p. A406-A408.
21. Huang Y-H, Dass RI, Denyszyn JC, and Goodenough JB, *Synthesis and Characterization of $Sr_2MgMoO_{6-\delta}$.* Journal of the Electrochemical Society, (2006). **153**(7): p. A1266-A1272.
22. Huang Y-H, Dass RI, Xing Z-L, and Goodenough JB, *Double perovskites as Anode Materials for Solid-Oxide Fuel Cells.* Science, (2006). **312**(5771): p. 254-257.
23. Ji Y, Huang Y-H, Ying J-R, and Goodenough JB, *Electrochemical performance of La-doped $Sr_2MgMoO_{6-\delta}$ in natural gas.* Electrochemistry Communications, (2007). **9**(8): p. 1881-1885.
24. Lu XC and Zhu JH, *Amorphous Ceramic Material as Sulfur-Tolerant Anode for SOFC.* Journal of the Electrochemical Society, (2008). **155**(10): p. B1053-B1057.
25. Greenblatt M, *Molybdenum and Tungsten Bronzes: Low-Dimensional Metals with Unusual properties*, in *Physics and chemistry of low-dimensional inorganic conductors*, C. Schlenker, Editor. (1996). p. 15.
26. Xue Y, Zhang Y, and Zhang P, *Theory of the color change of Na_xWO_3 as a function of Na-charge doping.* Physical Review B (Condensed Matter and Materials Physics), (2009). **79**(20): p. 205113-4.

27. Brown BW and Banks E, *Conductivity of the Sodium Tungsten Bronzes.* Physical Review, (1951). **84**(3): p. 609.
28. Huibregtse EJ, Barker DB, and Danielson GC, *Electrical properties of Sodium Tungsten Bronze.* Physical Review, (1951). **84**(1): p. 142.
29. Garif'yanov N, Khlebnikov S, Khlebnikov I, and Garifullin I, *Superconductivity of sodium tungsten bronze with cubic structure.* Czechoslovak Journal of Physics, (1996). **46**(0): p. 855-856.
30. Wang ZL, *Perovskite and Related Structure Systems*, in *Functional and smart materials: structural evolution and structure analysis*. (1998), Springer - Verlag. p. 124.
31. Brixner LH, *X-ray study and electrical properties of system $Ba_xSr_{(1-x)}MoO_3$.* Journal of Inorganic and Nuclear Chemistry, (1960). **14**(3-4): p. 225-230.
32. Maekawa T, Kurosaki K, Muta H, Uno M, and Yamanaka S, *Thermal and electrical properties of perovskite-type strontium molybdate.* Journal of Alloys and Compounds, (2005). **390**(1-2): p. 314-317.
33. Madeira LM, Portela MF, and Mazzocchia C, *Nickel Molybdate Catalysts and Their Use in the Selective Oxidation of Hydrocarbons.* Catalysis Reviews: Science and Engineering, (2004). **46**(1): p. 53 - 110.
34. Katrib A, Leflaive P, Hilaire L, and Maire G, *Molybdenum based catalysts. I. MoO_2 as the active species in the reforming of hydrocarbons.* Catalysis Letters, (1996). **38**(1): p. 95-99.
35. Kubo J and Ueda W, *Catalytic behavior of AMoOx (A = Ba, Sr) in oxidation of 2-propanol.* Materials Research Bulletin, (2009). **44**(4): p. 906-912.
36. Schulz R, Huot JY, Trudeau ML, Dignardbailey L, Yan ZH, Jin S, et al., *Nanocrystalline Ni-Mo Alloys and their Application in Electrocatalysis.* Journal of Materials Research, (1994). **9**(11): p. 2998-3008.
37. Kawashima A, Akiyama E, Habazaki H, and Hashimoto K. *Characterization of sputter-deposited Ni-Mo and Ni-W alloy electrocatalysts for hydrogen evolution in alkaline solution*. (1997): Elsevier Science Sa Lausanne.
38. Hashimoto K, Sasaki T, Meguro S, and Asami K, *Nanocrystalline electrodeposited Ni-Mo-C cathodes for hydrogen production.* Materials Science and Engineering A, (2004). **375-377**: p. 942-945.
39. Panek J and Budniok A, *Ni plus Mo composite coatings for hydrogen evolution reaction.* Surface and Interface Analysis, (2008). **40**(3-4): p. 237-241.
40. *FactSage 5.5 software.*
41. Itoh M, Ohta I, and Inaguma Y, *Valency pair and properties of 1:1 ordered perovskite-type compounds Sr_2MMoO_6 (M = Mn,Fe,Co).* Materials Science and Engineering B, (1996). **41**(1): p. 55-58.
42. Viola MC, Martinez-Lope MJ, Alonso JA, Velasco P, Martinez JL, Pedregosa JC, et al., *Induction of colossal magnetoresistance in the double perovskite Sr_2CoMoO_6.* Chemistry of Materials, (2002). **14**(2): p. 812-818.
43. Shi JB, Peng PH, Fan YY, Lee CY, Lai WT, Ku HC, et al., *Preparation and physical properties in the double perovskite $Ba_2Fe_{1+x}Mo_{1-x}O_6$.* Physica B: Condensed Matter, (2003). **329-333**(Part 2): p. 731-732.
44. Teraoka Y, Wei MD, and Kagawa S, *Double perovskites containing hexavalent molybdenum and tungsten: synthesis, structural investigation and proposal of a fitness factor to discriminate the crystal symmetry.* Journal of Materials Chemistry, (1998). **8**(11): p. 2323-2325.
45. Shannon RD, *Revised Effective Ionic Radii and Systematic Studies of Interatomic Distances in Halides and Chalcogenides.* Acta Cryst., (1976). **A32**: p. 751-767.
46. Odgaard M and Skou E, *SOFC cathode kinetics investigated by the use of cone shaped electrodes: The effect of polarization and mechanical load.* Solid State Ionics, (1996). **86-8**: p. 1217-1222.
47. Baker R, Guindet J, and Kleitz M, *Classification criteria for solid oxide fuel cell electrode materials.* Journal of the Electrochemical Society, (1997). **144**(7): p. 2427-2432.
48. Kammer K and Mogensen M. *Electro-catalytic processes Studied by the Use of point Electrodes.* in *The 26th Risø International Symposium on Materials Science: Solid State Electrochemistry*. (2005). Roskilde, Denmark: Risø National Laboratory.
49. Kammer K, *Studies of Fe-Co based perovskite cathodes with different A-site cations.* Solid State Ionics, (2006). **177**(11-12): p. 1047-1051.
50. Blennow P, Hansen KK, Wallenberg LR, and Mogensen M, *Effects of Sr/Ti-ratio in $SrTiO_3$-based SOFC anodes investigated by the use of cone-shaped electrodes.* Electrochimica Acta, (2006). **52**(4): p. 1651-1661.

51. Hansen KK, *Electrochemical reduction of NO_2 studied by the use of cone-shaped electrodes.* Electrochemistry Communications, (2007). **9**(11): p. 2721-2724.
52. Hansen KK and Mogensen M, *Evaluation of LSF based SOFC Cathodes using Cone-shaped Electrodes.* ECS Transactions, (2008). **13**(26): p. 153-160.
53. Blennow P, Hansen KK, Wallenberg LR, and Mogensen M, *Electrochemical characterization and redox behavior of Nb-doped $SrTiO_3$.* Solid State Ionics, (2009). **180**(1): p. 63-70.
54. Blennow P, Hagen A, Hansen KK, Wallenberg LR, and Mogensen M, *Defect and electrical transport properties of Nb-doped $SrTiO_3$.* Solid State Ionics, (2008). **179**(35-36): p. 2047-2058.
55. Marina OA, Canfield NL, and Stevenson JW, *Thermal, electrical, and electrocatalytical properties of lanthanum-doped strontium titanate.* Solid State Ionics, (2002). **149**(1-2): p. 21-28.
56. Li X, Zhao H, Xu N, Zhou X, Zhang C, and Chen N, *Electrical conduction behavior of La, Co co-doped $SrTiO_3$ perovskite as anode material for solid oxide fuel cells.* International Journal of Hydrogen Energy, (2009). **34**(15): p. 6407-6414.
57. Li X, Zhao H, Shen W, Gao F, Huang X, Li Y, et al., *Synthesis and properties of Y-doped $SrTiO_3$ as an anode material for SOFCs.* Journal of Power Sources, (2007). **166**(1): p. 47-52.
58. Li X, Zhao H, Gao F, Zhu Z, Chen N, and Shen W, *Synthesis and electrical properties of Co-doped $Y_{0.08}Sr_{0.92}TiO_{3-d}$ as a potential SOFC anode.* Solid State Ionics, (2008). **179**(27-32): p. 1588-1592.
59. Hui SQ and Petric A, *Evaluation of yttrium-doped $SrTiO_3$ as an anode for solid oxide fuel cells.* Journal of the European Ceramic Society, (2002). **22**(9-10): p. 1673-1681.
60. Sun X-F, Guo R-S, and Li J, *Preparation and properties of yttrium-doped $SrTiO_3$ anode materials.* Ceramics International, (2008). **34**(1): p. 219-223.
61. Sun X, Wang S, Wang Z, Qian J, Wen T, and Huang F, *Evaluation of $Sr_{0.88}Y_{0.08}TiO_3$-CeO_2 as composite anode for solid oxide fuel cells running on CH_4 fuel.* Journal of Power Sources, (2009). **187**(1): p. 85-89.
62. Lu XC, Zhu JH, Yang Z, Xia G, and Stevenson JW, *Pd-impregnated SYT/LDC composite as sulfur-tolerant anode for SOFCs.* Journal of Power Sources. In Press**.**
63. Kamata K, Nakamura T, and Sata T, *Valence Stability of Molybdenum in Alkaline Earth Molybdates.* Materials Research Bulletin, (1975). **10**(5): p. 373-378.
64. Hayashi S, Aoki R, and Nakamura T, *Metallic conductivity in perovskite-type compounds $AMoO_3$ (A = Ba, Sr, Ca) down to 2.5K.* Materials Research Bulletin, (1979). **14**(3): p. 409-413.
65. Agarwal R, Singh Z, and Venugopal V, *Calorimetric investigations of $SrMoO_3$ and $BaMoO_3$ compounds.* Journal of Alloys and Compounds, (1999). **282**(1-2): p. 231-235.
66. Yamanaka S, Kurosaki K, Maekawa T, Matsuda T, Kobayashi S-i, and Uno M, *Thermochemical and thermophysical properties of alkaline-earth perovskites.* Journal of Nuclear Materials, (2005). **344**(1-3): p. 61-66.
67. Veith GM, Greenblatt M, Croft M, Ramanujachary KV, Hattrick-Simpers J, Lofland SE, et al., *Synthesis and Characterization of $Sr_3FeMoO_{6.88}$: An Oxygen-Deficient 2D Analogue of the Double perovskite Sr_2FeMoO_6.* Chemistry of Materials, (2005). **17**(10): p. 2562-2567.
68. Prasatkhetragarn A, Ketsuwan P, Maensiri S, Yimnirun R, Huang CC, and Cann DP, *Structure and electrical properties of double perovskite $Sr(Ni_{1/2}Mo_{1/2})O_3$ ceramics.* Journal of Applied Physics, (2009). **106**(9): p. 4.
69. Brixner LH, *X-ray study and electrical properties of the systems $SrMo_xZr_{(1-x)}O_3$ and $SrMo_xTi_{(1-x)}O_3$.* Journal of Inorganic and Nuclear Chemistry, (1960). **15**(3-4): p. 356-358.
70. Fotiev VA, Bazuev GV, and Zubkov VG, *Synthesis and Electric properties of the Solid-solutions $SrV_xMo_{1-x}O_3$ with the perovskite Structure.* Inorganic Materials, (1987). **23**(6): p. 895-898.
71. Karen P, Moodenbaugh AR, Goldberger J, Santhosh PN, and Woodward PM, *Electronic, magnetic and structural properties of A_2VMoO_6 perovskites (A=Ca, Sr).* Journal of Solid State Chemistry, (2006). **179**(7): p. 2120-2125.
72. Fresia EJ, Katz L, and Ward R, *Cation Substitution in perovskite-like phases1,2.* Journal of the American Chemical Society, (1959). **81**(18): p. 4783-4785.
73. Nomura S and Nakagawa T, *Structural and Magnetic Transitions in $Sr_2(NiMo)O_6$.* Journal of the Physical Society of Japan, (1966). **21**(6): p. 1068-&.

74. Gateshki M and Igartua JM, *Crystal structures and phase transitions of the double-perovskite oxides Sr_2CaWO_6 and Sr_2MgWO_6.* Journal of Physics: Condensed Matter, (2004). **16**(37): p. 6639-6649.
75. Lufaso MW, Macquart RB, Lee Y, Vogt T, and Loye H-Cz, *Structural studies of Sr_2GaSbO_6, Sr_2NiMoO_6, and Sr_2FeNbO_6 using pressure and temperature.* Journal of Physics: Condensed Matter, (2006). **18**(39): p. 8761-8780.
76. Ivanov SA, Eriksson SG, Tellgren R, Rundlof H, and Tssegai M. *Structural and magnetic study of magnetoelectric perovskite Sr_2CoMoO_6.* (2006).
77. Eriksson AK, Eriksson SG, Ivanov SA, Knee CS, Eriksen J, Rundlöf H, et al., *High temperature phase transition of the magnetoelectric double perovskite Sr_2NiMoO_6 by neutron diffraction.* Materials Research Bulletin, (2006). **41**(1): p. 144-157.
78. Marrero-López D, Peña-Martínez J, Ruiz-Morales JC, Martín-Sedeño MC, and Núñez P, *High temperature phase transition in SOFC anodes based on Sr_2MgMoO_{6-d}.* Journal of Solid State Chemistry, (2009). **182**(5): p. 1027-1034.
79. Nagai I, Shirakawa N, Ikeda S-i, Iwasaki R, Nishimura H, and Kosaka M, *Highest conductivity oxide $SrMoO_3$ grown by a floating-zone method under ultralow oxygen partial pressure.* Applied Physics Letters, (2005). **87**(2): p. 024105.
80. Zhao BC, Sun YP, Zhang SB, Zhu XB, and Song WH, *Flux growth and characterization of $SrMo_{0.93}O_3$ single crystal.* Journal of Crystal Growth, (2006). **290**(1): p. 292-295.
81. Wang HH, Cui DF, Zhou YL, Chen ZH, Chen F, Zhao T, et al., *Growth and characterization of $SrMoO_3$ thin films.* Journal of Crystal Growth, (2001). **226**(2-3): p. 261-266.
82. Aguadero A, de la Calle C, Alonso JA, Pérez-Coll D, Escudero MJ, and Daza L, *Structure, thermal stability and electrical properties of $Ca(V_{0.5}Mo_{0.5})O_3$ as solid oxide fuel cell anode.* Journal of Power Sources, (2009). **192**(1): p. 78-83.
83. Lan YC, Chen XL, and He M, *Structure, magnetic susceptibility and resistivity properties of $SrVO_3$.* Journal of Alloys and Compounds, (2003). **354**(1-2): p. 95-98.
84. Maekawa T, Kurosaki K, and Yamanaka S, *Physical properties of polycrystalline $SrVO_{3-d}$.* Journal of Alloys and Compounds, (2006). **426**(1-2): p. 46-50.
85. Gross MD, Vohs JM, and Gorte RJ, *A strategy for achieving high performance with SOFC ceramic anodes.* Electrochemical and Solid State Letters, (2007). **10**(4): p. B65-B69.
86. MacManus-Driscoll JL, Sharma A, Bugoslavsky Y, Branford W, Cohen LF, and Wei M, *Reversible Low-Field Magnetoresistance in $Sr_2Fe_{2-x}Mo_xO_{6-d}$ by Oxygen Cycling and the Role of Excess Mo ($x > 1$) in Grain-Boundary Regions.* Advanced Materials, (2006). **18**(7): p. 900-904.
87. Marrero-Lopez D, Pena-Martinez J, Ruiz-Morales JC, Perez-Coll D, Aranda MAG, and Nunez P, *Synthesis, phase stability and electrical conductivity of Sr_2MgMoO_{6-d} anode.* Materials Research Bulletin, (2008). **43**(8-9): p. 2441-2450.
88. Kong L, Liu B, Zhao J, Gu Y, and Zhang Y, *Synthesis of nano-crystalline Sr_2MgMoO_{6-d} anode material by a sol-gel thermolysis method.* Journal of Power Sources, (2009). **188**(1): p. 114-117.
89. Wei T, Ji Y, Meng X, and Zhang Y, *Sr_2NiMoO_{6-d} as anode material for $LaGaO_3$-based solid oxide fuel cell.* Electrochemistry Communications, (2008). **10**(9): p. 1369-1372.
90. Huang Y-H, Liang G, Croft M, Lehtimäki M, Karppinen M, and Goodenough JB, *Double-Perovskite Anode Materials Sr_2MMoO_6 (M = Co, Ni) for Solid Oxide Fuel Cells.* Chemistry of Materials, (2009). **21**(11): p. 2319-2326.
91. Chattopadhyay B, Poddar A, Das S, Majumder C, and Ranganathan R, *Studies of electrical transport properties of $Sr_2Fe(Mo,V)O_6$ compound.* Journal of Alloys and Compounds, (2004). **366**(1-2): p. 28-33.
92. Sher F, Venimadhav A, Blamire MG, Kamenev K, and Attfield JP, *Cation Size Variance Effects in Magnetoresistive Sr_2FeMoO_6 Double perovskites.* Chemistry of Materials, (2005). **17**(1): p. 176-180.
93. Azizi A, Kahoul A, Schmerber G, Colis S, and Dinia A, *H_2/N_2 mixture atmosphere effects on the behavior of the double perovskite compound Sr_2CoMoO_6.* International Journal of Modern Physics B, (2008). **22**(21): p. 3579-3588.
94. Hirama T, Tsujii N, Kitazawa H, and Kido G, *La-substitution effects on double perovskite compound Ba_2CoMoO_6.* Physica B: Condensed Matter, (2005). **359-361**: p. 1336-1338.

95. Gagulin VV, Korchagina SK, Ivanova VV, and Shevchuk YA, *Synthesis and properties of Sr_2CoMoO_6 and Sr_2NiMoO_6.* Inorganic Materials, (2003). **39**(6): p. 625-626.
96. Massa NE, Alonso JA, Martínez-Lope MJ, and Casais MT, *Defect-induced strong electron-phonon interaction and localization in $Sr_2FeMo_{1-x}W_xO_6$ (x=0.0,0.2,0.5,0.8,1.0).* Physical Review B, (2005). **72**(21): p. 214303.
97. Carvajal E, Navarro O, Allub R, Avignon M, and Alascio B, *Electronic properties of double perovskite compounds.* physica status solidi (b), (2005). **242**(9): p. 1942-1945.
98. Ikeda S-I, Shirakawa N, Bando H, and Ootuka Y, *Orbital-Degenerate paramagnetic Metal Sr_2MoO_4: An Electronic Analogue to Sr_2RuO_4.* Journal of the Physical Society of Japan, (2000). **69**(10): p. 3162.
99. Shirakawa N and Ikeda SI, *Phase-relations study of Sr-Mo-O system for new superconductors search.* Physica C: Superconductivity, (2000). **341-348**(Part 2): p. 783-784.
100. Tkachenko EV, Kruglyashov AL, Neiman AY, and Kalyakin AS, Journal of Physical Chemistry, (1977). **51**.
101. Kovalevsky AV, Kharton VV, and Naumovich EN, *Oxygen ion conductivity of hexagonal $La_2W_{1.25}O_{6.75}$.* Materials Letters, (1999). **38**(4): p. 300-304.
102. Matsuda Y, Karppinen M, Yamazaki Y, and Yamauchi H, *Oxygen-vacancy concentration in $A_2MgMoO_{6-\delta}$ double-perovskite oxides.* Journal of Solid State Chemistry, (2009). **182**(7): p. 1713-1716.
103. Marrero-López D, Peña-Martínez J, Ruiz-Morales JC, Gabás M, Núñez P, Aranda MAG, et al., *Redox behaviour, chemical compatibility and electrochemical performance of Sr_2MgMoO_{6-d} as SOFC anode.* Solid State Ionics. **180**(40): p. 1672-1682.
104. Hayakawa T, Andersen AG, Shimizu M, Suzuki K, and Takehira K, *Partial oxidation of methane to synthesis gas over some titanates based perovskite oxides.* Catalysis Letters, (1993). **22**(4): p. 307-317.
105. Hayakawa T, Harihara H, Andersen AG, York APE, Suzuki K, Yasuda H, et al., *A Sustainable Catalyst for the partial Oxidation of Methane to Syngas: $Ni/Ca_{1-x}Sr_xTiO_3$, prepared In Situ from perovskite precursors.* Angewandte Chemie International Edition in English, (1996). **35**(2): p. 192-195.
106. Suzuki S, Hayakawa T, Hamakawa S, Suzuki K, Shishido T, and Takehira K, *Sustainable Ni catalysts prepared by SPC method for CO_2 reforming of CH_4*, in *Natural Gas Conversion V*, A. Parmaliana, et al., Editors. (1998). p. 783-788.
107. Nishihata Y, Mizuki J, Akao T, Tanaka H, Uenishi M, Kimura M, et al., *Self-regeneration of a pd-perovskite catalyst for automotive emissions control.* Nature, (2002). **418**(6894): p. 164-167.
108. Tanaka H, Tan I, Uenishi M, Taniguchi M, Kimura M, Nishihata Y, et al., *$LaFePdO_3$ perovskite automotive catalyst having a self-regenerative function.* Journal of Alloys and Compounds, (2006). **408**: p. 1071-1077.
109. Madsen BD, Kobsiriphat W, Wang Y, Marks LD, and Barnett SA, *Nucleation of nanometer-scale electrocatalyst particles in solid oxide fuel cell anodes.* Journal of Power Sources, (2007). **166**(1): p. 64-67.
110. Kobsiriphat W, Madsen BD, Wang Y, Shah M, Marks LD, and Barnett SA, *Nickel- and Ruthenium-Doped Lanthanum Chromite Anodes: Effects of Nanoscale Metal precipitation on Solid Oxide Fuel Cell performance.* Journal of the Electrochemical Society, (2010). **157**(2): p. B279-B284.
111. Falcón H, Barbero JA, Araujo G, Casais MT, Martínez-Lope MJ, Alonso JA, et al., *Double perovskite oxides A_2FeMoO_{6-d} (A=Ca, Sr and Ba) as catalysts for methane combustion.* Applied Catalysis B: Environmental, (2004). **53**(1): p. 37-45.
112. Thijssen JHJS. *The Impact of Scale-Up and production Volume on SOFC Stack Cost.* in *7th Annual SECA Workshop and peer Review.* (2006).
113. Thijssen J. *SOFC Stack Operating Strategies.* in *10th Annual Solid State Energy Conversion Alliance (SECA) Workshop.* (2009). Pittsburgh, PA: NETL.

Chapter 7

7. Conclusions and Outlook

This research has shown that recycling CO_2 and H_2O into hydrocarbon fuels, using renewable or nuclear energy, is certainly feasible and could be used to provide sustainable fuels for transportation and other uses at a large scale. Such fuels are a very interesting energy carrier from a sustainable energy perspective – they are convenient liquid hydrocarbons with high energy density, which can substitute directly into the existing fuel infrastructure, and they are produced from sustainable energy sources like solar and wind.

Ultimately the affordability of the process depends on reducing the cost of the energy source used to drive the process as well as the cost of the energy conversion system used to convert that energy to fuel (and for a closed-loop fuel cycle, the cost of the system that captures CO_2 from the atmosphere also needs to be improved). In this work, high temperature electrolysis of CO_2 and H_2O using solid oxide cells was chosen as a very promising method to perform the energy conversion affordably (efficiently and with a low capital cost). The choice was made via a critical review of the many other methods of energy conversion, such as thermolysis, thermochemical loops, other types of electrolysis, and photoelectrolysis.

An economics analysis was conducted to determine what dominates the cost of fuel production using such a system. The dominant costs of the process are the electricity cost and the cost of the electrolyzer. High temperature electrolysis cells can be run at near-100% electricity-to-syngas efficiency (and the total electricity-to-liquid fuel efficiency was estimated at about 70% on a higher heating value basis). It is in the capital cost that there is room for improvement. Lower internal resistance, lower performance degradation, and lower manufacturing cost of the cell can each reduce the capital cost, and can be traded off. It was found that with reasonable technological developments in the electrolysis cells, CO_2 air capture, and mass production, synthetic hydrocarbons can be produced at a price competitive with today's wholesale gasoline prices (USD \$2/gal) using intermittent renewable electricity that costs 2-3 U.S. cents per kWh.

The three experimental studies of high temperature electrolysis that were conducted were applicable to different aspects of improving the capital cost. The experimental studies yielded the following notable results and discoveries.

- The performance for co-electrolysis of CO_2 and H_2O was found to be high, using a state-of-the-art full cell with a nickel based negative-electrode. The area-specific

resistance for co-electrolysis was slightly lower than for CO_2 electrolysis and slightly higher than for H_2O electrolysis, and closer to that of H_2O electrolysis, suggesting that besides the CO_2 and H_2O electrolysis reactions, the reverse WGS reaction occurs.

- An impedance analysis technique, calculating the distribution function of relaxation times (DRT), was applied to identify the contributions of the various electrode processes to the total cell resistance. Comparison the DRTs of impedance measurements taken under systematically varied test conditions enabled clear visual identification of five electrode processes that contribute to the cell resistance. The processes could be assigned to each electrode and to gas concentration effects by examining their dependence on gas composition changes and temperature. A similar analysis had been done in prior work on different cells in different conditions. Here the technique was further applied to study the degradation mechanisms of the cell without relying on a model. The durability was tested at consecutively higher current densities (and corresponding overpotentials). By analyzing the impedance spectra before and after each segment, it was found that at low current density operation (–0.25 A/cm^2 segment) degradation at the Ni/YSZ electrode was dominant, whereas at higher current densities (–0.5 A/cm^2 and –1.0 A/cm^2), the Ni/YSZ electrode continued to degrade but the serial resistance and degradation at the LSM/YSZ electrode began to also play a major role in the total loss in cell performance. This suggests different degradation mechanisms for high and low current density operation.
- Improving understanding of the reaction mechanisms at the negative-electrode that limit performance and cause it to deteriorate could enable significant improvements in the economics of the full system. In the point-contact metal electrodes study, widely different responses of the different metals to the same changes in test conditions (gas composition, temperature, and polarization) were observed, indicating that the same reaction mechanisms are not shared by the different metals, contrary to some recent studies. Evidence was also found that supports the explanation that impurities segregated to the TPB play a major role and are largely responsible for inconsistencies in the electrode kinetics literature. The significance of microstructure at the TPB was also revealed – the electrodes were activated by an order of magnitude when subjected to extreme conditions of oxidation-reduction and strong cathodic polarization, which induced the formation of a micro/nanostructured TPB. These results, along with an examination of trends in electrode kinetics literature, suggested possible reaction mechanisms for H_2O/CO_2 reduction as well as H_2/CO oxidation.
- Ceramic materials offer potential improvements in several aspects of solid oxide cell affordability. In the ceramic materials study, novel high performance materials were obtained that can provide high electronic conductivity and electrocatalytic activity as part of a solid oxide cell negative-electrode. Unique phenomena were observed for some of the materials – they decomposed into multiple, beneficial phases which

formed a nanostructured surface upon exposure to operating conditions (in certain reducing atmospheres). The new phases and surface features enhanced the electronic conductivity and electrocatalytic activity. Preparing an electrode by performing controlled formation/decomposition of multiple desirable phases and a desirable microstructure (which can take place *in situ*) using these materials is a novel way to produce potentially high-performance electrodes for solid oxide cells.

- By modifying the composition of the molybdate, it was possible to prevent decomposition. Other members of the molybdate family exhibited similarly high electronic conductivity and electrocatalytic activity but did not decompose. The high activity was the result of a different mechanism (besides a nanostructured surface), probably related to the defect chemistry of the material.
- Many of the molybdate materials were significantly activated by cathodic polarization, and they exhibited much higher performance for cathodic (electrolysis) polarization than anodic (fuel cell) polarization, which makes them especially interesting for electrolysis electrodes.
- The polarization resistances of the best molybdate materials were two orders of magnitude lower than that of donor-doped strontium titanates. Whereas nearly all of the molybdates showed higher performance for H_2O electrolysis than CO_2 electrolysis, one with vanadium showed nearly equal performance, and a non-molybdate which exhibits some complementary properties to the best molybdates, Gd-doped ceria in nanoparticle form, was found to be an excellent electrocatalyst for CO_2 electrolysis and CO oxidation (moreso than for H_2O/H_2 for which it is known to be good).

While this work has investigated several important aspects of CO_2 recycling to fuels and solid oxide cells, there is of course much more work to be done. The work presented here points towards some opportunities for exciting research to pursue in the future, such as the following:

- A more thorough systems analysis and optimization of the CO_2 recycling process will be important. The operation of the electrolysis plant needs to be studied in detail and optimized. This includes heat management which will be complicated by intermittent operation, using solar or wind power for example. As well the cell operating point must be optimized, e.g. the current density versus the durability, which is also probably affected significantly by intermittent operation. It is not well known how intermittent operation might affect the cell durability. These parameters have not been studied and it seems they should be a high priority as the cost is approaching feasibility.
- The experimental work presented here sought to discover ways to improve the performance and durability of the electrolysis cells. Further modeling and simulation studies to determine where the possible optimums are in the tradeoff between manufacturing cost, current density, and durability would be very worthwhile.

- The electrode kinetics study provided insight into the reaction mechanisms that take place in the conventional Ni-YSZ negative-electrode. The logical next step would be to derive an electrochemical model based on the proposed mechanism and determine how well it describes the electrochemical measurements.
- The molybdate materials that were investigated showed exceptional electrochemical performance. The composition and extent of reduction play an important role in the electrochemical performance. A more detailed study of the effects of modifying the composition and reduction conditions would be of great interest. In addition, finding the best way to incorporate these high-performance materials into an electrode with optimal porous microstructure could lead to a high performance electrode. Testing out new electrode structures with these materials, and studying the rich interfacial chemistry of these systems, would be a very exciting line of future research.
- In order to implement CO_2 recycling at a large scale, advances in automated operation, and mass production of the components, will most likely be necessary. As mentioned, the active components (the electrodes) of the electrolysis cells seem to only make up a small fraction of the total cost – the cost may be dominated by the balance of the system. Increasing the current density and improving the durability are two avenues towards decreasing the capital cost. Mass production is another possible avenue towards cost reduction of the electrolysis cell (via the manufacturing cost) that was not explored in the present work. Developments in mass production would most likely apply to the rest of the system as well, potentially reducing the cost of each component. Designing the system as modular components that work together would be an interesting way to facilitate mass production and automated operation. Many of the components of the CO_2 recycling system – including the electrolyzers, and photovoltaic panels if one wishes to deploy the system with solar power – are already small scale, modular, and mass produced (which is in fact not the usual paradigm for energy systems, which tend to scale to larger size to reduce the cost). Automated operation may be necessary even if implemented at a small scale if the control schemes for e.g. managing intermittency are complicated. Automated control systems are being developed and are becoming more common in all technological fields to reduce costs. It seems that pushing forward these developments and applying them to this system could significantly improve the cost, and there is a wealth of opportunity for research to figure out the best ways to do this.

8. Appendix 1. Additional Metal-YSZ Electrochemistry Data

After the second oxidation of a Ni point electrode, further characterization was performed, as mentioned in **section 5.3.5.1**. This high-resolution impedance data is included here. It contributes to the description of the original mechanisms (or close to the original mechanisms) of the Ni electrode before oxidation and may be useful for modeling purposes in the future.

Impedance spectra were measured under DC bias at 1000 °C in 50% H_2O/H_2 (**Figure 8-1**). The instability/oscillations at high anodic polarization, observed earlier in the 1000 °C 50% H_2O/H_2 polarization curves, are evident in the impedance spectra (**Figure 8-1a**). As before oxidation, the activity is strongly enhanced during anodic polarization with rising characteristic frequency and not during cathodic polarization. These results show a clear trend during cathodic polarization with first an increase in resistance, with slight decrease in the summit frequency and a diffusion-type limitation, followed by decreasing resistance, with increasing summit frequency and a switch to inductive loop behavior.

At 850 °C after the measurements described above, IS were measured under bias in 50% H_2O/H_2 and then 50% CO_2/CO (**Figure 8-2** and **Figure 8-3** respectively). In comparison with **Figure 5-20**, the results are similar – although under anodic polarization in H_2/H_2O (**Figure 8-2a**), two distinct arcs are not evident as before, and comparison is imperfect because the electrode was not allowed to fully relax and reach steady state before and between measurements. For both H_2/H_2O and CO/CO_2, increasing cathodic bias resulted in the same trend as seen in **Figure 8-1** – increasing resistance to a maximum at around –150 to –200 mV bias followed by decreasing resistance until –300 mV.

Note because the change in impedance did not span orders of magnitude for some cases, the Bode plots of those data do not have a log scale vertical axis as in many prior figures.

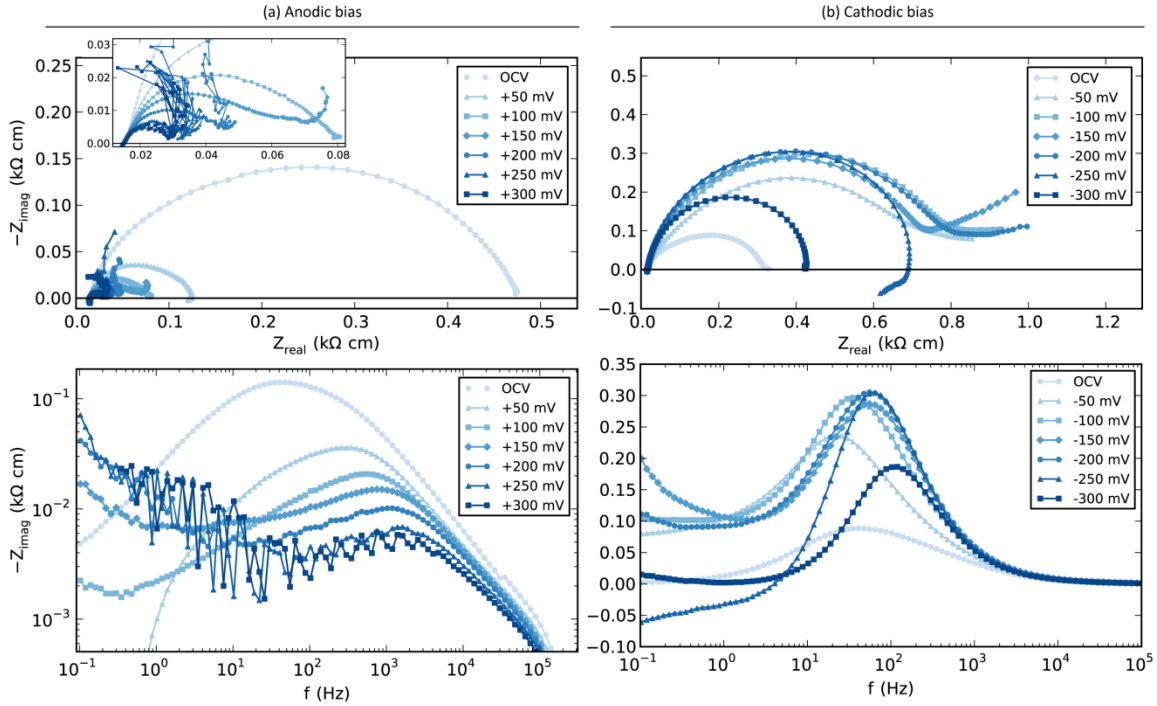

Figure 8-1. Impedance spectra measured on the Ni electrode after oxidation at 1000 °C in 50 % H_2O/H_2 under (a) anodic bias and (b) cathodic bias. No time was allowed for relaxation.

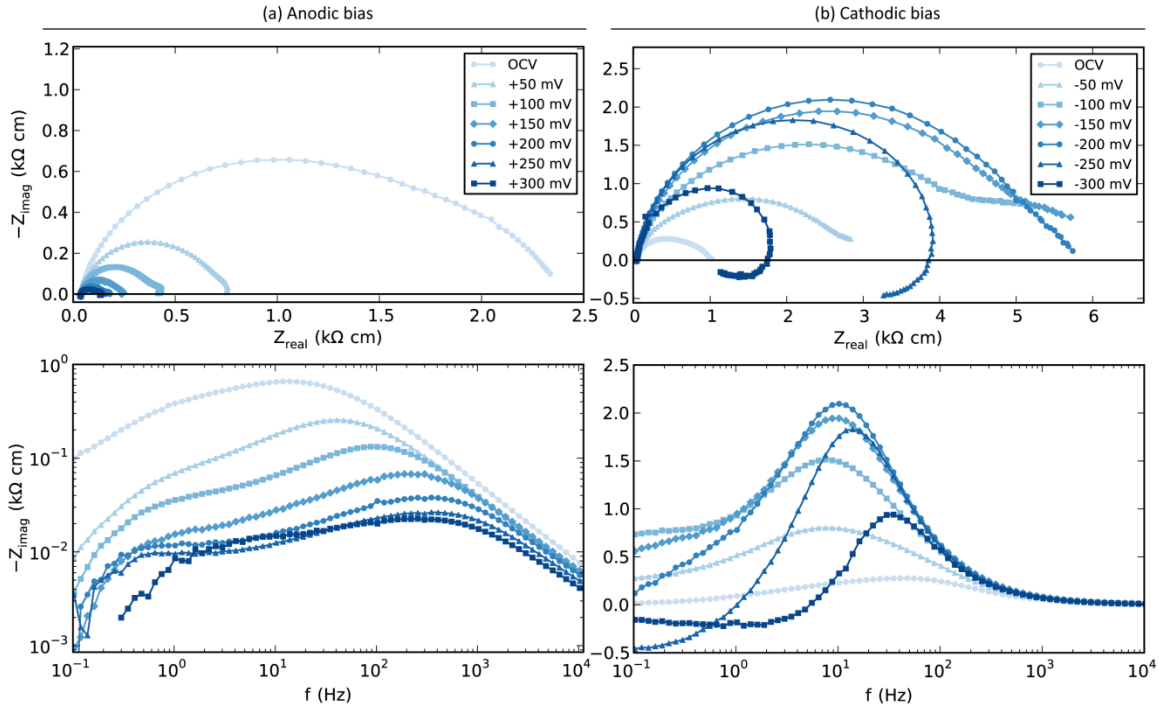

Figure 8-2. Impedance spectra measured on the Ni electrode after oxidation at 850 °C in 50 H_2O/H_2 under (a) anodic bias and (b) cathodic bias. The order was anodic then cathodic. No time was allowed for relaxation.

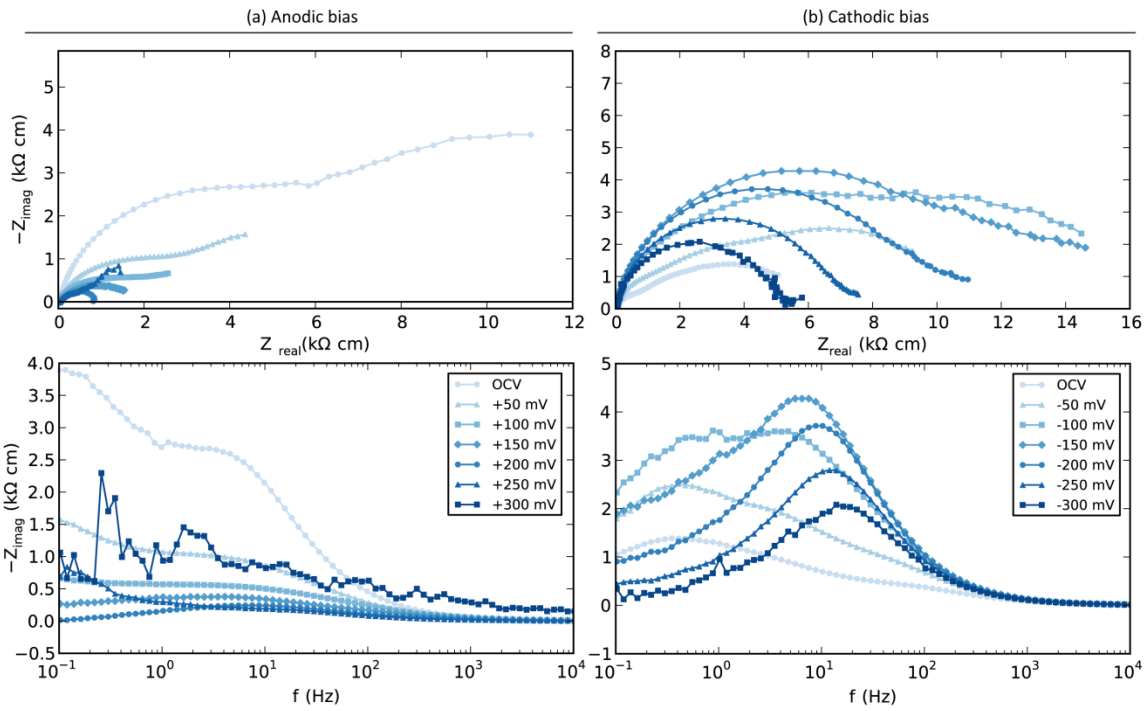

Figure 8-3. Impedance spectra measured on the Ni electrode after oxidation at 850 °C in 50 CO_2/CO under (a) anodic bias and (b) cathodic bias. Note: in the Nyquist plot in (a) the +300 mV spectrum is not shown because it was noisy and would obscure the other data. The order was anodic then cathodic. No time was allowed for relaxation.

9. Appendix 2. Summary of Experiments Conducted

Much more work went into these studies than has been presented, especially for the extensive metal and ceramic electrode materials studies of **Chapter 5** and **6**. A number of additional ceramic materials were prepared, and others were attempted but the desired phase could not be obtained. The additional materials that were prepared and have not been included were left out simply because either they did not exhibit especially interesting properties or no new information was obtained that had not been reported in literature. In these cases the materials were abandoned, but the work done was still useful as it contributed to understanding other related materials.

For the materials that were included in these studies, a number of tests were most often conducted in order to properly understand the material and obtain the desired results (and to repeat experiments when things went wrong with the test set-ups). The experimental process was iterative, with each new result feeding back into the planning of the next tests. By the end, an optimized set of procedures was obtained, from the synthesis of the desired phase to the preparation and testing of the electrodes with an optimal sequence of conditions, with phase and microstructural checks at each stage. These methods took advantage of automated test set-ups, especially for the conductivity and electrochemistry tests (4 cells were tested simultaneously in the electrochemistry set-up), and produced almost more results than could be properly analyzed.

In the end, it was necessary to automate the data analysis as well – automated data collection necessitates automated data processing. A collection of interactive Python scripts were written, as mentioned in the Acknowledgements at the start of this thesis. Creating these tools required a large up-front time investment which saved an enormous amount of time later. The most rewarding part of the analysis part of the work was when the tools became useable, enabling a transition to a productive and enjoyable workflow in which it was exciting (rather than unbearable) to pour through the data, graphically. Without this effort, if the measurements could only be analyzed one at a time, it seems rather certain that the work would have been impossible[i], evident in the statistics given in **Table 9-1**.

[i] That is not to say that this is always the case – a very clearly planned set of experiments can be conducted with a minimal amount of measurements or carefully selected measurements, but this often requires knowing a lot beforehand about how the sample will behave. It most likely depends on the degree to which the work is exploratory in nature.

Table 9-1. Summary of experiments conducted.

Full-cell test[a] (Chapter 4)		
Number of cells tested	7	
Number of electrochemistry measurements[b]		1314
Metals (Chapter 5)		
Number of electrodes tested	26	
Number of electrochemistry measurements[b]		6849
Ceramics (Chapter 6)		
Number of powder samples	367	
Number of dense sintered samples	211	
Number of conductivity samples tested	41	
Number of electrodes tested[c]	64	
Number of electrochemistry measurements[b]		4852
Number of X-ray diffractograms	344	
Number of SEM images taken	1103	

[a] Including the electrolysis test described in **Chapter 4** and a few additional related tests (preliminary button-cell tests at Columbia and two additional full-cell tests conducted in cooperation with Sune Ebbesen at Risø).

[b] The electrochemistry measurements included impedance spectroscopy (accounting for the vast majority), polarization curves, and chronoamperometry. Impedance spectra were measured almost continually during many of the metal and ceramic point electrode tests to monitor the electrodes and determine when steady states were reached. These monitoring measurements account for a large fraction of the total number of measurements.

[c] As mentioned in **section 6.2**, a side project was carried out to compare different simplified electrode geometries, which required a number of different electrodes made from the same material just for that purpose.